

Title	Synthesis of Aza-Polycyclic Aromatic Compounds by Oxidative Transformations of Binaphthalenediamines and Applications to Functional Emissive Molecules
Author(s)	岡崎, 真人
Citation	大阪大学, 2017, 博士論文
Version Type	VoR
URL	https://doi.org/10.18910/61715
rights	
Note	

Osaka University Knowledge Archive : OUKA

<https://ir.library.osaka-u.ac.jp/>

Osaka University

Doctoral Dissertation

**Synthesis of Aza-Polycyclic Aromatic Compounds by
Oxidative Transformations of Binaphthalenediamines and
Applications to Functional Emissive Molecules**

Masato Okazaki

January 2017

Department of Applied Chemistry

Graduate School of Engineering

Osaka University

**Synthesis of Aza-Polycyclic Aromatic Compounds by
Oxidative Transformations of Binaphthalenediamines and
Applications to Functional Emissive Molecules**

(ビナフタレンジアミンの酸化変換による含窒素多環芳香族化合物の合成および
機能性発光分子への応用)

2017

Masato Okazaki

Department of Applied Chemistry

Graduate School of Engineering

Osaka University

Preface

The studies presented in this thesis were conducted under the supervision of Professor Dr. Satoshi Minakata, Department of Applied Chemistry, Graduate School of Engineering, Osaka University during the period of 2011-2017.

The objects of this thesis cover the synthesis of aza-polycyclic aromatic compounds (aza-PACs) through novel oxidative transformations of binaphthalenediamines (BINAMs) and the applications of the resulting aza-PACs to functional emissive molecules. The author hopes sincerely that the fundamental work described in this thesis contributes to further development of synthetic methods and applications in aromatic chemistry, functional material chemistry, and other related fields of chemistry.



Masato Okazaki

Department of Applied Chemistry

Graduate School of Engineering

Osaka University

Suita, Osaka

JAPAN

January, 2017

Contents

Abbreviations	1
General Introduction	3
Chapter 1 A Facile Synthesis of Functionalized 7,8-Diaza[5]helicenes through an Oxidative Ring-Closure of BINAMs	13
Chapter 2 Selective Synthesis of Dibenzo[<i>a,j</i>]phenazines and Spiro[benzo[<i>e</i>]indole-1,1'-inden]-2-amines through Oxidative Skeletal Rearrangements of BINAMs and their Applications to Emissive Molecules	37
Chapter 3 Thermally Activated Delayed Fluorescent Phenothiazine-Dibenzo[<i>a,j</i>]phenazine-Phenothiazine Triads Exhibiting Tricolor-Changing Mechanochromic Luminescence	91
Conclusion	137
List of Publications	141
Copyright	143
Acknowledgement	144

Abbreviations

A	acceptor	Eq	equation
abs	absorption	EQE	external quantum efficiency
Ac	acetyl	equiv	equivalent
AIEE	aggregation-induced emission enhancement	eq-ax	quasi-equatorial/quasi-axial
Alq ₃	tris(8-hydroxyquinoline) aluminum	eq-eq	quasi-equatorial/quasi-equatorial
Ar	aryl	ΔE_{ST}	difference between excited singlet state and triplet state
ATR	attenuated total reflection	Et	ethyl
ax-ax	quasi-axial/quasi-axial	ex	excitation
BDE	bond dissociation energy	FAB	fast atom bombardment
BINAM	binaphthalenediamine	Fc	ferrocene
br	broad	FG	functional group
Bu	butyl	FL	fluorescence
CBP	4,4'-bis(<i>N</i> -carbazolyl)-1,1'-biphenyl	HOMO	highest occupied molecular orbital
cin	cinnamyl	HPLC	high-performance liquid chromatography
const.	constant	HRMS	high-resolution mass spectra
CT	charge transfer	<i>i</i>	iso
CV	cyclic voltammetry	ICT	intramolecular charge transfer
D	donor	IP	ionization potential
d	doublet	IQE	internal quantum efficiency
DABCO	1,4-diazabicyclo[2.2.2]octane	IR	infrared
DBH	1,3-dibromo-5,5-dimethylhydantoin	ISC	intersystem crossing
DBPHZ	dibenzo[<i>a,j</i>]phenazine	ITO	indium tin oxide
DBU	1,8-diazabicyclo[5.4.0]undec-7-ene	LE	locally excited
DCH	1,3-dichloro-5,5-dimethylhydantoin	LUMO	lowest unoccupied molecular orbital
DDQ	2,3-dichloro-5,6-dicyano-1,4-benzoquinone	m	multiplet
dec.	decomposition	max	maximum
DF	delayed fluorescence	MCL	mechanochromic luminescence
DFT	density functional theory	<i>m</i> CPBA	<i>meta</i> -chloroperoxybenzoic acid
DIH	1,3-diiodo-5,5-dimethylhydantoin	Me	methyl
DME	1,2-dimethoxyethane	mp	melting point
DMF	<i>N,N</i> -dimethylformamide	MS	mass spectroscopy
DMSO	dimethyl sulfoxide	<i>n</i>	normal
DSC	differential scanning calorimetry	NBS	<i>N</i> -bromosuccinimide
EA	electron affinity	NCPH	<i>N</i> -chlorophthalimide
E_a	activation energy	NCS	<i>N</i> -chlorosuccinimide
ee	enantiomeric excess	NHC	<i>N</i> -heterocyclic carbene
EI	electron ionization	NIPh	<i>N</i> -iodophthalimide
em	emission	NIPy	<i>N</i> -iodopyrrolidone
		NIR	near infrared
		NIS	<i>N</i> -iodosuccinimide
		NISac	<i>N</i> -iodosaccharin
		NMR	nuclear magnetic resonance

Abbreviations

NPB	<i>N,N'</i> -di-1-naphthyl- <i>N,N'</i> -diphenylbenzidine
OLED	organic light emitting diode
<i>p</i>	para
PAC	polycyclic aromatic compound
PF	prompt fluorescence
PH	phosphorescence
Ph	phenyl
PL	photoluminescence
POZ	phenoxazine
Pr	propyl
PTZ	phenothiazine
PXRD	powder X-ray diffraction
q	quartet
R_f	retention factor
rISC	reverse intersystem crossing
rt	room temperature
s	singlet
SIPr	1,3-bis(2,6-diisopropylphenyl)-2-imidazolidinylidene
SOC	spin orbit coupling
SPhos	2-dicyclohexylphosphino-2',6'-dimethoxybiphenyl
S_1	excited singlet state
t	triplet
<i>t, tert</i>	tertiary
TADF	thermally activated delayed fluorescence
TCCA	trichloroisocyanuric acid
T_d	decomposition temperature
TD-DFT	time-dependent density functional theory
TEA	triethylamine
TFA	trifluoroacetic acid
TGA	thermogravimetric analysis
THF	tetrahydrofuran
TICT	twisted intramolecular charge transfer
TIPS	triisopropylsilyl
TLC	thin layer chromatography
TMS	trimethylsilyl
TPBi	2,2',2''-(1,3,5-benzinetriyl)-tris(1-phenyl-1- <i>H</i> -benzimidazole)
T_1	excited triplet state
UV	ultraviolet
vis	visible

General Introduction

1. Aza-Polycyclic Aromatic Compounds

Aza-polycyclic aromatic compounds (aza-PACs) consist of π -conjugated frameworks that contain fused aromatic rings and more than one nitrogen atoms. Aza-PACs are involved in numerous natural products such as alkaloids, hormones, chlorophyll, vitamins, and antibiotics. They also serve as a key component of industrial products including dyes, pharmaceuticals, and organic electronic materials, due to their interesting features such as aromaticity, electronic structures, and self-assembling properties.¹

Aza-PACs are divided into two categories, i.e., π -electron sufficient type and π -electron deficient type, based on the electronic densities of the fused nitrogen-containing aromatic ring compared with benzene-fused analogues (Figure 1). For example, pyrrole-fused aza-PACs, which are isoelectronic to the cyclopentadienyl anion-fused polycyclic aromatic hydrocarbons, are categorized into π -electron sufficient type (Figure 1a). In contrast, pyridine-fused aza-PACs, which are isoelectronic to benzene-fused polycyclic aromatic compounds, are classified into π -electron deficient type (Figure 1b).

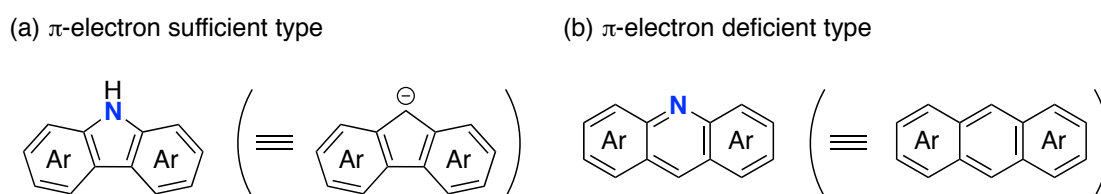
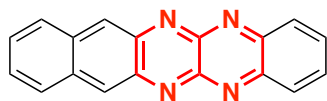
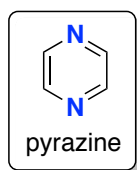


Figure 1. Examples of Two Categories of Aza-PACs

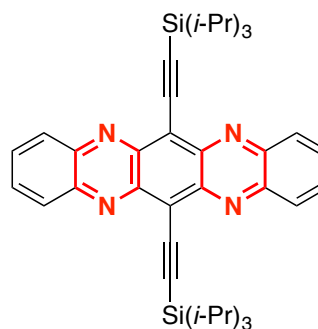
2. π -Electron Deficient Aza-PACs and Their Utility

π -Electron deficient aza-PACs have been emerging as promising candidates for electron-transporting (n-type) materials in organic electronics.¹⁻⁵ The replacement of the parts of C=CH fragments of benzene-fused hydrocarbon frameworks with isoelectronic imine (C=N) moieties allows for increasing electron affinities (EAs) to lower the barriers for electron injection from metal electrodes.⁶ Furthermore, owing to the decrease in the number of C-H \cdots π contacts, π -electron deficient aza-PACs show a high propensity for adopting densely stacked packing-structures in the solid states, which favor a carrier-transporting process.⁷ Therefore, pyrazine-fused aza-PACs have been well studied as electron-transporting materials (Figure 2a).¹⁻⁴ Recently, a few examples of pyridazine-fused aza-PACs have also been exploited as n-type materials (Figure 2b).⁵

(a) pyrazine-fused aza-PACs

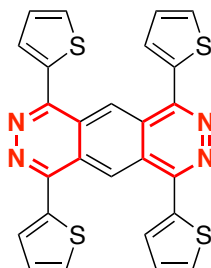
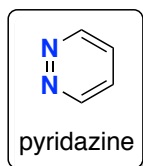


Isoda, K. and Tadokoro, M. et al.
Chem. Lett. **2012**, *41*, 937–939.

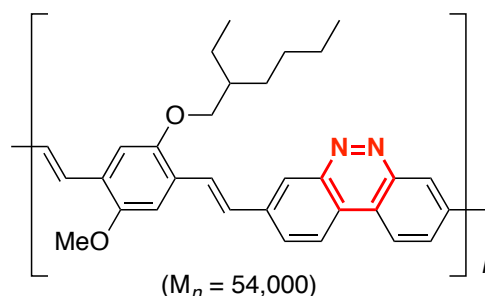


Miao, Q. et al.
Adv. Mater. **2011**, *23*, 1535–1539.

(b) pyridazine-fused aza-PACs



Zhang, F. and Feng, X. et al.
Chem. Commun. **2012**, *48*, 4166–4168.



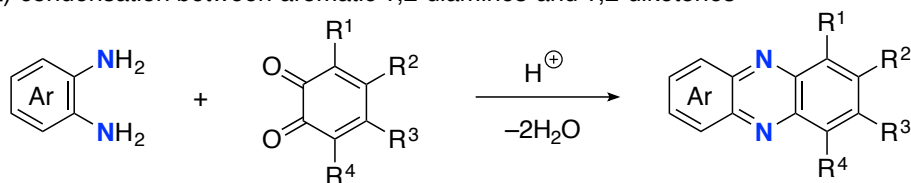
Chen, J.-C. et al.
J. Mater. Chem. C **2014**, *2*, 4835–4846.

Figure 2. Pyrazine- and Pyridazine-Fused Aza-PACs as n-Type Materials

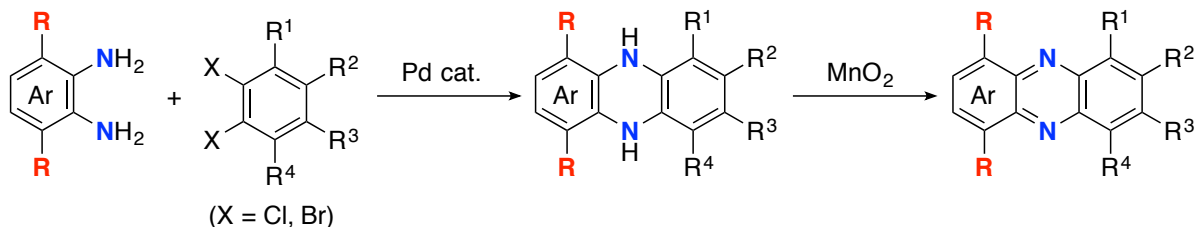
3. Synthetic Methods for Pyrazine- and Pyridazine-Fused Aza-PACs

Traditionally, syntheses of pyrazine-fused aza-PACs have exclusively relied on a condensation protocol using simple aromatic 1,2-diamines and 1,2-diketones (Scheme 1a).³ However, the presence of the *ortho*-substituents on the aromatic diamine substrates severely curtail their reactivities towards the condensation, resulting in relatively low product yields. Recently, a new synthetic protocol for efficient preparation of linear pyrazine-fused aza-PACs, which consists of a Pd-catalyzed double Buchwald-Hartwig amination of activated 1,2-dihaloarenes with aromatic 1,2-diamines and a successive oxidation, has been reported by the Bunz group (Scheme 1b).⁴ Hiroto and Shinokubo have reported a DDQ-promoted oxidative annulation of anthracenylamines, giving pyrazine-cored kinked aza-PACs (Scheme 1c).⁸

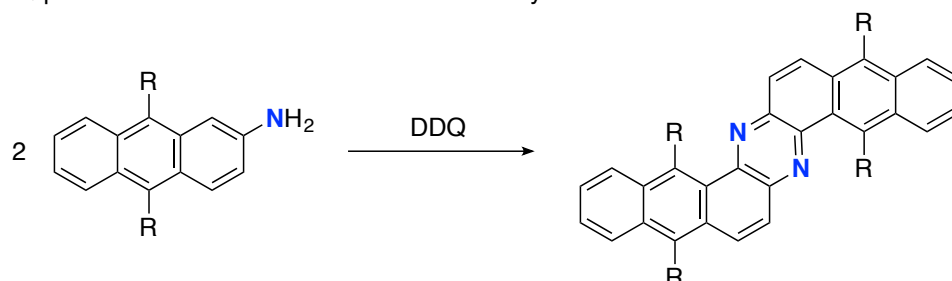
(a) condensation between aromatic 1,2-diamines and 1,2-diketones



(b) Pd-catalyzed cross-coupling of aromatic 1,2-diamines with 1,2-dihaloarenes and successive oxidation



(c) DDQ-promoted oxidative annulation of anthracenylamines



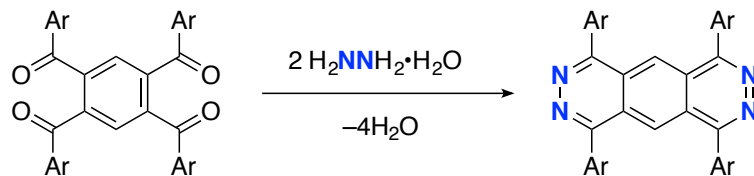
Scheme 1. Conventional Synthetic Methods for Pyrazine-Fused Aza-PACs

Similar to pyrazine-based aza-PACs, linear-type pyridazine-fused aza-PACs are synthesized through condensation of aromatic 1,4-diketones and hydrazine monohydrate (Scheme 2a).^{5a} Bent-type benzo[*c*]cinnoline-containing aza-PACs are conventionally synthesized through reductive ring-closure of 2,2'-dinitrobiaryls (Scheme 2b).^{5b,9} As other methods, the Diels-Alder reaction of perylenes with *in situ* generated diacyldiazenes,^{10a} a base-catalyzed cyclization of 2-amino-3-(2-nitroaryl)quinolines,^{10b} and an oxidative cyclization of 2,2'-biaryldiamines,^{10c,d} have been reported.

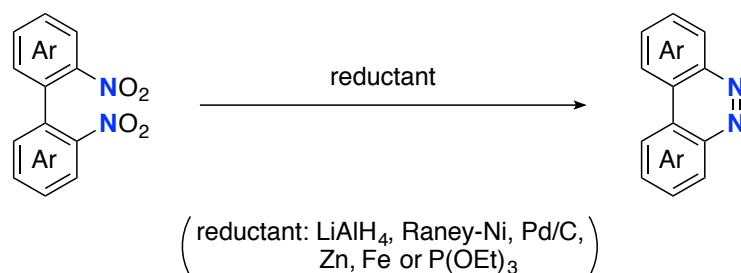
Although synthetic methods for pyrazine- and pyridazine-fused aza-PACs have been widely studied, synthetic approaches to produce aza-PACs possessing various functional groups and repertoire of accessible aza-PAC skeletons are still limited. Due to the synthetic limitations, the exploration of aza-PAC-based materials has fatally lagged behind that of their hydrocarbon counterparts. Therefore, the development of novel synthetic methods for

functionalized aza-PACs is fundamentally important from the viewpoints not only of synthetic chemistry but also of materials science.

(a) condensation between aromatic 1,4-diketones and hydrazine monohydrate



(b) reductive ring-closure of 2,2'-dinitrobiaryls



Scheme 2. Conventional Synthetic Methods for Pyridazine-Fused Aza-PACs

4. Twisted Donor–Acceptor Motifs as Promising Functional Emissive Materials¹¹

In addition to the applicability to n-type materials, another motivation for the development of synthetic approaches to π -electron deficient aza-PACs in material science would be that they can serve as the key component of functional emissive materials by taking advantage of their potentially high electron affinities. Upon photoexcitation, twisted donor–acceptor (D–A) molecules which consist of an electron-donating and an electron-accepting units linked through a single bond can radiate fluorescence from twisted intramolecular charge transfer (TICT) excited state (Figure 3). Due to the polarized nature of the excited state, the emission properties are highly sensitive to surrounding environments such as polarity and viscosity, and therefore, TICT-based emitters can find many possible applications in chemical sensors for solvent polarity, viscosity, and chemical species.¹¹ Furthermore, the TICT phenomenon has been widely studied in the fields of organic optoelectronics and non-linear optics. For these reasons, construction of novel D–A motifs is of significance in applications to emissive materials.

Therefore, the utilization of novel π -electron deficient aza-PACs as an acceptor for D-A molecules would provide diversity in molecular structures and give a tremendous boost to develop functional emissive materials.

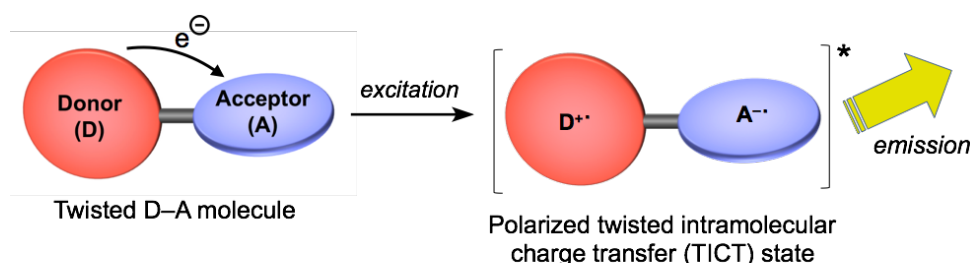
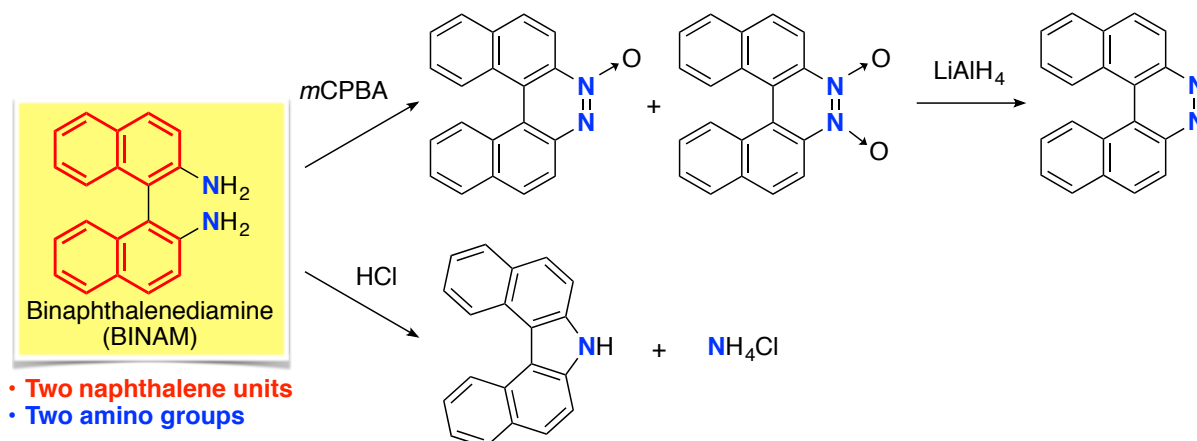


Figure 3. Twisted Intramolecular Charge Transfer (TICT) Dynamics

5. Binaphthalenediamine as a Starting Substrate for the Construction of Novel Aza-PACs

As a platform for the construction of novel aza-PACs, the author focused on binaphthalenediamine (BINAM), which already possesses two extended π -conjugated units (naphthalene) and the nitrogen source (amino groups) in the molecule (Scheme 3). The author envisioned that the establishment of ring-forming reaction by utilizing these functionalities (naphthalene and amino groups) would open up to create novel aza-PACs. Conventionally, functionalized BINAMs can be easily synthesized through a Cu(II)-mediated oxidative dimerization of 2-aminonaphthalenes¹² or a [3,3]-rearrangement of *N,N'*-binaphthyl hydrazines.¹³ Although BINAMs are regarded as a useful scaffold for chiral ligands and organocatalysts,¹⁴ only two transformations of BINAM into aza-PACs have been reported previously.^{10c,15} One involves the oxidative cyclization of BINAM and subsequent reduction of over-oxidized products (*N*-oxide and *N,N'*-dioxide) to produce 7,8-diaza[5]helicene (Scheme 3, the upper equation),^{10c} while another involves an acid-catalyzed condensation for the synthesis of 7*H*-dibenzo[*c,g*]carbazole (Scheme 3, the lower equation).¹⁵ Given these facts, there is a chance to develop transformations of BINAMs into aza-PACs, which would lead to fascinating functional molecules.



Scheme 3. Previously Reported Transformations of BINAMs to Aza-PACs

6. Synopsis of This Thesis

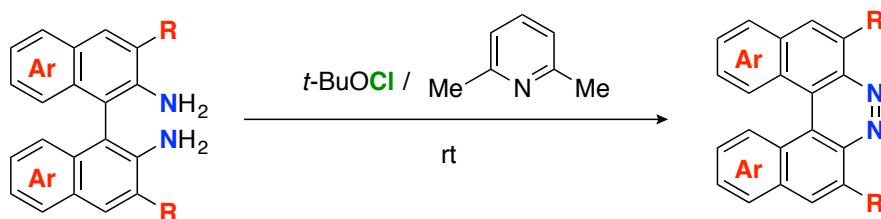
On the basis of these backgrounds, the author has developed three novel transformations of BINAMs to give different aza-PACs and revealed the physicochemical properties of the synthesized aza-PACs and their derivatives (Figure 4). Furthermore, making the use of developed aza-PAC scaffolds, the author has designed and synthesized novel functional emissive molecules (Figure 4). This thesis consists of General Introduction, three Chapters, and Conclusion.

In Chapter 1, a facile synthesis of functionalized 7,8-diaza[5]helicenes through an oxidative ring-closure of BINAMs is described.

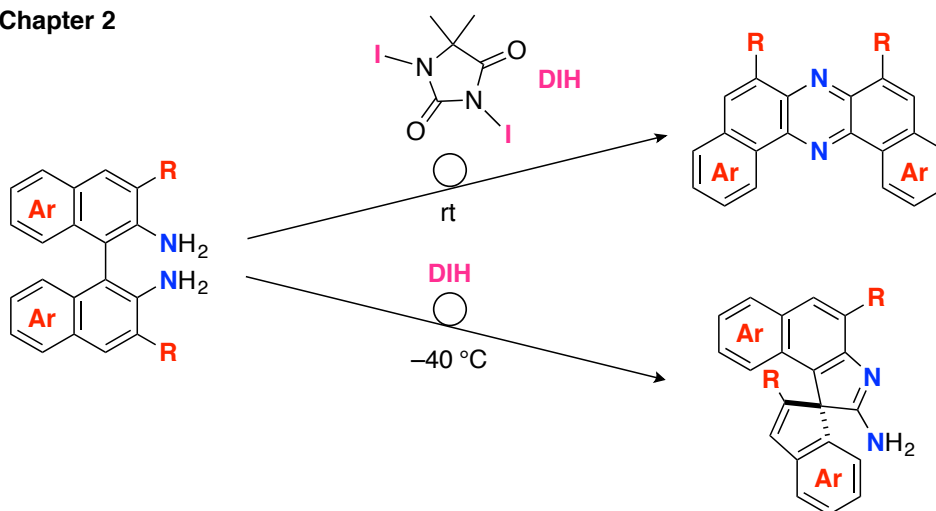
In Chapter 2, selective synthesis of dibenzo[*a,j*]phenazines and spiro[benzo[*e*]indole-1,1'-inden]-2-amines through oxidative skeletal rearrangements of BINAMs and their applications to emissive molecules are described.

In Chapter 3, tricolor-changing mechanochromic luminescence and thermally activated delayed fluorescence properties of dibenzo[*a,j*]phenazine-cored D-A-D molecules are described.

Chapter 1



Chapter 2



Chapter 3

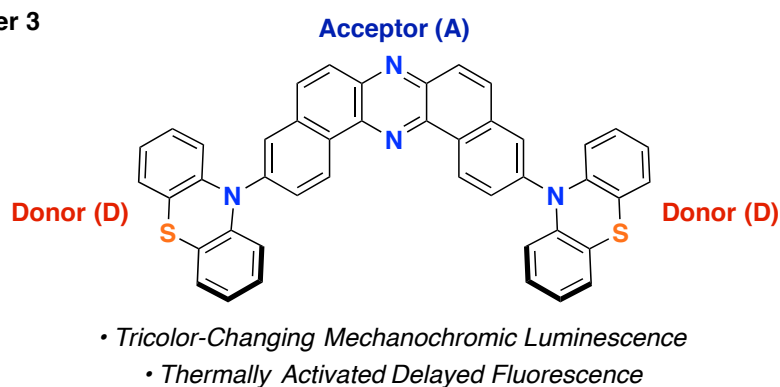


Figure 4. Summary of This Thesis

7. References

1. Miao, Q. *Polycyclic Arenes and Heteroarenes: Synthesis, Properties, and Applications*; Wiley-VCH: Weinheim, Germany, 2016.
2. For reviews on pyrazine-fused aza-PACs, see: (a) Bunz, U. H. F. *Pure Appl. Chem.* **2010**, 82, 953–968. (b) Miao, Q. *Synlett* **2012**, 23, 326–336. (c) Bunz, U. H. F.; Engelhart, J. U.;

- Lindner, B. D.; Schaffroth, M. *Angew. Chem., Int. Ed.* **2013**, *52*, 3810–3821. (d) Miao, Q. *Adv. Mater.* **2014**, *26*, 5541–5549. (e) Bunz, U. H. F. *Acc. Chem. Res.* **2015**, *48*, 1676–1686.
3. (a) Fogel, Y.; Kastler, M.; Wang, Z.; Andrienko, D.; Bodwell, G. J.; Müllen, K. *J. Am. Chem. Soc.* **2007**, *129*, 11743–11749. (b) Gao, B.; Wang, M.; Cheng, Y.; Wang, L.; Jing, X.; Wang, F. *J. Am. Chem. Soc.* **2008**, *130*, 8297–8306. (c) Appleton, A. L.; Brombosz, S. M.; Barlow, S.; Sears, J. S.; Bredas, J.-L.; Marder, S. R.; Bunz, U. H. F. *Nat. Commun.* **2010**, *1*, 91. (d) Mateo-Alonso, A.; Kulisic, N.; Valenti, G.; Marcaccio, M.; Paolucci, F.; Prato, M. *Chem. Asian J.* **2010**, *5*, 482–485. (e) More, S.; Bhosale, R.; Choudhary, S.; Mateo-Alonso, A. *Org. Lett.* **2012**, *14*, 4170–4173.
4. (a) Tverskoy, O.; Rominger, F.; Peters, A.; Himmel, H.-J.; Bunz, U. H. F. *Angew. Chem., Int. Ed.* **2011**, *50*, 3557–3560. (b) Lindner, B. D.; Engelhart, J. U.; Tverskoy, O.; Appleton, A. L.; Rominger, F.; Peters, A.; Himmel, H.-J.; Bunz, U. H. F. *Angew. Chem., Int. Ed.* **2011**, *50*, 8588–8591.
5. (a) Liu, Y.; Zhang, F.; He, C.; Wu, D.; Zhuang, X.; Xue, M.; Liu, Y.; Feng, X. *Chem. Commun.* **2012**, *48*, 4166–4168. (b) Chen, J.-C.; Wu, H.-C.; Chiang, C.-J.; Chen, T.; Xing, L. *J. Mater. Chem. C* **2014**, *2*, 4835–4846.
6. Winkler, M.; Houk, K. N. *J. Am. Chem. Soc.* **2007**, *129*, 1805–1815.
7. Maly, K. E. *Cryst. Growth Des.* **2011**, *11*, 5628–5633.
8. (a) Akita, M.; Hiroto, S.; Shinokubo, H. *Angew. Chem., Int. Ed.* **2012**, *51*, 2894–2897. (b) Goto, K.; Yamaguchi, R.; Hiroto, S.; Ueno, H.; Kawai, T.; Shinokubo, H. *Angew. Chem., Int. Ed.* **2012**, *51*, 10333–10336. (c) Yokoi, H.; Wachi, N.; Hiroto, S.; Shinokubo, H. *Chem. Commun.* **2014**, *50*, 2715–2717.
9. Buntrock, R. E.; Taylor, E. C. *Chem. Rev.* **1968**, *68*, 209–227.
10. (a) Tokita, S.; Hiruta, K.; Ishikawa, S.; Kitahara, K.; Nishi, H. *Synthesis* **1982**, 854–855. (b) Haddadin, M. J.; Bou Zerdan, R. M.; Kurth, M. J.; Fettinger, J. C. *Org. Lett.* **2010**, *12*, 5502–5505. (c) Caronna, T.; Fontana, F.; Mele, A.; Sora, I. N.; Panzeri, W.; Viganò, L. *Synthesis* **2008**, 413–416. (d) Racané, L.; Čičak, H.; Mihalić, Z.; Karminski-Zamola, G.;

- Tralić-Kulenović, V. *Tetrahedron* **2011**, *67*, 2760–2767.
11. For reviews on TICT, see: (a) Grabowski, Z. R.; Rotkiewicz, K.; Rettig, W. *Chem. Rev.* **2003**, *103*, 3899–4031. (b) Sasaki, S.; Drummen, G. P. C.; Konishi, G. *J. Mater. Chem. C* **2016**, *4*, 2731–2743.
12. (a) Smrčina, M.; Lorenc, M.; Hanuš, V.; Kočovský, P. *Synlett* **1991**, 231–232. (b) Smrčina, M.; Lorenc, M.; Hanuš, V.; Sedmera, P.; Kočovský, P. *J. Org. Chem.* **1992**, *57*, 1917–1920. (c) Vyskočil, Š.; Smrčina, M.; Lorenc, M.; Tišlerová, I.; Brooks, R. D.; Kulagowski, J. J.; Langer, V.; Farrugia, L. J.; Kočovský, P. *J. Org. Chem.* **2001**, *66*, 1359–1365.
13. (a) Lim, Y.-K.; Jung, J.-W.; Lee, H.; Cho, C.-G. *J. Org. Chem.* **2004**, *69*, 5778–5781. (b) De, C. K.; Pesciaoli, F.; List, B. *Angew. Chem., Int. Ed.* **2013**, *52*, 9293–9295. (c) Li, G.-Q.; Gao, H.; Keene, C.; Devonas, M.; Ess, D. H.; Kürti, L. *J. Am. Chem. Soc.* **2013**, *135*, 7414–7417.
14. For selected papers on BINAMs for chiral ligands and organocatalysts, see: (a) Huang, H.; Okuno, T.; Tsuda, K.; Yoshimura, M.; Kitamura, M. *J. Am. Chem. Soc.* **2006**, *128*, 8716–8717. (b) Kano, T.; Tanaka, Y.; Maruoka, K. *Org. Lett.* **2006**, *8*, 2687–2689. (c) Sakakura, A.; Suzuki, K.; Nakano, K.; Ishihara, K. *Org. Lett.* **2006**, *8*, 2229–2232. (d) Sakakura, A.; Suzuki, K.; Ishihara, K. *Adv. Synth. Catal.* **2006**, *348*, 2457–2465. (e) Kano, T.; Tanaka, Y.; Osawa, K.; Yurino, T.; Maruoka, K. *J. Org. Chem.* **2008**, *73*, 7387–7389. (f) Rabalakos, C.; Wulff, W. D. *J. Am. Chem. Soc.* **2008**, *130*, 13524–13525. (g) Alamsetti, S. K.; Mannam, S.; Mutupandi, P.; Sekar, G. *Chem. Eur. J.* **2009**, *15*, 1086–1090.
15. Lim, B.-Y.; Choi, M.-K.; Cho, C.-G. *Tetrahedron Lett.* **2011**, *52*, 6015–6017.

Chapter 1

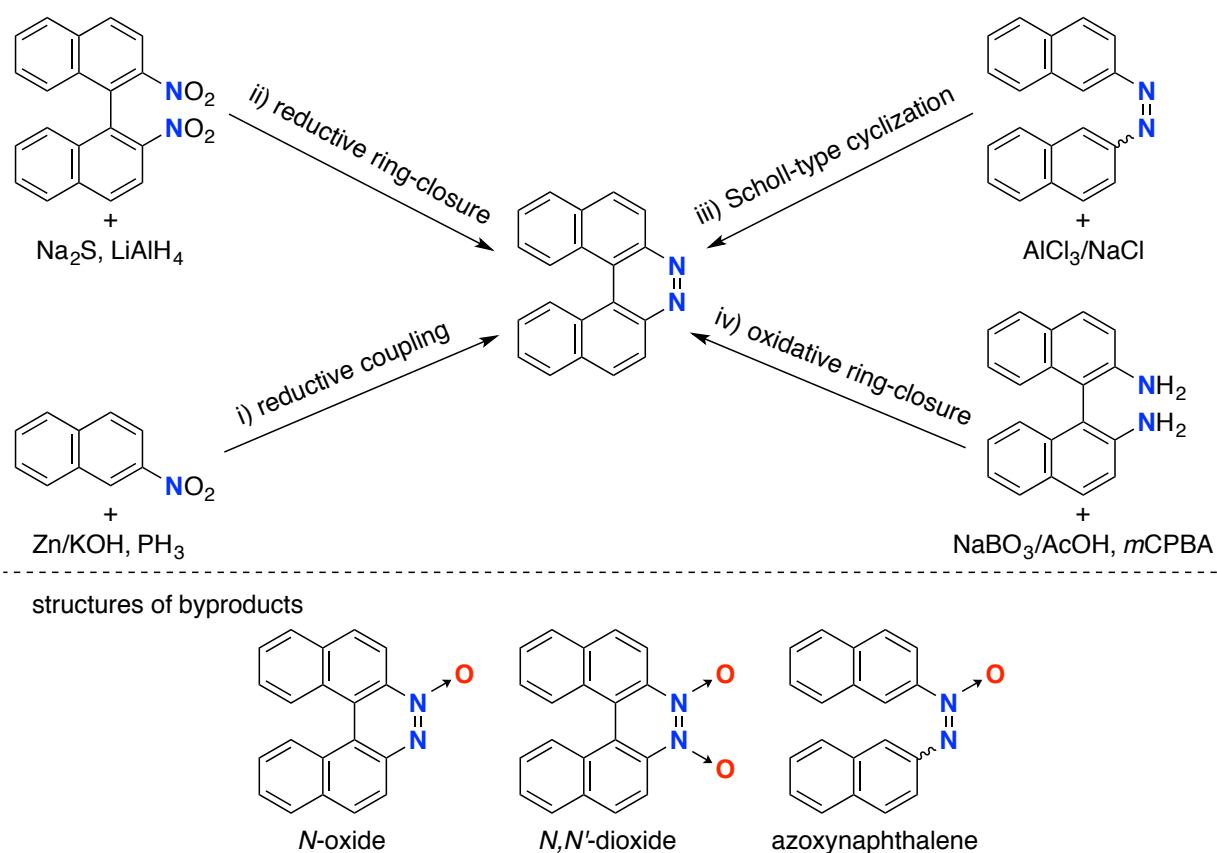
A Facile Synthesis of Functionalized 7,8-Diaza[5]helicenes through an Oxidative Ring-Closure of BINAMs

1-1. Introduction

As mentioned in the General Introduction, little is known about transformations of BINAMs to aza-PACs. Chapter 1 describes the development of a synthetic method for functionalized 7,8-diaza[5]helicenes starting from BINAMs. In addition, the basic photophysical and electrochemical properties of newly synthesized diazahelicenes have been investigated.

Helicenes, *ortho*-fused polycyclic aromatic compounds, have been fascinating organic chemists over the last century since the first synthesis of azahelicenes was reported by Meisenheimer in 1903,¹ because of their aesthetically attractive structures and their unique properties arising from the helical chirality.² In fact, helicenes have been finding more and more potential applications such as optoelectronic materials, asymmetric catalysts, and chemosensors.^{2h} Therefore, the development of synthetic methods for the preparation of helicenes that are difficult to access by conventional methodologies, would offer us many opportunities not only for creating helicene-based novel functional molecules but also

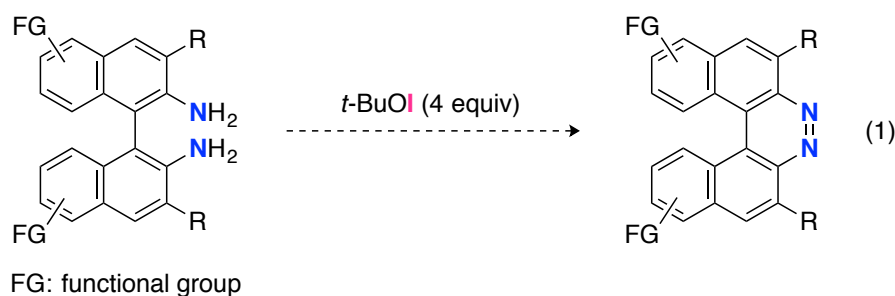
uncovering missing pieces of unique aspects of helicenes. A bibliographic survey about helicenes led the author to focus on diazahelicenes having a diazene ($-N=N-$) moiety, which is a member of the azahelicene family:^{2d} These compounds would be a suitable model for probing the effects of the replacement of carbon atoms at the *K*-region of the carbohelicenes with nitrogen atoms on their structures and physicochemical properties,³ and should serve as ligands to metal complexes through the coordination at the diazene unit.⁴ Taking 7,8-diaza[5]helicene as an example, conventional preparative methods (Scheme 1) involve i) a reductive coupling of 2-nitronaphthalenes using strong reductants like Zn dust^{1,5} and PH_3 ,⁶ ii) a reductive ring-closure of 2,2'-dinitro-1,1'-binaphthalenes using various reductants such as Na_2S and LiAlH_4 ,^{7,8} and iii) the Scholl-type cyclization of 2,2'-azonaphthalenes using a eutectic melt of $\text{AlCl}_3/\text{NaCl}$.⁹ However, these methods require harsh reaction conditions such as the use of strong reductants or oxidants, leading to low functional group compatibility. More importantly, the reductive



Scheme 1. Synthetic Routes to 7,8-Diaza[5]helicene

methods i) and ii) hardly avoid the production of *N*-oxide of diazahelicenes as well as azoxynaphthalenes (Scheme 1), which should be reduced by a strong reductant to the corresponding diazahelicenes. Another synthetic route to 7,8-diaza[5]helicenes would involve an oxidative ring-closure of BINAM (Scheme 1, iv). Corbett and Holt reported that the oxidation of BINAM with NaBO_3 only gave a trace amount of the corresponding diazahelicene.¹⁰ As mentioned in the General Introduction, Caronna and co-workers have recently reported a simple protocol for synthesizing 7,8-diaza[5]helicene through oxidation of BINAM with *m*CPBA and the subsequent reduction of its oxides.¹¹ Although the method is high yielding in two steps, it is not straightforward due to the formation of major amounts of its *N*-oxide and *N,N'*-dioxide (Scheme 1). Furthermore, functional group compatibility of the method still remains an open question, because of the involvement of the reduction process of the oxides employing LiAlH_4 . Therefore, in conjunction with recent advances in preparative methods of functionalized BINAMs,¹² the development of oxidative ring-closing methods that allow for one-step and functional-group-tolerant synthesis of 7,8-diaza[5]helicenes from BINAMs would be desirable.

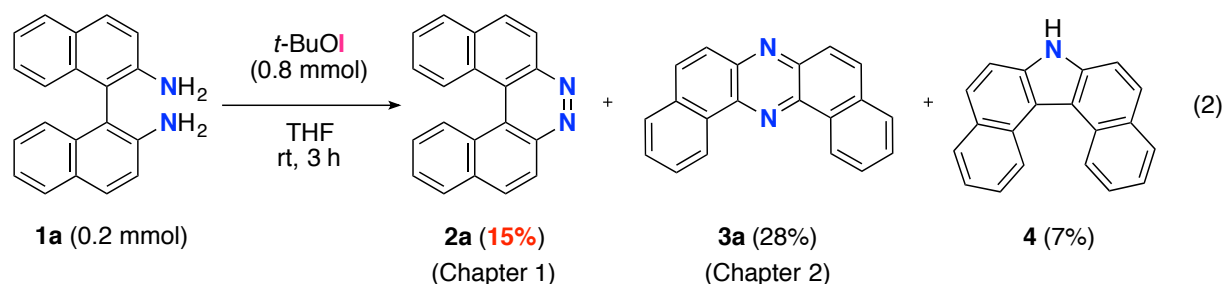
Takeda and Minakata previously developed a synthetic method for various functionalized azo compounds through an oxidative dimerization of aromatic amines utilizing *tert*-butyl hypoiodite (*t*-BuOI) under mild conditions.¹³ The author envisioned that this method would be an effective method for the synthesis of functionalized 7,8-diaza[5]helicenes through an oxidative ring-closure of BINAMs (Eq 1).



Results and Discussion

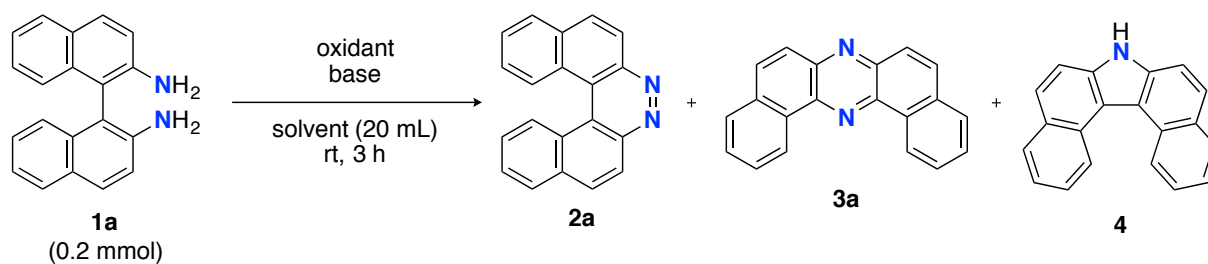
1-2. Reaction of BINAM (1a) with *t*-BuOI

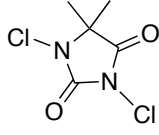
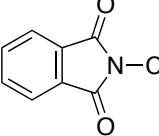
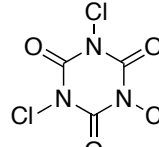
On the basis of the hypothesis described in Introduction, the author examined an oxidative cyclization of BINAM (**1a**) using *t*-BuOI (Eq 2). When 0.2 mmol of **1a** was treated with *t*-BuOI (0.8 mmol) in THF at room temperature for 3 h, the target compound **2a** was isolated in 15% yield and characterized by ¹H and ¹³C NMR spectroscopy.¹¹ Contrary to expectations, in addition to **2a**, a skeletal rearrangement product, that is dibenzo[*a,j*]phenazine (**3a**, characterized by X-ray analysis), and dibenzocarbazole **4**^{12b} were produced in 28% and 7% yield, respectively. The details of the selective synthesis and characterization of **3a** are described in Chapter 2.



1-3. Survey of Reaction Conditions for Selective Synthesis of 2a

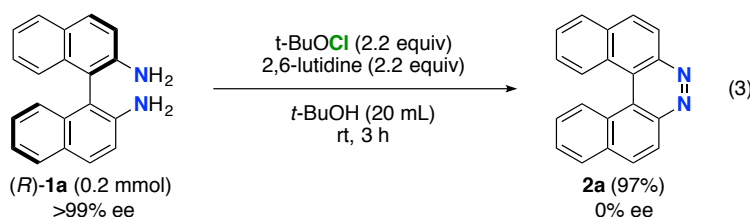
Initially, the author began to identify the optimum reaction conditions (oxidants, bases, and solvents) for the oxidative ring-closure of BINAMs using **1a** as the model substrate (Table 1). As aforementioned, the author recognized that the treatment of **1a** (0.2 mmol) with 0.8 mmol of *t*-BuOI gave diazahelicene **2a** in 15% yield, accompanied with the production of **3a** and **4** (Table 1, entry 1). When *t*-BuOH was used instead of THF, the yield of **2a** decreased, and dibenzophenazine **3a** was produced in a moderate yield (Table 1, entry 2). Chlorine-containing oxidant (*t*-BuOCl) dramatically changed the selectivity of the products to exclusively give **2a** in a high yield (Table 1, entry 3). Encouraged with these results, the author tested a variety of chlorine-containing oxidants to probe the influence of oxidants on the

Table 1. Survey of Reaction Conditions for Selective Synthesis of **2a**

entry	oxidant (mmol)	base (mmol)	solvent	yield (%) ^b			recovery (%) ^b
				2a	3a	4	
1	<i>t</i> -BuOI (0.8)	–	THF ^a	15 ^c	28 ^c	7 ^c	0
2	<i>t</i> -BuOI (0.8)	–	<i>t</i> -BuOH	6	51	3	0
3	<i>t</i> -BuOCl (0.8)	–	<i>t</i> -BuOH	89 ^c	0	0	0
4	NCS (0.8)	–	<i>t</i> -BuOH	0	0	0	63
5	 DCH (0.4)	–	<i>t</i> -BuOH	24 ^c	0	0	0
6	 NCPH (0.8)	–	<i>t</i> -BuOH	0	0	0	95
7	 TCCA (0.27)	–	<i>t</i> -BuOH	20	0	0	0
8	<i>t</i> -BuOCl (0.8)	–	EtOH	61	0	0	0
9	<i>t</i> -BuOCl (0.8)	–	MeOH	58	0	0	0
10	<i>t</i> -BuOCl (0.8)	–	THF	30	0	0	0
11	<i>t</i> -BuOCl (0.8)	–	MeCN	22	0	0	0
12	<i>t</i> -BuOCl (0.8)	–	toluene	68	0	0	0
13	<i>t</i> -BuOCl (0.4)	–	<i>t</i> -BuOH	54	0	0	34
14	<i>t</i> -BuOCl (0.4)	K ₂ CO ₃ (0.4)	<i>t</i> -BuOH	69	0	0	20
15	<i>t</i> -BuOCl (0.4)	DABCO (0.4)	<i>t</i> -BuOH	32	0	0	45
16	<i>t</i> -BuOCl (0.4)	DBU (0.4)	<i>t</i> -BuOH	0	0	0	34
17	<i>t</i> -BuOCl (0.4)	2,6-lutidine (0.4)	<i>t</i> -BuOH	90	0	0	10
18	<i>t</i>-BuOCl (0.44)	2,6-lutidine (0.44)	<i>t</i> -BuOH	97^c	0	0	0

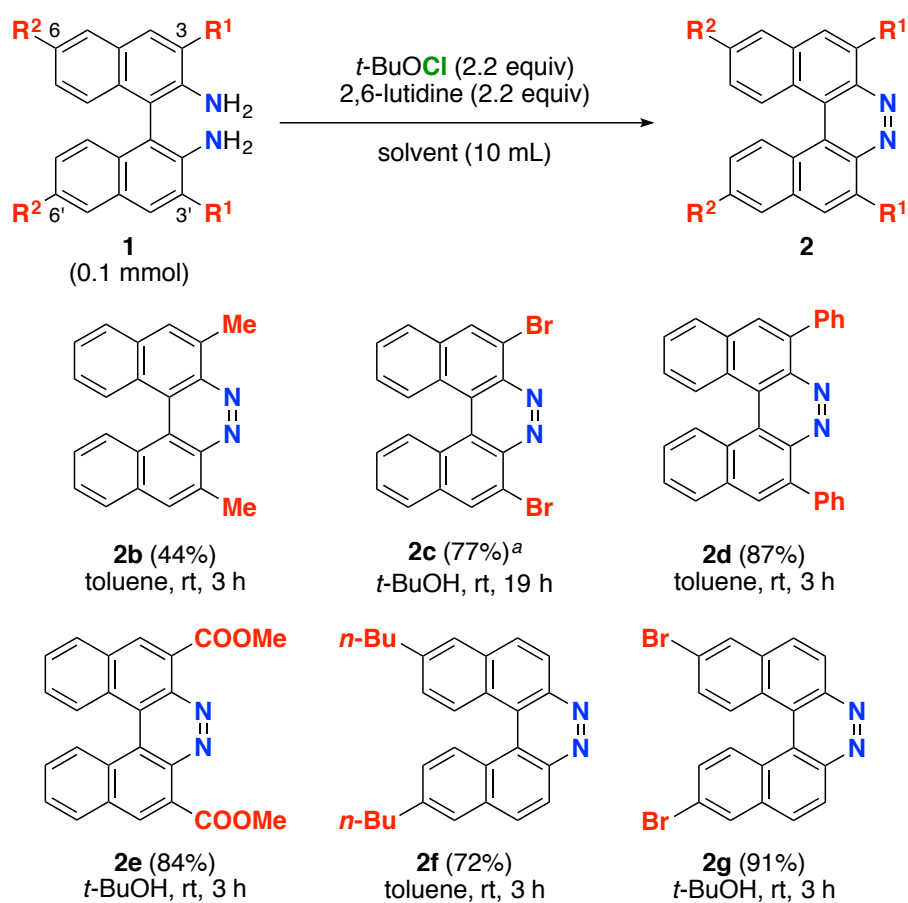
^a 5 mL of THF was used. ^b ¹H NMR yields. ^c isolated yield.

chemical yields of **2a** (Table 1, entries 4–7). The *N*-monochlorinated reagents, *N*-chlorosuccinimide (NCS, entry 4) and *N*-chlorophthalimide (NCPH, entry 6), did not produce **2a** at all, while di and trichlorinated oxidants 1,3-dichloro-5,5-dimethylhydantoin (DCH, entry 5) and trichloroisocyanuric acid (TCCA, entry 7) gave low yields (ca. 20%) of **2a**. Solvents also significantly affected the yields of **2a** (Table 1, entries 8–12), and *t*-BuOH gave the best yield. In terms of the amounts of oxidant, the use of 0.4 mmol of *t*-BuOCl gave a lower yield of **2a** (54%, entry 13) with a moderate conversion of **1a**, in comparison with the case of using 0.8 mmol of *t*-BuOCl (89%, entry 3). In light of the reaction stoichiometry of the oxidative process, 0.4 mmol of HCl are supposed to be concomitantly generated. Since the reaction would proceed *via* *N*-chlorination (for the detail, see Scheme 2), the protonation on the amino group of **1a** might lead to inhibition of conversion of **1a**. To trap the resulting HCl, the efficacy of base addition was investigated by applying an ideal stoichiometry (0.4 mmol) of *t*-BuOCl (Table 1, entries 14–18). The addition of an inorganic base (K_2CO_3) slightly improved the yield (Table 1, entry 14), while strong organic bases like DABCO (pK_a 8.93 in DMSO¹⁴) and DBU (pK_a 23.9 in MeCN¹⁵) gave a lower yield (32%) and no product, respectively (Table 1, entries 15 and 16). As results, the use of the moderately weak organic base 2,6-lutidine (pK_a 6.72 in water¹⁶) successfully afforded **2a** in high yield (Table 1, entry 17), and a small excess amount (0.44 mmol) of *t*-BuOCl and 2,6-lutidine gave diazahelicene **2a** quantitatively (Table 1, entry 18). When optically pure (*R*)-BINAM (**1a**) (99% ee) was applied to the optimized reaction conditions, racemic **2a** ($[\alpha]_D^{22} = 0.0^\circ$, c 1.0, $CHCl_3$) was obtained, losing the chiral information of **1a** through rapid racemization of optically active **2a** or of the reaction intermediates (Eq 3).



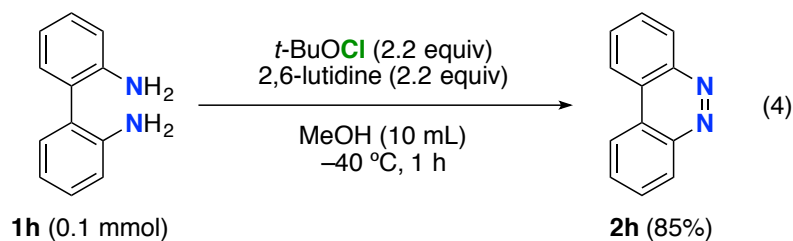
1-4. Selective Synthesis of Various 7,8-Diaza[5]helicenes

Having identified the optimized conditions for the oxidative ring-closure of **1a**, the author then turned his attention to applying this method to the preparation of functionalized 7,8-diaza[5]helicenes (Table 2). When diamine **1b** bearing 3,3'-dimethyl substituents was subjected to the optimized conditions [*t*-BuOCl/2,6-lutidine (2.2 equiv) in *t*-BuOH at room temperature for 3 h], the desired helicene **2b** was obtained in a low yield (32%), even though electron-rich benzylic carbons labile to oxidative conditions are present. Modification studies revealed that the use of toluene as a solvent slightly improved the yield of **2b** (Table 2). Notably, 3,3'-dibromo-substituted diamine **1c** gave a high yield of dibrominated diazahelicene **2c** even in the absence of 2,6-lutidine, albeit in a longer reaction time (Table 2). Such brominated helicene would be difficult to prepare by reductive methods using strong reductants like Zn dust, due to competitive over-reduction of the bromo functionality. It should be noted that the reaction efficiency of the oxidative process was not affected by the steric congestion around the aromatic amino moieties (Table 2, **2d**). Diazahelicene **2e** bearing two electron-withdrawing carboxylic ester groups was also successfully obtained in a high yield (84%) without impairing the ester functionality (Table 2). Again, it is worth emphasizing that such a type of diazahelicene would be difficult to prepare by conventional reductive methods. Furthermore, a BINAM derivative installed with two alkyl substituents at the 6,6'-position, **1f**, was efficiently transformed to the corresponding diazahelicene **2f** in a good yield. Bromo functionalities at the 6,6'-position of BINAM also survived the oxidative conditions to give the corresponding diazahelicene **2g** (Table 2). Regarding the limitation of this oxidative method, diamine substrates having strongly electron-donating substituents (both the 3,3'-MeO and 7,7'-MeO) were not successful, probably due to background side-reactions such as chlorination on the aromatic rings and oxidative oligomerization of BINAMs.

Table 2. Selective Synthesis of 7,8-Diaza[5]helicenes

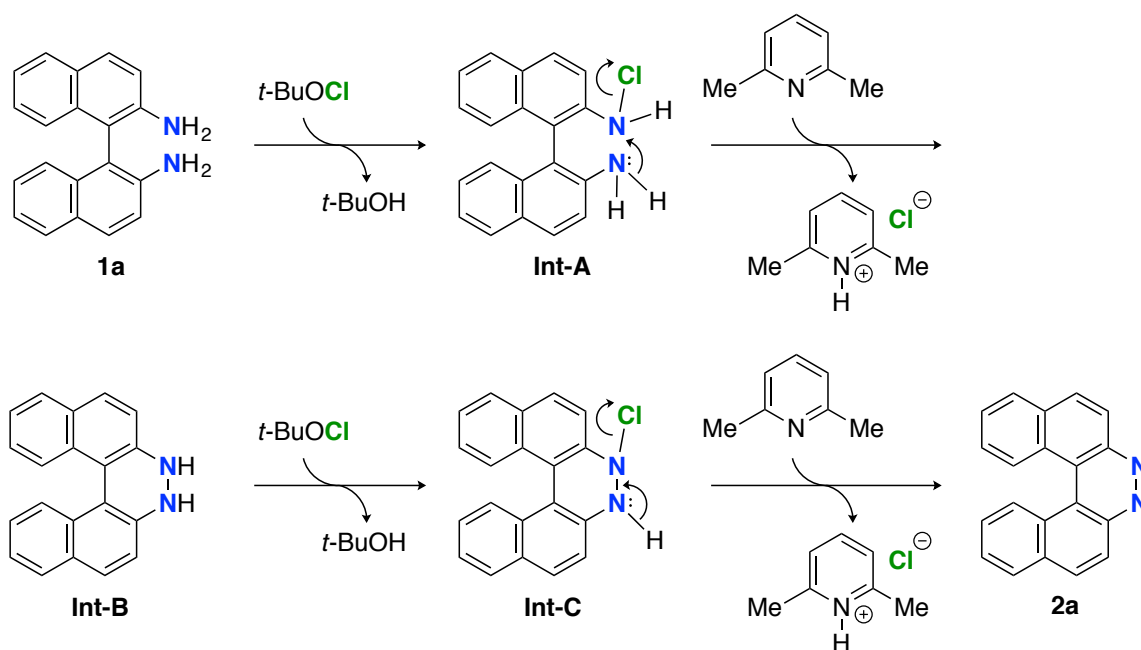
^a *t*-BuOCl (4 equiv) was used without 2,6-lutidine.

Furthermore, this new oxidative method was found to be applicable to the ring-closing of 1,1'-biphenyl-2,2'-diamine (**1h**) leading to benzo[*c*]cinnoline (**2h**) in a good yield, although the reaction temperature was required to be lowered (Eq 4).



1-5. Plausible Reaction Pathway to 7,8-Diaza[5]helicene

A possible reaction pathway of the oxidative ring-closure of **1a** leading to **2a** is illustrated in Scheme 2. Chlorination of an amino group of **1a** with *t*-BuOCl would generate *N*-monochlorinated BINAM (**Int-A**) and release *t*-BuOH. The *N*-chlorination would induce electrophilicity of the amino moiety because of the attachment of electronegative halogen species on the N atom,¹³ and thereby an intramolecular nucleophilic unit ($-NH_2$) would attack the electrophilic N-center to form the N–N single bond (**Int-B**). The organic base (2,6-lutidine) would trap HCl, which was generated through this process. Another repetition of a similar *N*-chlorination/HCl elimination cycle should give **2a** via **Int-C**.



Scheme 2. Plausible Reaction Pathway to **2a**

1-6. Physicochemical Properties of **2**

Since some of the synthesized diazahelicenes **2** are new members of 7,8-diaza[5]helicenes, basic physicochemical properties of **2** were also investigated (Tables 3, 4 and Figure 1 for the full spectra, see the Experimental Section). Diluted dichloromethane solutions of **2** (ca. 10^{-5} M) exhibited UV–vis absorption spectra featuring weak absorptions ascribed to $n-\pi^*$ transitions in

the lower energy region (400–450 nm), an absorption (shoulder at 330–350 nm) and a strong absorption (300–330 nm) ascribed to π - π^* transitions, which are typical to aromatic ring-fused cinnoline derivatives^{3b} (representative spectra are shown in Figure 1). The introduction of two methyl (**2b**) and phenyl groups (**2d**) at the 3,3'-position of BINAM skeleton resulted in a red-shift of the absorption spectra over the whole region (Figure 1). In contrast, the introduction of 6,6'-*n*-Bu substituents (**2f**) caused a blue-shift of n - π^* transitions (380–430 nm), while π - π^* transitions (300–340 nm) were red-shifted. Regarding the emission properties of **2**, it has been known that diazahelicene **2a** shows very low emission quantum yield, due to the small difference between the energy levels of the singlet excited state $^1(n, \pi^*)$ and the triplet excited state $^3(n, \pi^*)$, which accelerate the intersystem crossing and the subsequent non-radiative decay of the triplet excitons.¹⁷ The author expected that the introduction of substituents into a diazahelicene unit would result in improvement of the quantum yield of diazahelicenes. However, dichloromethane solutions (10^{-5} M) of diazahelicenes **2** did not show significant photoluminescence ($\Phi_{\text{FL}} < 0.02$, for the detailed values of quantum yields, Table 3).

Table 3. Summary of Photophysical Properties of Diazahelicenes **2a–2g** and Cinnoline **2h**

	Absorption ^a		Emission (solution) ^a	
	λ_{max} (nm)	ϵ (M ⁻¹ cm ⁻¹)	λ_{ex} (nm)	Φ_{FL}
2a	306, 398, 421	27700, 2300, 2500	300	0.02
2b	312, 408, 431	25300, 2400, 2400	300	<0.01
2c	318, 410, 434	30300, 2600, 2700	300	<0.01
2d	316, 413, 436	31500, 3200, 3300	300	<0.01
2e	309, 397, 419	34000, 3200, 3200	300	<0.01
2f	311, 392, 418	40500, 2700, 2300	300	<0.01
2g	310, 395, 418, 445	31100, 3600, 4300, 2500	300	<0.01
2h	298, 308, 351, 357	9000, 9200, 1500, 1300	300	0.15

^a CH₂Cl₂ solution (10^{-5} M order)

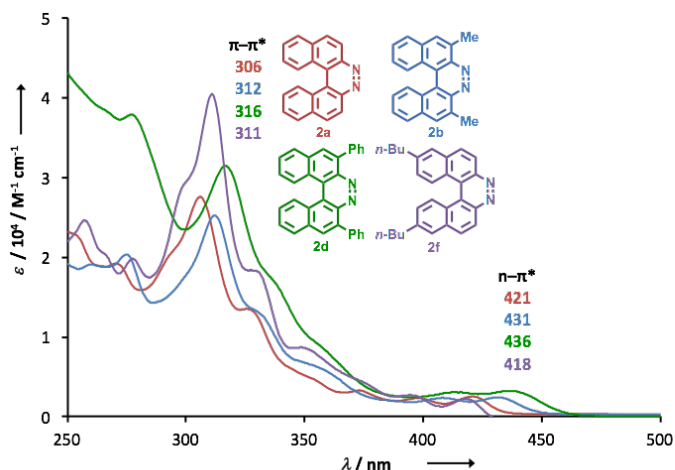


Figure 1. UV-vis Absorption Spectra of CH_2Cl_2 Solutions (10^{-5} order) of **2a**, **2b**, **2d**, and **2f**

Due to the presence of the electronegative diazene ($-\text{N}=\text{N}-$) moiety, diazahelicenes **2** are expected to possess stabilized LUMO energies. The LUMO energies, which were estimated from cyclic voltammetry (CV) experiments [$E_{\text{LUMO}} = -(4.8 + {}^{\text{red}}E_{1/2})$ eV] using diluted CH_2Cl_2 solutions (10^{-4} M) of **2**, range from -2.92 to -3.13 eV (Table 4). These LUMO energy levels fall in a similar range of a well-known electron-transporting materials Alq_3 ¹⁸, suggesting promising electron-accepting abilities of diazahelicenes. Thermogravimetric analysis (Table 4) of **2a–2g** also revealed their high thermal stabilities [T_d (5 wt % loss) = 222 – 315 °C], which are demanded for purification and fabrication of organic optoelectronic devices.

Table 4. Summary of Electrochemical and Thermal Properties of Diazahelicenes **2a–2g** and Cinnoline **2h**

	CV (vs. Fc/Fc^+) ^a				TGA
	${}^{\text{red}}E_{\text{pc}}$ (V)	${}^{\text{red}}E_{\text{pa}}$ (V)	${}^{\text{red}}E_{1/2}$ (V)	LUMO level (eV)	T_d (5 wt% loss) (°C)
2a	-1.92	-1.83	-1.88	-2.92	251
2b	-	-	-	-	268
2c	-1.70	-1.62	-1.66	-3.13	306
2d	-1.93	-1.80	-1.86	-2.93	222
2e	-1.74	-1.61	-1.67	-3.12	315
2f	-	-	-	-	300
2g	-1.80	-1.72	-1.76	-3.03	277
2h	-	-	-	-	172

^a CH_2Cl_2 solution (10^{-4} M order)

1-7. Conclusion

The author has developed a facile and moderately functional-group-tolerant method for the synthesis of 7,8-diaza[5]helicenes through an efficient oxidative ring-closure of BINAMs with the combination of *t*-BuOCl as an oxidant and 2,6-lutidine as a base. This method has been applied to functionalized BINAMs except for highly electron-rich substrates to produce functionalized 7,8-diaza[5]helicenes in a single-step from BINAMs. Furthermore, basic properties of the azahelicenes have also been investigated.

1-8. Experimental Section

General Remarks

All reactions were carried out under an atmosphere of nitrogen unless otherwise noted. Melting points were determined on a Stanford Research Systems MPA100 OptiMelt Automated Melting Point System. ¹H and ¹³C NMR spectra were recorded on a JEOL JMTC-400/54/SS spectrometer (¹H NMR, 400 MHz; ¹³C NMR, 100 MHz) using tetramethylsilane as an internal standard. Infrared spectra were acquired on a SHIMADZU IRAffinity-1 FT-IR Spectrometer. Mass spectra were obtained on a JEOL JMS-DX303HF mass spectrometer. High-resolution mass spectra were obtained on a JEOL JMS-DX303HF mass spectrometer. UV/vis spectra were recorded on a Shimadzu UV-2550 spectrophotometer. Emission spectra were recorded on a HAMAMATSU C11347-01 spectrometer with an integrating sphere. Cyclic voltammetry (CV) was performed with ALS-600 (BAS Inc.) system. Thermogravimetric analysis (TGA) was performed with TG/DTA-7200 (SII) system. Products were purified by chromatography on silica gel BW-300 and Chromatorex NH (Fuji Silysia Chemical Ltd.). Analytical thin-layer chromatography (TLC) was performed on pre-coated silica gel glass plates (Merck silica gel 60 F₂₅₄ and Fuji Silysia Chromatorex NH, 0.25 mm thickness). Compounds were visualized with UV lamp.

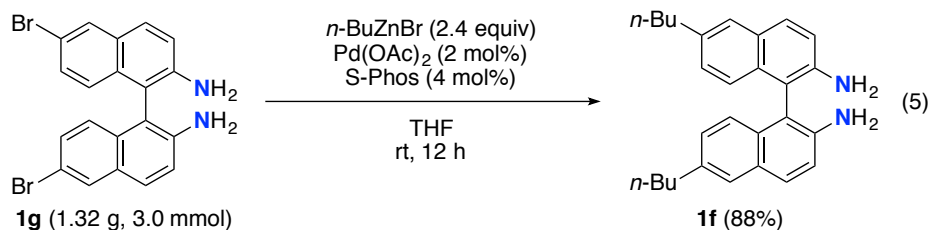
Materials

BINAM (**1a**) was purchased from Sigma-Aldrich and used as received. DBU and 2,6-lutidine were distilled with Kugelrohr apparatus, and other commercial reagents were

purchased from Sigma-Aldrich, TCI, or Wako Pure Chemical Industries, Ltd. and used as received. Alcohol solvents were dried over activated molecular sieves 3A. THF and Et₂O were purchased as dehydrated grade and dried by passing through a glass contour solvent dispensing system (Nikko Hansen & Co., Ltd.). Dehydrated toluene was purchased from Kanto Chemical Co., Inc. and used as received. CH₂Cl₂ (fluorescence spectroscopic grade) was purchased from Kanto Chemical Co., Inc. for the measurement of UV-vis and emission spectra. Biaryldiamines **1b**¹⁹ [360779-01-7], **1c**²⁰ [1051425-55-8, (*R*)-enantiomer], **1d**²¹ [1229013-43-7], **1e**²² [155855-47-3], **1g**²³ [861890-12-2], and **1h**²⁴ [1454-80-4] were prepared according to the procedures in literature.

*Preparation of 6,6'-di-*n*-butyl-1,1'-binaphthalene-2,2'-diamine (1f)*

Binaphthalenediamine **1f** was prepared by modified cross-coupling method²⁵ from binaphthalenediamine **1g** as follows (Eq 5): THF was degassed through freeze-pump-thaw cycling for three times before used. To a two-necked reaction tube (20 mL) equipped with a magnetic stir bar, were added binaphthalenediamine **1g** (1.32 g, 3.0 mmol), Pd(OAc)₂ (13.4 mg, 0.06 mmol), and SPhos (49.2 mg, 0.12 mmol) under the air. The tube was capped with a rubber septum, evacuated, and then refilled with N₂ gas for three times. THF (2 mL) and 0.5 M THF solution of *n*-BuZnBr (14.4 mL, 7.2 mmol) were added to the tube through the septum, and the mixture was stirred under N₂ atmosphere at room temperature for 12 h. To the reaction mixture, was added saturated aqueous NH₄Cl solution (10 mL), and the resulting mixture was extracted with EtOAc (20 mL × 3). The organic extract was dried over Na₂SO₄ and concentrated under vacuum to give the crude product. Purification by flash column chromatography on silica gel (eluent: hexane/EtOAc 8:2) gave binaphthalenediamine **1f** as pale brown solid (1.05 g, 88%). mp 130 °C (dec.); *R*_f 0.13 (hexane/EtOAc 8:2); ¹H NMR (400 MHz, CDCl₃) δ 0.92 (t, *J* = 7.2 Hz, 6H), 1.37 (tq, *J* = 7.2, 7.6 Hz, 4H), 1.63 (tt, *J* = 7.6, 7.6 Hz, 4H), 2.68 (t, *J* = 7.6 Hz, 4H), 3.60 (br, 4 H), 7.01 (d, *J* = 8.8 Hz, 2H), 7.05 (dd, *J* = 1.6, 8.8 Hz, 2H), 7.11 (d, *J* = 8.8 Hz, 2H), 7.56 (d, *J* = 1.6 Hz, 2H), 7.72 (d, *J* = 8.8 Hz, 2H); ¹³C NMR (100 MHz, CDCl₃) δ 13.9, 22.4, 33.5, 35.4, 112.9, 118.3, 123.9, 126.6, 128.3, 128.6, 128.8, 132.0, 136.8, 141.9; IR (ATR) ν 2929, 1606, 1500, 1382, 1282, 824, 810 cm⁻¹; MS (EI): *m/z* (relative intensity, %) 396 (M⁺, 100), 353 ([C₂₅H₂₅N₂]⁺, 45); HRMS (EI): *m/z* calcd for C₂₈H₃₂N₂ (M) 396.2565, found 396.2568.

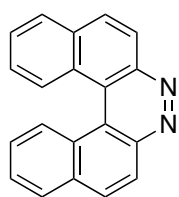


Optimization Studies of Reaction Conditions (Table 1, Eqs 2 and 3)

Typical procedure for the optimization studies using **1a** as substrate

To a two-necked reaction tube (20 mL, entry 1 in Table 1) or a two-necked round-bottomed flask (50 mL, entries 2–18 in Table 1) equipped with a magnetic stir bar, was added binaphthalenediamine **1a** (56.8 mg, 0.2 mmol) under the air. The vessel was capped with a rubber septum and evacuated and refilled with N_2 gas for three times, and an appropriate solvent was added through the septum. To the mixture, were added a base and an appropriate oxidant under a stream of N_2 gas at the indicated temperature. The resulting solution was stirred for 3 h before quenched with aqueous $\text{Na}_2\text{S}_2\text{O}_3$ solution (1.0 M, 20 mL), and the resulting mixture was extracted with CH_2Cl_2 (20 mL \times 3). The combined organic extracts were dried over Na_2SO_4 and concentrated under vacuum to give the crude product. The yields of products were calculated by the integration of ^1H NMR signals of the crude product. Separation by flash column chromatography on silica gel gave product **2a**.

7,8-Diaza[5]helicene (**2a**) [188-55-6]

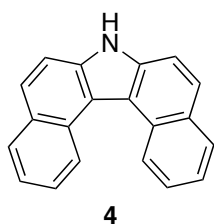


2a

280.1002.

Spectroscopic data were in good agreement with those previously reported;¹¹ Purified by flash column chromatography on silica gel (eluent: hexane/EtOAc, 99:1 to 5:5) and recrystallization from CHCl_3 ; Yellow solid; R_f 0.15 (hexane/EtOAc 8:2); MS (EI): m/z (relative intensity, %) 280 (M^+ , 70), 252 ($[\text{C}_{20}\text{H}_{12}]^+$, 100); HRMS (EI): m/z calcd for $\text{C}_{20}\text{H}_{12}\text{N}_2$ (M) 280.1000, found

7H-Dibenzo[*c,g*]carbazole (**4**) [194-59-2]



4

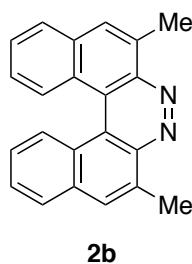
Spectroscopic data were in agreement with those previously reported;^{12b} Purified by flash column chromatography on silica gel (hexane/EtOAc, 99:1 to 7:3); Colorless solid; R_f 0.25 (hexane/EtOAc 8:2). MS (EI): m/z (relative intensity, %) 267 (M^+ , 100); HRMS (EI): m/z calcd for $\text{C}_{20}\text{H}_{13}\text{N}$ (M) 267.1048, found 267.1051.

Oxidative Ring-closure of Biaryldiamines **1b–1h** (Table 2 and Eq 4)

Typical procedure for the oxidative ring-closure of biaryldiamines **1b–1h**

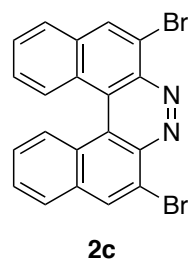
To a two-necked round-bottomed flask (50 mL) equipped with a magnetic stir bar, was added biaryldiamine **1** (0.1 mmol) under the air. The flask was capped with a rubber septum, evacuated, and refilled with N₂ gas for three times. Solvent (10 mL) and 2,6-lutidine (23.5 mg, 0.22 mmol or none) were added to the tube through the septum. To the mixture, was added *t*-BuOCl (23.8 mg, 0.22 mmol or 43.4 mg, 0.40 mmol) through the septum at the indicated temperature. The resulting solution was stirred for the indicated time (Table 2) before quenched with aqueous Na₂S₂O₃ solution (1.0 M, 20 mL), and the resulting mixture was extracted with CH₂Cl₂ (20 mL × 3). The combined organic extracts were dried over Na₂SO₄ and concentrated under vacuum to give the crude product. Purification by flash column chromatography on silica gel gave the corresponding 7,8-diaza[5]helicene (for example, compound **2b**: 13.6 mg, 44%).

6,9-Dimethyl-7,8-diaza[5]helicene (**2b**)



Purified by flash column chromatography on NH silica gel (eluent: hexane/EtOAc 99:1) and recrystallization from hexane; Yellow solid (13.6 mg, 44%); mp 196 °C (dec.); *R*_f 0.33 (hexane/EtOAc 8:2, NH); ¹H NMR (400 MHz, CDCl₃) δ 3.16 (s, 6H), 7.31 (dd, *J* = 8.0, 8.0 Hz, 2H), 7.64 (dd, *J* = 8.0, 8.0 Hz, 2H), 7.91 (d, *J* = 8.0 Hz, 2H), 7.95 (s, 2H), 8.71 (d, *J* = 8.0 Hz, 2H); ¹³C NMR (100 MHz, CDCl₃) δ 18.5, 120.0, 124.5, 127.3, 127.5, 129.2, 129.5, 129.8, 134.0, 134.2, 145.9; IR (ATR) ν 2922, 1734, 1457, 1425, 1261, 1160, 1116, 889, 753 cm⁻¹; MS (EI): *m/z* (relative intensity, %) 308 (M⁺, 100), 280 ([C₂₂H₁₆]⁺, 31); HRMS (EI): *m/z* calcd for C₂₂H₁₆N₂ (M) 308.1313, found 308.1312.

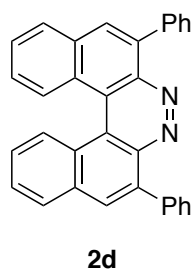
6,9-Dibromo-7,8-diaza[5]helicene (**2c**)



Purified by flash column chromatography on silica gel (eluent: hexane/EtOAc 99:1–95:5) and recrystallization from hexane/CHCl₃; Yellow solid (19.3 mg, 44% or 33.7 mg, 77%); mp 307 °C (dec.); *R*_f 0.40 (hexane/EtOAc 8:2); ¹H NMR (400 MHz, CDCl₃) δ 7.41 (dd, *J* = 8.0, 8.0 Hz, 2H), 7.71 (dd, *J* = 8.0, 8.0 Hz, 2H), 7.94 (d, *J* = 8.0 Hz, 2H), 8.51 (s, 2H), 8.64 (d, *J* = 8.0 Hz, 2H); ¹³C NMR (100 MHz, CDCl₃) δ 121.3, 121.6, 126.0, 127.4, 127.5, 129.5, 130.3, 134.4, 134.5,

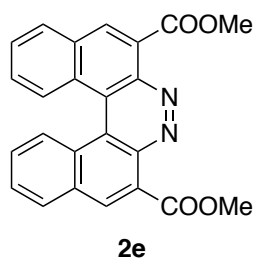
143.6; IR (ATR) ν 3053, 1591, 1383, 1250, 1108, 960, 890, 837, 773, 753 cm^{-1} ; MS (EI): m/z (relative intensity, %) 438 (M^+ , 50), 357 ($[\text{C}_{20}\text{H}_{10}\text{BrN}_2]^+$, 14), 278 ($[\text{C}_{20}\text{H}_{10}\text{N}_2]^+$, 23), 250 ($[\text{C}_{20}\text{H}_{10}]^+$, 100); HRMS (EI): m/z calcd for $\text{C}_{20}\text{H}_{10}\text{Br}_2\text{N}_2$ (M) 435.9211, found 435.9210.

6,9-Diphenyl-7,8-diaza[5]helicene (2d)

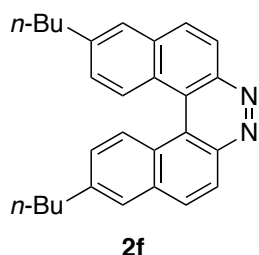


Purified by flash column chromatography on silica gel (eluent: hexane/EtOAc 97:3) and recrystallization from hexane/ CHCl_3 ; Yellow solid (37.6 mg, 87%); mp 239 °C (dec.); R_f 0.35 (hexane/EtOAc 8:2); ^1H NMR (400 MHz, CDCl_3) δ 7.43–7.45 (m, 4H), 7.50 (dd, $J = 7.6, 7.6$ Hz, 4H), 7.72 (dd, $J = 7.6, 7.6$ Hz, 2H), 7.82 (d, $J = 6.8$ Hz, 4H), 8.06 (d, $J = 7.6$ Hz, 2H), 8.17 (s, 2H), 8.79 (d, $J = 8.8$ Hz, 2H); ^{13}C NMR (100 MHz, CDCl_3) δ 120.1, 125.4, 127.7, 128.0, 128.1, 128.3, 129.4, 129.5, 130.9, 131.2, 133.8, 137.8, 138.4, 144.6; IR (ATR) ν 3027, 1494, 1445, 898, 766, 754 cm^{-1} ; MS (EI): m/z (relative intensity, %) 432 (M^+ , 67), 431 ($[\text{C}_{32}\text{H}_{19}\text{N}_2]^+$, 100); HRMS (EI): m/z calcd for $\text{C}_{32}\text{H}_{20}\text{N}_2$ (M) 432.1626, found 432.1624.

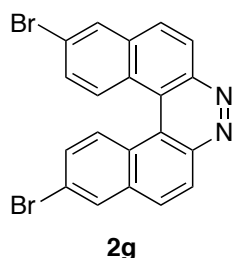
Dimethyl 7,8-diaza[5]helicene-6,9-dicarboxylate (2e)



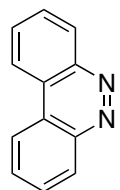
Purified by flash column chromatography on silica gel (eluent: hexane/EtOAc 8:2–5:5) and recrystallization from hexane/ CHCl_3 ; Yellow solid (33.3 mg, 84%); mp 215 °C (dec.); R_f 0.35 (hexane/EtOAc 5:5); ^1H NMR (400 MHz, CDCl_3) δ 4.14 (s, 6H), 7.48 (dd, $J = 8.0, 8.0$ Hz, 2H), 7.75 (dd, $J = 8.0, 8.0$ Hz, 2H), 8.07 (d, $J = 8.0$ Hz, 2H), 8.45 (s, 2H), 8.69 (d, $J = 8.0$ Hz, 2H); ^{13}C NMR (100 MHz, CDCl_3) δ 53.1, 119.7, 127.2, 128.8, 129.1, 129.2, 129.4, 130.1, 132.1, 132.6, 143.3, 168.0; IR (ATR) ν 2942, 1724, 1425, 1269, 1220, 1137, 781, 761 cm^{-1} ; MS (EI): m/z (relative intensity, %) 396 (M^+ , 32), 338 ($[\text{C}_{22}\text{H}_{14}\text{N}_2\text{O}_2]^+$, 100), 250 ($[\text{C}_{20}\text{H}_{10}]^+$, 18); HRMS (EI): m/z calcd for $\text{C}_{24}\text{H}_{16}\text{N}_2\text{O}_4$ (M) 396.1110, found 396.1112.

3,12-Di-*n*-butyl-7,8-diaza[5]helicene (2f)

Purified by flash column chromatography on silica gel (eluent: hexane/EtOAc 9:1–8:2) and recrystallization from hexane; Pale yellow solid (28.2 mg, 72%); mp 161 °C (dec.); R_f 0.18 (hexane/EtOAc 8:2); ^1H NMR (400 MHz, CDCl_3) δ 0.99 (t, $J = 7.6$ Hz, 6H), 1.44 (tq, $J = 7.6, 7.6$ Hz, 4H), 1.76 (tt, $J = 7.6, 7.6$ Hz, 4H), 2.86 (t, $J = 7.6$ Hz, 4H), 7.28 (dd, $J = 1.6, 8.4$ Hz, 2H), 7.80 (d, $J = 1.6$ Hz, 2H), 8.09 (d, $J = 8.8$ Hz, 2H), 8.49 (d, $J = 8.8$ Hz, 2H), 8.75 (d, $J = 8.4$ Hz, 2H); ^{13}C NMR (100 MHz, CDCl_3) δ 13.9, 22.5, 33.3, 35.7, 120.0, 126.1, 126.5, 126.9, 129.1, 130.5, 134.4, 144.6, 146.6 (one carbon is unsatisfied, probably due to the overlap of signals.); IR (ATR) ν 2930, 1618, 1464, 1259, 1105, 891, 827, 810 cm^{-1} ; MS (EI): m/z (relative intensity, %) 392 (M^+ , 100), 364 ($[\text{C}_{28}\text{H}_{28}]^+$, 15), 349 ($[\text{C}_{27}\text{H}_{25}]^+$, 12), 335 ($[\text{C}_{26}\text{H}_{23}]^+$, 31), 321 ($[\text{C}_{25}\text{H}_{21}]^+$, 17), 307 ($[\text{C}_{24}\text{H}_{19}]^+$, 47); HRMS (EI): m/z calcd for $\text{C}_{28}\text{H}_{28}\text{N}_2$ (M) 392.2252, found 392.2251.

3,12-Dibromo-7,8-diaza[5]helicene (2g)

Purified by flash column chromatography on silica gel (eluent: hexane/EtOAc 9:1–7:3) and recrystallization from CHCl_3 ; Brown solid (39.9 mg, 91%); mp 205 °C (dec.); R_f 0.18 (hexane/EtOAc 8:2); ^1H NMR (400 MHz, CDCl_3) δ 7.55 (dd, $J = 2.0, 8.8$ Hz, 2H), 8.09 (d, $J = 8.8$ Hz, 2H), 8.20 (d, $J = 2.0$ Hz, 2H), 8.58 (d, $J = 8.8$ Hz, 2H), 8.61 (d, $J = 8.8$ Hz, 2H); ^{13}C NMR (100 MHz, CDCl_3) δ 119.4, 123.8, 126.4, 127.9, 129.0, 129.8, 130.4, 130.5, 135.6, 146.5; IR (ATR) ν 3061, 1591, 1495, 1436, 1263, 1086, 876, 852, 833, 820, 803 cm^{-1} ; MS (EI): m/z (relative intensity, %) 438 (M^+ , 69), 278 ($[\text{C}_{20}\text{H}_{10}\text{N}_2]^+$, 79), 250 ($[\text{C}_{20}\text{H}_{10}]^+$, 100); HRMS (EI): m/z calcd for $\text{C}_{20}\text{H}_{10}\text{N}_2\text{Br}_2$ (M) 435.9211, found 435.9208.

Benzo[*c*]cinnoline (4) [230-17-1]

Spectroscopic data were in agreement with those previously reported;²⁶ Purified by flash column chromatography on silica gel (hexane/EtOAc 95:5 to 8:2); Yellow solid; R_f 0.18 (hexane/EtOAc 8:2).

Measurements of Photophysical Properties (Table 3, Figures 1 and 2)

CH₂Cl₂ (fluorescence spectroscopic grade) was purged with N₂ for 30 min before the measurements. UV-vis and emission spectra of diazahelicenes **2a–2g** and cinnoline **2h** were measured at room temperature using the CH₂Cl₂ solutions (1.0×10^{-5} M).

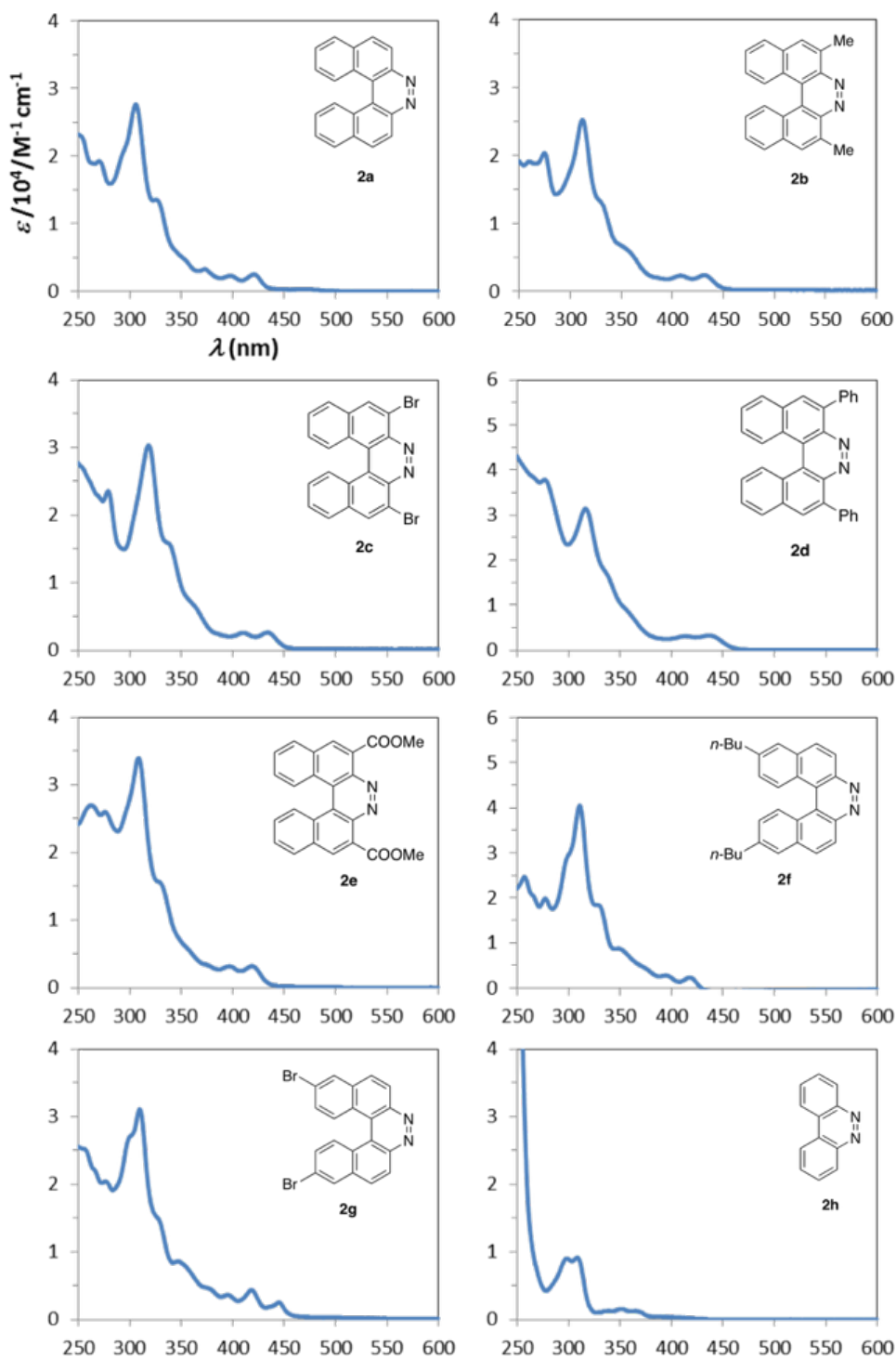


Figure 2. UV-vis Absorption Spectra of **2**

Cyclic Voltammetry (Table 4 and Figure 3)

Cyclic voltammetry experiments were conducted at room temperature with CH_2Cl_2 solutions of diazahelicenes **2a–2g** and cinnoline **2h** (5.0×10^{-4} M) containing 0.1 M tetrabutylammonium hexafluorophosphate as a supporting electrolyte in a cell equipped with a Pt as the working electrode (scanning rate: 100 m/V). A Pt wire and an Ag wire were applied as the counter and the reference electrode, respectively. All the potentials were corrected against the Fc/Fc^+ (Fc = ferrocene) couple and the values of LUMO levels were calculated with the equation 6.

$$\text{LUMO} = -(4.8 + {}^{\text{red}}E_{1/2} \text{ vs. Fc/Fc}^+) [\text{eV}] \quad (6)$$

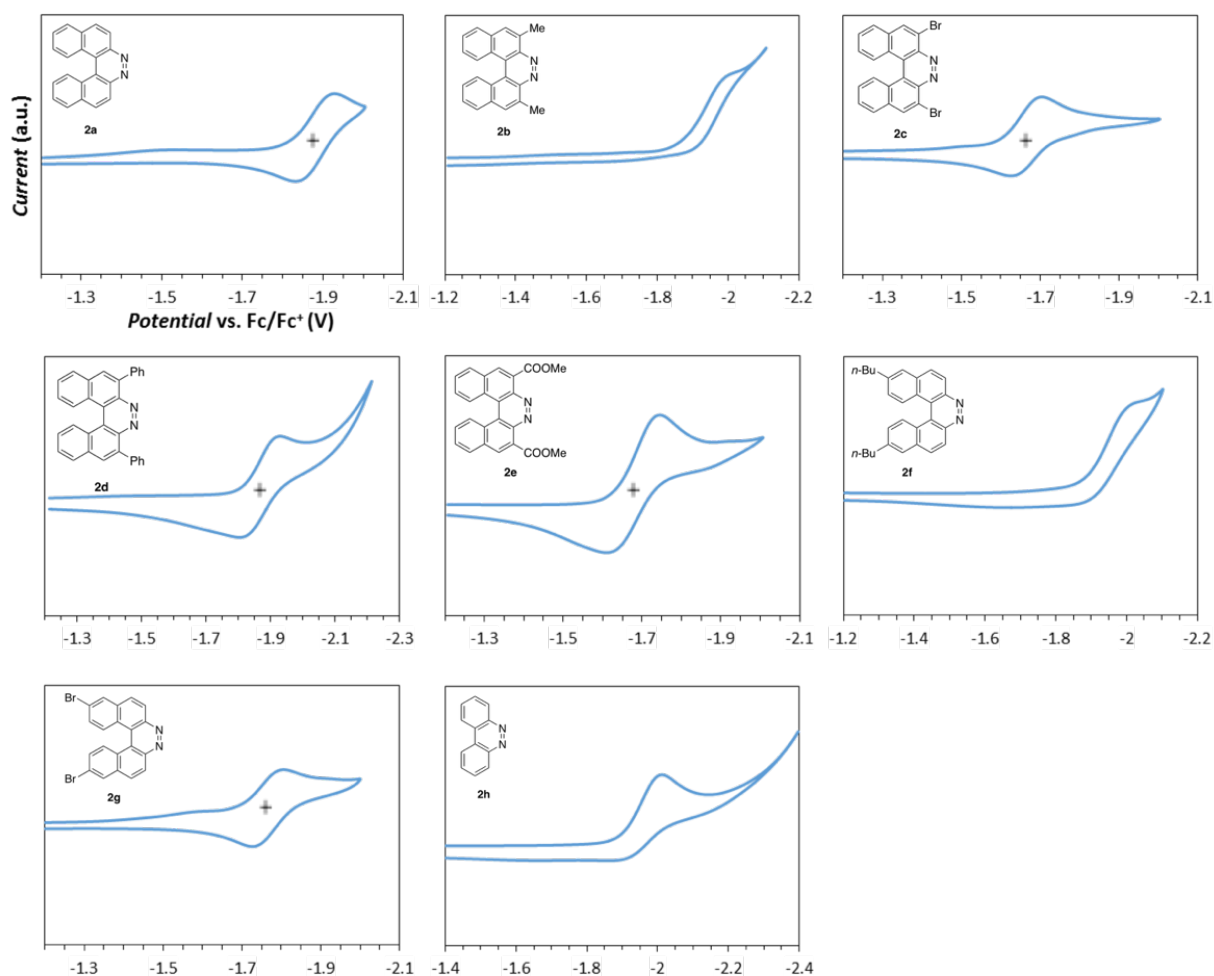


Figure 3. Cyclic Voltammogram of **2**

Thermogravimetric Analysis (TGA) (Table 4 and Figure 4)

All the TGA profiles of diazahelicenes **2a–2g** and cinnoline **2h** were measured under the nitrogen flow (200 mL/min), starting from 40 °C to 600 °C at the ramp rate of 10 °C/min.

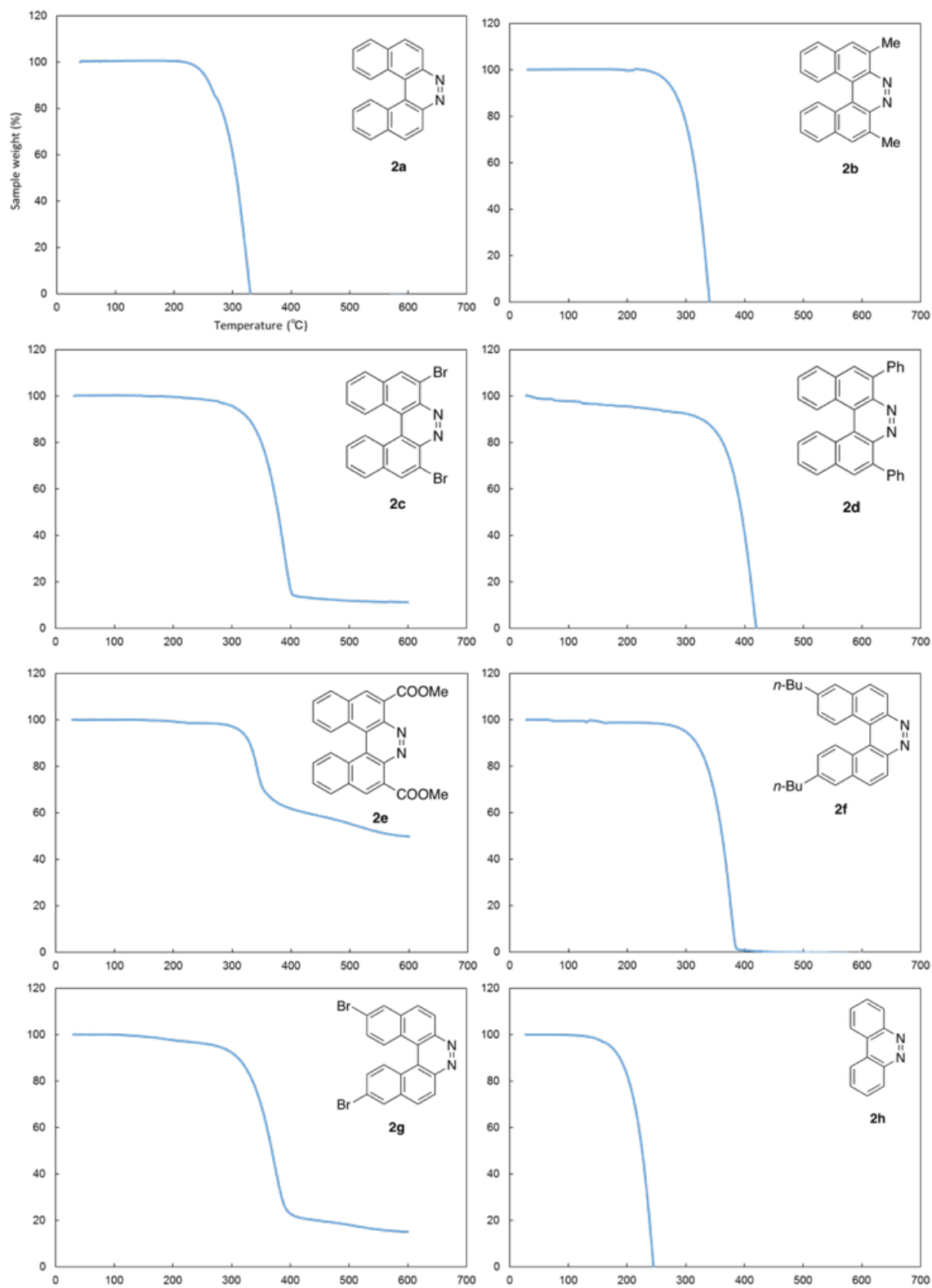


Figure 4. TGA Profiles of **2**

1-9. References and Notes

1. Meisenheimer, J.; Witte, K. *Ber. Dtsch. Chem. Ges.* **1903**, *36*, 4153–4164.
2. (a) Martin, R. H. *Angew. Chem., Int. Ed. Engl.* **1974**, *13*, 649–660. (b) Urbano, A. *Angew. Chem., Int. Ed.* **2003**, *42*, 3986–3989. (c) Collins, S. K.; Vachon, M. P. *Org. Biomol. Chem.* **2006**, *4*, 2518–2524. (d) Dumitrascu, F.; Dumitrescu, D. G.; Aron, I. *ARKIVOC* **2010**, No. i, 1–32. (e) Shen, Y.; Chen, C.-F. *Chem. Rev.* **2012**, *112*, 1463–1535. (f) Gingras, M. *Chem. Soc. Rev.* **2013**, *42*, 968–1006. (g) Gingras, M.; Félix, G.; Peresutti, R. *Chem. Soc. Rev.* **2013**, *42*, 1007–1050. (h) Gingras, M. *Chem. Soc. Rev.* **2013**, *42*, 1051–1095. (i) Aillard, P.; Voituriez, A.; Marinetti, A. *Dalton Trans.* **2014**, *43*, 15263–15278. (j) Saleh, N.; Shen, C.; Crassous, J. *Chem. Sci.* **2014**, *5*, 3680–3694.
3. (a) Corbett, J. F.; Holt, P. F.; Hughes, A. N. *J. Chem. Soc.* **1961**, 1363–1369. (b) Li, W.; Cai, X.; Hu, Y.; Ye, Y.; Luo, M.; Hu, J. *J. Mol. Struct.: THEOCHEM* **2005**, *732*, 21–32. (c) Caronna, T.; Castiglione, F.; Famulari, A.; Fontana, F.; Malpezzi, L.; Mele, A.; Mendola, D.; Sora, I. N. *Molecules* **2012**, *17*, 463–479.
4. (a) Porter, J. J.; Murray, J. L. *J. Am. Chem. Soc.* **1965**, *87*, 1628–1630. (b) Ellgen, P. C.; McMullin, S. L. *Inorg. Chem.* **1973**, *12*, 2004–2007. (c) Nixon, J. F.; Kooti, M. *J. Organomet. Chem.* **1978**, *149*, 71–79.
5. Cumming, W. M.; Ferrier, G. S. *J. Chem. Soc.* **1924**, *125*, 1108–1111.
6. Bellaart, A. C. *Tetrahedron* **1965**, *21*, 3285–3288.
7. Braithwaite, R. S. W.; Holt, P. F. *J. Chem. Soc.* **1959**, 3025–3031.
8. Corbett, J. F.; Holt, P. F. *J. Chem. Soc.* **1960**, 3646–3653.
9. Holt, P. F.; Went, C. W. *J. Chem. Soc.* **1963**, 4099–4102.
10. Corbett, J. F.; Holt, P. F. *J. Chem. Soc.* **1961**, 3695–3699.
11. Caronna, T.; Fontana, F.; Mele, A.; Sora, I. N.; Panzeri, W.; Viganò, L. *Synthesis* **2008**, 413–416.

12. (a) De, C. K.; Pesciaioli, F.; List, B. *Angew. Chem., Int. Ed.* **2013**, *52*, 9293–9295. (b) Li, G.-Q.; Gao, H.; Keene, C.; Devonas, M.; Ess, D. H.; Kürti, L. *J. Am. Chem. Soc.* **2013**, *135*, 7414–7417.
13. (a) Takeda, Y.; Okumura, S.; Minakata, S. *Angew. Chem., Int. Ed.* **2012**, *51*, 7804–7808. (b) Takeda, Y.; Okumura, S.; Minakata, S. *Synthesis* **2013**, *45*, 1029–1033. (c) Okumura, S.; Lin, C.-H.; Takeda, Y.; Minakata, S. *J. Org. Chem.* **2013**, *78*, 12090–12105.
14. Benoit, R. L.; Lefebvre, D.; Fréchet, M. *Can. J. Chem.* **1987**, *65*, 996–1001.
15. Leffek, K. T.; Pruszynski, P.; Thanapaalasingham, K. *Can. J. Chem.* **1989**, *67*, 590–595.
16. Andon, R. J. L.; Cox, J. D.; Herington, E. F. G. *Trans. Faraday Soc.* **1954**, *50*, 918–927.
17. Greiner, G.; Rau, H.; Bonneau, R. *J. Photochem. Photobiol. A: Chem.* **1996**, *95*, 115–125.
18. Burrows, P. E.; Shen, Z.; Bulovic, V.; McCarty, D. M.; Forrest, S. R.; Cronin, J. A.; Thompson, M. E. *J. Appl. Phys.* **1996**, *79*, 7991–8006.
19. Mikami, K.; Korenaga, T.; Yusa, Y.; Yamanaka, M. *Adv. Synth. Catal.* **2003**, *345*, 246–254.
20. Kano, T.; Tanaka, Y.; Osawa, K.; Yurino, T.; Maruoka, K. *J. Org. Chem.* **2008**, *73*, 7387–7389.
21. Scarborough, C. C.; McDonald, R. I.; Hartmann, C.; Sazama, G. T.; Bergant, A.; Stahl, S. *J. Org. Chem.* **2009**, *74*, 2613–2615.
22. (a) Taffarel, E.; Chirayil, S.; Thummel, R. P. *J. Org. Chem.* **1994**, *59*, 823–828. (b) Smrcina, M.; Vyskocil, S.; Maca, B.; Polasek, M.; Claxton, T. A.; Abbott, A. P.; Kocovsky, P. *J. Org. Chem.* **1994**, *59*, 2156–2163.
23. (a) Vilches-Herrera, M.; Miranda-Sepúlveda, J.; Rebolledo-Fuentes, M.; Fierro, A.; Lühr, S.; Iturriaga-Vasquez, P.; Cassels, B. K.; Reyes-Parada, M. *Bioorg. Med. Chem.* **2009**, *17*, 2452–2460. (b) Yan, P.; Millard, A. C.; Wei, M.; Loew, L. M. *J. Am. Chem. Soc.* **2006**, *128*, 11030–11031.
24. Dehghanpour, S.; Afshariazar, F.; Assoud, J. *Polyhedron* **2012**, *35*, 69–76.

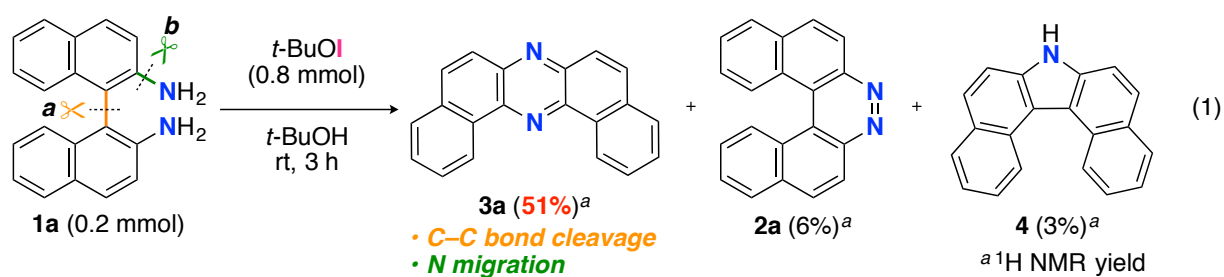
25. Manolikakes, G.; Hernandez, C. M.; Schade, M. A.; Metzger, A.; Knochel, P. *J. Org. Chem.* **2008**, *73*, 8422–8436.
26. Bjørsvik, H.-R.; González, R. R.; Liguori, L. *J. Org. Chem.* **2004**, *69*, 7720–7727.

Chapter 2

Selective Synthesis of Dibenzo[*a,j*]phenazines and Spiro[benzo[*e*]indole-1,1'-inden]-2-amines through Oxidative Skeletal Rearrangements of BINAMs and their Applications to Emissive Molecules

2-1. Introduction

As mentioned in Chapter 1, the author serendipitously found out that the treatment of BINAM (**1a**) with *t*-BuOI produced dibenzo[*a,j*]phenazine (**3a**) in 51% yield along with the production of reasonably expected compounds **2a** (6%) and **4** (3%) (Eq 1).



The structure of **3a** was unambiguously confirmed by the X-ray crystallographic analysis of its yellow single crystal (Figure 1).¹ Spectroscopic data were in agreement with those previously reported.² Considering the electron deficient pyrazine-cored π -extended structure of **3a**, the author expected that dibenzo[*a,j*]phenazines **3** and its derivatives can serve as novel functional materials themselves and as useful building blocks for the construction of D–A type

emissive molecules.

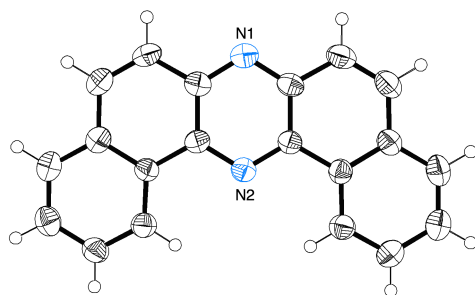
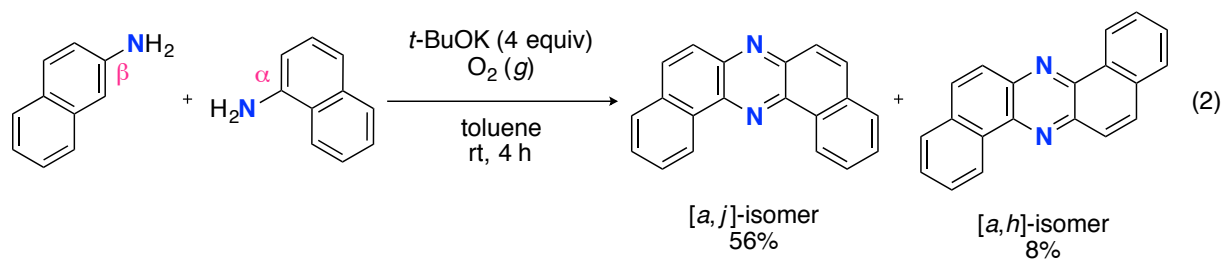


Figure 1. X-Ray Crystal Structure of **3a** (Thermal ellipsoids are set at the 50% probability level)

Most importantly, the discovered transformation leading to **3a** formally involves the cleavage of the strong C(Ar)–C(Ar) bond [**a** in Eq 1] of the binaphthyl unit (*e.g.*, the bond dissociation energy (BDE) of Ph–Ph is as large as 118 kcal mol⁻¹)³ without the aid of transition metal complexes⁴ and also involves the migration of a nitrogen atom [**b** in Eq 1] to the adjacent carbon. Encouraged by this finding, the author envisioned that the utilization of this unique rearrangement reaction would offer a versatile route to pyrazine-fused aza-PACs.

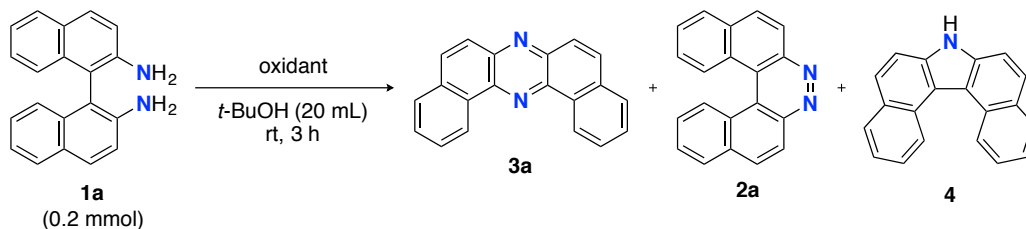
As a relevant work, there is a single report that describes selective preparation of [*a,j*]-isomer through an oxidative cross-annulation of α - and β -aminonaphthalenes mediated by a strong base (*t*-BuOK) under an O₂ atmosphere (Eq 2).² However, this known method intrinsically requires two regioisomers of aminonaphthalenes and suffers from the concomitant production of a constitutional [*a,h*]-isomer, thereby lacking the versatility as a synthetic approach to such “U-shaped” [*a,j*]-isomer.



Results and Discussion

2-2. Survey of Reaction Conditions for Selective Synthesis of 3a

Table 1. Survey of Reaction Conditions for Selective Synthesis of 3a



entry	oxidant (mmol)	yield (%) ^a			recovery (%) ^a
		3a	2a	4	
1	<i>t</i> -BuOI (0.8)	51	6	3	0
2	 NIPy (0.8)	36	0	trace	0
3	 NIS (0.8)	47	0	4	0
4	 NIPh (0.8)	0	0	0	100
5	 NISac (0.8)	0	0	0	47
6	 DIH (0.4)	49	0	3	0
7	DIH (1.6)	77^b	0	0	0
8 ^c	DIH (1.6)	72 ^b	0	0	0
9	I ₂ (0.8)	0	0	0	100
10	 NBS (0.8)	0	0	0	0 ^d

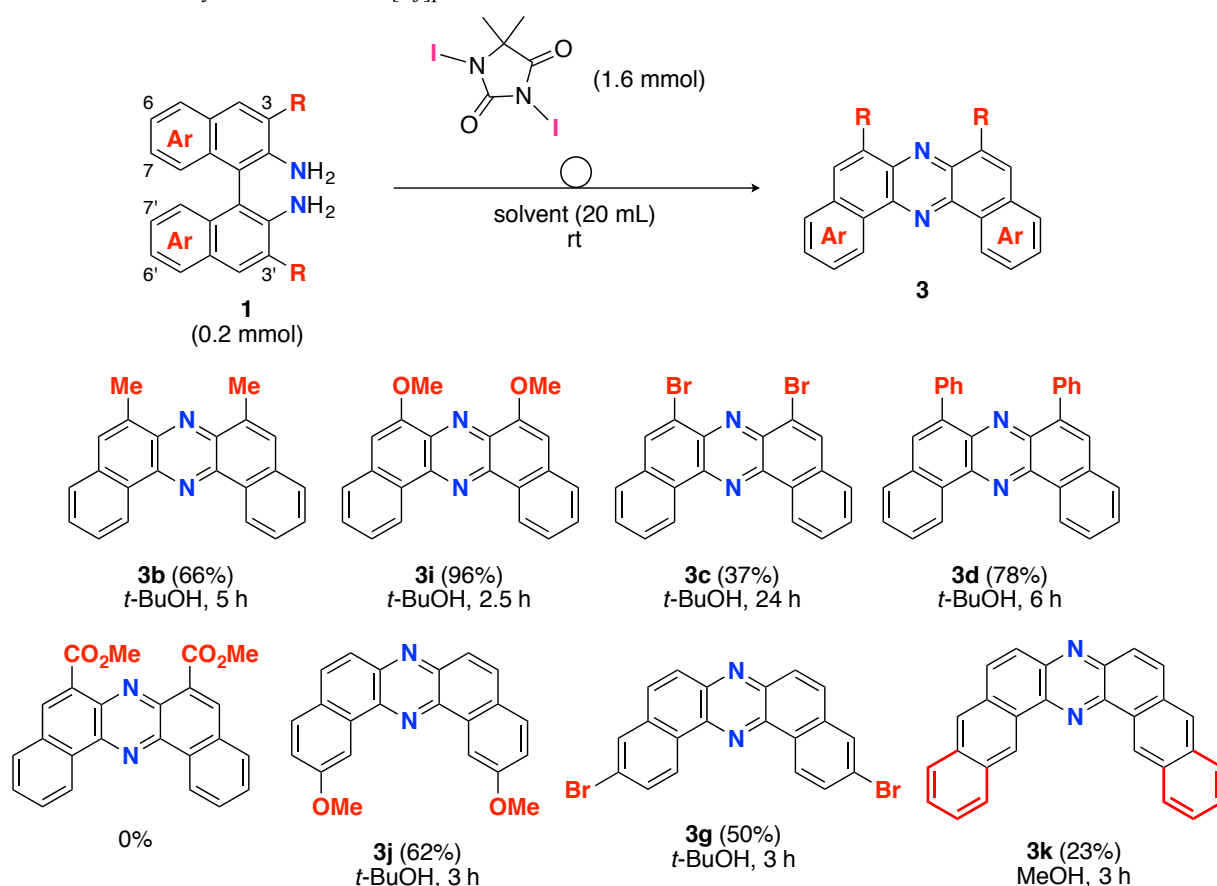
^a ¹H NMR yields. ^b isolated yield. ^c 20 mL of MeOH was used.^d 6,6'-dibromo BINAM was produced in 31% yield.

To establish a novel approach to synthesize U-shaped aza-PACs, reaction parameters were scrutinized to identify the conditions to selectively provide **3a** (Table 1). The use of *N*-iodolactams as oxidants like NIS, NIPy, and DIH in *t*-BuOH selectively gave **3a** in moderate yields along with trace amounts of **4** without affording **2a**. The use of 1.6 mmol of DIH gave **3a** in 77% yield. Other types of oxidants like I₂, NBS, DDQ, PhI(OAc)₂, and MnO₂ failed to furnish **3a**.

2-3. Selective Synthesis of Various Dibenzo[*a,j*]phenazines

Having identified the optimal conditions for the rearrangement reaction, the scope and limitation of BINAM substrates were surveyed (Table 2). The treatment of BINAMs bearing two electron-donating substituents (Me and MeO) at the 3,3'-position with DIH successfully provided dibenzophenazines **3b** and **3i** in 66% and 96% yields, respectively. The reaction using

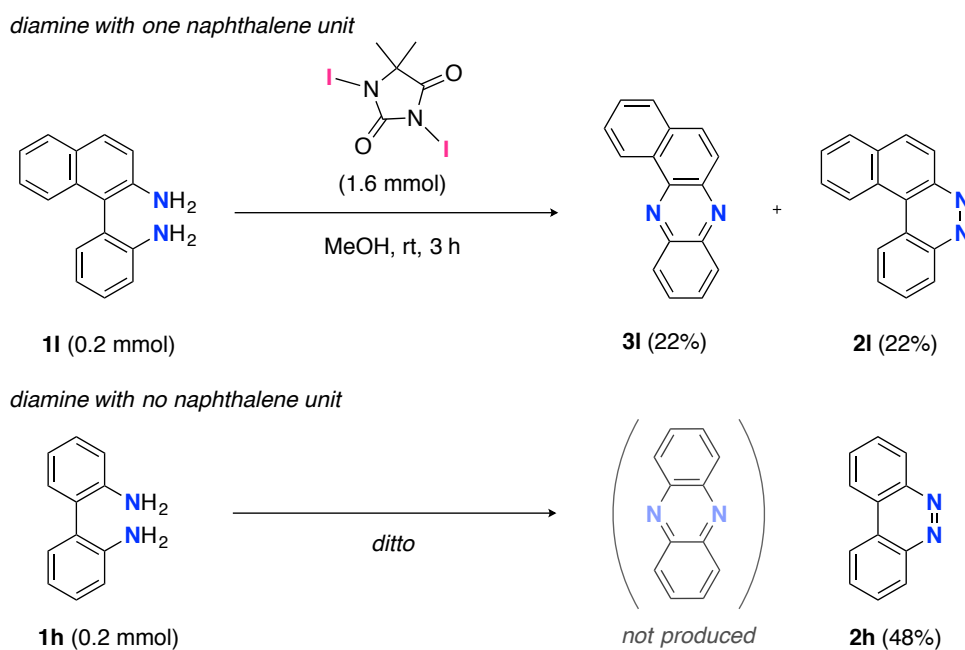
Table 2. Selective Synthesis of Dibenzo[*a,j*]phenazines



3,3'-dibrominated BINAM **1c** gave desired product **3c** in a low yield, probably because of the poor solubility of the diamine in *t*-BuOH. Notably, the rearrangement of 3,3'-diphenyl diamine **1d** also efficiently proceeded to afford **3d** in a high yield, indicating that steric hindrance around the amino moieties does not affect the reaction efficiency. In sharp contrast, diamine bearing two ester groups (CO₂Me) at the 3,3'-position did not undergo the rearrangement at all. This significant lack of reactivity might be ascribed to the low nucleophilicity of amino moieties, inhibiting the formation of N–I bonds (*vide infra*). Diamines bearing the 7,7'- and 6,6'-disubstituent also underwent rearrangement to selectively provide **3j** and **3g** in moderate yields. Notably, the rearrangement of bianthracene diamine **1k** gave highly conjugated heptacyclic aza-PAC **3k**, which should be quite difficult to synthesize by conventional organic reactions.

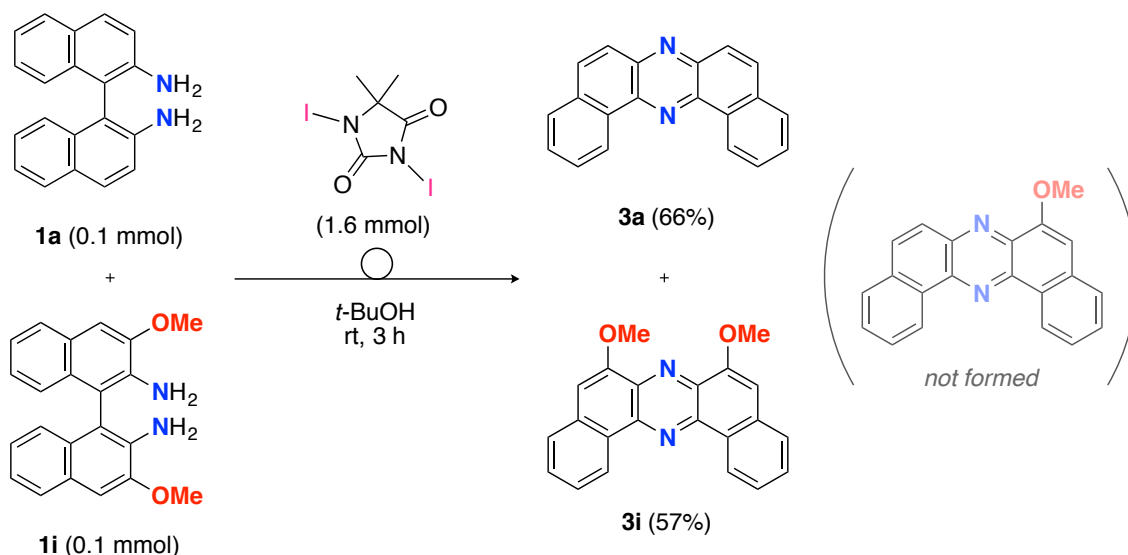
2-4. Investigation of Reaction Pathway to Dibenzo[*a,j*]phenazine

Regarding mechanistic aspects, importantly, the existence of at least one naphthalene unit is indispensable for the unique rearrangement (Scheme 1): when biaryldiamines bearing one

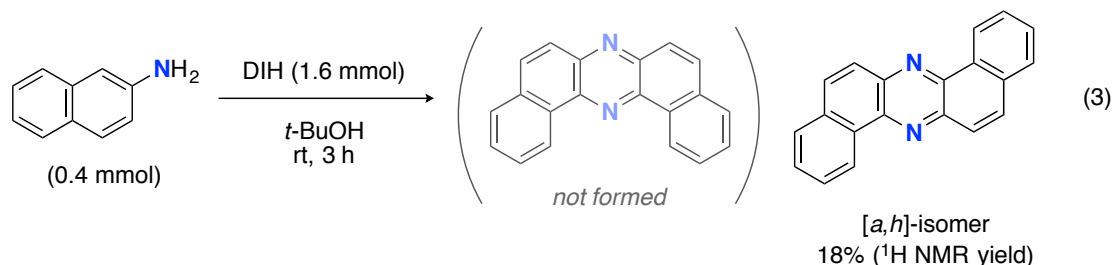


Scheme 1. Influence of a Naphthalene Unit

(**1l**) or no (**1h**) naphthyl unit were subjected to the reaction conditions, the ratios of rearranged products/pyridazine-fused products were found to be positively correlated with the number (n) of naphthalene units. These results might indicate the involvement of dearomatization processes in the reaction pathway (*vide infra*), which would be more favorable with naphthalene units than benzene units.⁵ On the other hand, a cross-over experiment applying an equimolar mixture of **1a** and **1i** resulted in no production of cross-products at all (Scheme 2), and a control experiment using β -naphthylamine under the optimal conditions led to the production of the $[a,h]$ -isomer without the formation of **3a** (Eq 3), suggesting the *intramolecularity* of the rearrangement.

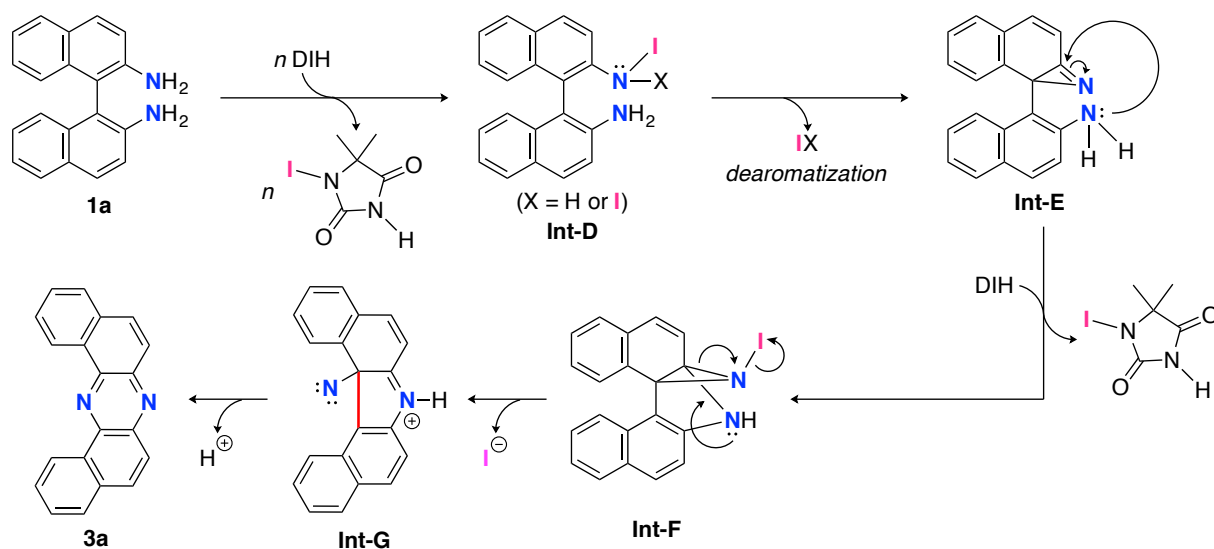


Scheme 2. Cross-Over Experiment



In conjunction with the accumulated knowledge of the reactivities of aromatic amines toward electrophilic iodinating oxidants, a tentative reaction pathway is illustrated in Scheme 3. The reaction would start with exchange of N–H hydrogen(s) with iodine, leading to mono or di

N-iodoamine **Int-D**.⁶ Previously, it was reported that naphthoazirines were transiently formed from the naphthyl nitrenes through the photoirradiation and thermal decomposition of naphthylazides.⁷ The dearomatization process to form azirine **Int-E** could explain the indispensability of the naphthyl unit for the rearrangement. Upon the formation of **Int-E**, the highly strained intermediate would be attacked by an intramolecular amino nucleophile (Ar-NH₂), and the developing anion would be trapped by the extra iodinating reagent to form **Int-F**.⁸ Nitrene **Int-G** could be generated from **Int-F** driven by the release of its strain energy, and the subsequent insertion of nitrene to the C(Ar)-C(Ar) bond would give phenazine **3a**. Alternatively, the path from **Int-F** to **3a** could be interpreted as a variant of Stieglitz rearrangement.⁹

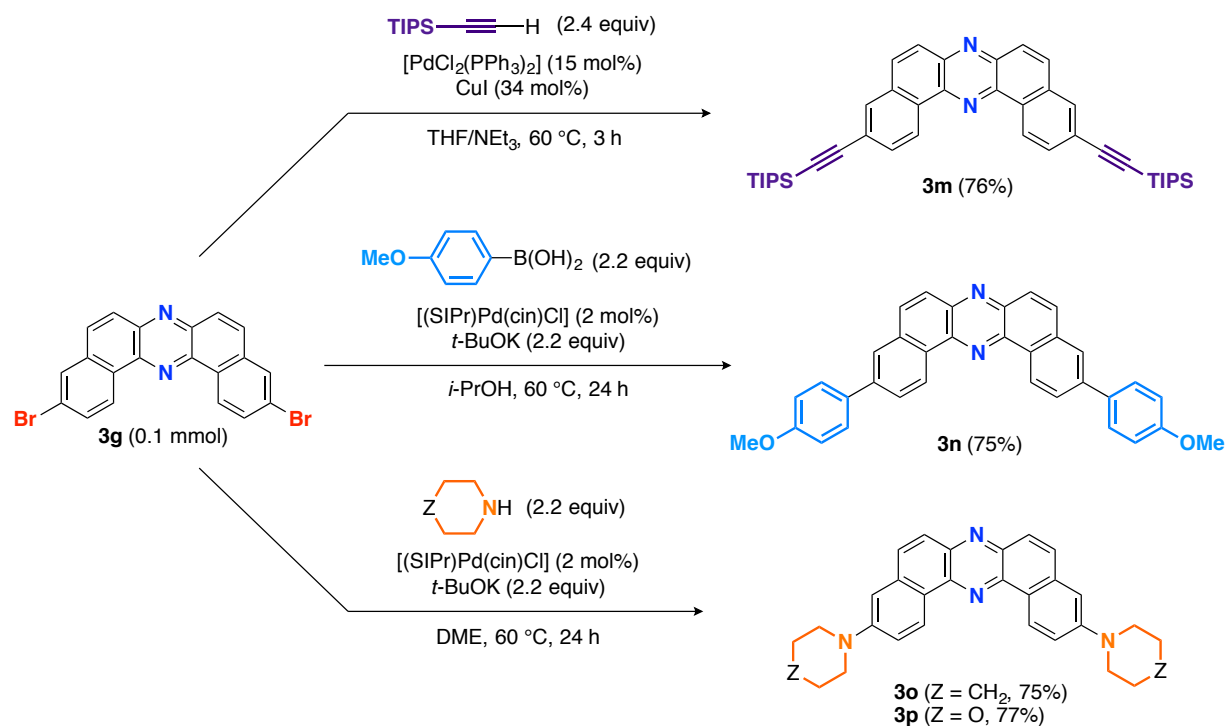


Scheme 3. Plausible Reaction Pathway to **3a**

2-5. Pd-Catalyzed Functionalization of **3g**

In light of bromo functionality of **3c** and **3g**, these compounds should serve as useful building blocks for functionalized aza-PACs. Synthetic versatility of **3g** was clearly demonstrated by the preparation of **3m–3p** via Pd catalysis (Scheme 4). TIPS-acetylene was efficiently cross-coupled with **3g** to afford conjugation-extended aza-PAC **3m** in 76% yield.

For the purpose of the construction of D–A–D molecules by utilizing dibenzophenazine as an acceptor (*vide infra*), the author attempted to introduce 4-methoxypheny group and cyclic amino group into the dibenzo[*a,j*]phenazine core using NHC/Pd-catalyzed cross-coupling of **3g** with slight modifications of the Nolan's original conditions¹⁰ to give the corresponding molecules **3n–3p** in good yields.



Scheme 4. Pd-Catalyzed Functionalization of **3g**

2-6. Physicochemical Properties of **3**

Basic physicochemical properties of dibenzophenazines **3** were investigated (Tables 3, 4 and Figure 2, for the full spectra, see the Experimental Section). UV-vis and fluorescence (FL) spectra for **3a**, D–A–D molecules **3o** and **3p** are shown in Figure 2 as a representative example. The mirror-image type UV and FL spectra with fine vibrational structures and a small Stokes shift (9 nm) reflects the rigid structure of **3a** (Figure 2). Likewise, diluted CH₂Cl₂ solutions of other U-shaped aza-PACs emit fluorescence ranging from blue ($\lambda_{\text{em}} = 425$ nm) to yellow ($\lambda_{\text{em}} = 561$ nm) depending on the substituents on the conjugated core (Table 3). Especially, the

introduction of sterically demanding and strongly electron-donating groups like piperidino and morpholino functionalities (*i.e.*, **3o** and **3p**) resulted in significant Stokes shifts and greatly enhanced quantum yields (**3a**: $\lambda_{\text{em}} = 425$ nm, $\Phi_{\text{FL}} 0.14$; **3o**: $\lambda_{\text{em}} = 561$ nm, $\Phi_{\text{FL}} 0.47$; **3p**: $\lambda_{\text{em}} = 543$ nm, $\Phi_{\text{FL}} 0.42$), probably ascribed to intramolecular charge-transfer (ICT) emission (Figure 2).

Table 3. Summary of Photophysical Properties of Phenazines **3**

	Absorption ^a		Emission (solution) ^a			Emission (solid)		
	λ_{max} (nm)	ϵ ($\text{M}^{-1}\text{cm}^{-1}$)	λ_{ex} (nm)	λ_{max} (nm)	Φ_{FL}	λ_{ex} (nm)	λ_{max} (nm)	Φ_{FL}
3a	416	29700	300	425	0.14	350	524	0.18
3b	417	21000	300	431	0.10	300	481	0.02
3i	418	8200	300	499	0.24	300	508	0.11
3c	418	37900	300	428	0.02	300	-	0.01
3d	422	17300	300	454	0.03	300	469	<0.01
3j	425	9600	300	475	0.11	300	-	0.02
3g	418	35100	300	427	0.02	300	-	0.01
3k	467	22500	300	485	0.55	300	537	0.11
3m	432	55700	300	464	0.32	400	471	0.07
3n	435	39000	300	461	0.50	350	483	0.07
3o	463	27900	300	561	0.47	280	543	0.05
3p	452	28000	300	543	0.42	370	543	<0.01

^a CH_2Cl_2 solution (10^{-5} M order)

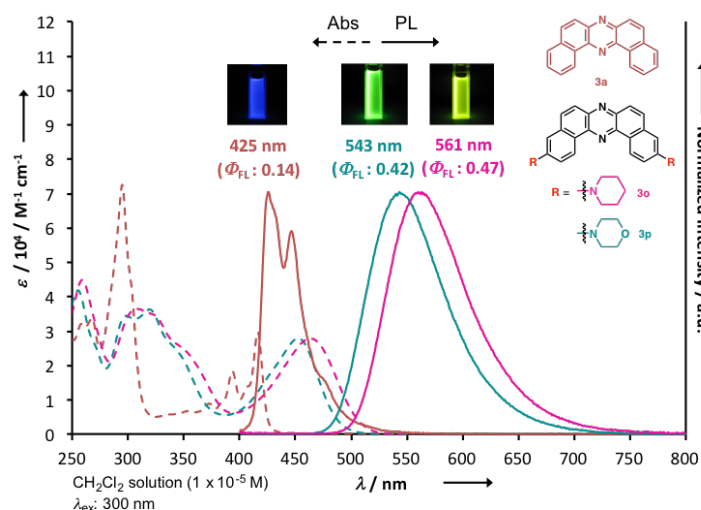


Figure 2. UV-vis Absorption and Emission Spectra of CH_2Cl_2 Solutions (10^{-5} order) of **3a**, **3o** and **3p**

Notably, most of the phenazines **3** showed one pair of reversible redox waves at the potentials ranging from -1.76 to -1.98 V against the Fc/Fc^+ redox couple indicating the good electron-accepting abilities of **3** (Table 4). These values are almost same as those of diaza[5]helicenes **2** described in Chapter 1 and Alq_3 .¹¹ Thermogravimetric analysis (Table 4) of **3** also showed their high thermal stabilities [T_d (5 wt % loss) = 116–403 °C].

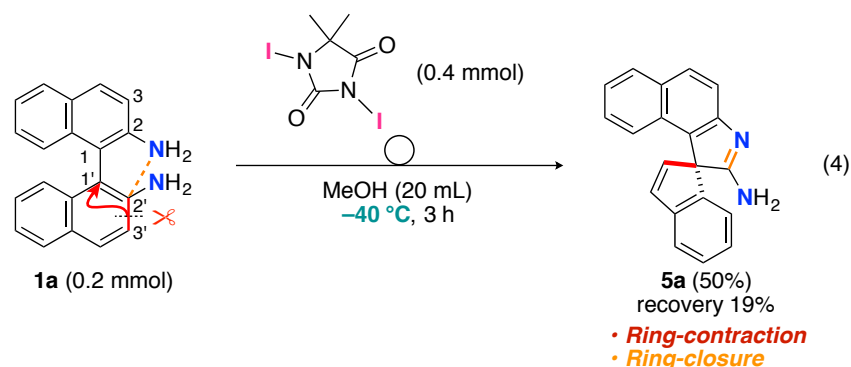
Table 4. Summary of Electrochemical and Thermodynamic Properties of Phenazines **3**

	CV (vs. Fc/Fc^+) ^a				TGA
	$\text{red}E_{\text{pc}}$ (V)	$\text{red}E_{\text{pa}}$ (V)	$\text{red}E_{1/2}$ (V)	LUMO level (eV)	T_d (5 wt% loss) (°C)
3a	-1.93	-1.83	-1.88	-2.92	221
3b	-2.03	-1.93	-1.98	-2.82	230
3i	-1.96	-1.85	-1.90	-2.90	192
3c	-1.80	-1.72	-1.76	-3.04	116
3d	-1.94	-1.85	-1.90	-2.90	313
3j	-1.94	-1.86	-1.90	-2.90	283
3g	-1.81	-1.73	-1.77	-3.03	280
3k	-1.98	-1.88	-1.93	-2.87	310
3m	-1.80	-1.72	-1.76	-3.04	365
3n	-	-	-	-	403
3o	-	-	-	-	360
3p	-	-	-	-	354

^a CH_2Cl_2 solution (10^{-4} M order)

2-7. Unexpected Formation of Spiro[benzo[*e*]indole-1,1'-inden]-2-amine

During the course of the author's studies on the development of novel oxidative rearrangement of BINAM (**1a**), further pursuit of this reaction system led him to another serendipitous finding: when **1a** (0.2 mmol) was treated with DIH (0.4 mmol) at a lower temperature (-40 °C), spiro[benzo[*e*]indole-1,1'-inden]-2-amine (**5a**), which was characterized by X-ray analysis (*vide infra*), was exclusively formed (50%) instead of dibenzo[*a,j*]phenazine (**3a**) (Eq 4). It should be noted that this reaction formally involves the ring-contraction of one naphthalene unit (the disconnection of the C2'–C3' bond and the formation of the C1'–C3' bond) and the ring-closure between the C2' and the nitrogen atom on the C2 atom.



The X-ray crystallographic analysis of the single crystal of **5a**, which was grown from an acetone solution, unambiguously confirmed its geometric structure (Figure 3a).¹² As illustrated, a 1*H*-indenylidene and a 2-amino-1*H*-benzo[*e*]indolylidene groups share the spiro carbon C1, and these aromatic planes are almost perpendicular to each other (dihedral angle: 85.2°). In general, amidine compounds can exhibit prototropic tautomerism, which influences their pK_a s and reactivities.¹³ The C2–N2 bond (1.308 Å) was shorter than the C2–N1 bond (1.333 Å) by about 0.025 Å, while these bond lengths almost agree with the values of C(sp²)=N bond (1.298–1.329 Å) and C(sp²)–NH₂(sp²) bond (1.336 Å), respectively.¹⁴ The values of these C–N bond lengths are similar to those of spiro[bicyclo[2.2.1]-heptane-2,3'-indol]-2'-amine, whose crystallographic structural data are reported in the literature.¹⁵ Furthermore, two hydrogen atoms (H1A and H2B) on the amidino group were located in the different Fourier map around

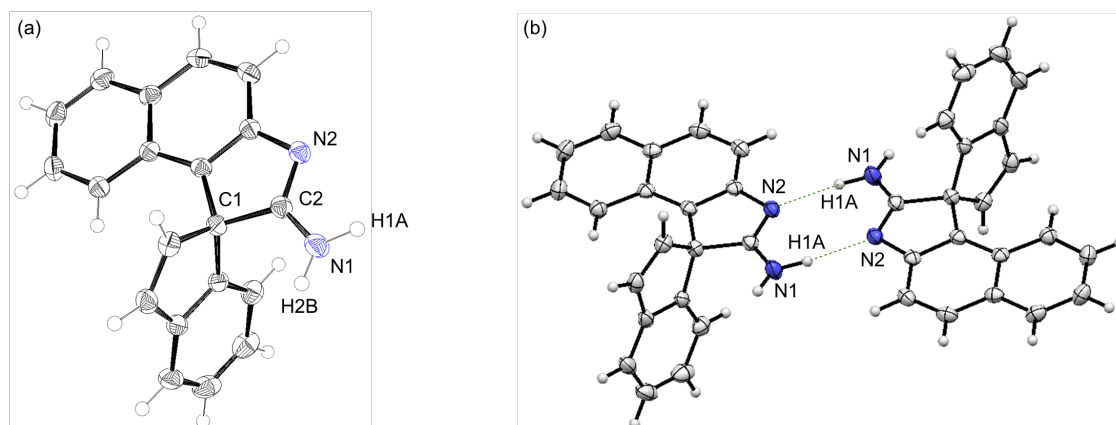
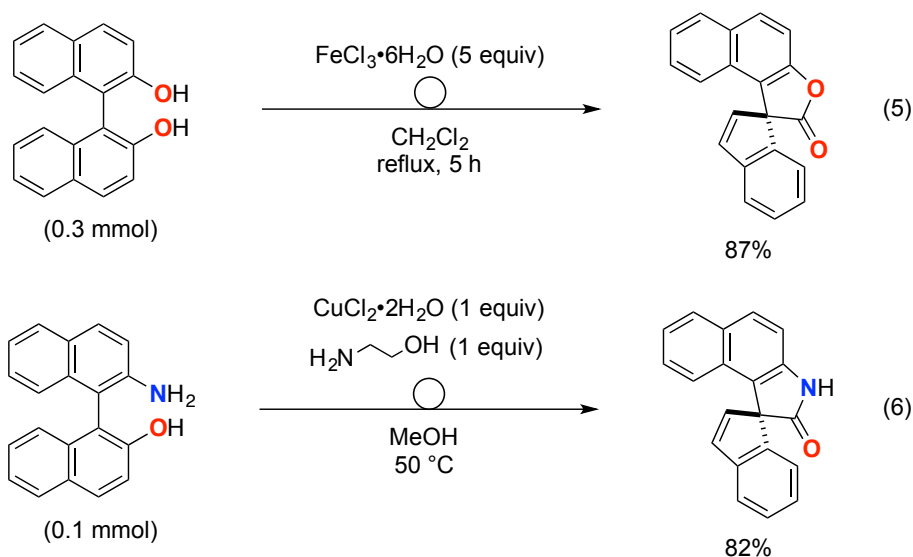


Figure 3. (a) ORTEP Diagram of **5a** (Thermal ellipsoids are set at the 50% probability level.); Selected bond length (Å): C2–N1, 1.3333(1); C2–N2, 1.3080(1); (b) A Dimeric Motif of **5a**

the N1 atom. These results might indicate that **5a** exists as the tautomer in the solid state. Another characteristic about **5a** involves a dimeric motif formed by adjacent two molecules through two pairs of intermolecular hydrogen bonding (N1–H1A···N2) in a similar way to a known spiro cyclic amidine (Figure 3b).¹⁵

Although similar oxidant-promoted rearrangements of 2,2'-disubstituted 1,1'-binaphthalenes have been reported (1,1'-binaphthalene-2,2'-diols with $\text{FeCl}_3 \cdot 6\text{H}_2\text{O}$ (Eq 5)¹⁶ and 2'-amino-[1,1'-binaphthalen]-2-ol with $\text{CuCl}_2 \cdot 2\text{H}_2\text{O}$ /ethanolamine (Eq 6)¹⁷), there is no report about the variant using BINAMs as a substrate.



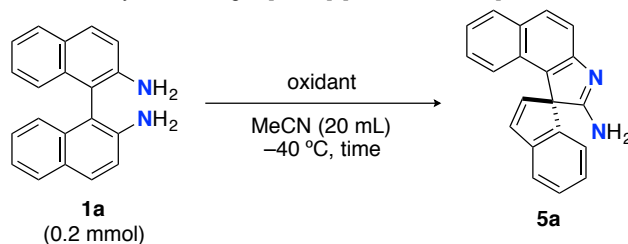
Spiro heterocycles are ubiquitous motifs found in natural products,¹⁸ and relatedly, they can serve as leading compounds for the discovery of pharmaceuticals.¹⁹ Also, the successful use of spiro heterocycles as axially chiral ligands in transition-metal-catalyzed reactions represents their importance.²⁰ Moreover, spiro heterocycles containing π -conjugated fragments are promising candidates for organic optoelectronic materials, because their rigid and sterically demanding perpendicular structures should allow for unique physicochemical properties like high glass transition temperatures (T_g) and high quantum efficiencies in the solid state.²¹ Although there have been numerous synthetic methodologies reported for spiro heterocycles,²²

the development of new synthetic reactions that open the door to novel spiro heterocyclic compounds would be desired for further quest for their potential usage.

2-8. Survey of Reaction Conditions for Selective Synthesis of **5a**

To optimize the reaction conditions, the author began by screening reaction parameters using **1a** as a model substrate (Table 5). The reaction in acetonitrile gave **5a** in almost the same yield as that in MeOH with a moderate conversion of the starting material **1a** (entry 1). In order to further consume **1a**, reaction time was elongated to 7 h, which enhanced the yield to 69% (entry 2). However, further extension of reaction time resulted in a lower yield, probably due to the decomposition of **5a** with DIH (entry 3)²³. Oxidants significantly affected the yields of **5a**:

Table 5. Selective Synthesis of Spiro[benzo[*e*]indole-1,1'-inden]-2-amine

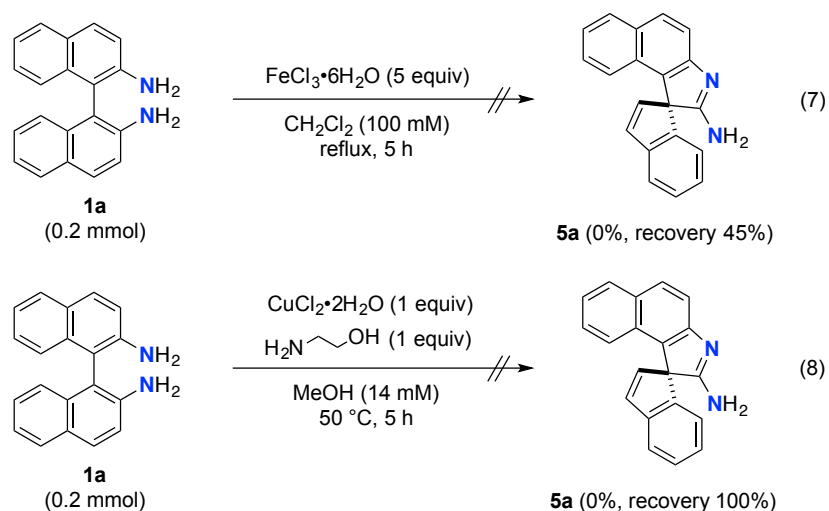


entry	oxidant (mmol)	time (h)	yield (%) ^a	recovery (%) ^a
1	DIH (0.4)	3	47 ^b	36 ^b
2	DIH (0.4)	7	69 ^b	17 ^b
3	DIH (0.4)	12	43	7
4	 NIS (0.8)	7	45	49
5	 NIPy (0.8)	5	3	55
6	<i>t</i> -BuOI (0.8)	7	0	5
7	 DBH (0.4)	7	0	0

^a ¹H NMR yields. ^b isolated yield.

N-iodosuccinimide (NIS, entry 4) and *N*-iodopyrrolidone (NIPy, entry 5) gave a moderate and a low yield, respectively, whereas *t*-BuOI (entry 6) and 1,3-dibromo-5,5-dimethylhydantoin (DBH, entry 7) did not produce **5a** at all.

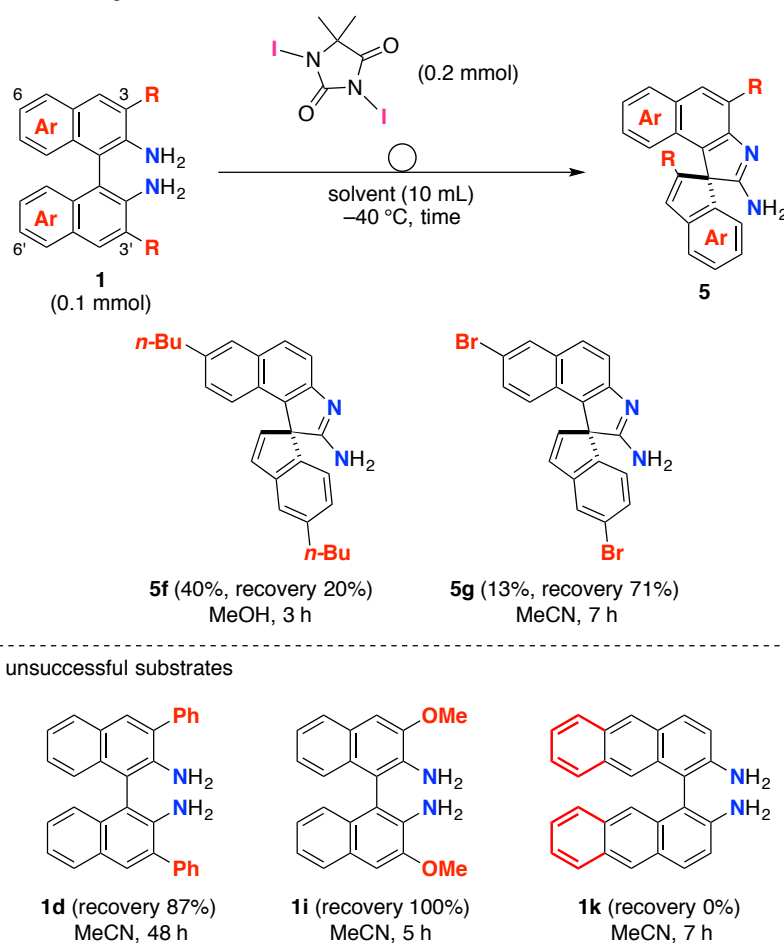
On one hand, the reported reaction conditions for similar type rearrangements of 1,1'-binaphthalene-2,2'-diols ($\text{FeCl}_3 \cdot 6\text{H}_2\text{O}$)¹⁶ and 2'-amino-[1,1'-binaphthalen]-2-ol ($\text{CuCl}_2 \cdot 2\text{H}_2\text{O}$ /ethanolamine)¹⁷ did not give **5a** (Eqs 7 and 8).



2-9. Selective Synthesis of Spiro[benzo[*e*]indole-1,1'-inden]-2-amines

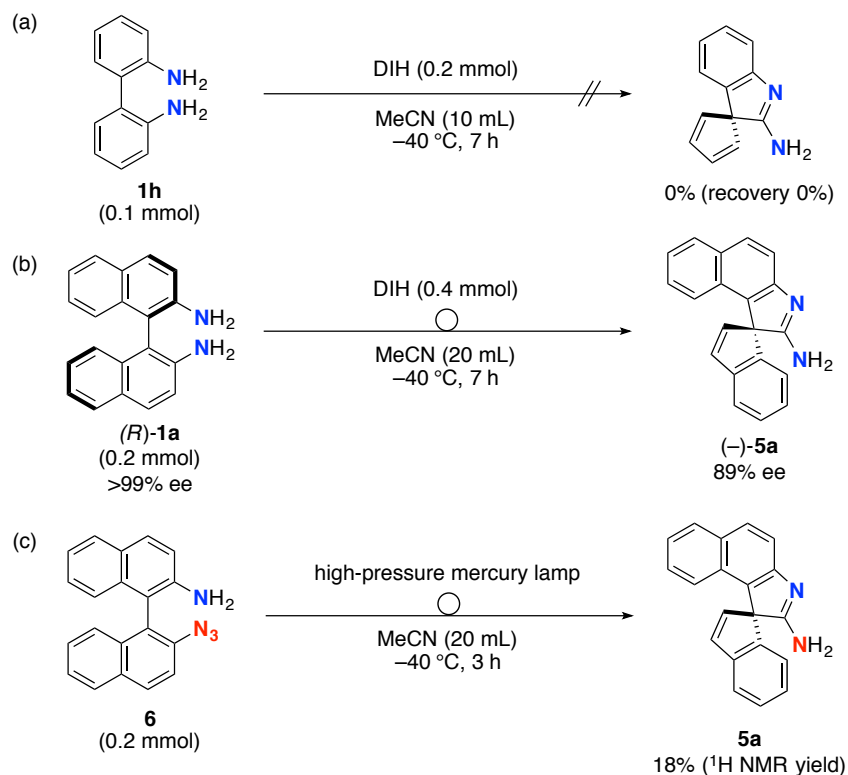
Having identified the optimized conditions for the oxidative rearrangement, the scope of substrates was surveyed (Table 6). The reaction using 6,6'-di-*n*-butyl-substituted BINAM **1f** (0.1 mmol) in MeOH gave the expected spiro product **5f** in 40% yield (Table 6). The treatment of a BINAM bearing 6,6'-dibromo substituents **1g** with DIH provided the corresponding spiro amidine **5g**, albeit in a low yield (13%) (Table 6). Since bromo group can be transformed into various functionalities through transition-metal-catalyzed coupling reactions, **5g** would serve as a building block for the construction of functionalized aza-spiro compounds. Regarding the limitation of substrates, 3,3'-disubstituted BINAMs **1d** (Ph) and **1i** (OMe) were not successful, probably due to steric congestion around the spiro carbon center to be formed. Bianthracene diamine **1k** also failed to provide the desired product **5k**.

Table 6. Scope and Limitations of Substrates



2-10. Investigation on Reaction Pathway to Spiro[benzo[*e*]indole-1,1'-inden]-2-amine

For understanding the mechanistic aspects of the rearrangement, a few experiments were conducted (Scheme 5). The treatment of diamine **1h** under the optimized conditions for **1a** did not give the corresponding spiro product **5h** (Scheme 5a), suggesting that the existence of naphthalene units in diamine is indispensable for the oxidative rearrangement, and thereby that dearomatization processes could be involved in the reaction pathway. To check the stereochemical outcome of the reaction, optically pure (*R*)-BINAM (**1a**) (>99% ee) was subjected to the optimized reaction conditions (Scheme 5b). As a result, optically active product (–)-**5a** ($[\alpha]_{\text{D}}^{20} -4.00$, c 1.00, CHCl_3)²⁴ was obtained with a slight loss of enantiopurity (89% ee, HPLC), suggesting that the axial chirality of **1a** was mostly translated into the

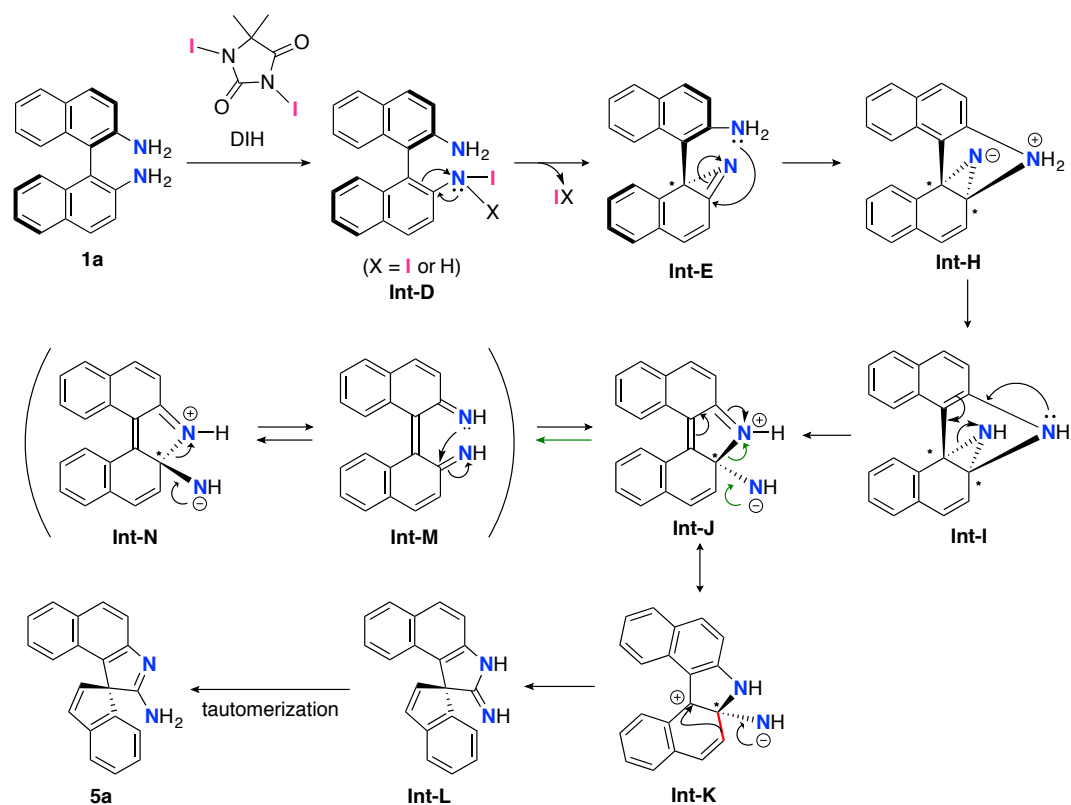


Scheme 5. Mechanistic Studies on the Oxidative Rearrangement of BINAMs to **5**

chirality of **5a** through the reaction. Photo-induced decomposition of 2'-azido-[1,1'-binaphthalen]-2-amine (**6**) effected by the irradiation of UV light (high-pressure mercury lamp) at $-40\text{ }^{\circ}\text{C}$ gave spiro compound **5a** in 18% yield (Scheme 5c). Since the photo- and thermal-decomposition of β -naphthyl azides transiently generate β -naphthyl nitrenes, which promptly isomerize to β -naphthazirines with dearomatization, the experimental result would indicate the intermediacy of such β -naphthazirine species through the reaction pathway.⁷

Taking account of the experimental results shown in Scheme 5, a possible reaction pathway of the rearrangement of **1a** leading to **5a** is proposed in Scheme 6. Hydrogen(s) of an amino group of **1a** would exchange with iodine(s) to give mono or diiodinated intermediate **Int-D** in the same way as Takeda and Minakata's works,⁶ which would be dearomatized to give naphthazirine **Int-E**. The resulting azirine would undergo intramolecular nucleophilic attack by the other amino group to give **Int-H**, which should be converted to aziridine **Int-I** through proton transfer.⁸ The 3-membered ring of **Int-I** would be opened driven by the release

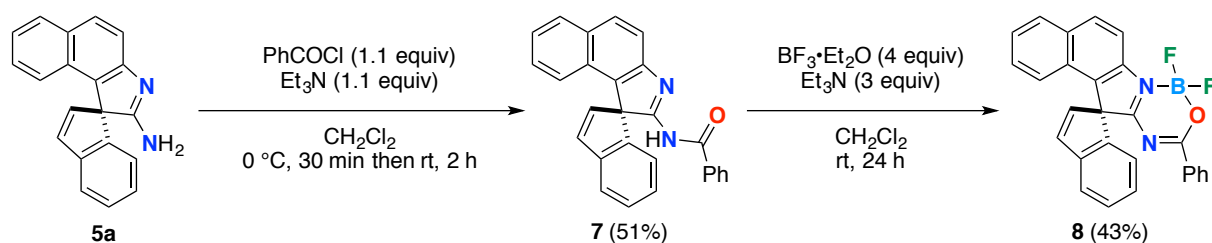
of its strain energy to provide zwitterionic intermediate **Int-J**. A resonance structure of **Int-J** can be illustrated like **Int-K**, whose contribution would be more significantly dominated because it would gain more stabilization by the recovery of aromaticity of a naphthalene unit. Aza-pinacol type rearrangement of **Int-K** would generate spiro compound **Int-L**,²⁵ which then would tautomerize to **5a**. With regard to the stereochemical outcome of the reaction, the chiral information of **1a** would be kept through axial-to-central (from **Int-D** to **Int-E**) and central-to-axial (from **Int-K** to **Int-L**) chirality transfer. The reason why a slight degree of enantiopurity was lost through a reaction might be that a racemization process *via* an intermediate **Int-M** exists.



2-11. Functionalization of **5a**

Taking advantage of the amidino functionality of rearranged products, **5a** was successfully transformed into BF_2 complex **8** possessing a bidentate $\text{N}^-\text{N}^+\text{O}$ group (Scheme 7).

To date, several examples of BF_2 complexes containing a bidentate $\text{N}^{\wedge}\text{N}^{\wedge}\text{O}$ group have been reported,^{26–28} and they have been shown to be promising luminophores in the solid state as well as in the solution.²⁸ In conjunction with these precedents, the author surmised that the BF_2 complex **8** would also serve as an emissive organic solid, because the sterically demanding spiro moiety would avoid intermolecular electronic interactions such as π - π stacking that often cause concentration quenching of emission.²⁹ Amidine **5a** underwent *N*-acylation with benzoyl chloride to give amide **7** in a moderate yield, which was then converted to BF_2 complex **8** by the treatment with $\text{BF}_3 \cdot \text{Et}_2\text{O}$ in the presence of Et_3N in dry CH_2Cl_2 at ambient temperature.



Scheme 7. Synthetic Route to $\text{N}^{\wedge}\text{N}^{\wedge}\text{O}$ Chelated BF_2 Complex **8**

Figure 4a shows the molecular structure of **8** determined by X-ray crystallographic analysis.³⁰ The BF_2 unit is coordinated by the N2 and O1 atoms, and the B1 center adopts a slightly distorted tetrahedral geometry with the bond angles around the B1 atom ($\angle \text{X-B1-Y}$; X, Y = N2, O1, F1, F2) ranging from $105.5(2)$ to $111.4(3)^\circ$. The B1–F1, B1–F2, B1–N2, and B1–O1 distances are 1.368(4), 1.371(4), 1.548(4) and 1.485(4) Å, respectively. The B1–N2 bond is slightly shorter and the B1–O1 slightly longer than those of known $\text{N}^{\wedge}\text{N}^{\wedge}\text{O}$ chelated BF_2 complexes.^{27,28} The sum of the interior angles of the boron-containing 6-membered ring is 719.6° ($\sim 720^\circ$), indicating that these atoms are located almost on the same plane. Importantly, this 6-membered heterocycle and the phenyl ring connected to the C21 are nearly coplanar, suggesting the highly extended π -conjugation in the solid state. In fact, effective π -conjugation along the heterocycle–benzene plane was supported by DFT calculations: the LUMO orbital is

delocalized over the boron-containing 6-membered ring and the phenyl moiety, and the LUMO energy is significantly decreased (Figure 10). Furthermore, it is noteworthy that any intermolecular π - π close contacts were not observed in the packing structure of **8** (Figure 4b), probably due to the existence of the perpendicular indene moiety. Two 1*H*-indenylidene planes (colored in yellow) are aligned in a slipped face-to-face fashion with the interplanar distance being 2.75 Å, although these planes do not overlap with each other.

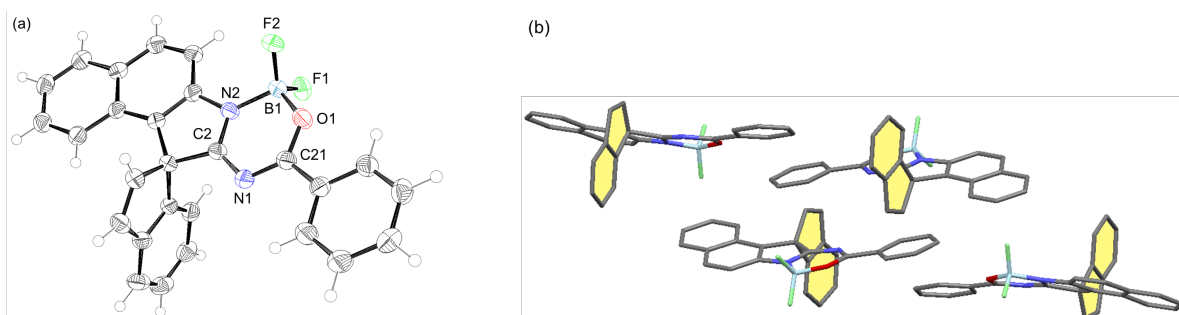


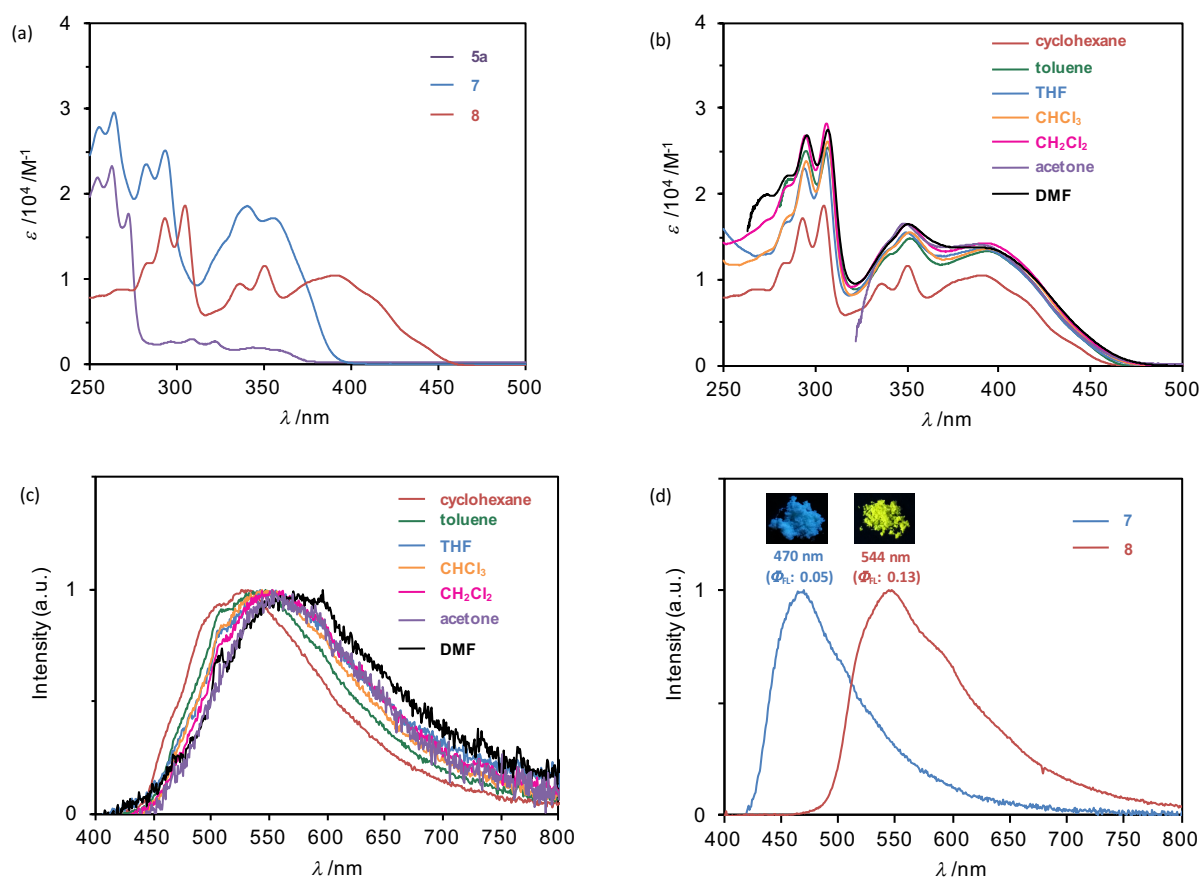
Figure 4. (a) ORTEP Diagram of **8** (Thermal ellipsoids are set at the 50% probability level.); Selected bond lengths (Å) and angles (°): B1–F1, 1.368(4); B1–F2, 1.371(4); B1–N2, 1.548(4); B1–O1, 1.485(4); N2–B1–O1, 105.5(2); N2–B1–F1, 110.8(3); N2–B1–F2, 110.0(2); O1–B1–F1, 109.7(3); O1–B1–F2, 109.2(3); F1–B1–F2, 111.4(3); B1–N2–C2, 121.8(3); N2–C2–N1, 125.9(3); C2–N1–C21, 115.5(3); N1–C21–O1, 125.3(3); C21–O1–B1, 125.5(3); (b) Packing Structure of **8** (Hydrogen atoms are omitted, and indene planes are painted in yellow for clarity.)

2-12. Physicochemical Properties of Spiro Compounds

To understand the influence of the complexation with BF₂ moiety, photophysical properties of **5a**, **7**, and **8** were investigated (Table 7 and Figure 5). UV-vis absorption spectrum of a cyclohexane solution of **5a** exhibited weak absorptions ($\epsilon \sim 2900 \text{ M}^{-1}\text{cm}^{-1}$) in the lower energy region (300–350 nm) and strong absorptions ($\epsilon \sim 23200 \text{ M}^{-1}\text{cm}^{-1}$) in the higher energy region (250–270 nm) that were ascribed to π - π^* transitions by TD-DFT calculations (Table 16). The *N*-acylation of **5a** drastically increased the molar absorption coefficients in the lower energy region of **7**. Compared with **5a** and **7**, the absorption edge of **8** exhibited a distinct red-shift (λ_{edge} 470 nm; λ_{edge} of **5a** and **7** were 379 and 408 nm, respectively), and the strong absorptions ($\epsilon \sim 11500 \text{ M}^{-1}\text{cm}^{-1}$) in the lower energy region (340–450 nm) ascribed to π - π^* transition were observed. To investigate the effect of solvent polarity on its photophysical properties, the absorption and emission spectra of dilute solutions of **8** prepared from various solvents were measured (Figure 5b and 5c). Although the absorption spectra

Table 7. Summary of Photophysical Properties of Spiro Compounds **5a**, **7** and **8**

solvent	Absorption ^a			Emission ^a		
	λ_{abs} (nm)	ϵ ($\text{M}^{-1}\text{cm}^{-1}$)	λ_{edge} (nm)	λ_{ex} (nm)	λ_{em} (nm)	Φ_{FL}
5a cyclohexane	254, 263, 272, 297, 308, 322, 344, 359	21900, 23200, 17600, 2700, 2900, 2700, 2000, 1700	379	260	391	0.02
5a (solid)	-	-	-	300	-	<0.01
7 cyclohexane	255, 264, 282, 293, 340, 355	28000, 29700, 23600, 25200, 18700, 17200	408	300	-	<0.01
7 (solid)	-	-	-	300	470	0.05
8 cyclohexane	293, 305, 336, 350, 391	17100, 18500, 9400, 11500, 10400	470	300	527	0.06
8 toluene	295, 307, 352, 394	25100, 25500, 15000, 13400	480	300	547	0.03
8 THF	294, 305, 349, 390	23000, 25200, 15500, 13500	479	300	543	0.02
8 CHCl_3	295, 307, 351, 394	23900, 26200, 15600, 13700	485	300	544	0.03
8 CH_2Cl_2	295, 306, 350, 392	26800, 28200, 16400, 14200	481	300	553	0.02
8 acetone	348, 387	16600, 14200	484	350	552	0.01
8 DMF	295, 307, 350, 383	26800, 27400, 16400, 13700	491	300	571	0.01
8 (solid)	-	-	-	300	544	0.13

^a 10^{-5} M order**Figure 5.** (a) UV-vis Absorption Spectra of **5a**, **7**, and **8** in Cyclohexane (c : 10^{-5} M order); (b) UV-vis Absorption Spectra of Diluted Solutions of **8** (c : 10^{-5} M order); (c) Emission Spectra of Diluted Solutions of **8** (c : 10^{-5} M order); (d) Emission Spectra of **7** and **8** in the Solid State

became more broadened as the polarity of solvents increased, the maximum absorption wavelengths were almost unchanged in the all solvents tested (Figure 5b). In contrast to the absorption spectra, the maximum emission wavelength (λ_{em}) exhibited slight red-shifts in polar solvents (Figure 5c). A positive but small slope in the plot of the Stokes shifts ($\Delta\nu$, cm^{-1}) against the orientation polarizability (Δf) (the Lippert–Mataga plot)³¹ indicates that the variation in the dipole moment of **8** between the ground and excited states is very small (Table 10 and Figure 9). Importantly, both **7** and **8** were emissive in the solid state as expected, and the quantum yields (Φ_{FL}) were much higher than those of any solutions of **7** and **8** (AIEE-active²⁹) (Figure 5d). Moreover, the λ_{em} of **8** in the solid state (544 nm) was almost the same as that of its cyclohexane solution (527 nm), indicating that **8** rarely interacts electronically with each other in the solid state.

2-13. Conclusion

The author has developed two types of oxidative skeletal rearrangements of BINAMs by controlling the reaction conditions such as the equivalents of an oxidant and the reaction temperature. One is the rearrangement that involves the cleavage of a strong C–C single bond of the binaphthalene unit and the nitrogen migration to produce U-shaped dibenzo[*a,j*]phenazines, and the other is the ring-contractive and -closing skeletal rearrangement which gives spiro[benzo[*e*]indole-1,1'-inden]-2-amines. These unprecedented rearrangements enable access to a series of aza-PACs otherwise difficult to prepare in a selective manner by classical methods. Moreover, physicochemical properties of the rearranged products have been comprehensively investigated and the utility of the synthesized products as building blocks for emissive molecules has been demonstrated.

2-14. Experimental Section

General Remarks

All reactions were carried out under an atmosphere of nitrogen unless otherwise noted. Melting points were determined on a Stanford Research Systems MPA100 OptiMelt Automated Melting Point System. ^1H and ^{13}C NMR spectra were recorded on a JEOL JMTC-400/54/SS spectrometer (^1H NMR, 400 MHz; ^{13}C NMR, 100 MHz) for **1–6**, and a Bruker Avance III 600 spectrometer (^1H NMR, 600 MHz; ^{13}C NMR, 150 MHz) for **7** and **8** using tetramethylsilane as an internal standard. ^{19}F NMR spectra were recorded on a Bruker Avance III 600 spectrometer (564 MHz) relative to α,α,α -trifluorotoluene (δ –64.0 ppm in CDCl_3). ^{11}B NMR spectra were recorded on a Bruker Avance III 600 spectrometer (192 MHz) using $\text{BF}_3\cdot\text{Et}_2\text{O}$ as an external standard. Infrared spectra were acquired on a SHIMADZU IRAffinity-1 FT-IR Spectrometer. Mass spectra were obtained on a JEOL JMS-DX303HF mass spectrometer. High-resolution mass spectra (HRMS) were obtained on a JEOL JMS-DX303HF mass spectrometer. Chiral-phase high-performance liquid chromatography (HPLC) was performed on a SHIMADZU prominence series instruments equipped with chiral columns. Specific optical rotations were measured in a thermostated (20 °C) conventional 10 cm cell on a JASCO P-2200 polarimeter using the sodium-D line (589 nm). UV/vis spectra were recorded on a Shimadzu UV-2550 spectrophotometer. Emission spectra were recorded on a HAMAMATSU C11347-01 spectrometer with an integrating sphere. Cyclic voltammetry (CV) was performed with ALS-600 (BAS Inc.) system. Thermogravimetric analysis (TGA) was performed with TG/DTA-7200 (SII) system. Single crystal X-ray diffraction data were collected on a Rigaku R-AXIS RAPID diffractometer with a graphite monochromated $\text{Cu-K}\alpha$ radiation. Products were purified by chromatography on silica gel BW-300 and Chromatorex NH (Fuji Silysia Chemical Ltd.). Analytical thin-layer chromatography (TLC) was performed on pre-coated silica gel glass plates (Merck silica gel 60 F₂₅₄ and Fuji Silysia Chromatorex NH, 0.25 mm thickness). Compounds were visualized with UV lamp.

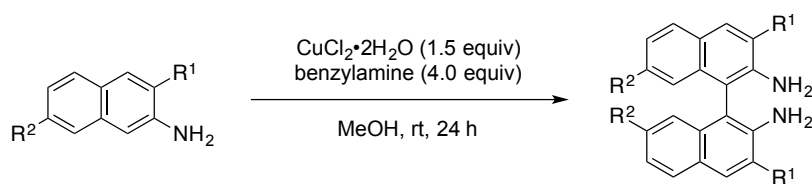
Materials

BINAM (**1a**) and (*R*)-BINAM (**1a**) (99% ee) were purchased from Sigma-Aldrich and used as received. *N*-iodopyrrolidone (NIPy)³² [1267636-41-8], *N*-iodophthalimide (NIPh)³³ [20919-42-0], *N*-iodosaccharin (NISac)³⁴ [86340-94-5], 2-aminonaphthalene³⁵ [91-59-8] and [SIPr-Pd(cinnamyl)Cl]¹⁰ [884879-24-7] were prepared according to the literature procedures.

Piperidine, morpholine and triethylamine were distilled with Kugelrohr and other commercial reagents were purchased from Sigma-Aldrich, TCI or Wako Pure Chemical Industries, Ltd. and used as received. Alcohols were dried over molecular sieves 3A. THF, CH₃CN and Et₂O were dried on a glass contour solvent dispensing system (Nikko Hansen & Co., Ltd.). Dehydrated CH₂Cl₂, toluene, benzene and dimethoxyethane (DME) were purchased from Kanto Chemical Co., Inc and used as received. Solvents (fluorescence spectroscopic grade) were purchased from Nacalai Tesque Inc. and Kanto Chemical Co., Inc. for measurement UV-vis spectra and emission spectra. Biaryldiamines **1b**³⁶ [360779-01-7], **1c**³⁷ [1051425-55-8, (*R*)-enantiomer], **1d**³⁸ [1229013-43-7], **1g**³⁹ [861890-12-2], **1k**⁴⁰ [103278-14-4], **1l**⁴¹ [93013-27-5], **1h**⁴² [1454-80-4], **1e**⁴³ [155855-47-3] and **1f**⁴⁴ were prepared according to the procedures in the literature. Binaphthalenediamines **1i** and **1j** were prepared by modified oxidative coupling method⁴⁰ of corresponding aminonaphthalene, and 2'-azido-[1,1'-binaphthalen]-2-amine (**6**) [CAS No. 1620543-69-2] was prepared from BINAM (**1a**) according to the procedures in literature⁴⁵ as follows.

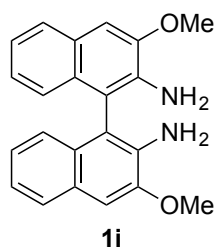
Typical procedure for preparation of dimethoxy-substituted BINAMs

Methanol was degassed through freeze-pump-thaw cycling for three times before used. To a 500 mL of three necked round-bottomed flask equipped with a magnetic stir bar, was added CuCl₂•2H₂O (3.27 g, 19.2 mmol) under the air. The flask was capped with a septum rubber and evacuated and refilled with N₂ gas three times. Methanol (105 mL) and a methanol solution of benzylamine (5.49 g, 51.2 mmol, 64 mL) were added through the septum, and the mixture was purged with N₂ for 5 min. A methanol solution of 3-methoxynaphthalen-2-amine (2.22 g, 12.8 mmol, 64 mL) was added to the solution through the septum, and the mixture was stirred under N₂ atmosphere at room temperature for 24 h. In an ice bath, the reaction mixture was acidified with 12 M HCl (64 mL) and stirred for 5 min, and then treated with 28% ammonia solution (128 mL) and stirred for another 5 min. The resulting mixture was diluted with water (1.28 L) and extracted with CH₂Cl₂ (100 mL × 3). The organic extract was dried over Na₂SO₄ and concentrated under vacuum to give the crude product. Purification by flash column chromatography on silica gel gave biaryldiamine **1i**.

Table 8. Preparation of Dimethoxy-Substituted BINAMs

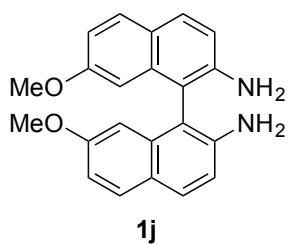
entry	starting material	product	yield (%)
1	 (12.8 mmol)	1i	31
2	 (7.0 mmol)	1j	31

3,3'-Dimethoxy-1,1'-binaphthalene-2,2'-diamine (**1i**) [1434075-68-9, (*S*)-enantiomer]



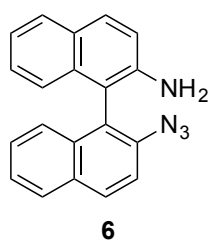
Spectroscopic data were in agreement with those previously reported;⁴⁶ Purified by flash column chromatography on silica gel (hexane/EtOAc 95:5 to 8:2); Pale yellow solid; R_f 0.13 (hexane/EtOAc 8:2).

7,7'-Dimethoxy-1,1'-binaphthalene-2,2'-diamine (**1j**) [1434075-66-7, (*S*)-enantiomer]



Spectroscopic data were in agreement with those previously reported;⁴⁶ Purified by flash column chromatography on silica gel (hexane/EtOAc 8:2); Pale yellow solid; R_f 0.18 (hexane/EtOAc 7:3).

Preparation of 2'-azido-[1,1'-binaphthalen]-2-amine (**6**)



To a 100 mL of two necked round-bottomed flask equipped with a magnetic stir bar, was added diamine **1a** (1.42 g, 5.0 mmol) under the air. The flask was capped with a septum rubber and evacuated and refilled with N_2 gas three times. CH_3CN (50 mL) was added through the septum, and

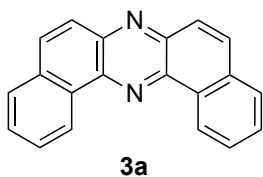
the mixture was cooled to 0 °C in an ice bath. To this stirred mixture, was added *t*-BuONO (386.7 mg, 3.75 mmol), followed by adding TMSN₃ (345.6 mg, 3.0 mmol) dropwise. The resulting solution was stirred at room temperature for 1 h. The reaction mixture was concentrated under vacuum, and the crude product was purified by column chromatography on NH silica gel (hexane/EtOAc 10:0 to 9:1) to give product **6**. Pale yellow solid (636.2 mg, 41%); mp 62 °C (dec.); *R*_f 0.25 (hexane/EtOAc 8:2, NH); ¹H NMR (400 MHz, CDCl₃) δ 3.57 (br, 2H), 6.89 (d, *J* = 7.2 Hz, 1H), 7.13 (d, *J* = 8.8 Hz, 1H), 7.18–7.28 (m, 3H), 7.32 (dd, *J* = 7.6, 8.0 Hz, 1H), 7.45 (dd, *J* = 7.6, 8.8 Hz, 1H), 7.50 (d, *J* = 8.8 Hz, 1H), 7.80 (d, *J* = 7.6 Hz, 1H), 7.83 (d, *J* = 8.8 Hz, 1H), 7.92 (d, *J* = 8.4 Hz, 1H), 8.03 (d, *J* = 8.8 Hz, 1H); ¹³C NMR (100 MHz, CDCl₃) δ 112.8, 117.9, 118.0, 122.5, 123.4, 123.8, 125.5, 125.6, 126.8, 127.6, 128.0, 128.2, 128.3, 129.8, 130.2, 131.4, 133.4, 133.8, 136.6, 142.0; IR (ATR) ν 2104, 1618, 1506, 1287, 808, 746 cm⁻¹; MS (EI): *m/z* (relative intensity, %) 310 (M⁺, 48), 281 ([C₂₀H₁₃N₂]⁺, 100), 140 ([C₁₀H₆N]⁺, 41); HRMS (EI): *m/z* calcd for C₂₀H₁₄N₄ (M) 310.1218, found 310.1216.

Optimization Studies of Reaction Conditions for Selective Synthesis of **3a** (Eq 1 and Table 1)

Typical procedure for optimization studies using 1a as substrate

To a 50 mL of two necked round-bottomed flask equipped with a magnetic stir bar, was added BINAM (**1a**) (0.2 mmol) under the air. The vessel was capped with a septum rubber and evacuated and refilled with N₂ gas three times, and appropriate solvent was added through the septum. To this stirred mixture, was added an appropriate oxidant under a stream of N₂ gas at room temperature. The resulting solution was stirred for 3 h before quenched with aqueous Na₂S₂O₃ (1.0 M, 20 mL), and the resulting mixture was extracted with CH₂Cl₂ (20 mL × 3). The combined organic extracts were dried over Na₂SO₄ and concentrated under vacuum to give the crude product. The yields of products were calculated by the integration of ¹H NMR signals of the crude product. Separation by flash column chromatography on silica gel gave the compounds **3a**, **2a** and **4**.

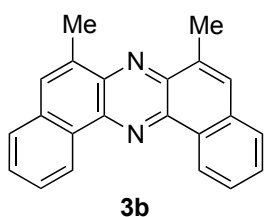
Note: t-BuOI was prepared in situ from NaI and t-BuOCl as follows:* To a 50 mL of two necked round-bottomed flask equipped with a magnetic stir bar, was added BINAM (1a**) (0.2 mmol) and NaI (0.8 mmol) under the air. The tube was capped with a septum rubber and evacuated and refilled with N₂ gas three times, and *t*-BuOH (20 mL) was added through the septum. To this stirred mixture, was added *t*-BuOCl (0.8 mmol) through the septum.

Dibenzo[*a,j*]phenazine (3a) [224-56-6]

Spectroscopic data were in agreement with those previously reported;² Purified by flash column chromatography on silica gel (hexane/EtOAc 99:1 to 8:2) and recrystallization from CHCl₃; Yellow solid; mp 243 °C; *R*_f 0.38 (hexane/EtOAc 8:2); ¹H NMR (400 MHz, CDCl₃) δ 7.78–7.88 (m, 4H), 7.98 (d, *J* = 8.0 Hz, 2H), 8.07 (d, *J* = 9.2 Hz, 2H), 8.10 (d, *J* = 9.2 Hz, 2H), 9.62 (d, *J* = 7.6 Hz, 2H); ¹³C NMR (100 MHz, CDCl₃) δ 125.1, 126.9, 127.6, 128.1, 129.2, 131.3, 132.4, 133.2, 140.5, 142.7; IR (ATR) ν 3035, 1350, 840, 800, 746 cm⁻¹; MS (EI): *m/z* (relative intensity, %) 280 (M⁺, 100), 140 ([C₁₀H₆N]⁺, 15), 126 ([C₁₀H₆]⁺, 11); HRMS (EI): *m/z* calcd for C₂₀H₁₂N₂ (M) 280.1000, found 280.1001.

Oxidative Skeletal Rearrangement of BINAMs 1 to Dibenzo[*a,j*]phenazines 3 (Table 2)**Typical procedure for skeletal rearrangement of BINAMs 1 to dibenzo[*a,j*]phenazines 3**

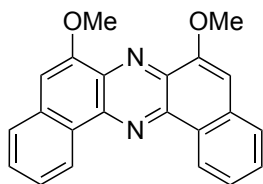
To a 50 mL of two necked round-bottomed flask equipped with a magnetic stir bar, was added biaryldiamine **1** (0.2 mmol) under the air. The flask was capped with a septum rubber and evacuated and refilled with N₂ gas three times, and ROH (R = *t*-Bu or Me) (20 mL) was added through the septum. To this stirred mixture, was added 1,3-diiodo-5,5-dimethylhydantoin (DIH) (607.8 mg, 1.6 mmol) under a stream of N₂ gas at room temperature. The resulting solution was stirred for the indicated time before quenched with aqueous Na₂S₂O₃ (1.0 M, 20 mL), and the resulting mixture was extracted with CH₂Cl₂ (20 mL × 3). The combined organic extracts were dried over Na₂SO₄ and concentrated under vacuum to give the crude product. Purification by flash column chromatography on silica gel gave the corresponding dibenzo[*a,j*]phenazine (for example, compound **3b**: 40.7 mg, 66%).

6,8-Dimethyldibenzo[*a,j*]phenazine (3b)

Purified by flash column chromatography on silica gel (hexane/EtOAc 95:5) and recrystallization from CHCl₃; Yellow solid (40.7 mg, 66%); mp 234 °C; *R*_f 0.60 (hexane/EtOAc 8:2); ¹H NMR (400 MHz, CDCl₃) δ 2.95 (d, *J* = 1.2 Hz, 6H), 7.72–7.79 (m, 4H), 7.87–7.89 (m, 4H), 9.54 (d, *J* = 7.8 Hz, 2H); ¹³C NMR (100 MHz, CDCl₃) δ 17.9, 125.0, 126.5, 127.3, 129.0, 130.2, 130.6, 133.4, 135.1, 139.8, 142.0; IR (ATR) ν 2916, 1479, 1331, 1119,

881, 756 cm^{-1} ; MS (EI): m/z (relative intensity, %) 308 (M^+ , 100), 154 ($[\text{C}_{11}\text{H}_8\text{N}]^+$, 12), 140 ($[\text{C}_{11}\text{H}_8]^+$, 7); HRMS (EI): m/z calcd for $\text{C}_{22}\text{H}_{16}\text{N}_2$ (M) 308.1313, found 308.1313.

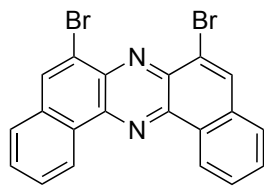
6,8-Dimethoxydibenzo[*a,j*]phenazine (3i)



3i

Purified by flash column chromatography on NH silica gel (hexane/EtOAc 9:1 to 5:5) and recrystallization from CHCl_3 ; Yellow solid (65.4 mg, 96%); mp 305 °C (dec.); R_f 0.18 (hexane/EtOAc 5:5, NH); ^1H NMR (400 MHz, CDCl_3) δ 4.23 (s, 6H), 7.29 (s, 2H), 7.69–7.77 (m, 4H), 7.87 (d, $J = 8.0$ Hz, 2H), 9.50 (d, $J = 8.4$ Hz, 2H); ^{13}C NMR (100 MHz, CDCl_3) δ 56.1, 106.5, 125.2, 125.3, 126.9, 127.1, 129.9, 133.9, 136.3, 141.3, 152.6; IR (ATR) ν 2924, 1624, 1572, 1472, 1344, 1288, 1165, 1136, 839, 744 cm^{-1} ; MS (EI): m/z (relative intensity, %) 340 (M^+ , 100), 311 ($[\text{C}_{20}\text{H}_{11}\text{N}_2\text{O}_2]^+$, 44), 294 ($[\text{C}_{20}\text{H}_{10}\text{N}_2\text{O}]^+$, 82), 170 ($[\text{C}_{11}\text{H}_8\text{NO}]$); HRMS (EI): m/z calcd for $\text{C}_{22}\text{H}_{16}\text{N}_2\text{O}_2$ (M) 340.1212, found 340.1211.

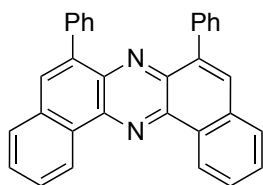
6,8-Dibromodibenzo[*a,j*]phenazine (3c)



3c

Purified by flash column chromatography on silica gel (hexane/EtOAc, 95:5 to 8:2) and recrystallization from CHCl_3 ; Yellow solid (32.4 mg, 37%); mp 286–287 °C (dec.); R_f 0.48 (hexane/EtOAc 8:2); ^1H NMR (400 MHz, CDCl_3) δ 7.82–7.92 (m, 6H), 8.49 (s, 2H), 9.52 (d, $J = 8.0$ Hz, 2H); ^{13}C NMR (100 MHz, CDCl_3) δ 122.0, 125.8, 127.6, 128.2, 130.3, 130.4, 133.6, 135.5, 140.0, 140.9; IR (ATR) ν 3064, 1506, 1378, 1324, 1216, 1012, 913, 890, 746 cm^{-1} ; MS (EI): m/z (relative intensity, %) 438 (M^+ , 100), 278 ($[\text{C}_{20}\text{H}_{10}\text{N}_2]^+$, 35), 218 ($[\text{C}_{10}\text{H}_5\text{BrN}]^+$, 8), 139 ($[\text{C}_{10}\text{H}_5\text{N}]^+$, 21); HRMS (EI): m/z calcd for $\text{C}_{20}\text{H}_{10}\text{Br}_2\text{N}_2$ (M) 435.9211, found 435.9207.

6,8-Diphenyldibenzo[*a,j*]phenazine (3d)

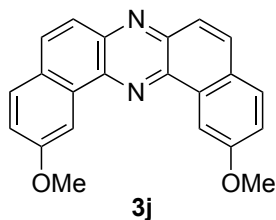


3d

Purified by flash column chromatography on silica gel (hexane/ CH_2Cl_2 , 10:0 to 9:1) and recrystallization from CHCl_3 ; Yellow solid (67.5 mg, 78%); mp 267–268 °C; R_f 0.30 (hexane/ CH_2Cl_2 8:2); ^1H NMR (400 MHz, CDCl_3) δ 7.39–7.40 (m, 6H), 7.78–7.89 (m, 8H), 8.00 (d, $J = 7.6$ Hz, 2H), 8.14 (s, 2H), 9.66 (d, $J = 7.6$ Hz, 2H); ^{13}C NMR (100 MHz, CDCl_3) δ 125.2, 127.3, 127.4, 127.7, 128.2, 129.5, 130.9, 131.0, 131.7, 133.2, 138.2, 138.3, 140.1, 140.9; IR (ATR) ν 3061, 1960, 1495, 1379, 1335, 897,

768 cm^{-1} ; MS (EI): m/z (relative intensity, %) 432 (M^+ , 100), 216 ($[\text{C}_{16}\text{H}_{10}\text{N}]^+$, 9); HRMS (EI): m/z calcd for $\text{C}_{32}\text{H}_{20}\text{N}_2$ (M) 432.1626, found 432.1624.

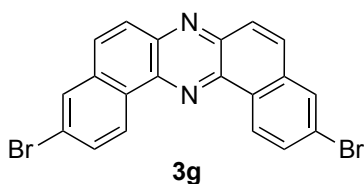
2,12-Dimethoxydibenzo[*a,j*]phenazine (3j)



Purified by flash column chromatography on NH silica gel (hexane/EtOAc 9:1 to 5:5) and recrystallization from CHCl_3 ; Yellow solid (42.2 mg, 62%); mp 260–261 $^\circ\text{C}$; R_f 0.23 (hexane/EtOAc 8:2, NH); ^1H NMR (400 MHz, CDCl_3) δ 4.15 (s, 6H), 7.41 (dd, $J = 2.4, 8.8$ Hz, 2H), 7.89 (d, $J = 8.8$ Hz, 2H), 7.93 (d, $J = 9.2$

Hz, 2H), 8.03 (d, $J = 9.2$ Hz, 2H), 8.99 (d, $J = 2.4$ Hz, 2H); ^{13}C NMR (100 MHz, CDCl_3) δ 55.6, 106.3, 118.8, 124.4, 127.7, 129.7, 132.1, 132.9, 139.6, 143.2, 159.3; IR (ATR) ν 3004, 2960, 1611, 1519, 1465, 1336, 1223, 1029, 873, 828 cm^{-1} ; MS (EI): m/z (relative intensity, %) 340 (M^+ , 100), 310 ($[\text{C}_{20}\text{H}_{10}\text{N}_2\text{O}_2]^+$, 8), 170 ($[\text{C}_{11}\text{H}_8\text{NO}]^+$, 11); HRMS (EI): m/z calcd for $\text{C}_{22}\text{H}_{16}\text{N}_2\text{O}_2$ (M) 340.1212, found 340.1211.

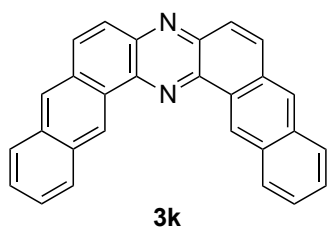
3,11-Dibromodibenzo[*a,j*]phenazine (3g)



Purified by flash column chromatography on silica gel (hexane/EtOAc, 95:5 to 8:2) and recrystallization from CHCl_3 ; Yellow solid (43.8 mg, 50%); mp 317–318 $^\circ\text{C}$ (dec.); R_f 0.35 (hexane/EtOAc 8:2); ^1H NMR (400 MHz, CDCl_3) δ 7.95 (dd, $J =$

2.0, 8.8 Hz, 2H), 8.01 (d, $J = 9.2$ Hz, 2H), 8.10 (d, $J = 9.2$ Hz, 2H), 8.15 (d, $J = 2.0$ Hz, 2H), 9.44 (d, $J = 8.4$ Hz, 2H); ^{13}C NMR (100 MHz, CDCl_3) δ 124.0, 127.0, 128.3, 129.8, 130.5, 130.9, 131.4, 134.6, 140.4, 142.8; IR (ATR) ν 3053, 1589, 1462, 1352, 1180, 1072, 991, 877, 848, 804, 788, 713 cm^{-1} ; MS (EI): m/z (relative intensity, %) 438 (M^+ , 100), 278 ($[\text{C}_{20}\text{H}_{10}\text{N}_2]^+$, 17), 218 ($[\text{C}_{10}\text{H}_5\text{BrN}]^+$, 7), 139 ($[\text{C}_{10}\text{H}_5\text{N}]^+$, 17); HRMS (EI): m/z calcd for $\text{C}_{20}\text{H}_{10}\text{Br}_2\text{N}_2$ (M) 435.9211, found 435.9209.

Dinaphtho[2,3-*a*:2',3'-*j*]phenazine (3k)



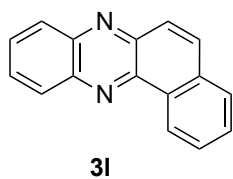
Purified by flash column chromatography on silica gel (hexane/EtOAc 8:2) and recrystallization from CHCl_3 ; Yellow solid (17.5 mg, 23%); mp 331 $^\circ\text{C}$ (dec.); R_f 0.15 (hexane/EtOAc 8:2); ^1H NMR (400 MHz, CDCl_3) δ 7.66–7.73 (m, 4H), 7.95 (d, J

= 9.2 Hz, 2H), 8.13–8.16 (m, 4H), 8.44 (d, $J = 7.2$ Hz, 2H), 8.47 (s, 2H), 10.17 (s, 2H); ^{13}C NMR (100 MHz, CDCl_3) δ 125.1, 126.5, 127.0, 127.2, 128.2, 129.2, 131.0, 132.3, 133.0, 133.4, 141.4, 143.4 (Two carbons are unsatisfied, probably due to the overlap of signals.); IR (ATR) ν 3048, 1491, 1320, 896, 885, 749 cm^{-1} ; MS (EI): m/z (relative intensity, %) 380 (M^+ , 100), 190 ($[\text{C}_{14}\text{H}_8\text{N}]^+$, 31), 176 ($[\text{C}_{14}\text{H}_8]^+$, 8); HRMS (EI): m/z calcd for $\text{C}_{28}\text{H}_{16}\text{N}_2$ (M) 380.1313, found 380.1309.

Experiments for the Survey of the Influence of Naphthalene Unit (Scheme 1)

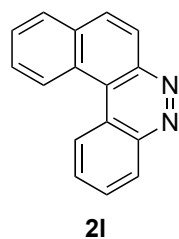
The experiments were conducted in the same way as those for the oxidative skeletal rearrangement of BINAM (**1a**), using biaryldiamine **1l** and **1h** as a starting material instead of **1a**.

Benzo[*a*]phenazine (**3l**) [225-61-6]



Spectroscopic data were in agreement with those previously reported;⁴⁷ Purified by flash column chromatography on silica gel (hexane/EtOAc 10:0 to 9:1); Brown solid (10.1 mg, 22%); ^1H NMR (400 MHz, CDCl_3) δ 7.80–8.05 (m, 7H), 8.29–8.31 (m, 1H), 8.38–8.40 (m, 1H), 9.44 (d, $J = 7.2$ Hz, 1H); ^{13}C NMR (100 MHz, CDCl_3) δ 125.4, 127.2, 128.0, 128.2, 129.2, 129.7, 129.8, 129.9, 130.1, 131.1, 133.2, 133.4, 142.0, 142.7 (2C), 143.6; MS (EI): m/z (relative intensity, %) 230 (M^+ , 100).

Dibenzo[*c,f*]cinnoline (**2l**) [195-31-3]



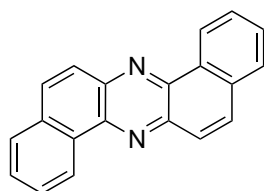
Purified by flash column chromatography on silica gel (hexane/EtOAc 95:5 to 8:2); Yellow solid (12.3 mg, 22%); mp 122–124 °C; R_f 0.38 (hexane/EtOAc 7:3); ^1H NMR (400 MHz, CDCl_3) δ 7.80–7.84 (m, 2H), 7.94–8.02 (m, 2H), 8.10–8.14 (m, 1H), 8.18 (d, $J = 8.8$ Hz, 1H), 8.61 (d, $J = 7.6$ Hz, 1H), 8.85 (d, $J = 7.6$ Hz, 1H), 9.13 (d, $J = 8.8$ Hz, 1H), 9.20–9.22 (m, 1H); ^{13}C NMR (100 MHz, CDCl_3) δ 119.1, 121.7, 125.5, 127.5, 128.2, 128.7, 128.8 (2C), 129.1, 130.6, 131.3, 131.4, 131.6, 134.8, 144.8, 147.4; IR (ATR) ν 2926, 1715, 1516, 1379, 1287, 1092, 829, 781, 752 cm^{-1} ; MS (EI): m/z (relative intensity, %) 230 (M^+ , 97), 202 ($[\text{C}_{16}\text{H}_{10}]^+$, 100); HRMS (EI): m/z calcd for $\text{C}_{16}\text{H}_{10}\text{N}_2$ (M) 230.0844, found 230.0842.

Cross-Over Experiment (Scheme 2)

The experiments were conducted in the same way as those for the oxidative skeletal rearrangement of BINAM (**1a**) except for using mixture of biaryldiamines **1a** (0.1 mmol) and **1i** (0.1 mmol) as a starting material.

Reaction of 2-aminonaphthalene with DIH (Eq 3)

The experiments were conducted in the same way as those for the oxidative skeletal rearrangement of BINAM (**1a**), using 2-aminonaphthalene (0.4 mmol) as a starting material instead of **1a**.

Dibenzo[*a,h*]phenazine [226-47-1]

Spectroscopic data were in agreement with those previously reported;²
Purified by flash column chromatography on silica gel (hexane/EtOAc 95:5 to 8:2); Yellow solid.

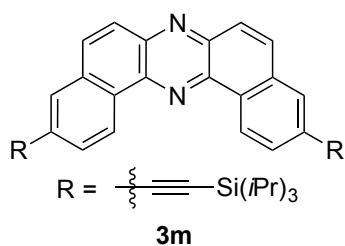
Photo-induced Decomposition of 2'-Azido-[1,1'-binaphthalen]-2-amine (6**)⁷*****Typical procedure for photo-induced decomposition of 6***

t-BuOH was degassed through freeze-pump-thaw cycling for three times before used. To a 150 mL of quartz tube equipped with a magnetic stir bar, was added azide **6** (0.2 mmol) under the air. The tube was capped with a septum rubber and evacuated and refilled with N₂ gas three times, and *t*-BuOH (20 mL) was added through the septum. The resulting mixture was irradiated with UV light (Riko 400 W high pressure Hg lamp UVL-400HA) under N₂ atmosphere at room temperature. After irradiation for 3 h, the solvent was concentrated under vacuum to give the crude product. The yields of products were calculated by the integration of ¹H NMR signals of the crude product.

**Note: To maintain a constant temperature, the apparatus was submerged in a water bath during the reaction.*

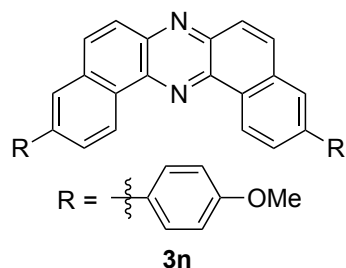
Pd-Catalyzed Functionalization of Phenazine **3g** (Scheme 4)

3,11-Bis((triisopropylsilyl)ethynyl)dibenzo[*a,j*]phenazine (**3m**)



Prepared from phenazine **3g** through Sonogashira coupling reaction:⁴⁸ THF (1.5 mL) and NEt₃ (0.15 mL) were degassed through freeze-pump-thaw cycling for three times before used. A 5 mL of two necked reaction tube equipped with a magnetic stir bar was capped with a septum rubber, and flame-dried and refilled with N₂ gas. To the tube, was added Phenazine **3g** (43.8 mg, 0.10 mmol), (triisopropylsilyl)acetylene (43.7 mg, 0.24 mmol), [PdCl₂(PPh₃)₂] (10.5 mg, 15 mol%), CuI (6.5 mg, 34 mol%), THF (1.5 mL) and NEt₃ (0.15 mL) under a stream of N₂ gas at room temperature, and the mixture was stirred at 60 °C for 3 h. The resulting mixture was cooled to room temperature and filtered. The solvent was evaporated in vacuo, and the crude product was purified by flash column chromatography on silica gel (hexane/EtOAc 95:5) and recrystallization from CHCl₃ to give product **3m**. Yellow solid (40.7 mg, 76%); mp 302–303 °C; *R*_f 0.53 (hexane/EtOAc 8:2); ¹H NMR (400 MHz, CDCl₃) δ 1.20–1.22 (m, 42H), 7.91 (dd, *J* = 1.2, 8.4 Hz, 2H), 8.03 (d, *J* = 9.2 Hz, 2H), 8.07 (d, *J* = 9.2 Hz, 2H), 8.10 (d, *J* = 1.2 Hz, 2H), 9.50 (*J* = 8.4 Hz, 2H); ¹³C NMR (100 MHz, CDCl₃) δ 11.3, 18.7, 93.3, 106.8, 124.5, 125.1, 127.6, 130.7, 130.9, 131.8, 132.1, 133.0, 140.4, 143.0; IR (ATR) ν 2941, 2862, 2156, 1470, 1354, 1147, 993, 881, 851, 799, 741 cm⁻¹; MS (EI): *m/z* (relative intensity, %) 640 (M⁺, 29), 597 ([C₃₉H₄₅N₂Si₂]⁺, 100), 555 ([C₃₆H₃₉N₂Si₂]⁺, 39), 541 ([C₃₅H₃₇N₂Si₂]⁺, 37), 527 ([C₃₄H₃₅N₂Si₂]⁺, 51), 221 ([C₁₅H₁₃Si]⁺, 45), 207 ([C₁₄H₁₁Si]⁺, 45); HRMS (EI): *m/z* calcd for C₄₂H₅₂N₂Si₂ (M) 640.3669, found 640.3671.

3,11-Bis(4-methoxyphenyl)dibenzo[*a,j*]phenazine (**3n**)

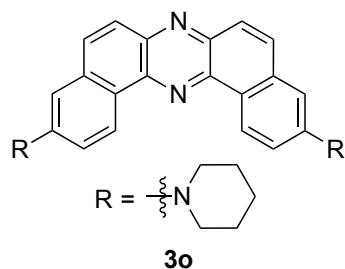


Prepared from phenazine **3g** by slight modified Nolan's method:¹⁰ 2-Propanol was degassed through freeze-pump-thaw cycling for three times before used. In a glovebox, to a 5 mL of two necked reaction tube equipped with a magnetic stir bar, was added potassium *tert*-butoxide (24.6 mg, 0.22 mmol) and closed the tube with a septum rubber. Outside the glovebox, phenazine **3g** (43.8 mg, 0.10 mmol), *p*-methoxyphenyl boronic acid (33.4 mg, 0.22 mmol), [SiPr-Pd(cinnamyl)Cl] (1.3 mg, 2 mol%) and 2-propanol (1 mL) were added under a stream of N₂

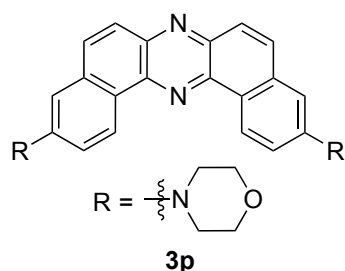
gas at room temperature, and the mixture was stirred at 60 °C for 24 h. Water was added to the reaction mixture, and the organic layer was extracted with CH₂Cl₂ (20 mL × 3). The combined organic extracts were dried over magnesium sulfate, and the solvent was evaporated in vacuo. The crude product was purified by flash column chromatography on silica gel (hexane/EtOAc 5:5 to 0:10) and recrystallization from CHCl₃ to give the product, **3n**. Yellow solid (36.9 mg, 77%); mp 265–266 °C; *R*_f 0.10 (hexane/EtOAc 5:5); ¹H NMR (400 MHz, CDCl₃) δ 3.91 (s, 6H), 7.08 (d, *J* = 8.4 Hz, 4H), 7.76 (d, *J* = 8.4 Hz, 4H), 8.05–8.11 (m, 8H), 9.62 (d, *J* = 8.4 Hz, 2H); ¹³C NMR (100 MHz, CDCl₃) δ 55.4, 114.5, 125.6, 125.8, 126.5, 127.3, 128.6, 129.8, 132.5, 133.0, 133.7, 140.7, 141.7, 142.6, 159.6; IR (ATR) ν 3036, 2835, 1607, 1512, 1474, 1354, 1248, 1179, 1032, 837, 812, 797, 718 cm⁻¹; MS (EI): *m/z* (relative intensity, %) 492 (M⁺, 100), 477 ([C₃₃H₂₁N₂O₂]⁺, 10), 246 ([C₁₇H₁₂NO]⁺, 19); HRMS (EI): *m/z* calcd for C₃₄H₂₄N₂O₂ (M) 492.1838, found 492.1840.

Typical procedure for preparation of diaminodibenzo[*a,j*]phenazines

Prepared from phenazine **3g** by slight modified Nolan's method:¹⁰ Dimethoxyethane (DME) was degassed through freeze-pump-thaw cycling for three times before used. In a glovebox, to a 5 mL of two necked reaction tube equipped with a magnetic stir bar, was added potassium *tert*-butoxide (24.6 mg, 0.22 mmol) and closed the tube with a septum rubber. Outside the glovebox, phenazine **3g** (43.8 mg, 0.10 mmol), [SIPr-Pd(cinnamyl)Cl] (1.3 mg, 2 mol%), DME (1 mL) and amine (piperidine or morpholine) (0.22 mmol) were added under a stream of N₂ gas at room temperature, and the mixture was stirred at 60 °C for 24 h. Water was added to the reaction mixture, and the organic layer was extracted with CH₂Cl₂ (20 mL × 3). The combined organic extracts were dried over magnesium sulfate, and the solvent was evaporated in vacuo to give the crude product. The crude product was purified by flash column chromatography on NH silica gel and recrystallization from benzene to give the corresponding diaminodibenzo[*a,j*]phenazine.

3,11-Dipiperidinodibenzo[*a,j*]phenazine (3o)

Purified by flash column chromatography on NH silica gel (hexane/EtOAc 97:3) and recrystallization from benzene; Orange solid (33.5 mg, 75%); mp 262 °C (dec.); R_f 0.20 (hexane/EtOAc 8:2, NH silica); ^1H NMR (400 MHz, CDCl_3) δ 1.65–1.71 (m, 4H), 1.77–1.83 (m, 8H), 3.43 (t, $J = 5.4$ Hz, 8H), 7.28 (d, $J = 2.8$ Hz, 2H), 7.49 (dd, $J = 2.8, 8.8$ Hz, 2H), 7.88 (d, $J = 9.2$ Hz, 2H), 7.94 (d, $J = 9.2$ Hz, 2H), 9.38 (d, $J = 8.8$ Hz, 2 H); ^{13}C NMR (100 MHz, CDCl_3) δ 24.4, 25.7, 50.0, 111.6, 117.8, 123.3, 126.2, 127.2, 131.5, 134.9, 141.0, 141.0, 152.5; IR (ATR) ν 3063, 2934, 1611, 1479, 1350, 1242, 1209, 1159, 1128, 957, 864, 847, 783, 716 cm^{-1} ; MS (EI): m/z (relative intensity, %) 446 (M^+ , 100), 223 ($[\text{C}_{15}\text{H}_{15}\text{N}_2]^+$, 9); HRMS (EI): m/z calcd for $\text{C}_{30}\text{H}_{30}\text{N}_4$ (M) 446.2470, found 446.2474.

3,11-Dimorpholinodibenzo[*a,j*]phenazine (3p)

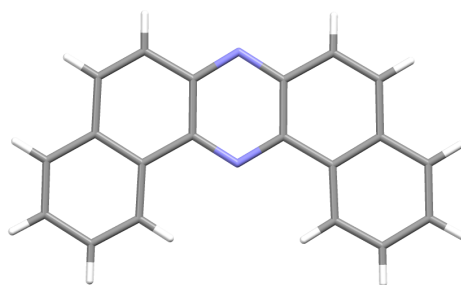
Purified by flash column chromatography on NH silica gel (hexane/EtOAc 9:1) and recrystallization from benzene; Yellow solid (34.7 mg, 77%); mp 284 °C (dec.); R_f 0.33 (hexane/EtOAc 5:5, NH silica); ^1H NMR (400 MHz, CDCl_3) δ 3.40 (t, $J = 4.8$ Hz, 8H), 3.96 (t, $J = 4.8$ Hz, 8H), 7.25 (d, $J = 2.4$ Hz, 2H), 7.46 (dd, $J = 2.4, 9.2$ Hz, 2H), 7.89 (d, $J = 8.8$ Hz, 2H), 7.97 (d, $J = 9.2$ Hz, 2H), 9.41 (d, $J = 8.8$ Hz, 2H); ^{13}C NMR (100 MHz, CDCl_3) δ 48.8, 66.8, 111.3, 117.0, 124.1, 126.3, 127.5, 131.5, 134.7, 140.9, 141.2, 151.8; IR (ATR) ν 2857, 1611, 1477, 1445, 1356, 1240, 1227, 1117, 961, 891, 852, 818, 789, 721 cm^{-1} ; MS (EI): m/z (relative intensity, %) 450 (M^+ , 100), 392 ($[\text{C}_{25}\text{H}_{20}\text{N}_4\text{O}]^+$, 15), 334 ($[\text{C}_{22}\text{H}_{14}\text{N}_4]^+$, 20), 225 ($[\text{C}_{14}\text{H}_{13}\text{N}_2\text{O}]^+$, 6), 167 ($[\text{C}_{10}\text{H}_5\text{N}_3]^+$, 19), 153 ($[\text{C}_{10}\text{H}_5\text{N}_2]^+$, 9), 139 ($[\text{C}_{10}\text{H}_5\text{N}]^+$, 4); HRMS (EI): m/z calcd for $\text{C}_{28}\text{H}_{26}\text{N}_4\text{O}_2$ (M) 450.2056, found 450.2053.

X-Ray Crystallographic Experiment of 3a (Figure 1 and Table 9)

The X-ray Diffraction data of the single crystal of **3a**, which has grown from a CHCl_3 solution, were collected on a Rigaku R-AXIS RAPID diffractometer with graphite monochromated $\text{CuK}\alpha$ radiation ($\lambda = 1.54187$ Å) to a $2\theta_{\text{max}}$ value of 136.4° at 277 K. The crystal structure was solved by direct methods (SHELX97) and refined by full-matrix least-squares method on F^2 (SHELX97). The non-hydrogen atoms were refined anisotropically, and

hydrogen atoms were refined using the riding model. The crystal data are summarized in Table 9. CCDC-1004407 contains the supplementary crystallographic data for **3a**, which are available free of charge from the Cambridge Crystallographic Data Center (CCDC) via www.ccdc.cam.ac.uk/data_request/cif.

Table 9. Summary of Crystallographic Data of **3a**



Empirical Formula	C ₂₀ H ₁₂ N ₂	
Formula Weight	280.33	
Crystal System	orthorhombic	
Space Group	P2 ₁ 2 ₁ 2 ₁ (#19)	
Unit cell dimensions	$a = 3.8813(1) \text{ \AA}$	$\alpha = 90^\circ$
	$b = 11.6430(3) \text{ \AA}$	$\beta = 90^\circ$
	$c = 29.5312(8) \text{ \AA}$	$\gamma = 90^\circ$
V	1334.50(6) \AA^3	
Z	4	
Density (calculated)	1.395 g/cm ³	
R_1 [$I > 2\sigma(I)$]	0.0503	
wR_2 (all data)	0.1344	
Crystal size	0.500 × 0.040 × 0.030 mm	
Goodness-of-fit on F^2	1.003	
Reflections collected/unique	15392/2436 [$R(\text{int}) = 0.0455$]	

Physicochemical Properties of Phenazines **3**

UV-vis and Emission Spectra (Table 3, Figures 2 and 6)

Solvents were purged with N₂ for 30 min before measurements. UV-vis and emission spectra of phenazines **3** were measured at room temperature in CH₂Cl₂ solutions (1.0 × 10⁻⁵ M).

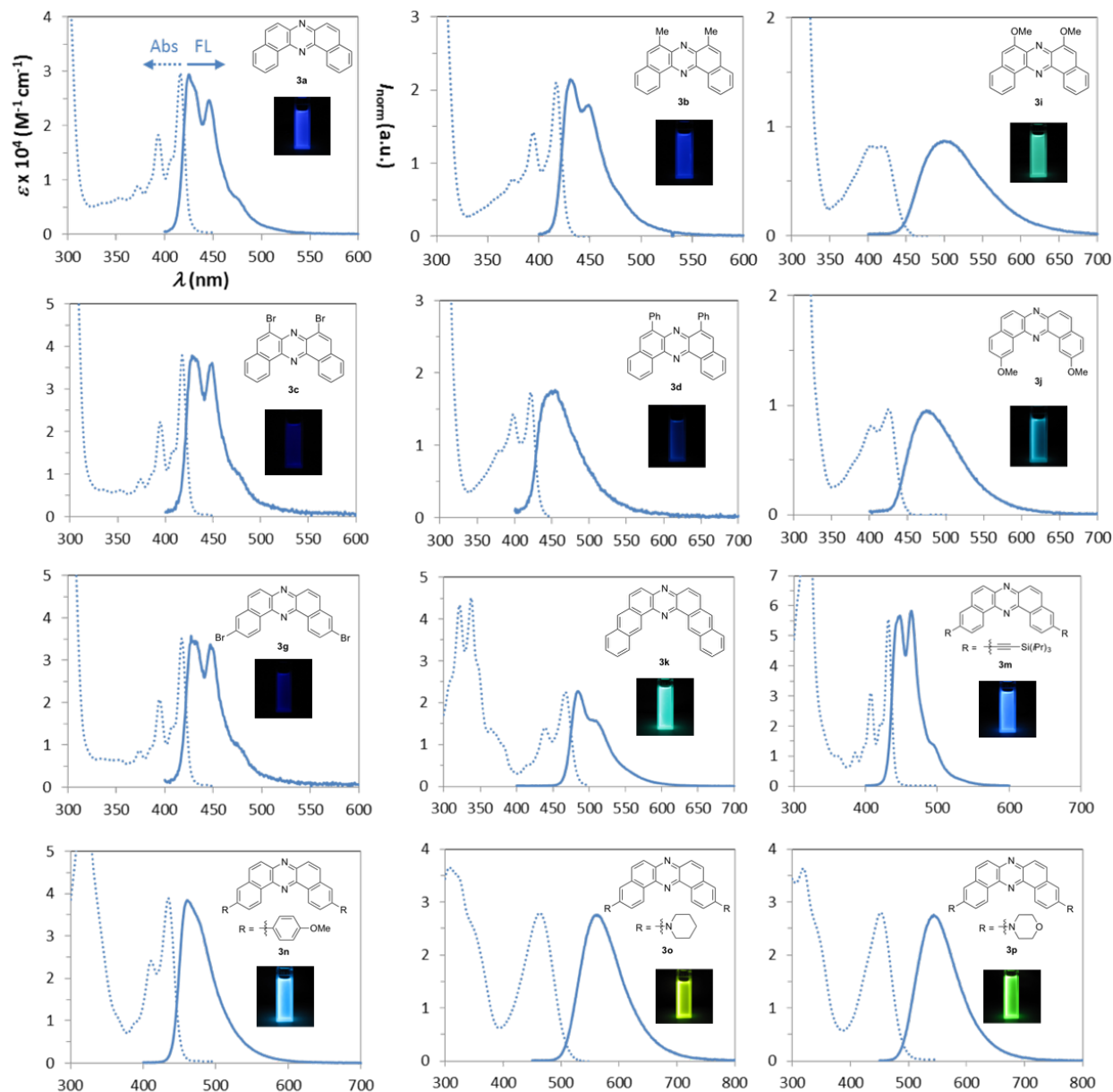


Figure 6. UV-vis and Emission Spectra of Phenazines 3

Cyclic Voltammograms (Table 4 and Figure 7)

Cyclic voltammograms of phenazines **3** were recorded at room temperature in CH_2Cl_2 solutions (5.0×10^{-4} M) containing 0.1 M tetrabutylammonium hexafluorophosphate as a supporting electrolyte and with a Pt as the working electrode at the scanning rate of 100 m/V. A Pt wire and an Ag wire were applied as the counter and the reference electrode, respectively. All the potentials were corrected against the Fc/Fc^+ (Fc = ferrocene) couple and the values of LUMO levels were calculated with the equation 9.

$$\text{LUMO} = -(4.8 + {}^{\text{red}}E_{1/2} \text{ vs. Fc/Fc}^+) [\text{eV}] \quad (9)$$

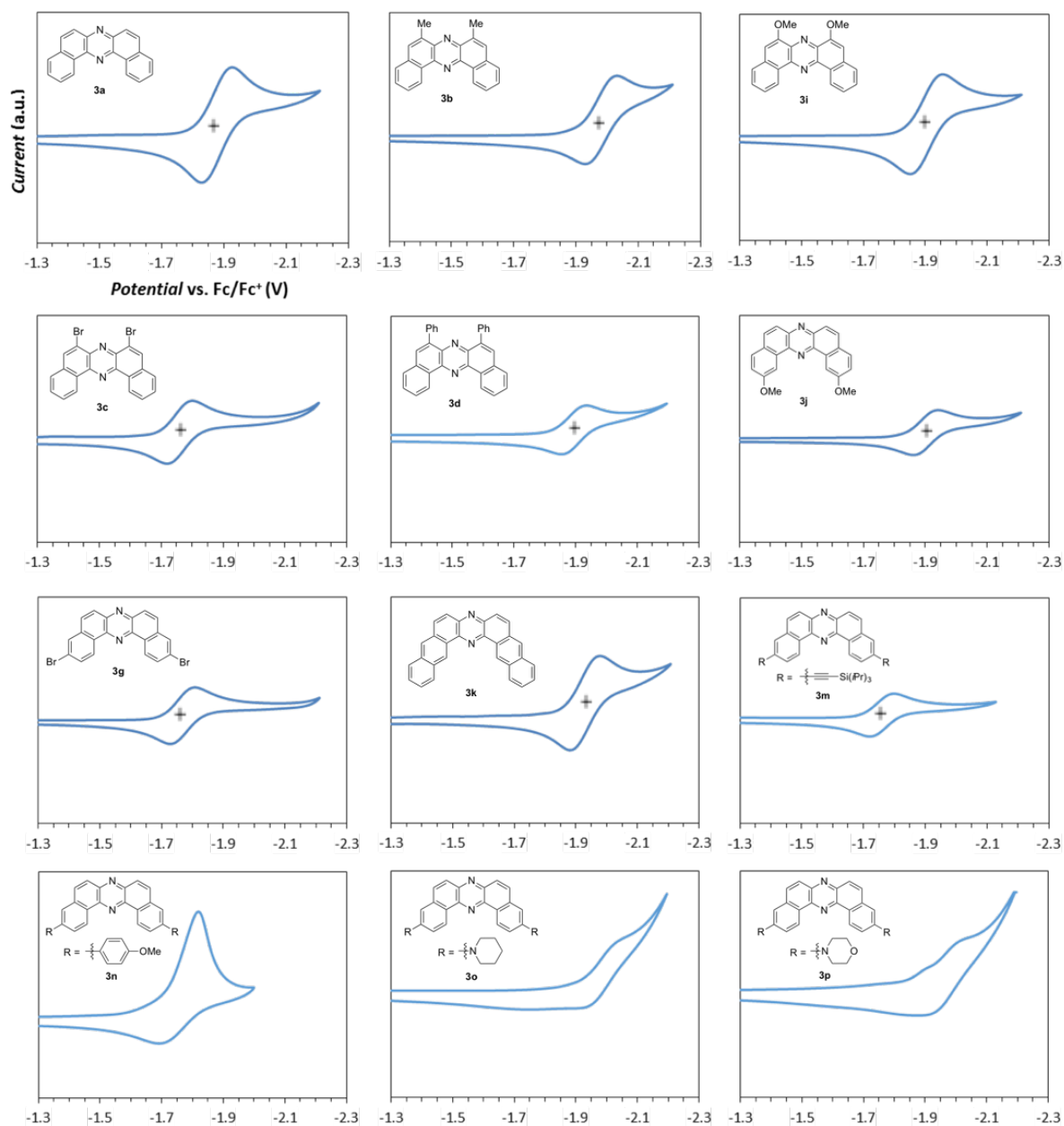


Figure 7. Cyclic Voltammograms of Phenazines **3**

Thermogravimetric Analysis (TGA) (Table 4 and Figure 8)

All the TGA profiles of phenazines **3** were measured under the nitrogen flow (200 mL/min) starting from 40 °C to 600 °C at the ramp rate of 10 °C/min.

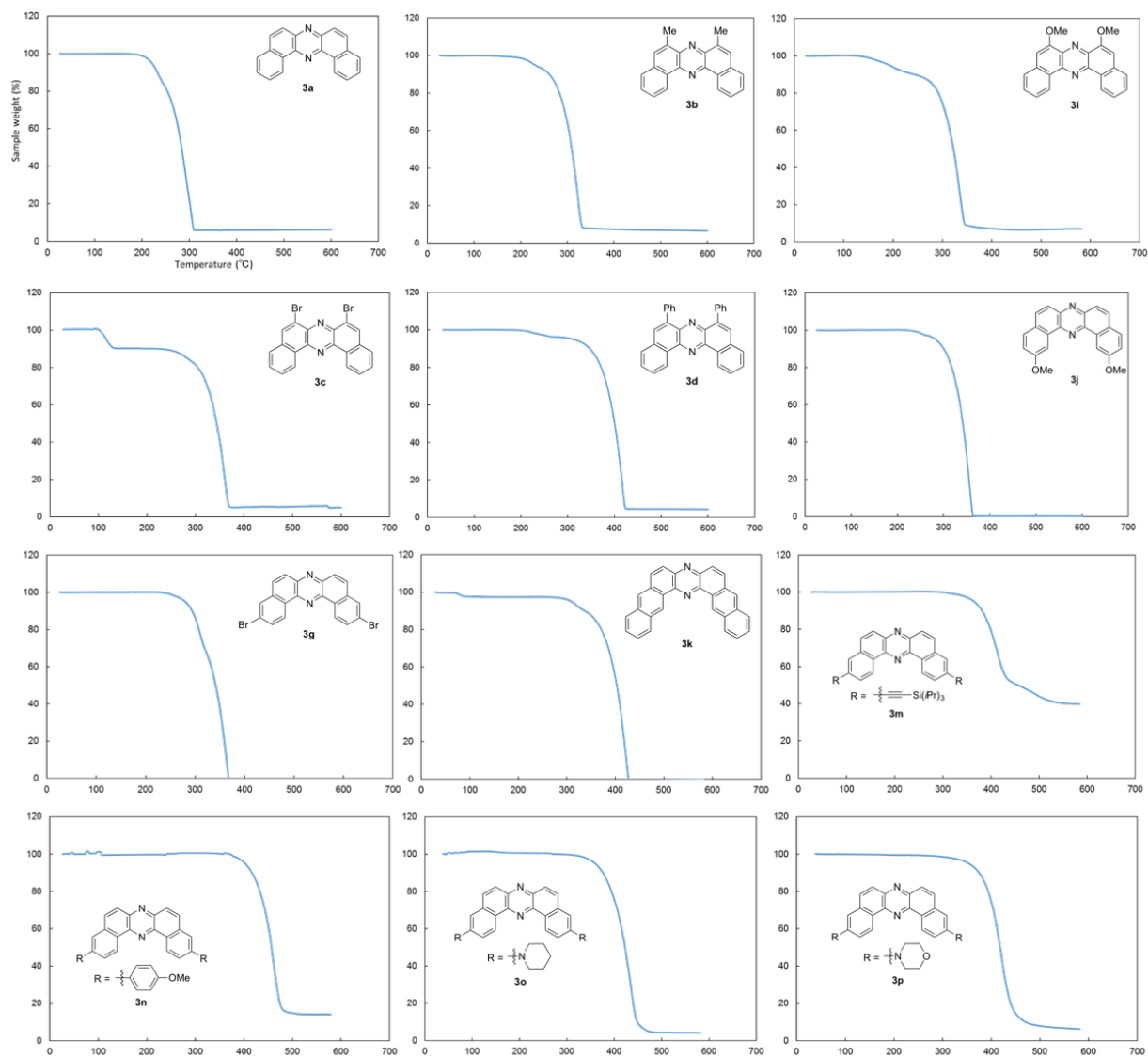


Figure 8. TGA Profiles of Phenazines **3**

Optimization Studies of Reaction Conditions for Selective Synthesis of **5a** (Eq 4, Table 5 and Scheme 5b)

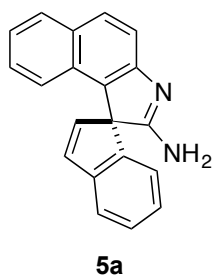
*Typical procedure for the optimization studies using **1a** as substrate*

To a two-necked round-bottomed flask (50 mL) equipped with a three-way stopcock and a magnetic stir bar, was added BINAM (**1a**) (56.8 mg, 0.2 mmol) under the air. The vessel was capped with a rubber septum, evacuated, and refilled with N₂ gas for three times, and acetonitrile (20 mL) was added through the septum. The resulting solution was cooled to –40 °C. To the solution, was an appropriate oxidant under a stream of N₂ gas at –40 °C. The resulting solution was stirred for indicated time before quenched with aqueous Na₂S₂O₃ solution (1.0 M, 20 mL), and the resulting mixture was extracted with CH₂Cl₂ (20 mL × 3).

The combined organic extracts were dried over Na_2SO_4 and concentrated under vacuum to give the crude product. The yields of products were calculated by the integration of ^1H NMR signals of the crude product. Separation by flash column chromatography on NH silica gel gave product **5a**.

Note: *t*-BuOI was generated in situ from NaI and *t*-BuOCl as follows:* To a two-necked round-bottomed flask (50 mL) equipped with a magnetic stir bar, was added BINAM (1a**) (56.8 mg, 0.2 mmol) and NaI (119.9 mg, 0.8 mmol) under the air. The flask was capped with a rubber septum, evacuated, and refilled with N_2 gas for three times, and then MeCN (20 mL) was added through the septum. The mixture was cooled to -40 °C. To the mixture, was added *t*-BuOCl (86.8 mg, 0.8 mmol) through the septum.

Spiro[benzo[*e*]indole-1,1'-inden]-2-amine (**5a**)



Colorless solid; mp 243 °C (dec.); R_f 0.10 (hexane/EtOAc 5:5 on an NH silica gel plate); ^1H NMR (400 MHz, CDCl_3) δ 4.80 (br, the peak was too broad to calculate the correct integration), 6.40 (d, $J = 5.2$ Hz, 1H), 6.71 (d, $J = 8.8$ Hz, 1H), 6.93 (d, $J = 7.6$ Hz, 1H), 7.08–7.20 (m, 3H), 7.28 (d, $J = 5.6$ Hz, 1H), 7.37 (dd, $J = 7.6, 7.6$ Hz, 1H), 7.56 (d, $J = 5.6$ Hz, 1H), 7.58 (d, $J = 6.4$ Hz, 1H), 7.77 (d, $J = 8.0$ Hz, 1H), 7.82 (d, $J = 8.0$ Hz, 1H); ^{13}C NMR (100 MHz, CDCl_3) δ 70.4, 117.9, 121.2, 122.1, 123.0, 123.1, 125.2, 126.5, 126.8, 128.3, 128.8, 129.0, 129.7, 130.4, 134.9, 138.0, 143.9, 144.5, 155.8, 173.6; IR (ATR) ν 3441, 3305, 3026, 1651, 1622, 1545, 1512, 1452, 1271, 829, 744 cm^{-1} ; MS (EI): m/z (relative intensity, %) 282 ($[\text{M}]^+$, 100), 264 ($[\text{C}_{20}\text{H}_{10}\text{N}]^+$, 21), 254 ($[\text{C}_{19}\text{H}_{12}\text{N}]^+$, 8), 239 ($[\text{C}_{19}\text{H}_{11}]^+$, 8), 140 ($[\text{C}_{10}\text{H}_6\text{N}]^+$, 7); HRMS (EI): m/z calcd for $\text{C}_{20}\text{H}_{14}\text{N}_2$ (M) 282.1157, found 282.1160.

Reaction of Spiro Product **5a** with DIH²³

To a two-necked round-bottomed flask (50 mL) equipped with a three-way stopcock and a magnetic stir bar, was added **5a** (56.4 mg, 0.2 mmol) under the air. The vessel was capped with a rubber septum, evacuated, and refilled with N_2 gas for three times, and acetonitrile (20 mL) was added through the septum. The resulting solution was cooled to -40 °C. To the solution, was added DIH (151.9 mg, 0.4 mmol) under a stream of N_2 gas at -40 °C. The resulting solution was stirred for indicated time before quenched with aqueous $\text{Na}_2\text{S}_2\text{O}_3$ solution (1.0 M, 20 mL), and the resulting mixture was extracted with CH_2Cl_2 (20 mL \times 3). The combined

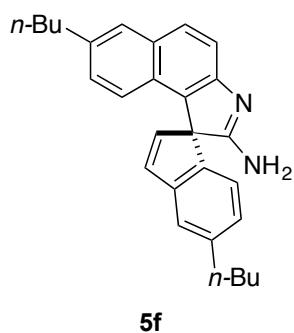
organic extracts were dried over Na_2SO_4 and concentrated under vacuum to give the crude product. The yields of products were calculated by the integration of ^1H NMR signals of the crude product.

Investigation of the Substrate Scope of the Rearrangement (Table 6 and Scheme 5a)

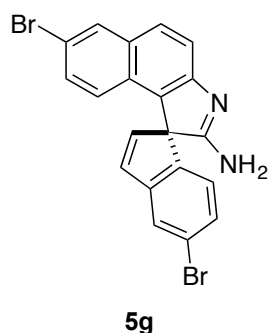
Typical procedure for investigation of the substrate scope of the rearrangement

To a two-necked round-bottomed flask (50 mL) equipped with a three-way stopcock and a magnetic stir bar, was added biaryldiamine **1** (0.1 mmol) under the air. The vessel was capped with a rubber septum, evacuated, and refilled with N_2 gas for three times, and an appropriate solvent (10 mL) was added through the septum. The resulting solution was cooled to indicated temperature. To the solution, was added DIH (0.2 mmol) under a stream of N_2 gas at indicated temperature. The resulting solution was stirred for indicated time before quenched with aqueous $\text{Na}_2\text{S}_2\text{O}_3$ solution (1.0 M, 20 mL), and the resulting mixture was extracted with CH_2Cl_2 (20 mL \times 3). The combined organic extracts were dried over Na_2SO_4 and concentrated under vacuum to give the crude product. The yields of products were calculated by the integration of ^1H NMR signals of the crude product. Separation by flash column chromatography on NH silica gel gave product **5**.

5',7-Di-*n*-butylspiro[benzo[*e*]indole-1,1'-inden]-2-amine (5f)



Purified by NH silica gel column chromatography (hexane/EtOAc 5:5); brown solid; mp 65 °C (dec.); R_f 0.15 (hexane/EtOAc 5:5, NH); ^1H NMR (400 MHz, CDCl_3) δ 0.89 (t, J = 7.2 Hz, 3H), 0.94 (t, J = 7.2 Hz, 3H), 1.28–1.43 (m, 4H), 1.54–1.67 (m, 4H), 2.60–2.68 (m, 4H), 6.35 (d, J = 5.2 Hz, 1H), 6.66 (d, J = 8.8 Hz, 1H), 6.81 (d, J = 7.6 Hz, 1H), 6.93–6.98 (m, 2H), 7.22 (d, J = 5.2 Hz, 1H), 7.36 (s, 1H), 7.53–7.55 (m, 2H), 7.74 (d, J = 8.8 Hz, 1H); ^{13}C NMR (100 MHz, CDCl_3) δ 13.9, 14.0, 22.3, 22.4, 33.5, 33.7, 35.6, 35.7, 70.2, 117.9, 121.1, 122.1, 122.7, 125.5, 127.1, 127.2, 127.5, 128.1, 129.0, 130.7, 134.9, 137.5, 138.1, 141.8, 143.2, 144.2, 154.9, 173.4; IR (ATR) ν 2926, 2854, 1649, 1624, 1550, 1463, 1263, 821 cm^{-1} ; MS (EI): m/z (relative intensity, %) 394 ($[\text{M}]^+$, 100), 351 ($[\text{C}_{25}\text{H}_{23}\text{N}_2]^+$, 60), 337 ($[\text{C}_{24}\text{H}_{21}\text{N}_2]^+$, 14), 308 ($[\text{C}_{22}\text{H}_{16}\text{N}_2]^+$, 10), 294 ($[\text{C}_{21}\text{H}_{14}\text{N}_2]^+$, 11); HRMS (EI): m/z calcd for $\text{C}_{28}\text{H}_{30}\text{N}_2$ (M) 394.2409, found 394.2409.

5',7-Dibromospiro[benzo[e]indole-1,1'-inden]-2-amine (5g)

Purified by NH silica gel column chromatography (hexane/EtOAc 5:5 to 0:10); Pale yellow solid; mp 160 °C (dec.); R_f 0.24 (EtOAc, NH); ^1H NMR (400 MHz, CDCl_3) δ 6.43 (d, $J = 5.6$ Hz, 1H), 6.55 (d, $J = 8.8$ Hz, 1H), 6.77 (d, $J = 7.6$ Hz, 1H), 7.19 (dd, $J = 2.0, 9.2$ Hz, 1H), 7.24 (d, $J = 5.6$ Hz, 1H), 7.26–7.28 (m, 1H), 7.59 (d, $J = 8.0$ Hz, 1H), 7.71 (d, $J = 1.6$ Hz, 1H), 7.74 (d, $J = 8.8$ Hz, 1H), 7.94 (d, $J = 1.6$ Hz, 1H); ^{13}C NMR (100 MHz, CDCl_3) δ 70.2, 116.9, 119.0, 122.6, 122.6, 124.3, 124.8, 125.5, 127.2, 129.1, 129.9, 130.0, 130.8, 131.6, 134.2, 139.4, 143.1, 145.8, 156.4, 172.8; IR (ATR) ν 3441, 3078, 1651, 1629, 1548, 1504, 1450, 1271, 815, 761 cm^{-1} ; MS (EI): m/z (relative intensity, %) 440 ($[\text{M}]^+$, 100), 359 ($[\text{C}_{20}\text{H}_{12}\text{BrN}_2]^+$, 58), 279 ($[\text{C}_{20}\text{H}_{11}\text{N}_2]^+$, 41), 237 ($[\text{C}_{19}\text{H}_9]^+$, 32), 140 ($[\text{C}_{10}\text{H}_6\text{N}]^+$, 32); HRMS (EI): m/z calcd for $\text{C}_{20}\text{H}_{12}\text{Br}_2\text{N}_2$ (M) 437.9367, found 437.9364.

Photo-induced Decomposition of 2'-Azido-[1,1'-binaphthalen]-2-amine (6) (Scheme 5c)

Acetonitrile was degassed through freeze-pump-thaw cycling for three times before use. To a quartz tube (150 mL) equipped with a magnetic stir bar, was added **6** (62.0 mg, 0.2 mmol) under the air. The tube was capped with a rubber septum, evacuated, and refilled with N_2 gas for three times, and acetonitrile (20 mL) was added through the septum. The resulting solution was irradiated with UV light (Riko 400 W high pressure Hg lamp UVL-400HA) under N_2 atmosphere at -40 °C. After irradiation for 3 h, the solvent was concentrated under vacuum to give the crude product. Separation by flash column chromatography on NH silica gel gave the compound **5a**.

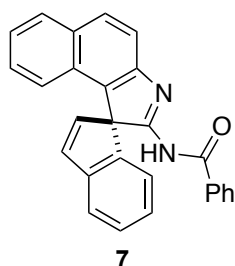
**Note: To maintain a constant reaction temperature, the apparatus was submerged in an acetonitrile and dry ice bath during the reaction.*

Synthesis of 7 and 8 (Scheme 7)**Procedure for the synthesis of 7**

7 was synthesized according to the procedures in literature.⁴⁹ To a two-necked reaction tube (20 mL) equipped with a three-way stopcock and a magnetic stir bar, was added **5a** (56.4 mg, 0.2 mmol) under the air. The vessel was capped with a rubber septum, evacuated, and refilled with N_2 gas for three times, and Et_3N (22.2 mg, 0.22 mmol) and CH_2Cl_2 (2 mL) were

added through the septum. The resulting solution was cooled to 0 °C. To the solution, was added benzoyl chloride (30.9 mg, 0.22 mmol) under a stream of N₂ gas, and the resulting solution was stirred for 30 min at 0 °C. The solution was warmed up to room temperature and stirred for 2 h. The solvent was concentrated under vacuum to give the crude product. Separation by flash column chromatography on silica gel (hexane/AcOEt 10:0–95:5) gave product **7**.

***N*-(Spiro[benzo[*e*]indole-1,1'-inden]-2-yl)benzamide (**7**)**

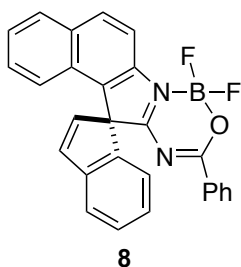


Pale yellow solid; mp 183 °C; *R*_f 0.33 (hexane/EtOAc 8:2); ¹H NMR (600 MHz, CDCl₃) δ 6.44 (d, *J* = 5.4 Hz, 1H), 6.90–6.92 (m, 2H), 7.09 (dd, *J* = 7.2, 7.2 Hz, 1H), 7.20 (dd, *J* = 7.2, 7.2 Hz, 1H), 7.29 (ddd, *J* = 0.6, 6.6, 7.8 Hz, 1H), 7.32–7.43 (m, 6H), 7.60 (d, *J* = 7.8 Hz, 1H), 7.82 (d, *J* = 8.4 Hz, 1H), 7.90 (d, *J* = 9.0 Hz, 1H), 8.08 (d, *J* = 7.2 Hz, 2H), 12.16 (br, 1H); ¹³C NMR (150 MHz, CDCl₃) δ 68.6, 111.8, 121.2, 122.0, 122.1, 122.6, 124.5, 126.6, 127.5, 128.0, 128.2, 129.0, 129.3, 130.0, 130.4, 131.1, 132.1, 135.8, 136.8, 136.9, 140.8, 144.9, 145.9, 174.8, 180.0; IR (ATR) ν 3290, 3059, 1610, 1562, 1552, 1284, 1255, 1172, 997 cm⁻¹; MS (EI): *m/z* (relative intensity, %) 386 ([M]⁺, 58), 309 ([C₂₁H₁₃N₂O]⁺, 11), 281 ([C₂₀H₁₃N₂]⁺, 17), 105 ([C₇H₅O]⁺, 100), 77 ([C₆H₅]⁺, 35); HRMS (EI): *m/z* calcd for C₂₇H₁₈N₂O (M) 386.1419, found 386.1423.

Procedure for the synthesis of 8

To a two-necked reaction tube (20 mL) equipped with a three-way stopcock and a magnetic stir bar, was added **7** (38.6 mg, 0.1 mmol) under the air. The vessel was capped with a rubber septum, evacuated, and refilled with N₂ gas for three times, and CH₂Cl₂ (3 mL), Et₃N (30.3 mg, 0.3 mmol) and BF₃•Et₂O (56.7 mg, 0.4 mmol) were added through the septum. The resulting solution was stirred for 24 h at room temperature. The solution was added CH₂Cl₂ (20 mL) and washed with water (20 mL × 3). The organic solvent was dried over MgSO₄ and concentrated under vacuum to give the crude product. Separation by flash column chromatography on silica gel (hexane/CH₂Cl₂ = 8:2–5:5) gave product **8**. Further purification was carried out by recrystallization from *n*-hexane/CHCl₃.

8,8-Difluoro-10-phenyl-8*H*-7λ⁴,8λ⁴-spiro[benzo[*e*][1,3,5,2]oxadiazaborinino[3,4-*a*]indole-12,1'-indene] (8)



Yellow solid; mp 244 °C (dec.); *R*_f 0.25 (hexane/CH₂Cl₂ 7:3); ¹H NMR (600 MHz, CDCl₃) δ 6.29 (d, *J* = 5.4 Hz, 1H), 6.83 (dd, *J* = 1.2, 7.2 Hz, 1H), 6.94 (dd, *J* = 1.2, 8.4 Hz, 1H), 7.12 (ddd, *J* = 1.2, 7.8, 8.4 Hz, 1H), 7.25–7.27 (m, 1H), 7.38–7.43 (m, 4H), 7.49 (dd, *J* = 0.6, 5.4 Hz, 1H), 7.57 (dd, *J* = 0.6, 8.4 Hz, 1H), 7.65 (d, *J* = 7.8 Hz, 1H), 7.89 (d, *J* = 8.4 Hz, 1H), 7.96 (d, *J* = 8.4 Hz, 1H), 8.02 (d, *J* = 9.0 Hz, 1H), 8.21 (dd, *J* = 1.2, 8.4 Hz, 2H); ¹³C NMR (150 MHz, CDCl₃) δ 69.6, 115.3, 122.4, 122.5, 122.8, 125.7, 125.8, 127.1, 127.6, 128.5, 128.6, 129.0, 129.1, 130.9, 130.9, 131.1, 132.5, 133.4, 134.7, 138.1, 141.7, 141.8, 145.5, 173.1, 180.1; IR (ATR) ν 3068, 2926, 1529, 1467, 1436, 1392, 1122, 1095, 1041, 987, 921, 806 cm⁻¹; ¹⁹F NMR (564 MHz, CDCl₃) δ -136.6 (ddd, *J* = 16.9, 84.6, 107.1 Hz); ¹¹B NMR (192 MHz, CDCl₃) δ 0.66 (t, *J* = 13.4 Hz); MS (EI): *m/z* (relative intensity, %) 434 ([M]⁺, 100), 265 ([C₂₀H₁₁N]⁺, 39), 105 ([C₇H₅O]⁺, 96), 77 ([C₆H₅]⁺, 30); HRMS (EI): *m/z* calcd for C₂₇H₁₇BF₂N₂O (M) 434.1402, found 434.1399.

Physicochemical Properties of Spiro Compounds 5a, 7 and 8

UV-vis and Emission Spectra (Table 7 and Figure 5)

Solvents were purged with N₂ for 30 min before the measurements. UV-vis absorption and emission spectra were measured at room temperature using the solutions (1.0 × 10⁻⁵ M).

Lippert-Mataga Plot (Table 10 and Figure 9)³¹

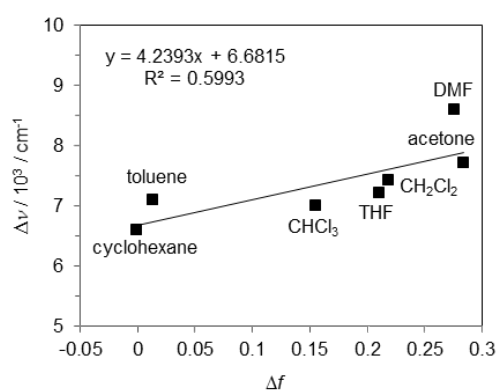
The Lippert-Mataga plot was constructed by using the relation

$$\Delta\nu = \nu_{\text{abs}} - \nu_{\text{em}} = -[2(\mu_{\text{e}} - \mu_{\text{g}})^2/hca^3] \Delta f + \text{const.} \quad (10)$$

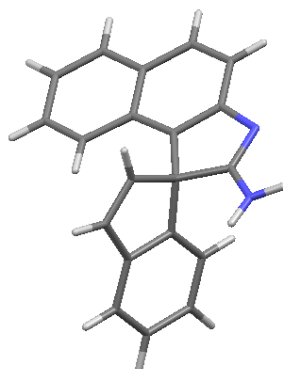
where Δν is the Stokes shift, μ_g and μ_e are dipole moments in the ground state and excited state, respectively. *a* is Onsager cavity radius and Δ*f* is the orientation polarizability of various solvents.

Table 10. Stokes shifts ($\Delta\nu$) of **8** and the orientation polarizability (Δf) of various solvents.

solvent	Δf	$\nu_{\text{abs}} (\text{cm}^{-1})$	$\nu_{\text{em}} (\text{cm}^{-1})$	$\Delta\nu (\text{cm}^{-1})$
cyclohexane	-0.001	25575	18975	6600
toluene	0.0135	25380	18281	7099
THF	0.210	25641	18416	7225
CHCl_3	0.155	25380	18382	6998
CH_2Cl_2	0.218	25510	18083	7427
acetone	0.284	25839	18115	7724
DMF	0.276	26109	17513	8596

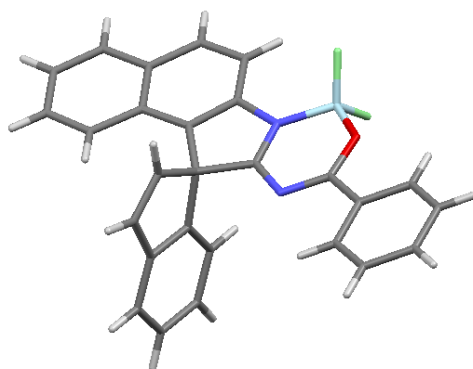
**Figure 9.** Lippert-Mataga plot of **8****X-ray Crystallographic Data** (Figures 3, 4, Tables 11 and 12)

The X-ray Diffraction data of the single crystal of **5a**, which has grown from an acetone solution, were collected on a Rigaku R-Axis RAPID diffractometer with graphite monochromated $\text{CuK}\alpha$ radiation ($\lambda = 1.54187 \text{ \AA}$) to a $2\theta_{\text{max}}$ value of 136.4° at 123 K. The crystal structure was solved by direct methods (SIR92)⁵⁰ and expanded using Fourier techniques. The non-hydrogen atoms were refined anisotropically, and hydrogen atoms were refined using the riding model. The crystal data are summarized in Table 11. CCDC-1416916 contains the supplementary crystallographic data for **5a**, which are available free of charge from the Cambridge Crystallographic Data Center (CCDC) via www.ccdc.cam.ac.uk/data_request/cif.

Table 11. Summary of Crystallographic Data of **5a**.

Empirical Formula	C ₂₀ H ₁₄ N ₂	
Formula Weight	282.34	
Crystal System	monoclinic	
Space Group	P2 _{1/c} (#14)	
Unit cell dimensions	$a = 12.8566(3) \text{ \AA}$	$\alpha = 90^\circ$
	$b = 7.1822(2) \text{ \AA}$	$\beta = 101.868(2)^\circ$
	$c = 16.5150(4) \text{ \AA}$	$\gamma = 90^\circ$
V	1492.38(5) Å ³	
Z	4	
Density (calculated)	1.257 g/cm ³	
Absorption coefficient	5.774 cm ⁻¹	
$R_1 [I > 2\sigma(I)]$	0.0408	
wR_2 (all data)	0.1064	
Crystal size	0.600 × 0.350 × 0.150 mm	
Goodness-of-fit on F^2	1.069	
Reflections collected/unique	16175/2740 [$R(\text{int}) = 0.0442$]	

The X-ray Diffraction data of the single crystal of **8**, which has grown from a *n*-hexane/CHCl₃ mixed solution, were collected on a Rigaku R-Axis RAPID diffractometer with graphite monochromated CuK α radiation ($\lambda = 1.54187 \text{ \AA}$) to a $2\theta_{\text{max}}$ value of 136.5° at 123 K. The crystal structure was solved by direct methods (SIR92)⁵⁰ and expanded using Fourier techniques. The non-hydrogen atoms were refined anisotropically, and hydrogen atoms were refined using the riding model. The crystal data are summarized in Table 12. CCDC-1416929 contains the supplementary crystallographic data for **8**, which are available free of charge from the Cambridge Crystallographic Data Center (CCDC) via http://www.ccdc.cam.ac.uk/data_request/cif.

Table 12. Summary of Crystallographic Data of **8**

Empirical Formula	$C_{27}H_{17}BF_2N_2O$
Formula Weight	434.25
Crystal System	monoclinic
Space Group	$P2_1/c$ (#14)
Unit cell dimensions	$a = 10.3671(4) \text{ \AA}$ $\alpha = 90^\circ$
	$b = 10.9631(4) \text{ \AA}$ $\beta = 101.136(3)^\circ$
	$c = 18.3325(5) \text{ \AA}$ $\gamma = 90^\circ$
V	$2044.4(2) \text{ \AA}^3$
Z	4
Density (calculated)	1.411 g/cm^3
Absorption coefficient	8.080 cm^{-1}
$R_1 [I > 2\sigma(I)]$	0.0627
wR_2 (all data)	0.1838
Crystal size	$0.250 \times 0.200 \times 0.050 \text{ mm}$
Goodness-of-fit on F^2	1.062
Reflections collected/unique	21844/3708 [$R(\text{int}) = 0.0692$]

Theoretical Studies

All the molecules were geometrically optimized by DFT method at the B3LYP/6-31G(d) level of theory using Gaussian 09 package.⁵¹ The excitation energies of the geometrically optimized molecules were calculated with the TD-DFT method at the same level of theory. Cartesian coordinates of the optimized structures of **5a**, **7** and **8** are listed below (Tables 13–15).

Table 13. Cartesian Coordinates of the Optimized Structure of **5a**

atom	x	y	z
N	9.710602	1.353135	7.741694
N	10.67058	-0.30327	6.386537
C	9.075996	1.133696	5.298265
C	9.856651	0.689149	6.562954
C	10.56729	-0.65164	5.022682
C	11.29044	-1.68573	4.39138
C	11.07844	-1.91153	3.048532
C	10.15529	-1.13524	2.293716
C	9.940322	-1.3743	0.910095
C	9.044017	-0.61998	0.187439
C	8.317121	0.416309	0.823657
C	8.496509	0.681052	2.162466
C	9.415924	-0.07959	2.938592
C	9.657711	0.128081	4.31508
C	7.566635	1.110857	5.521605
C	6.72637	0.046239	5.816558
C	5.360455	0.300996	5.999612
C	4.856072	1.60091	5.890916
C	5.701386	2.67481	5.593403
C	7.061842	2.424335	5.4072
C	8.180002	3.315682	5.075361
C	9.320013	2.604652	4.990354
H	8.862693	1.884201	7.883616
H	11.99461	-2.27909	4.966183
H	11.62425	-2.70212	2.538538
H	10.50183	-2.17189	0.428266
H	8.890863	-0.816201	-0.870269
H	7.610192	1.00727	0.246877
H	7.935173	1.477053	2.640989
H	7.11564	-0.96554	5.894105
H	4.686561	-0.52112	6.22432
H	3.79364	1.778204	6.03525
H	5.303633	3.682712	5.505424
H	8.084183	4.384809	4.915488
H	10.30928	2.982809	4.761165
H	10.09379	0.897371	8.559462

Table 14. Cartesian Coordinates of the Optimized Structure of **7**

atom	x	y	z
N	9.997882	1.021039	7.739176
N	10.80987	-0.64566	6.238431
C	9.300246	0.988395	5.321208
C	10.10906	0.399029	6.513877
C	10.5936	-0.90665	4.86531
C	11.18054	-1.96769	4.145211
C	10.87656	-2.096	2.807471
C	9.994902	-1.19327	2.148475
C	9.685665	-1.33201	0.768991
C	8.831212	-0.45552	0.139348
C	8.24266	0.60759	0.867433
C	8.516356	0.777441	2.205686
C	9.395943	-0.11027	2.886116
C	9.72845	-0.0054	4.255862
C	7.810317	1.090226	5.637418
C	6.890996	0.090811	5.924524
C	5.569854	0.459202	6.211043
C	5.187423	1.804754	6.213495
C	6.113219	2.813176	5.927042
C	7.429216	2.449456	5.636465
C	8.607733	3.253621	5.288665
C	9.666856	2.446667	5.082559
H	9.405487	1.840996	7.743347
H	11.85264	-2.65395	4.65016
H	11.3142	-2.90407	2.226045
H	10.14001	-2.15042	0.214901
H	8.605039	-0.57594	-0.91658
H	7.568124	1.29426	0.36259
H	8.061822	1.59422	2.757023
H	7.185487	-0.95517	5.920711
H	4.834612	-0.30973	6.4311
H	4.157622	2.069502	6.4377
H	5.810614	3.857289	5.926622
H	8.606431	4.335168	5.198155
H	10.67103	2.746114	4.805927
C	10.68278	0.729954	8.92528
O	11.56769	-0.10016	8.998802
C	10.2476	1.552889	10.10594
C	11.16368	1.685984	11.15897
C	8.983989	2.152298	10.2171
C	10.83443	2.428209	12.28974
H	12.12758	1.196195	11.06783
C	8.65271	2.88832	11.35505
H	8.234544	2.018178	9.441073
C	9.578847	3.033878	12.38905
H	11.55493	2.532991	13.09622
H	7.667749	3.339602	11.43648
H	9.320139	3.610047	13.27333

Table 15. Cartesian Coordinates of the Optimized Structure of **8**

atom	x	y	z
N	9.664651	1.289048	7.791861
C	9.089491	1.098579	5.337049
C	9.812352	0.669044	6.619305
C	10.53498	-0.73748	5.025923
C	11.2613	-1.76945	4.401045
C	11.05351	-1.95911	3.053092
C	10.14843	-1.15019	2.308802
C	9.942283	-1.35898	0.919228
C	9.067731	-0.57178	0.20498
C	8.355645	0.466748	0.852767
C	8.527762	0.703039	2.19808
C	9.423931	-0.09201	2.963765
C	9.653098	0.086911	4.349127
C	7.57294	1.107397	5.538696
C	6.709555	0.060629	5.822649
C	5.34505	0.344359	5.972759
C	4.869611	1.652321	5.841577
C	5.742431	2.707168	5.554586
C	7.10058	2.42857	5.403666
C	8.24106	3.294957	5.089846
C	9.369983	2.567566	5.029375
H	11.96113	-2.37163	4.968629
H	11.59325	-2.74439	2.530059
H	10.49129	-2.15821	0.426876
H	8.920289	-0.74491	-0.8574
H	7.66602	1.081711	0.28082
H	7.978066	1.499212	2.688266
H	7.074902	-0.95809	5.921939
H	4.651019	-0.46232	6.191129
H	3.808157	1.851779	5.961307
H	5.367464	3.72223	5.452051
H	8.169387	4.364732	4.922436
H	10.37066	2.92599	4.819649
C	10.41243	0.845646	8.798856
O	11.23692	-0.1579	8.730186
C	10.33518	1.537477	10.09753
C	11.10925	1.092746	11.18205
C	9.484933	2.644819	10.2552
C	11.03252	1.749853	12.40673
H	11.76093	0.236216	11.05112
C	9.412206	3.295791	11.48289
H	8.893696	2.974414	9.408448
C	10.18513	2.850704	12.55932
H	11.63234	1.403607	13.24359
H	8.75327	4.151167	11.60262
H	10.12659	3.361206	13.51701
N	10.59836	-0.37527	6.392149
B	11.36863	-1.09511	7.55098
F	12.69313	-1.23597	7.222641
F	10.75732	-2.28613	7.855829

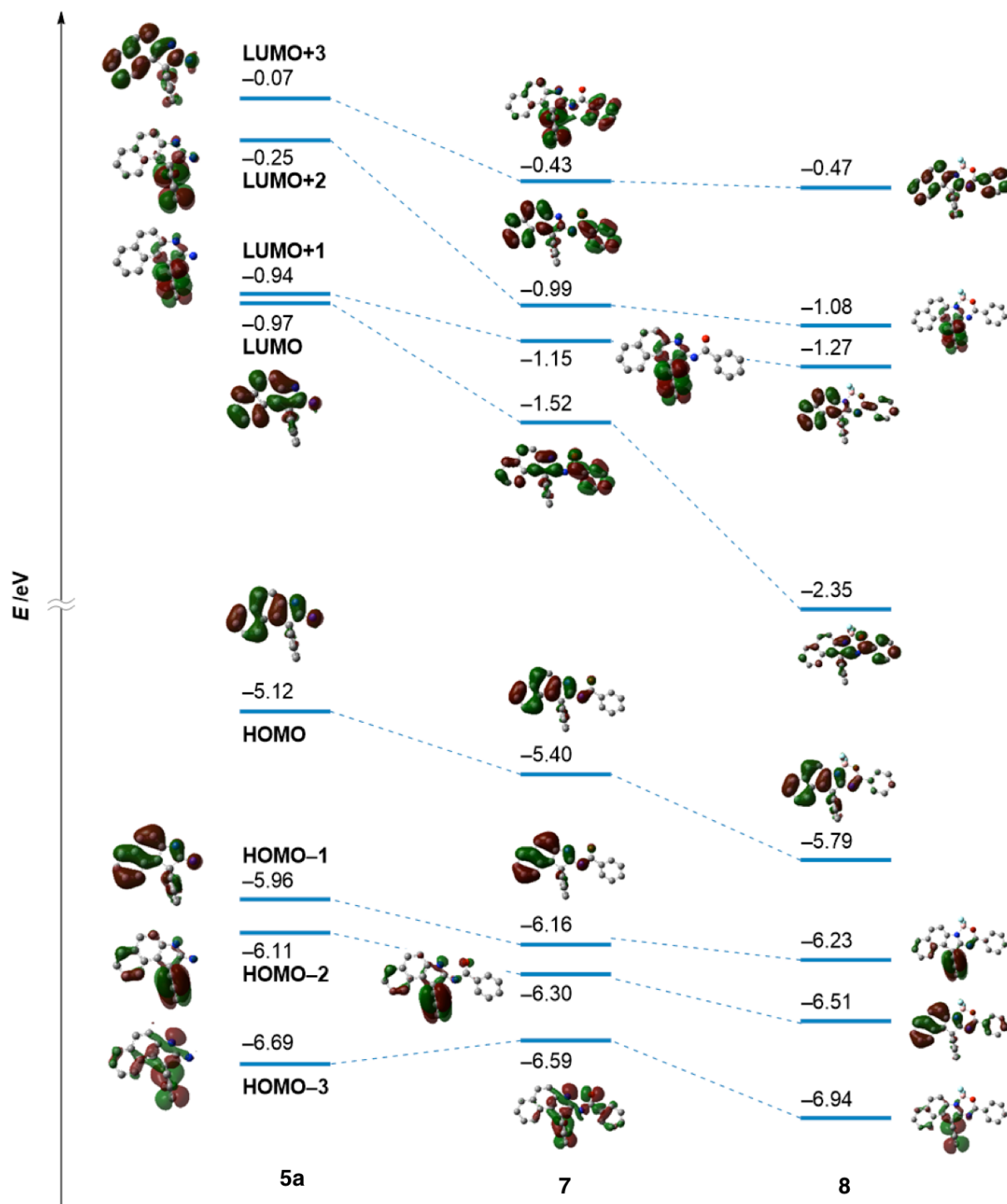


Figure 10. Energy Diagram and Molecular Orbitals of 5a, 7 and 8

Table 16. Selected Excitation Energies and Oscillator Strength (*f*) of **5a**, **7** and **8**^a

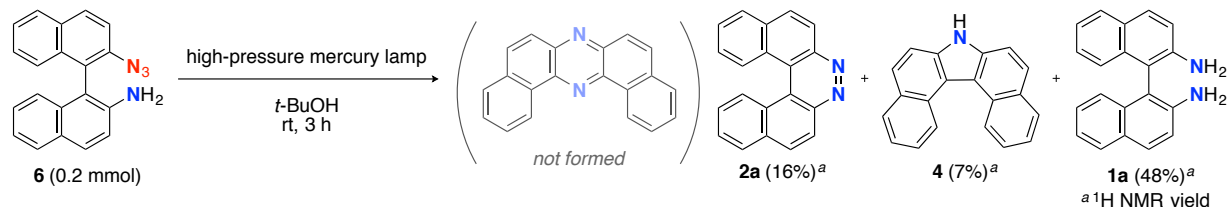
	5a	7	8
λ [nm] (<i>f</i>)	337.65 (0.0545)	361.61 (0.1860)	419.70 (0.1747)
transition mode	H→L (69%)	H→L (68%)	H→L (69%)
λ [nm] (<i>f</i>)	263.15 (0.1404)	300.84 (0.1725)	377.93 (0.1287)
transition mode	H-2→L+1 (53%)	H-1→L (50%)	H-1→L (68%)
λ [nm] (<i>f</i>)	256.35 (0.2794)	274.12 (0.1541)	342.22 (0.2420)
transition mode	H→L+3 (33%)	H-1→L+2 (41%)	H-2→L (67%)
λ [nm] (<i>f</i>)			302.63 (0.1733)
transition mode			H→L+1 (62%)

^a The coefficient percentages of orbitals involved in the transitions are shown in parentheses.

2-15. References and Notes

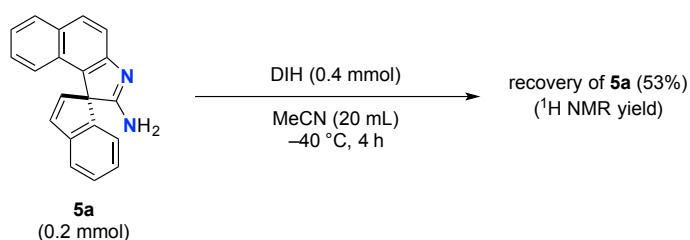
- For a summary of the crystal data of **3a**, see the Experimental Section. CCDC 1004407 contains the supplementary crystallographic data for this thesis. These data are available free of charge from the Cambridge Crystallographic Data Center (CCDC) via www.ccdc.cam.ac.uk/data_request/cif.
- Kosugi, Y.; Itoho, K.; Okazaki, H.; Yanai, T. *J. Org. Chem.* **1995**, *60*, 5690–5692.
- Zavitsas, A. A. *J. Phys. Chem. A*, **2003**, *107*, 897–898.
- For reviews on C–C bond activation by transition metal complexes, see: (a) Rybtchinski, B.; Milstein, D. *Angew. Chem., Int. Ed.* **1999**, *38*, 870–883. (b) Jun, C.-H. *Chem. Soc. Rev.* **2004**, *33*, 610–618. (c) Bonesi, S. M.; Fagnoni, M. *Chem. Eur. J.* **2010**, *16*, 13572–13589.
- The loss of aromatic resonance energies for naphthalene is 11 kcal/mol smaller than that for benzene: Smith, M. B.; March, J. *March's Advanced Organic Chemistry: Reactions, Mechanism, and Structure*; Wiley-Interscience, New York, 5th edn, 2001.
- (a) Takeda, Y.; Okumura, S.; Minakata, S. *Angew. Chem., Int. Ed.* **2012**, *51*, 7804–7808. (b) Takeda, Y.; Okumura, S.; Minakata, S. *Synthesis* **2013**, *45*, 1029–1033. (c) Okumura, S.; Lin, C.-H.; Takeda, Y.; Minakata, S. *J. Org. Chem.* **2013**, *78*, 12090–12105.
- (a) Maltsev, A.; Bally, T.; Tsao, M.-L.; Platz, M. S.; Kuhn, A.; Vosswinkel, M.; Wentrup, C. *J. Am. Chem. Soc.* **2003**, *126*, 237–249. (b) Gritsan, N. P.; Platz, M. S. *Chem. Rev.*

2006, *106*, 3844–3867. Nevertheless, photoirradiation of 2'-azido-[1,1'-binaphthalen]-2-amine (**6**) did not give **3a**, because of the absence of iodine-containing oxidant which would be necessary to the formation of **Int-G** from **Int-E**.



8. Naphthoazirines are trapped by various nucleophiles like alcohols and amines, see: (a) Rigaudy, J.; Igier, C.; Barcelo, J. *Tetrahedron Lett.* **1975**, *16*, 3845–3848. (b) Carroll, S. E.; Nay, B.; Scriven, E. F. V.; Suschitzky, H. *Tetrahedron Lett.* **1977**, *18*, 943–946. (c) Carroll, S. E.; Nay, B.; Scriven, E. F. V.; Suschitzky, H.; Thomas, D. R. *Tetrahedron Lett.* **1977**, *18*, 3175–3178. (d) Nay, B.; Scriven, E. F. V.; Suschitzky, H.; Khan, Z. U. *Synthesis* **1977**, 757–758.
9. (a) Stieglitz, J.; Leech, P. N. *Chem. Ber.* **1913**, *46*, 2147–2151. (b) Stieglitz, J.; Leech, P. N. *J. Am. Chem. Soc.* **1914**, *36*, 272–301.
10. Marion, N.; Navarro, O.; Mei, J.; Stevens, E. D.; Scott, N. M.; Nolan, S. P. *J. Am. Chem. Soc.* **2006**, *128*, 4101–4111.
11. Burrows, P. E.; Shen, Z.; Bulovic, V.; McCarty, D. M.; Forrest, S. R.; Cronin, J. A.; Thompson, M. E. *J. Appl. Phys.* **1996**, *79*, 7991–8006.
12. For a summary of the crystal data of **5a**, see the Experimental Section. CCDC 1416916 contains the supplementary crystallographic data for this thesis. These data are available free of charge from the Cambridge Crystallographic Data Center via www.ccdc.cam.ac.uk/data_request/cif.
13. Raczyńska, E. D.; Makowski, M.; Hallmann, M.; Kamińska, B. *RSC Adv.* **2015**, *5*, 36587–36604.
14. Haynes, W. M. *CRC Handbook of Chemistry and Physics*; CRC Press, Boca Raton, FL, 91st edn, 2010.
15. Lemmerer, A.; Michael, J. P. *Acta. Cryst.* **2011**, *E67*, o394.

16. Sue, D.; Kawabata, T.; Sasamori, T.; Tokitoh, N.; Tsubaki, K. *Org. Lett.* **2010**, *12*, 256–258.
17. Chen, J.-X.; Wang, Y.-Q.; Liu, S.-W.; Lin, W.-E.; Chen, Z.-P. *Acta. Cryst.* **2011**, *E67*, o9.
18. (a) Perron, F.; Albizati, K. F. *Chem. Rev.* **1989**, *89*, 1617–1661. (b) Williams, R. M.; Cox, R. J. *Acc. Chem. Res.* **2003**, *36*, 127–139.
19. (a) Zheng, Y.; Tice, C. M.; Singh, S. B. *Bioorg. Med. Chem. Lett.* **2014**, *24*, 3673–3682. (b) Yu, B.; Yu, D.-Q.; Liu, H.-M. *Eur. J. Med. Chem.* **2015**, *97*, 673–698.
20. Bajracharya, G. B.; Arai, M. A.; Koranne, P. S.; Suzuki, T.; Takizawa, S.; Sasai, H. *Bull. Chem. Soc. Jpn.* **2009**, *82*, 285–302.
21. Saragi, T. P. I.; Spehr, T.; Siebert, A.; Fuhrmann-Lieker, T.; Salbeck, J. *Chem. Rev.* **2007**, *107*, 1011–1065.
22. (a) Sannigrahi, M. *Tetrahedron* **1999**, *55*, 9007–9071. (b) Rios, R. *Chem. Soc. Rev.* **2012**, *41*, 1060–1074. (c) Borad, M. A.; Bhoi, M. N.; Prajapati, N. P.; Patel, H. D. *Synth. Commun.* **2014**, *44*, 897–922. (d) Santos, M. M. M. *Tetrahedron* **2014**, *70*, 9735–9757.
23. When spiro amidine **5a** was treated with 2 equivalents of DIH in MeCN at $-40\text{ }^{\circ}\text{C}$ for 4 h, almost half of the starting material **5a** was decomposed.



24. The absolute configuration of (–)-**5a** has not been determined, and the absolute configuration shown in Scheme 5b is only conjecture at this moment.
25. Sugihara, Y.; Iimura, S.; Nakayama, J. *Chem. Commun.* **2002**, 134–135.
26. Hand, E. S.; Baker, D. C. *Synthesis* **1989**, *12*, 905–908.
27. Hachiya, S.; Inagaki, T.; Hashizume, D.; Maki, S.; Niwa, H.; Hirano, T. *Tetrahedron Lett.* **2010**, *51*, 1613–1615.

28. (a) Wu, Y.-Y.; Chen, Y.; Gou, G.-Z.; Mu, W.-H.; Lv, X.-J.; Du, M.-L.; Fu, W.-F. *Org. Lett.* **2012**, *14*, 5226–5229. (b) Wu, Y.-Y.; Chen, Y.; Mu, W.-H.; Lv, X.-J.; Fu, W.-F. *J. Photochem. Photobiol. A* **2013**, *272*, 73–79. (c) Du, M.-L.; Hu, C.-Y.; Wang, L.-F.; Li, C.; Han, Y.-Y.; Gan, X.; Chen, Y.; Mu, W.-H.; Huang, M. L.; Fu, W.-F. *Dalton Trans.* **2014**, *43*, 13924–13931.
29. (a) Hong, Y.; Lam, J. W. Y.; Tang, B. Z. *Chem. Soc. Rev.* **2011**, *40*, 5361–5388. (b) Mei, J.; Hong, Y.; Lam, J. W. Y.; Qin, A.; Tang, Y.; Tang, B. Z. *Adv. Mater.* **2014**, *26*, 5429–5479.
30. For a summary of the crystal data of **8**, see the Experimental Section. CCDC 1416929 contains the supplementary crystallographic data for this thesis. These data are available free of charge from the Cambridge Crystallographic Data Center via www.ccdc.cam.ac.uk/data_request/cif.
31. Valeur, B.; Berberan-Santos, M. N. *Molecular Fluorescence: Principles and Applications*; WILEY-VCH, Weinheim, 2nd edn, 2012.
32. Hennecke, U.; Müller, C. H.; Fröhlich, R. *Org. Lett.* **2011**, *13*, 860–863.
33. Hadjiarapoglou, L.; Spyroudis, S.; Varvoglis, A. *Synthesis* **1983**, 207–208.
34. Dolenc, D. *Synlett* **2000**, 544–546.
35. Rao, H.; Fu, H.; Jiang, Y.; Zhao, Y. *Angew. Chem., Int. Ed.* **2009**, *48*, 1114–1116.
36. Mikami, K.; Korenaga, T.; Yusa, Y.; Yamanaka, M. *Adv. Synth. Catal.* **2003**, *345*, 246–254.
37. Kano, T.; Tanaka, Y.; Osawa, K.; Yurino, T.; Maruoka, K. *J. Org. Chem.* **2008**, *73*, 7387–7389.
38. Scarborough, C. C.; McDonald, R. I.; Hartmann, C.; Sazama, G. T.; Bergant, A.; Stahl, S. *S. J. Org. Chem.* **2009**, *74*, 2613–2615.
39. (a) Vilches-Herrera, M.; Miranda-Sepúlveda, J.; Rebolledo-Fuentes, M.; Fierro, A.; Lühr, S.; Iturriaga-Vasquez, P.; Cassels, B. K.; Reyes-Parada, M. *Bioorg. Med. Chem.* **2009**, *17*,

- 2452–2460. (b) Yan, P.; Millard, A. C.; Wei, M.; Loew, L. M. *J. Am. Chem. Soc.* **2006**, *128*, 11030–11031.
40. Vyskočil, Š.; Smrčina, M.; Lorenc, M.; Tišlerová, I.; Brooks, R. D.; Kulagowski, J. J.; Langer, V.; Farrugia, L. J.; Kočovský, P. *J. Org. Chem.* **2001**, *66*, 1359–1365.
41. Lim, Y.-K.; Jung, J.-W.; Lee, H.; Cho, C. G. *J. Org. Chem.* **2004**, *69*, 5778–5781.
42. Dehghanpour, S.; Afshariazar, F.; Assoud, J. *Polyhedron* **2012**, *35*, 69–76.
43. (a) Taffarel, E.; Chirayil, S.; Thummel, R. P. *J. Org. Chem.* **1994**, *59*, 823–828. (b) Smrcina, M.; Vyskocil, S.; Maca, B.; Polasek, M.; Claxton, T. A.; Abbott, A. P.; Kocovsky, P. *J. Org. Chem.* **1994**, *59*, 2156–2163.
44. Binaphthalenediamine **1f** was prepared by modified cross-coupling method (Manolikakes, G.; Hernandez, C. M.; Schade, M. A.; Metzger, A.; Knochel, P. *J. Org. Chem.* **2008**, *73*, 8422–8436.) from binaphthalenediamine **1g** as described in Chapter 1.
45. Barral, K.; Moorhouse, A. D.; Moses, J. E. *Org. Lett.* **2007**, *9*, 1809–1811.
46. Li, G.-Q.; Gao, H.; Keene, C.; Devonas, M.; Ess, D. H.; Kürti, L. *J. Am. Chem. Soc.* **2013**, *135*, 7414–7417.
47. Lou, S.-J.; Xu, D.-Q.; Shen, D.-F.; Wang, Y.-F.; Liu, Y.-K.; Xu, Z.-Y. *Chem. Commun.* **2012**, *48*, 11993–11995.
48. Joosten, A.; Trolez, Y.; Collin, J.-P.; Heitz, V.; Sauvage, J.-P. *J. Am. Chem. Soc.* **2012**, *134*, 1802–1809.
49. Zhao, H.; Al-Atar, U.; Pace, T. C. S.; Bohne, C.; Branda, N. R. *J. Photochem. Photobiol. A: Chem.* **2008**, *200*, 74–82.
50. Altomare, A.; Cascarano, G.; Giacovazzo, C.; Guagliardi, A.; Burla, M. C.; Polidori, G.; Camalli, M. *J. Appl. Cryst.* **1994**, *27*, 435.
51. Gaussian 09, Revision A.02, Frisch, M. J.; Trucks, G. W.; Schlegel, H. B.; Scuseria, G. E.; Robb, M. A.; Cheeseman, J. R.; Scalmani, G.; Barone, V.; Mennucci, B.; Petersson, G. A.; Nakatsuji, H.; Caricato, M.; Li, X.; Hratchian, H. P.; Izmaylov, A. F.; Bloino, J.; Zheng, G.; Sonnenberg, J. L.; Hada, M.; Ehara, M.; Toyota, K.; Fukuda, R.; Hasegawa,

J.; Ishida, M.; Nakajima, T.; Honda, Y.; Kitao, O.; Nakai, H.; Vreven, T.; Montgomery Jr., J. A.; Peralta, J. E.; Ogliaro, F.; Bearpark, M.; Heyd, J. J.; Brothers, E.; Kudin, K. N.; Staroverov, V. N.; Kobayashi, R.; Normand, J.; Raghavachari, K.; Rendell, A.; Burant, J. C.; Iyengar, S. S.; Tomasi, J.; Cossi, M.; Rega, N.; Millam, J. M.; Klene, M.; Knox, J. E.; Cross, J. B.; Bakken, V.; Adamo, C.; Jaramillo, J.; Gomperts, R.; Stratmann, R. E.; Yazyev, O.; Austin, A. J.; Cammi, R.; Pomelli, C.; Ochterski, J. W.; Martin, R. L.; Morokuma, K.; Zakrzewski, V. G.; Voth, G. A.; Salvador, P.; Dannenberg, J. J.; Dapprich, S.; Daniels, A. D.; Farkas, O.; Foresman, J. B.; Ortiz, J. V.; Cioslowski, J.; Fox, D. J. Gaussian, Inc., Wallingford CT, 2009.

Chapter 3

Thermally Activated Delayed Fluorescent Phenothiazine-Dibenzo[*a,j*]phenazine-Phenothiazine Triads Exhibiting Tricolor-Changing Mechanochromic Luminescence

3-1. Introduction

As mentioned in Chapter 2, the author has revealed that dibromo substituted dibenzo[*a,j*]phenazine **3g** serves as a useful building block for construction of D–A–D type emissive molecules. Especially, the resulting diaminodibenzophenazines **3o** and **3p** exhibited strong emission from the intramolecular charge transfer (ICT) excited states. On the basis of the background, the author has designed and created dibenzo[*a,j*]phenazine-cored D–A–D π -conjugated multi-functional molecules which exhibit tricolor-changing mechanochromic luminescence (MCL) and thermally activated delayed fluorescence (TADF). The molecular design, synthesis and their properties are described in Chapter 3.

Mechanochromic luminescent (MCL) materials,¹ which exhibit reversible distinct luminescence color change in response to external stimuli such as mechanical forces (e.g., grinding, pressing, rubbing, and shearing), temperature, vapor, and electric field, can find many

applications in optoelectronic devices, sensors, probes, optical data storages, and security inks.² Most of the MCL materials developed so far involving organic crystalline compounds,³ organometallic crystalline compounds,⁴ and liquid-crystalline compounds,⁵ show a reversible two-color switching MCL properties: an emission color (e.g., denoted as “state A”) is typically changeable by mechanical forces to a different color (denoted as “state B“), which is again reverted back to the original color (“state A”) by thermal treatment and/or solvent exposure. From mechanistic points of view, such two-color-changing MCL behavior is caused by reversible change in chemical structures (i.e., breaking and reforming of chemical bonds) or in physical structures (e.g., polymorphs and packing structures) between thermodynamically metastable and stable states.

In this context, distinct *multi*-color-changing (more than three colors) MCL compounds would be more promising materials for sensitive sensing of their environments (e.g., pressures, temperatures, and pH). Therefore, the last five years have witnessed an emerging of multi-color-changing MCL materials.⁶⁻⁸ In 2011, Kato pioneered distinct tricolor-switching MCL systems (green-yellow-red) comprising of a single luminophore liquid crystal by controlling complex self-assembled structures.^{7a} Zou and Tian found that bis(pyridylvinyl)anthracene (BP2VA) significantly exhibits pressure-dependent luminochromism ranging from green to red.^{7c} Saito and Yamaguchi nicely demonstrated the distinct difference in its luminochromic behavior of tetrathiazolylthiophene in response to anisotropic grinding and isotropic compression.^{7e} The integration of two different fluorophores into one molecule also has proven to be an effective strategy for tricolored MCL materials by Jian and co-workers.^{7f} Yagai and Ito devised an amphiphilic dipolar π -conjugated molecule exhibiting variable emission colors depending on the change in the (liquid-)crystalline phases.^{7g} Uekusa and Ito developed a tetracolored fluorochromic system based on crystal-to-crystal-to-amorphous phase transitions.^{7h}

More recently, Zhang, Zou and Ma reported that a donor-acceptor (D-A) type fluorescent molecule with intramolecular charge transfer (ICT) character shows multi-color MCL behavior caused by the change in twisting angles between the D and A units.⁷¹ In addition to these single molecule systems, the utilization of exciplex formation between D and A components has been emerging as another solution to creating multi-color-switching MCL materials.⁸ Despite of these excellent studies, the development of such distinct multi-color-changing and value-added MCL materials is still challenging partly due to the lack of general rational design principles thereof.

A new subset of optically functional materials are thermally activated (or “E-type”)⁹ delayed fluorescence (TADF) materials,¹⁰ which can find a wide range of applications such as emitters¹¹ and host materials¹² in organic light emitting diodes (OLEDs),¹¹ chemiluminescence emitters,¹³ and bioimaging probes.¹⁴ Specifically, TADF emitters can achieve internal quantum efficiency (IQE) in OLEDs close to 100% by up-conversion of triplet excited states into the singlet state (Figure 1).¹⁵ Such phenomenon occurs when the energy difference between the excited singlet states (S_1) and triplet states (T_1) ΔE_{ST} of the molecule is small, typically < 0.3 eV,^{11,15} and the local D (or A) triplet (3LE) couples to the triplet CT excited (3CT) state vibronically to mediate second order spin orbit coupling.¹⁶ To reduce ΔE_{ST} , twisted D–A structures with an effective HOMO/LUMO spatial separation is appropriate. Due to the

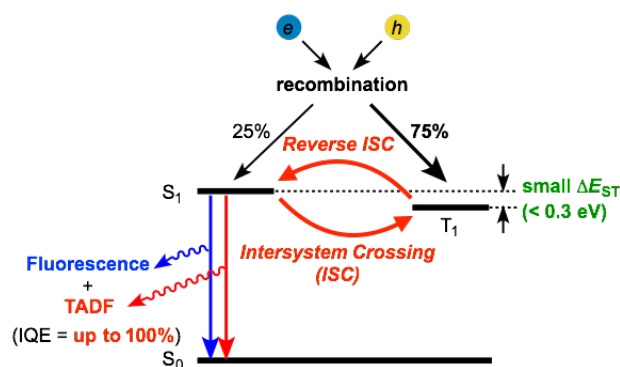


Figure 1. TADF Process in OLED Device

molecular design, TADF emitters can be composed of non-metal elements contrary to conventional phosphorescence materials including expensive rare metals such as Pt and Ir. Therefore, they have been intensively studied as next-generation OLED emitting materials.^{11,15-19} In this connection, Data and Takeda have recently developed novel TADF molecules that comprise of U-shaped dibenzo[*a,j*]phenazine (DBPHZ)²⁰ as an acceptor and diarylamines as donors.²¹ Especially, phenoxazine-DBPHZ-phenoxazine triad POZ-DBPHZ (Figure 2) was found to be an excellent orange-TADF emitter for organic light-emitting devices (OLEDs), achieving an external quantum efficiency (EQE) up to 16%. The effective HOMO/LUMO separation in the almost perpendicularly twisted D-A-D triad allowed an efficient intramolecular charge-transfer (ICT) and a very small singlet-triplet energy splitting ($\Delta E_{ST} \sim 20$ meV), which resulted in an efficient reverse intersystem crossing (rISC) to yield efficient TADF emission.

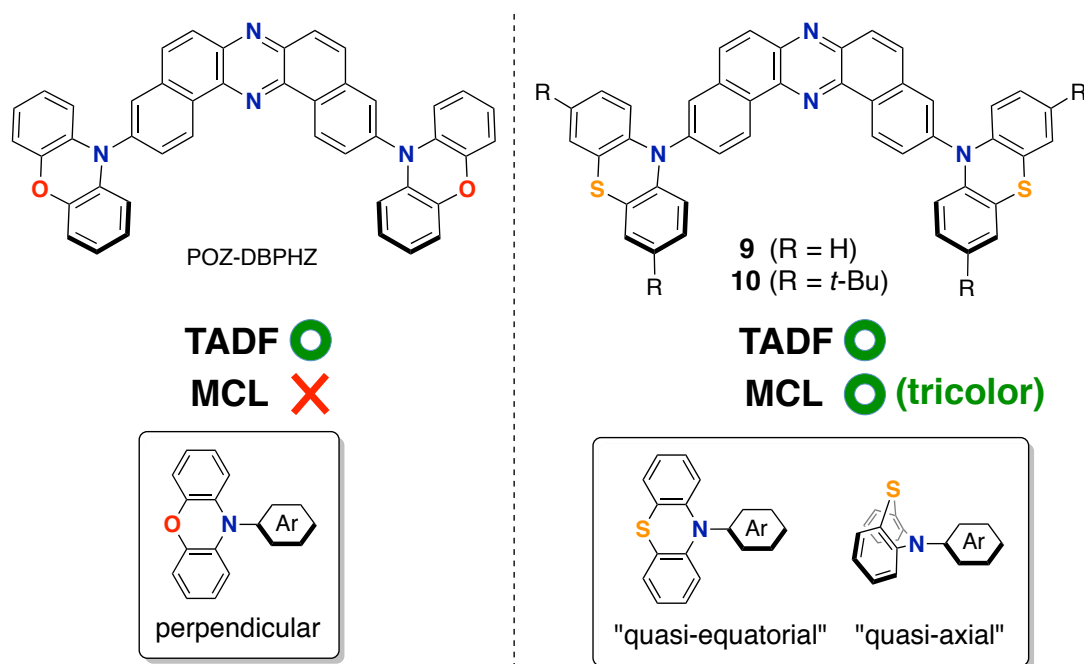


Figure 2. Structures of Dibenzo[*a,j*]phenazine-Cored D-A-D Molecules

The author envisaged that the merging of MCL and TADF functions would be a significantly powerful strategy for creating multi-functional organic materials: taking

advantage of both phenomena, more complex sensing can be feasible with such materials in principle, where emission colors and/or intensities vary with the increase (or decrease) of surrounding pressure and/or temperature. For instance, they could find applications in stress-, pressure-, and thermo indicators for high-tech industries like submarines and aerospace in the future. Although a few TADF emitting compounds that exhibit two-color-changing MCL properties have been reported,²² to the best of his knowledge, *TADF-active multi-color-changing (more than 3) MCL molecules have never been reported.* On the basis on the background, the author presents a novel TADF-active and distinct tricolor-changing MCL molecules **9** and **10** (Figure 2) comprising of DBPHZ as an acceptor and phenothiazines as donors. Importantly, phenothiazine (PTZ) units play a fundamentally important role in generating multiple thermodynamically (meta)stable states through conformational changes. Furthermore, these unprecedented multi-functional emitting materials have been applied to OLED device to achieve as high EQEs up to 16.8%.

Results and Discussion

3-2. Molecular Design

To develop TADF-active multi-color-changing materials, the author designed a phenothiazine-DBPHZ-phenothiazine triad **9**, because bowl-shaped structure of phenothiazine (PTZ) unit would allow PTZ-substituted molecules to exist as two distinct conformers: one is “quasi-equatorial” and the other is “quasi-axial” (Figure 2).²³ Recently, Adachi has reported that the D-A molecule containing a PTZ group as a donor and 2,4,6-triphenyl-1,3,5-triazine as an acceptor exhibited a dual-emission with TADF characteristics.²⁴ They concluded that two emissive ICT excited states are correlated with two different conformers of the PTZ-substituted molecules. Likewise, more

recently, Zhang and Chi have developed an asymmetric D-A-D' molecule (D = carbazolyl-, D' = PTZ, and A = benzophenone) which shows a TADF dual-emission (white light) in the solid state.^{22a} The author envisaged that the attachment of more than one PTZ units to his acceptor-core (DBPHZ) would be promising molecular design to achieve both of multi-color-changing MCL and TADF properties with a single molecule.

To evaluate the viability of this molecular design, the author initially conducted theoretical calculations using Gaussian 09 program with the DFT method at the B3LYP/6-31+G(d,p) level (Figure 3, Tables 5–13). An energy diagram and the frontier orbitals of four possible conformers of **9**, which could generate from the variation of PTZ conformation, are illustrated in Figure 3. The HOMO–LUMO band gaps decrease in the order of quasi-axial/quasi-axial (**ax-ax**), quasi-equatorial/quasi-axial (**eq-ax**), and quasi-equatorial/quasi-equatorial (**eq-eq**) conformers (Figure 3). Focusing on the HOMO and LUMO of **ax-ax**, the molecular orbitals are delocalized throughout the whole DBPHZ core in both cases, indicating that π - π^* transition would exclusively dominate in these conformers. In sharp contrast, in **eq-ax** and **eq-eq**, the HOMO is localized on one of the PTZ units, while the LUMO is delocalized on the

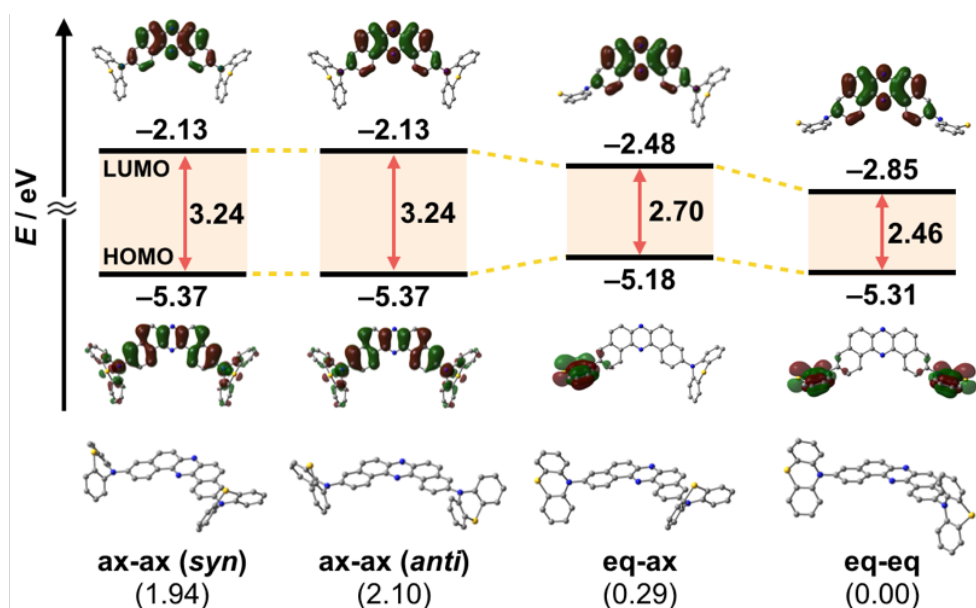
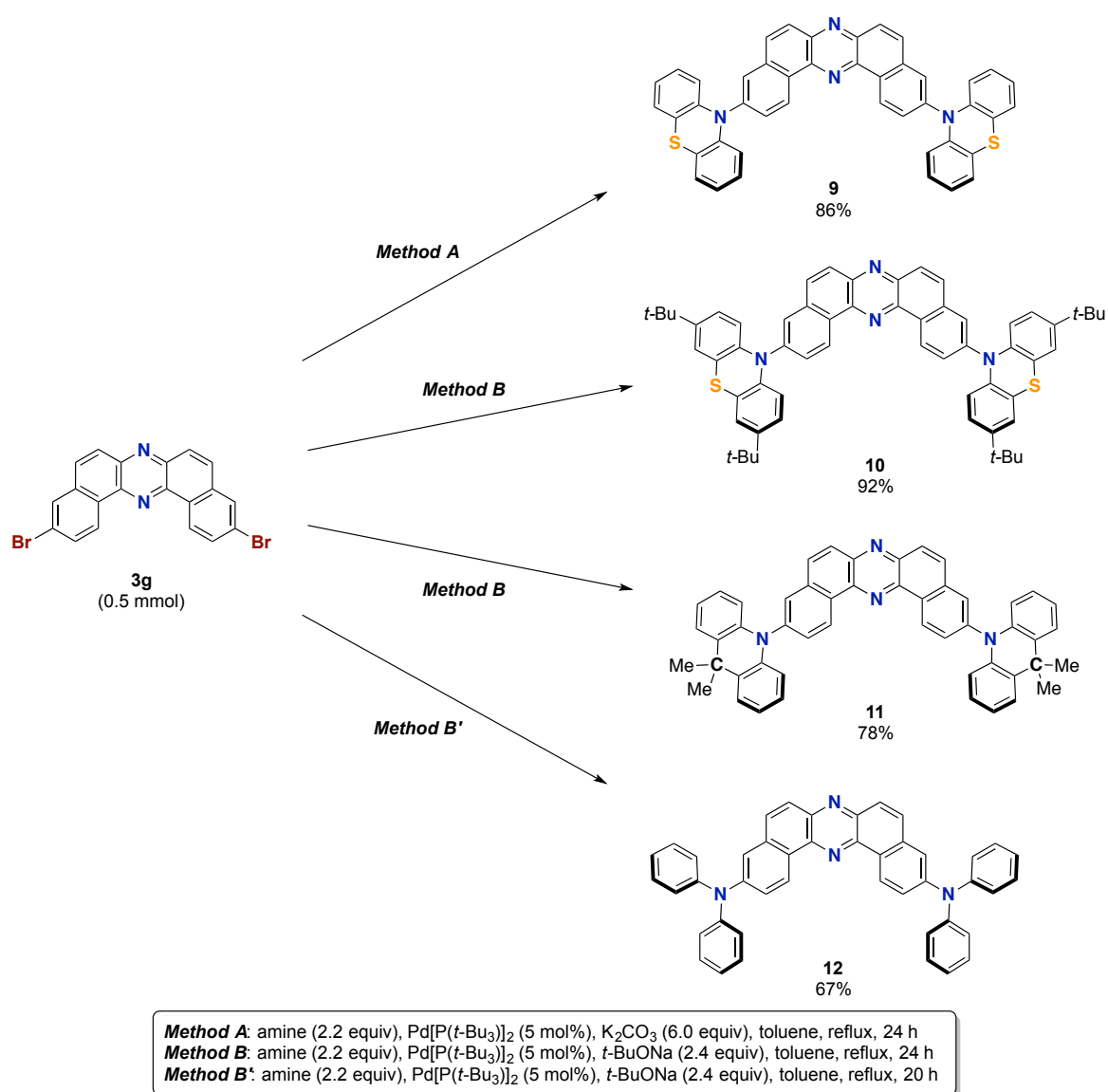


Figure 3. Energy Diagram and Molecular Orbitals of **9** Calculated by the DFT Method at the B3LYP/6-31+G(d,p) Level of Theory (Values in Parentheses Shown under the Molecules Indicate the Relative Energies of the Conformers in kcal/mol)

acceptor. Likewise, in **eq-eq**, the HOMO and LUMO are completely separated. These distributions of the frontier orbitals in **eq-ax** and **eq-eq** conformers would result in effective ICT as previously reported with POZ-DBPHZ.²¹ Although **ax-ax** conformers are less stable (*ca.* 2.0 kcal/mol) than **eq-ax** and **eq-eq**, such small energy differences suggest that all the four conformers can be thermodynamically interconvertible and thereby multiple excited states correlated with those conformers can exist.

3-3. Synthesis of Materials



Scheme 1. Synthesis of Dibenzo[*a,j*]phenazine-Cored D–A–D Molecules

PTZ-disubstituted DBPHZ **9** and its derivative **10** were successfully synthesized through a Pd-catalyzed Hartwig-Buchwald amination of 3,11-dibromo[*a,j*]phenazine (**3g**) with the corresponding phenothiazines in high yields (Scheme 1). To evaluate the efficacy of the sulfur-bridging in the donor unit, a carbon-bridging analogue **11** (78%) and a non-bridging analogue **12** (67%) were also synthesized in a similar manner (Scheme 1). DBPHZs **9–12** were characterized by spectroscopic analysis.

3-4. MCL Properties

Most importantly, solid samples of **9** and **10** clearly showed distinct multi-color-changing MCL behaviors in response to a variety of external stimuli (e.g., recrystallization, grinding, solvent exposure, and heating) compared with **11** and **12** (Figure 4). Two polymorphs of **9** were obtained through recrystallization (**9_Y** and **9_O**, Figure 4a): needle crystals **9_Y** grown from a two-phase solvent of *n*-hexane/CHCl₃ (3:1) exhibited bright yellow emission (λ_{em} 568 nm) under the UV irradiation, while block crystals **9_O** were obtained through slow evaporation of its CH₂Cl₂ solution and showed orange emission (λ_{em} 640 nm). Notably, upon grinding **9_Y** and **9_O** with a mortar and pestle, the solid color drastically turned to red in both cases, and the resulting red powder **9_R** emitted deep-red/near IR (NIR) light (λ_{em} 673 nm) with moderate quantum yield (Φ_{em} 0.12) for NIR-emissive organic solid.²⁵ Thermal annealing of the red solid **9_R** (220 °C for 5 min) yielded orange-emissive solid (**9_O2**, λ_{em} 646 nm). In contrast, the fuming of **9_R** to CH₂Cl₂ vapor caused a more blue-shift of the emission color (**9_YO**, λ_{em} 596 nm). Both of **9_O2** and **9_YO** samples reverted back to the ground sample **9_R** by grinding with high reproducibility. Recrystallization of any samples gave **9_Y** or **9_O**, depending on the used solvent systems.

Likewise, *t*-Bu-substituted PTZ-compound **10** also exhibited distinct MCL behaviors in

response to various external stimuli (Figure 4b). The needle crystals **10_YG** grown from a two-phase solvent of *n*-hexane/ CHCl_3 (20:1) showed yellow-green emission (λ_{em} 547 nm), and the emission color turned to red by grinding (**10_R**, λ_{em} 663 nm) with a large emission energy shift ($\Delta\tilde{\nu}$ 3199 cm^{-1}). With respect to **10**, other polymorphs were not observed even though various solvent systems were tested in recrystallization. Heating red solid **10_R** (240 °C for 5 min)

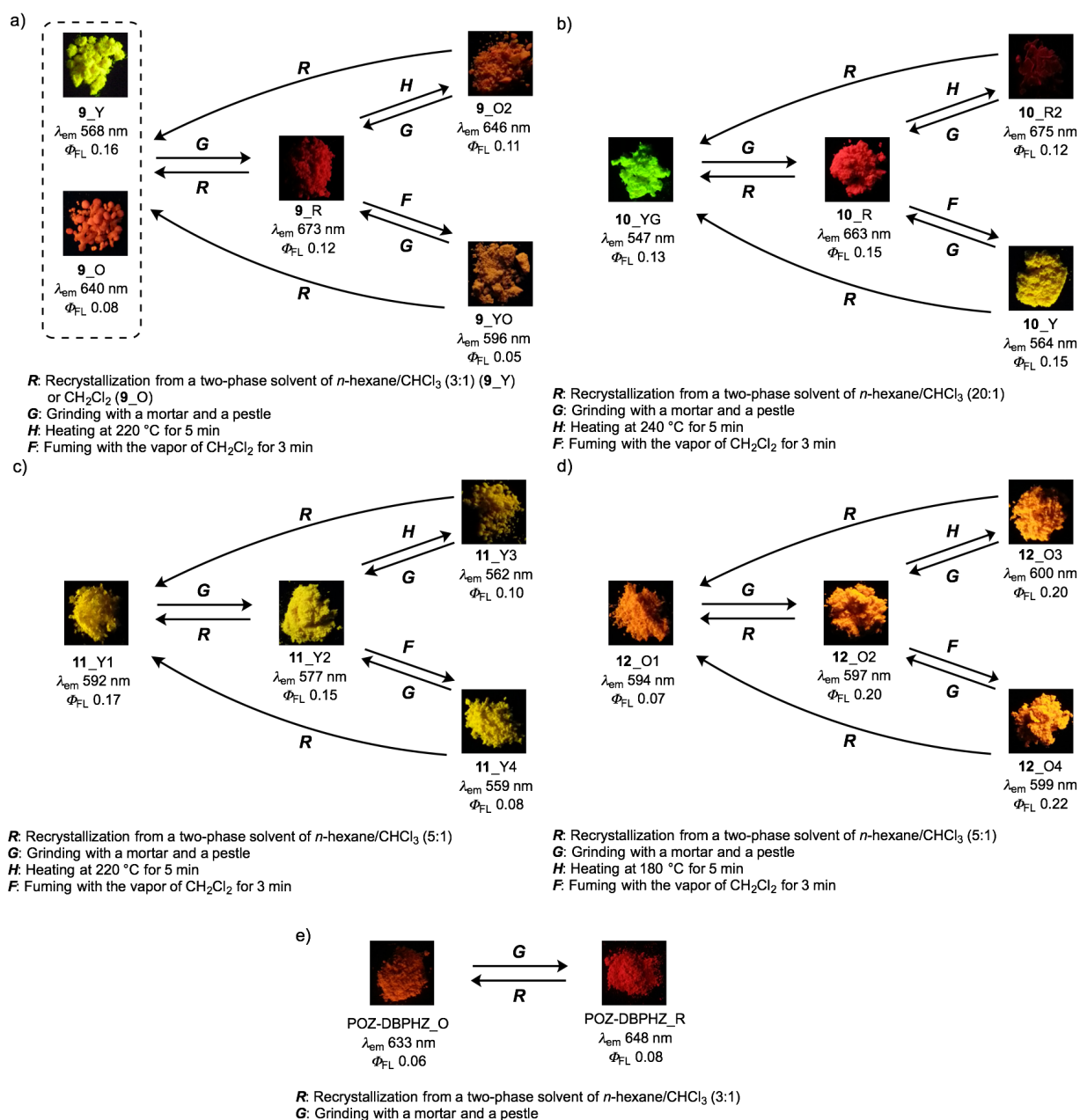


Figure 4. Schematic Diagrams of Multi-Color-Changing MCL Behaviors of a) **9**, b) **10**, c) **11**, d) **12**, and e) POZ-DBPHZ. Photographs are Taken under the Irradiation of UV Light (365 nm)

caused a slight red-shift of the emission (**10_R2**), which is the opposite behavior when compared to **9_R**. Fuming of **10_R** with CH_2Cl_2 vapor clearly changed the emission color to yellow (**10_Y**). Any solid samples reverted back to **10_YG** through the recrystallization process from *n*-hexane/ CHCl_3 . As clearly seen from Figures 4a and 4b, PTZ-substituted DBPHZs **9** and **10** exhibited distinct tricolor-changing MCL properties. In sharp contrast, sulfur-free analogues **11** and **12** did not show significant MCL behaviors (Figures 4c and 4d). Furthermore, the oxygen-bridged analogue POZ-DBPHZ²¹ (Figure 2) also did not show significant MCL behavior (Figure 4e). These results explicitly indicate that the sulfur-bridging of the *N,N*-diphenyl unit plays an important role in realizing multi-color-changing MCL characters based on DBPHZ-cored D-A-D scaffolds.

In addition to MCL behaviors, all the D-A-D molecules **9–12** exhibit acid-induced emission quenching in the solid state (Figure 5 and Table 1).²⁶ Upon exposure to trifluoroacetic acid (TFA) vapor for 10 s, the ground red samples turned to black and luminescence was completely quenched (“turn-off” state), probably due to the protonation of the pyrazine unit. In reverse, the exposure of these “turn-off state” samples to Et_3N vapor for 3 h “turned-on” emission in slightly different colors from the original emission. These results suggest that the

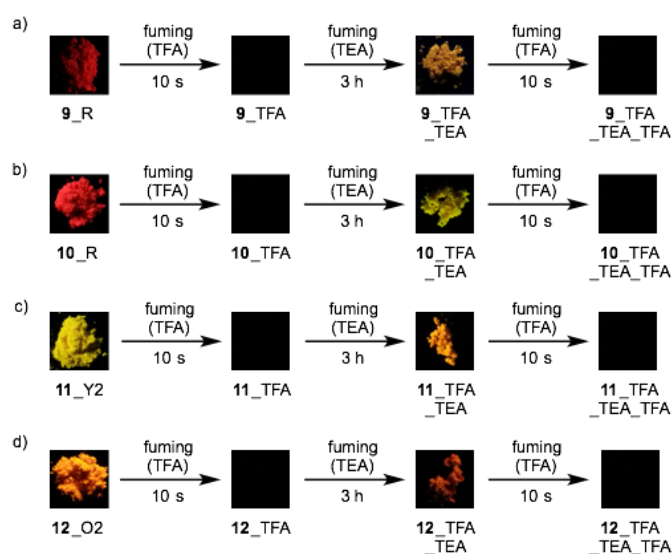


Figure 5. Emission “Turn-Off/On” Cycles Induced by the Treatment of **9–12** with Acid/Based Vapor

Table 1. Summary of the Properties of Acid/Base-Vapor-Treated Solids **9–12**

Sample	λ_{ex} (nm)	λ_{em} (nm)	Φ_{FL}
9_R	400	673	0.12
9_TFA	300	ND	<0.01
9_TFA_TEA	300	601	0.05
9_TFA_TEA_TFA	300	ND	<0.01
10_R	300	663	0.15
10_TFA	300	ND	<0.01
10_TFA_TEA	300	562	0.06
10_TFA_TEA_TFA	300	ND	<0.01
11_Y2	300	577	0.15
11_TFA	300	ND	<0.01
11_TFA_TEA	300	596	0.17
11_TFA_TEA_TFA	300	ND	<0.01
12_O2	300	597	0.20
12_TFA	300	ND	<0.01
12_TFA_TEA	300	602	0.05
12_TFA_TEA_TFA	300	ND	<0.01

D-A-D molecules are promising for the applications as acid/base-responsive on-off chemosensors.

3-5. PXRD and DSC Measurement

Powder X-ray diffraction (PXRD) analysis of **9** indicated that the ground solid **9**_R had an amorphous structure, and the other solids were composed of different crystalline polymorphs (Figure 6a). With regard to **10**, the PXRD pattern of the crystals **10**_{YG} was similar to that of **10**_Y, suggesting that solvent vapor can allow the ground solid **10**_R to partly turn to the crystalline phase **10**_{YG} (Figure 6b). Remarkably, the ground and heated solids **10**_R and **10**_{R2} were amorphous, indicating that the sterically demanding *tert*-butyl groups suppress thermal crystallization processes. The ground solids of **11** and **12** were also amorphous, and the other solids were almost same crystalline phases (Figures 6c and 6d).

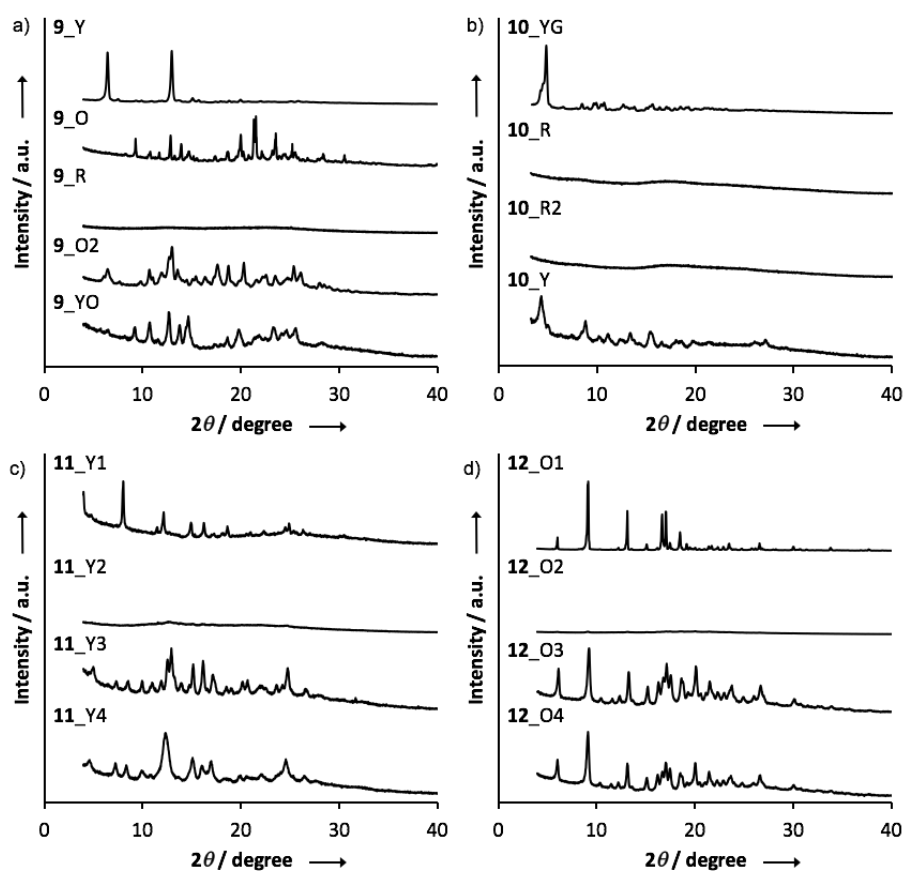


Figure 6. PXRD Patterns of the Solid Samples a) **9**, b) **10**, c) **11**, and d) **12**

To further investigate the MCL properties of the D-A-D molecules, differential scanning calorimetry (DSC) measurements were performed. Among the solid samples **9**, only the ground solid **9_R** displayed a glass transition point at 154 °C and a crystallization point at 218 °C, prior to an endothermic process at 293 °C (Figure 7a). This result suggests that **9_R** is a metastable state and therefore transformed into more thermodynamically stable state **9_O2** by heating through glass transition and crystallization processes. The ground solids of **11** and **12** also showed glass transition and crystallization points, indicating these solids are also metastable states (Figures 7c and 7d). Regarding the DSC curve of the ground solid **10_R**, a crystallization point was not observed, and only a glass transition point was found at 214 °C, prior to a melting point at 300 °C, indicating that **10_R** does not undergo crystallization by thermal annealing, which is consistent with amorphous character of solid **10_R2** (Figures 6b and 7b).

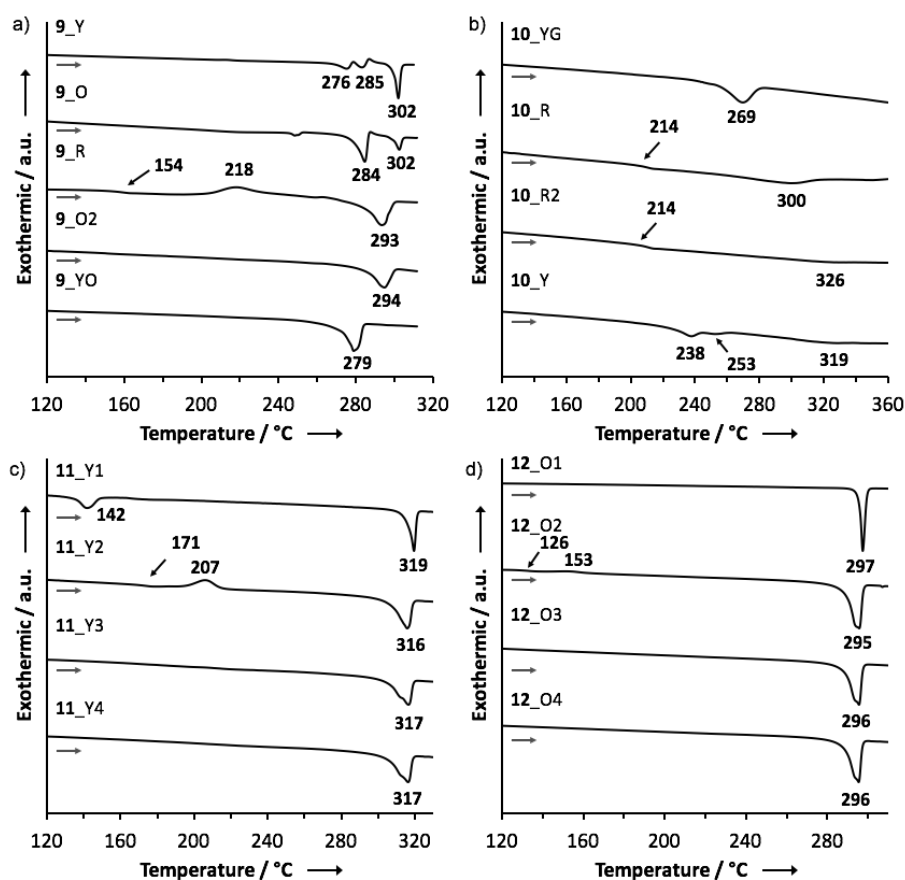


Figure 7. DSC Curves of the Solid Samples a) **9**, b) **10**, c) **11**, and d) **12**

3-6. Single Crystal X-ray Analysis of **9**_O

Importantly, the X-ray analysis of a single crystal of **9**_O revealed the conformation in the crystal (Figure 8).²⁷ As mentioned above, a PTZ moiety can adopt either “quasi-equatorial” or “quasi-axial” conformations.^{22a,23,24} Regarding PTZ units in **9**_O, one adopts a “quasi-equatorial” and the other a “quasi-axial” conformations against the DBPHZ core (Figures 8a and 8b). In the crystal, two molecules make a pair in which two phenazine cores form a slipped-stack (π – π interplane distance 3.58 Å), with the PTZ moieties pointing to the opposite sides of each other to cancel the dipole moment (Figure 8c). The molecular pairs are packed through close CH \cdots π , CH \cdots N, and CH \cdots S contacts, and the vacant spaces are filled with disordered CH₂Cl₂ molecules (Figure 8d). Thermogravimetric analysis (TGA) also indicated the inclusion of some CH₂Cl₂ molecules in the crystal **9**_O (Figure 23). The solvent exposed samples **9**_YO and **10**_Y also contained CH₂Cl₂ molecules (Figure 23).

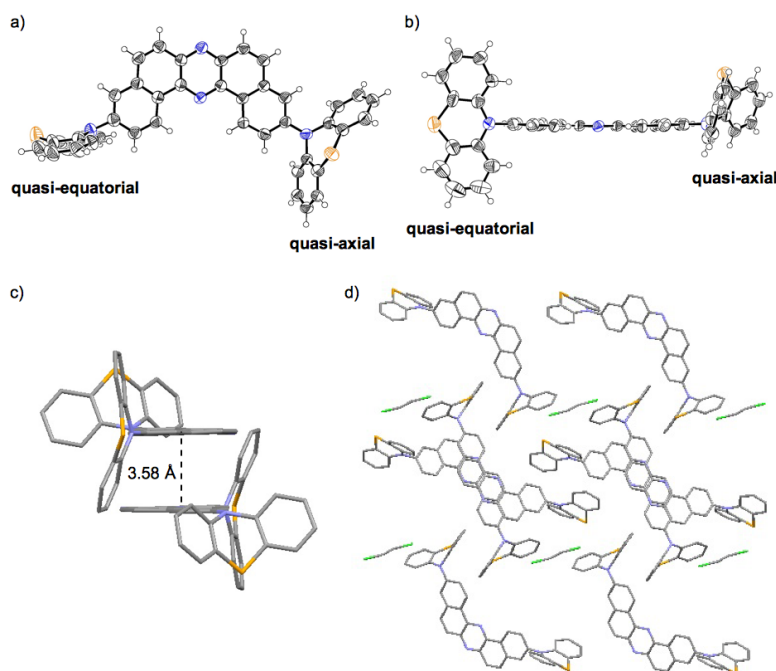


Figure 8. The ORTEP Drawings of the Single Crystal of **9**_O: a) Top View and b) Side View (Thermal Ellipsoids are Set at the 50% Probability Level); c) a Pair of Two Molecules; d) Packing Structure Seen Along the *b* Axis

3-7. Steady-state Photophysical Properties of Solutions

To investigate the ICT nature of **9–12**, UV-vis absorption and steady-state photoluminescence spectra of their dilute solutions, which were prepared from various solvents, were measured (Figure 9), and the properties are summarized in Table 2. The maximum absorption wavelengths (λ_{abs}) and molar absorption coefficients (ϵ) of the solutions of **9** almost did not change in any solvents tested (Figure 9). The cyclohexane solution of **9** showed green emission from a locally excited (^1LE) state (λ_{em} 543 nm, Φ_{FL} 0.06), while the toluene solution emitted red light (λ_{em} 657 nm, Φ_{FL} 0.07) from ^1CT , which are very similar to those of POZ-DBPHZ.²¹ In the case of more polar solvents (e.g., THF, CH_2Cl_2 , and DMF), no emission was observed, indicating its strong ICT character. It should be noted that emission profiles (λ_{em} and spectra shapes) of crystal **9_Y** (λ_{em} 568 nm) and the ground sample **9_R** (λ_{em} 673 nm) were almost the same as those of the ^1LE (λ_{em} 543 nm) and ICT (λ_{em} 657 nm) states, respectively (Figure 9a). This would imply that the drastic color-changing MCL in the solid samples of **9** and **10** (e.g., from **9_Y** to **9_R**) could be ascribed to the change in emissive states between ^1LE and ^1CT states. Likewise, the solution of **10** also exhibited ICT behavior (Figure 9b). Notably, both λ_{em} of **10** were red-shifted, compared with those of **9**, probably due to the electron-donating effect of *tert*-butyl groups. The carbon-bridged analogue **11** also showed strong ICT character (Figure 9c), but the degree of red-shift was decreased, compared with **9**, probably due to the less electron-donating nature of carbon bridging atoms. In polar solvents, a weak emission was observed around 500 nm for **9**, **10** and **11** (Figures 9a, 9b and 9c), ascribed to the remnant of the emission from ^1LE state. The non-bridged D-A-D compound **12** also showed distinct solvatochromism of emission (Figure 9d). The quantum yields of the solutions of **12** (Φ_{FL} 0.34–0.56) were higher than those of the other investigated D-A-D molecules, suggesting that the propeller structures of the diphenyl amino groups suppress the molecular motions that

would lead to non-radiative decay.

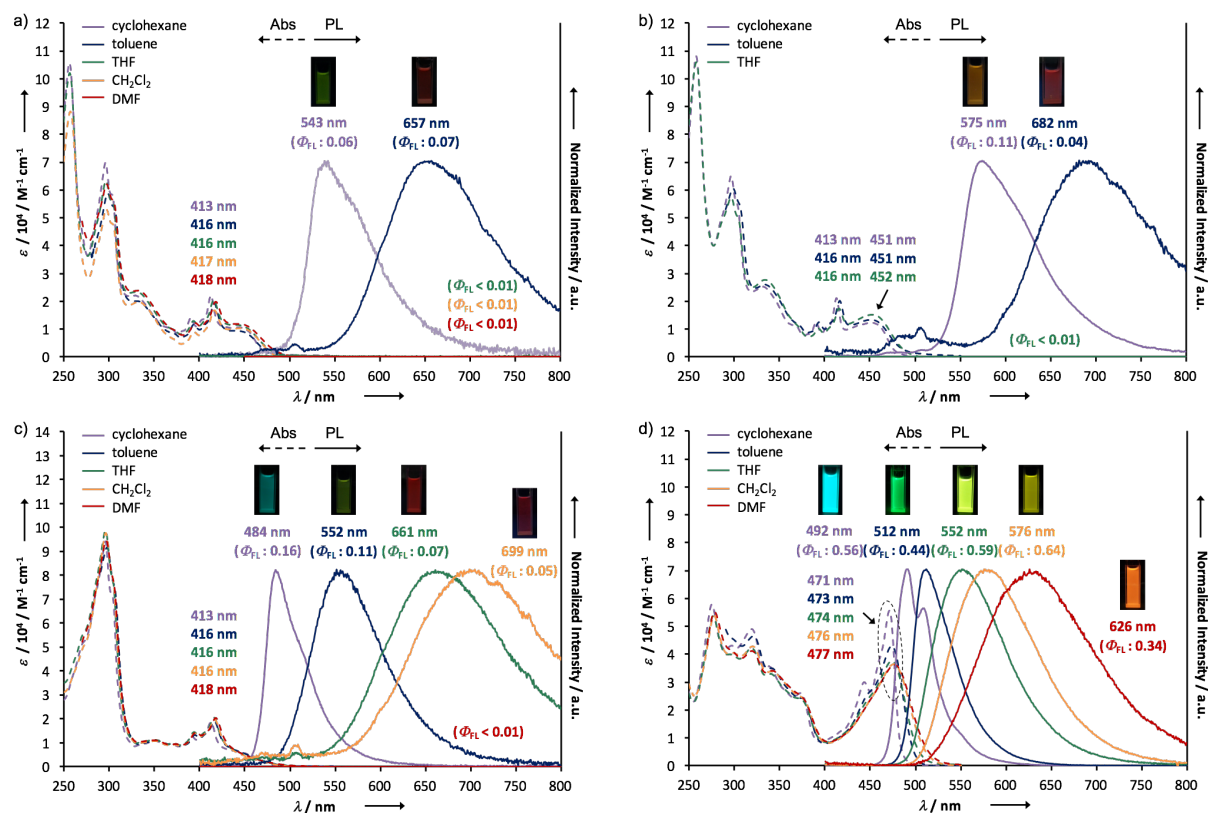


Figure 9. UV-vis Absorption and Emission Spectra of Solutions (10^{-5} M Order) of a) **9**, b) **10**, c) **11** and d) **12**

Table 2. Summary of Photophysical Properties of **9–12**

Compound	Solvent	Absorption ^a		Emission ^a		
		λ_{abs} (nm)	ϵ ($\text{M}^{-1}\text{cm}^{-1}$)	λ_{ex} (nm)	λ_{em} (nm)	Φ_{FL}
9	cyclohexane	296, 390, 413	69,900, 13,900, 22,000	300	543	0.06
	toluene	298, 394, 416	58,800, 11,600, 19,300	300	657	0.07
	THF	297, 394, 416	63,200, 12,800, 20,500	300	ND	<0.01
	CH_2Cl_2	297, 395, 417	53,200, 9,000, 16,800	300	ND	<0.01
	DMF	297, 396, 418	62,000, 12,200, 19,800	300	ND	<0.01
10	cyclohexane	297, 332, 391, 413, 451	65,100, 25,300, 12,500, 21,200, 12,400	300	575	0.11
	toluene	298, 334, 394, 416, 451	60,600, 26,000, 12,400, 20,100, 13,300	300	682	0.04
	THF	297, 335, 393, 416, 452	57,400, 27,800, 10,300, 17,500, 15,300	300	ND	<0.01
11	cyclohexane	296, 391, 413	94,100, 12,700, 18,600	300	484	0.16
	toluene	297, 395, 416	91,600, 13,200, 19,000	300	552	0.11
	THF	296, 394, 416	98,500, 14,400, 20,400	300	661	0.07
	CH_2Cl_2	296, 395, 416	97,600, 14,000, 19,800	300	699	0.05
	DMF	297, 396, 418	94,600, 14,500, 20,500	300	ND	<0.01
12	cyclohexane	275, 319, 337, 373, 444, 471	57,800, 48,900, 35,700, 26,000, 29,800, 55,500	300	492	0.56
	toluene	321, 341, 374, 473	46,400, 35,000, 24,300, 42,900	300	512	0.44
	THF	277, 319, 341, 474	53,800, 42,400, 33,100, 37,700	300	552	0.59
	CH_2Cl_2	278, 321, 343, 476	54,000, 42,800, 33,800, 36,400	300	576	0.64
	DMF	278, 319, 343, 477	55,200, 41,200, 34,100, 36,200	300	626	0.34

^a 10^{-5} order

A very small red shift ($\Delta\lambda_{\text{em}} \sim 2$ nm) of the emission spectra of **10** in a higher concentration solution (10^{-3} M) (Figure 10)²⁸ would imply that excimer formation does not significantly contribute to drastic color changes in the solid state such as observed from **10_YG** to **10_R** (*vide infra*). To obtain further information of PTZ-DBPHZ-PTZ triads, diffuse reflection spectra of solid samples **9** were measured (Figure 11). Notably, each spectra were different from each other, and the onset wavelengths (λ_{onset}) were red-shifted in the order of **9_Y** < **9_YO** < **9_O** < **9_O2** < **9_R** ranging from 516 to 587 nm, which is also consistent with the order of λ_{em} (Figure 4a). These results would indicate that the bandgap of the solid samples are significantly varied through the variation of PTZ conformations.

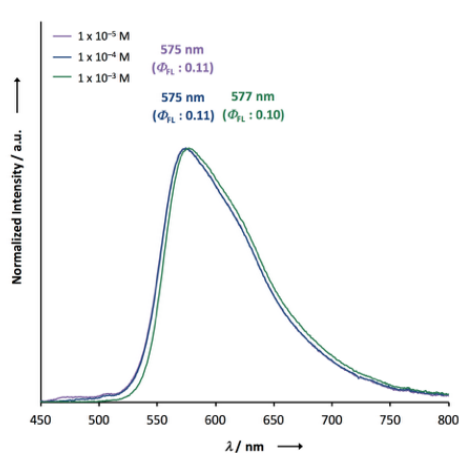


Figure 10. Emission Spectra of Cyclohexane Solutions of **10** Ranging from 1×10^{-5} to 1×10^{-3} M (λ_{ex} 300 nm)

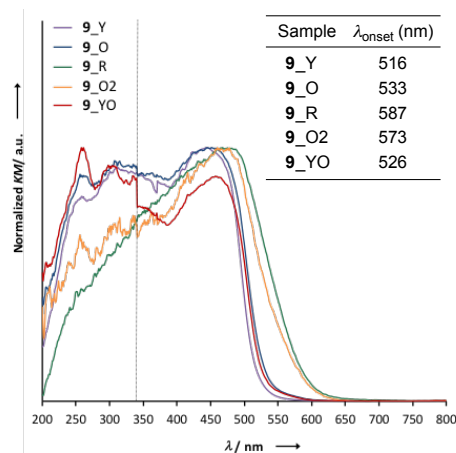


Figure 11. Diffuse Reflection Spectra of Solids **9** (The Dotted Line Indicates Switching of the Lamp)

3-8. Correlation of MCL Behavior with Conformers of **9**

A correlation diagram between emission colors and molecular conformations of **9** is illustrated in Figure 12. Since only sulfur-bridged D-A-D compounds (**9** and **10**) showed drastic color-change in response to external stimuli, conformational flexibility of PTZ units should induce distinct MCL character. Based on Data and Takeda's report, perpendicularly twisted POZ-DBPHZ exhibits red-TADF from an emissive ICT state.²¹ Therefore, the red emission from the solid **9_R** should come from highly twisted **eq-eq** conformer. On one hand, the orange emission of **9_O** would be attributed to the emission from a weaker ICT excited

state, which would be generated from **eq-ax** conformer as clearly shown from the crystallographic analysis (Figures 8a and 8b). Furthermore, the most high-energy emission of **9_Y** would derive from a radiative process from a ¹LE state associated with **ax-ax** conformer. The bottom line is that the presence of two “conformer-switchable“ PTZ units allow for producing various metastable states and thereby realizing multi-color changing MCL properties in the solid state. Also, the inclusion of solvent molecules (e.g., from **9_R** to **9_YO**) can cause the change in their packing modes by which the population of a conformer also varies through solvation/de-solvation cycles. This might result in the mixing of different conformers, leading to moderate color change derived from the mixture of different excited states.

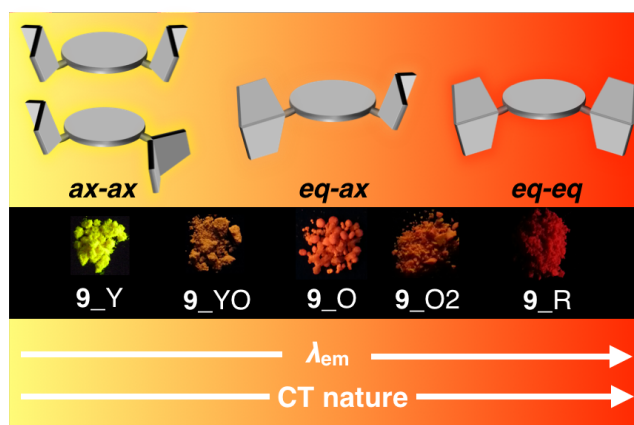


Figure 12. Schematic Correlation between Emission Colors and Molecular Conformations of **9**

3-9. Investigation of TADF Properties

Dynamic photophysical measurements revealed that all molecules exhibited TADF properties but the most promising was derivative **9** (Figures 13–16). In all of the cases, time-resolved photoluminescence from a blend film (1 wt% of compounds in zeonex[®]) at 300 K showed two components in the transient decay: these are attributed to prompt fluorescence (PF) and delayed fluorescence (DF), both of which have the same emission spectra (Figures 13a,b; 14a,b; 15a,b; 16a,b). The phosphorescence (PH) which corresponds to the PH of the acceptor unit²¹ was shifted bathochromically, when *t*-butyl groups were introduced (from **9** to

10). This result suggested that compound **10** has a more planar structure, thereby giving rise to increased conjugation. The energy levels of S_1 and T_1 for compound **9** were 2.48 and 2.40 eV, respectively, giving very low $\Delta E_{ST} = 0.08$ eV, indicating highly decoupled HOMO/LUMO orbitals on the donor and acceptor units. Notably, the values of S_1 and T_1 were the same as those of oxygen-bridged analogue POZ-DBPHZ as previously reported (Figure 2),²¹ suggesting that, in the zeonex[®] film, two PTZ units adopt electronically decoupled quasi-equatorial/quasi-equatorial conformations, which are perpendicular to the DBPHZ core. The S_1 and T_1 for compound **10** were 2.30 and 2.17 eV, respectively, giving $\Delta E_{ST} = 0.13$ eV (Figure 14) and showing increase of ΔE_{ST} gap and bathochromic shift resulted by *tert*-butyl group incorporation onto the PTZ donor group. The S_1 and T_1 for acridine derivative **11** were 2.67 and 2.38 eV, respectively, giving $\Delta E_{ST} = 0.29$ eV (Figure 15). The highest ΔE_{ST} was observed for the

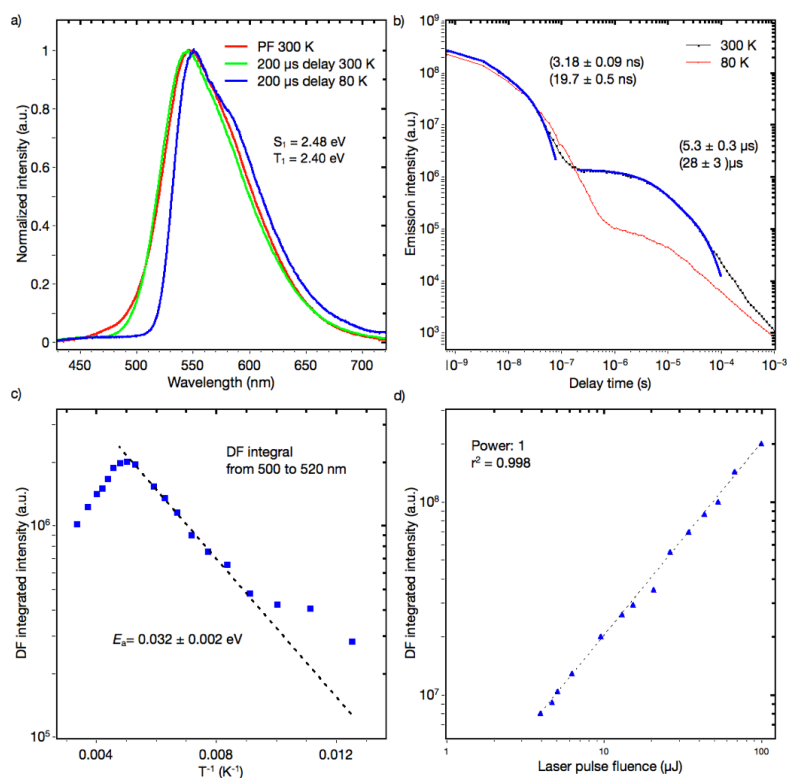


Figure 13. a) PF, DF and PH Spectra of 9:Zeonex[®] Blended Film; b) Transient Decays of 1 wt% 9:Zeonex[®] Blended Film at 300 K and 80 K; c) Temperature Dependence of Delayed Fluorescence of 1 wt% 9:Zeonex[®] Blended Film; d) Power Dependence of Delayed Fluorescence of 1 wt% 9:zeonex[®] Blended Film at 300 K

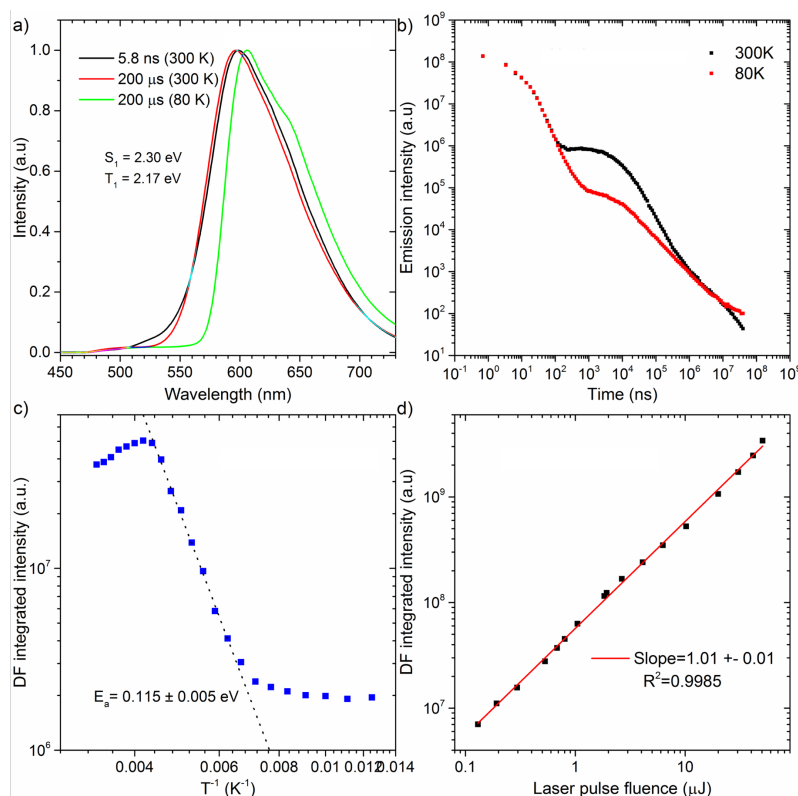


Figure 14. a) PL, DF and PH Spectra of 10:Zeonex® Blended Film; b) Transient Decays of 1 wt% 10:Zeonex® Blended Film at 300 K and 80 K; c) Temperature Dependence of Delayed Fluorescence of 1 wt% 10:Zeonex® Blended Film; d) Power Dependence of Delayed Fluorescence of 1 wt% 10:zeonex® Blended Film at 300 K

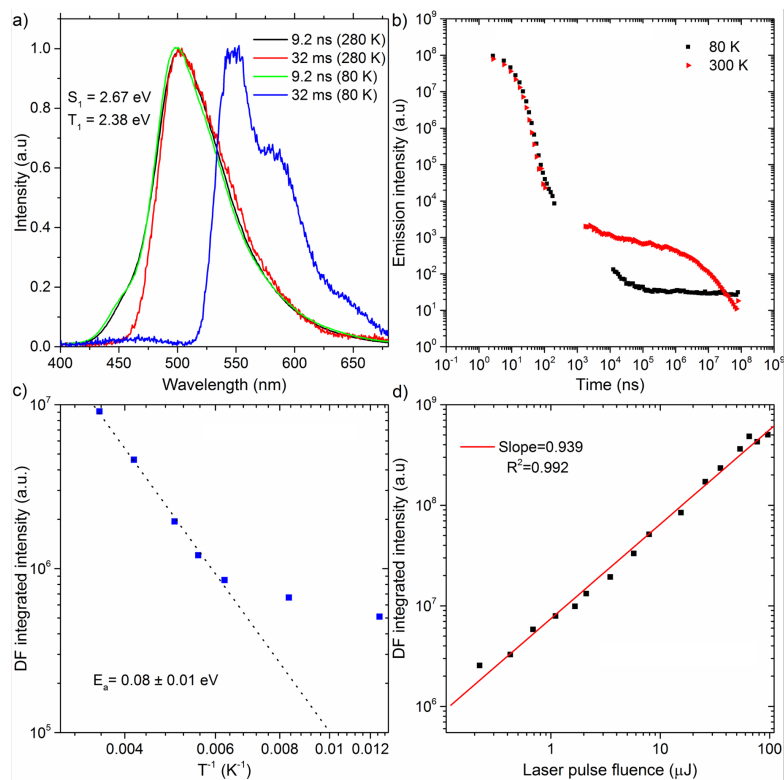


Figure 15. a) PL, DF and PH Spectra of 11:Zeonex® Blended Film; b) Transient Decays of 1 wt% 11:Zeonex® Blended Film at 300 K and 80 K; c) Temperature Dependence of Delayed Fluorescence of 1 wt% 11:Zeonex® Blended Film; d) Power Dependence of Delayed Fluorescence of 1 wt% 11:zeonex® Blended Film at 300 K

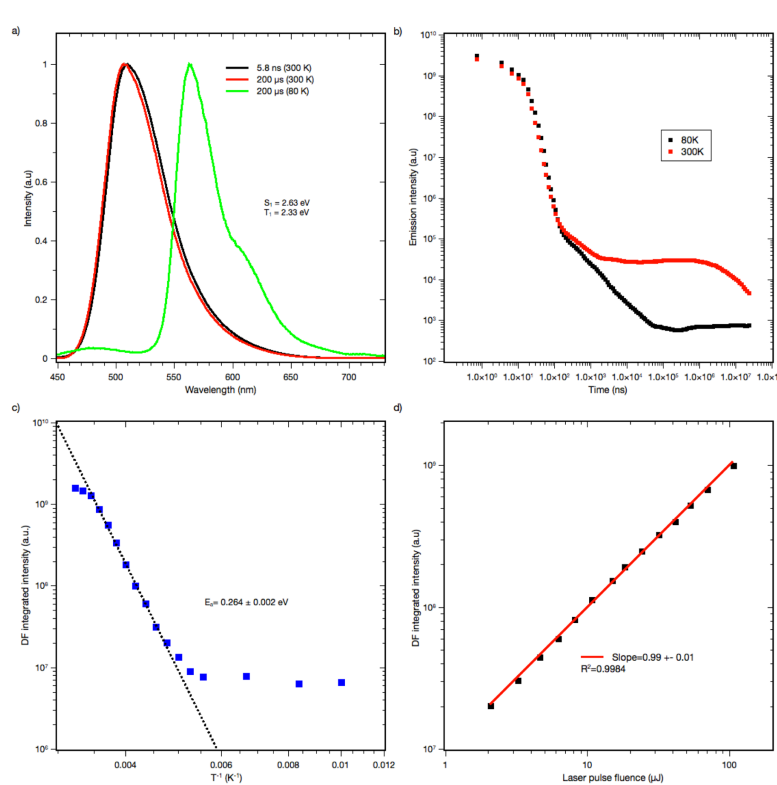


Figure 16. a) PF, DF and PH Spectra of **12**:Zeonex[®] Blended Film; b) Transient Decays of 1 wt% **12**:Zeonex[®] Blended Film at 300 K and 80 K; c) Temperature Dependence of Delayed Fluorescence of 1 wt% **12**:Zeonex[®] Blended Film; d) Power Dependence of Delayed Fluorescence of 1 wt% **12**:zeonex[®] Blended Film at 300 K

compound **12** as in previously presented work²¹ ($S_1 = 2.63$ eV and $T_1 = 2.33$ eV, $\Delta E_{ST} = 0.30$ eV). The Arrhenius plots for compound **9** (Figure 13c) showed very low delayed fluorescence (DF) activation energy (E_a) of about 0.03 eV close to ΔE_{ST} (0.08 eV), which was determined by the time-resolved photoluminescence, indicating **9** is an excellent candidate as a TADF emitter like POZ-DBPHZ.²¹ The maximum DF intensity was observed at about 200 K, and above this temperature, DF intensity started to decrease (Figure 13c). In the case of **9**, three important processes of relaxation of the excited state can be proposed along with prompt ¹CT (S_1) decay: 1) radiative transition $T_1 \rightarrow S_0$ (phosphorescence); 2) $T_1 \rightarrow S_1$ transition (rISC) and then radiative transition $S_1 \rightarrow S_0$ (TADF); 3) non-radiative relaxation $T_1 \rightarrow S_0$. When the temperature increased, the rate constant of process 2 would increase to give strong TADF emission. However, over 200 K, process 3 starts to dominate and the DF intensity decreases. At 80 K, DF still can be observed and pure PH (process 1) was observed at very late times (Figure 13b). This feature

would indicate that there was still enough vibrational energy for some molecules to overcome the S_1-T_1 energy gap at this temperature to form the mixed 3LE - 3CT state required for spin orbit coupling (SOC) to occur.¹⁶ A Linear power dependence of the delayed emission intensity with laser pulse fluence of **9** doped (1 wt%) in zeonex[®] at 300 K confirms that the observed DF component is TADF (Figure 13d).

Time-resolved photoluminescence of a 10 wt% **9**:CBP blend film indicated a far more complex situation, due to an inhomogeneous environment of **9** evaporated in the host material (Figure 17a). Analysis of spectra at 300 K showed contributions of several excited states in the total photoluminescence. At 0.7 ns, PF from the CBP blend film had the same onset as that from the zeonex[®] blend film at 500 nm (Figure 17b). However, the emission peak λ_{em} from the CBP blend film was red-shifted (581 nm) compared with that observed in zeonex[®] (546 nm), and the spectrum was definitely structureless (Figure 17b). When the delay time increased, the emission spectrum monotonically red-shifted, and the largest λ_{em} (600 nm) was observed at 57.8 ns (Figure 17b). From 57.8 ns to 1.1 μ s, λ_{em} plateaued at about 600 nm, but then from 1.1 μ s to 2.5 ms, λ_{em} slowly blue-shifted back to 587 nm and stayed at this value (Figure 17c). It is concluded that PF at very early delay time included some small contribution of 1LE emission of **9**, although 1CT emission dominates. The monotonic red-shift over the first 60 ns is indicative of an inhomogeneous system where the bluest 1CT states decay first and the redder states decay at longer times, to give the impression of a time dependent relaxation.^{15c} The emission observed from 57.8 ns to 1.1 μ s at 600 nm could indicate the emission from an excimer species of **9** (Figure 17c). Formation of excimers is normal in highly concentrated samples. After 1.1 μ s, 1CT emission from isolated **9** molecules starts to dominate ($\lambda_{em} = 587$ nm) and shows strong temperature dependence in line with TADF. The small difference of λ_{em} between the 1CT emission and the excimer emission ($\Delta\lambda_{em}$ 13 nm) suggests that the drastic change of the

emission color yellow (568 nm) to red (673 nm) ($\Delta\lambda_{em}$ 105 nm) in the fluorochromism would be derived from the switching of the 1LE and ICT excited states, not from excimer formation. Fitting of the DF transient measured at 300 K gave multiexponential decay components with more than four time constants, therefore, only a part of the whole decay was fitted, using four

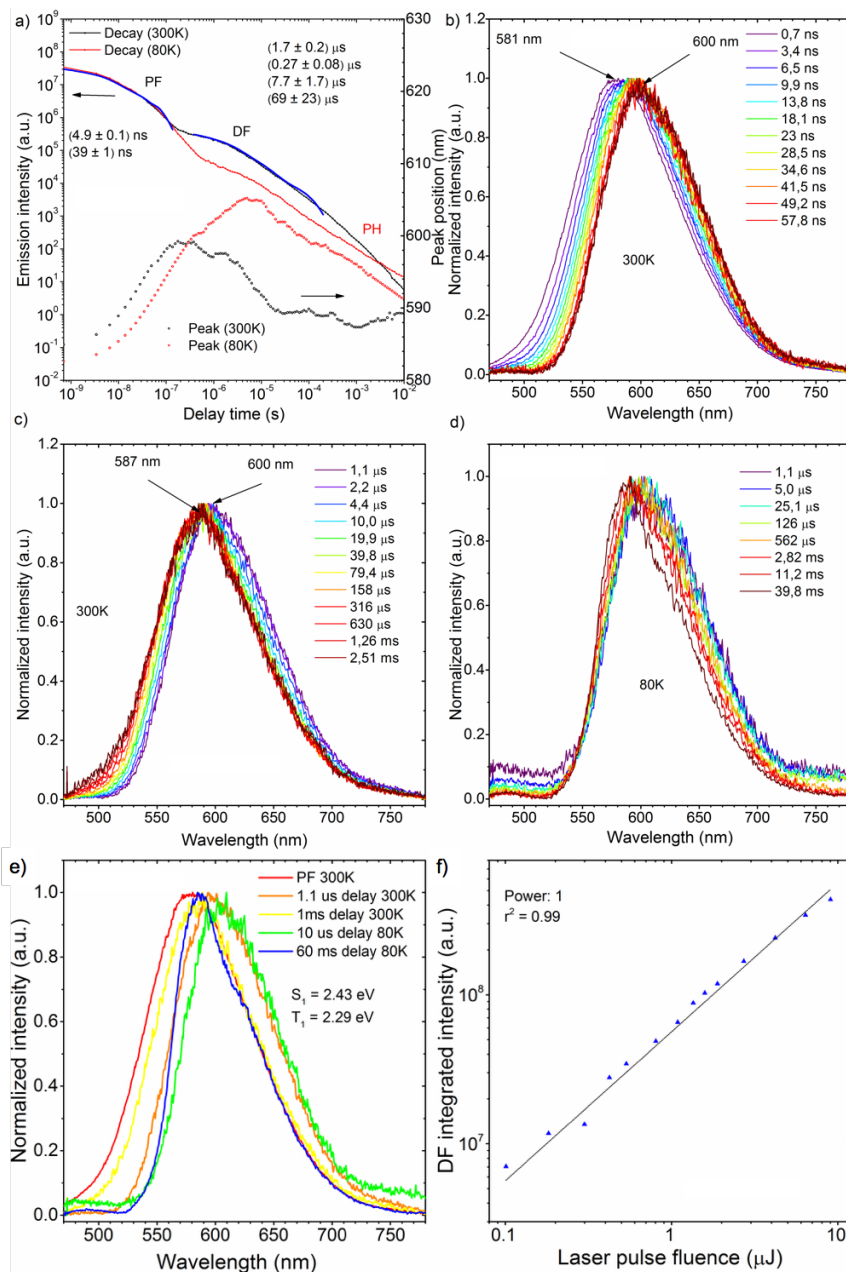


Figure 17. a) Transient Decays and Movement of Emission Maximum of 10wt% 9:CBP Blended Film at 300K and 80K; Time Dependence Spectra of 10wt% 9:CBP Blended Film in Different Time Range: b) and c) are Spectra Measured at 300 K, while d) at 80 K, and e) are Selected Spectra; f) Power Dependence of Delayed Fluorescence from 10% 9: CBP Blend. Recorded at 300K.

exponents. Such a multiexponential decay transient is indicative of an inhomogeneous system, along with mixing of ^1CT and excimer delayed emission. Behavior of the **9**-doped (10 wt%) CBP blend film at 80 K was also complicated (Figure 17d). It seems that ^1CT emission decreased significantly and becomes negligible, therefore the excimer emission spectrum appears to red-shifted further to $\lambda_{\text{em}} = 605$ nm at 6 ms delay. After 6 ms, another component builds in and λ_{em} gradually blue-shifts. The spectrum recorded 60 ms after excitation clearly showed vibrational structure and the triplet energy level was 2.29 eV. Isolated **9** molecules are expected to have the same triplet energy as in zeonex[®] ($T_1 = 2.40$ eV). Therefore, the observed DF at 60 ms at 80 K is ascribed to ^3LE phosphorescence of **9** excimer (Figure 17e). Linear laser power dependence of DF from 10 wt% **9**:CBP blend film at 300 K indicated clear TADF character (Figure 17f).

All four materials were analyzed for TADF emission, and derivative **10** showed similar results to the unsubstituted derivative **9**, but the emission was shifted by ca. 30 nm to the red region, and the overall DF contribution was lower (Figures 14 and 20), resulting in a lower device efficiency (Fig. 18, *vide infra*). Acridine derivative **11** exhibited some TADF behavior, but the ΔE_{ST} was much larger than for the other derivatives which resulted in a small TADF contribution (Figures 15 and 21) and the lowest device efficiency in this novel series of compounds (Fig. 18d, *vide infra*).

3-10. Fabrication of TADF-based OLED Devices

To investigate possibilities of applying the D-A-D compounds **9–12** as OLED emitters, thermogravimetric analysis (TGA) of the recrystallized, ground, heated and solvent treated samples was performed (Figure 23). High thermal decomposition temperatures [T_d (5 wt% loss) 439–450 °C for **9**, 455–459 °C for **10**, 428–434 °C for **11**, and 403–424 °C for **12**]

indicated that these molecules would be applicable to vacuum thermal deposition for purification and fabrication of OLEDs. Cyclic voltammetry (CV) exhibited reversible redox curves for the D-A-D molecules **9** and **10**, indicating their high electrochemical stability (Figure 24). Regarding the molecules **11** and **12**, when a negative voltage was applied, a reversible redox couple was clearly observed, while it was quasi-reversible in the case of a positive voltage (Figure 24). The curves of **9–12** in the positive and negative side are attributed to the redox processes of donors and acceptor, respectively. The IP/EA energy levels were determined by the CV experiments: $-5.33/-3.38$ eV (**9**); $-5.20/-3.35$ eV (**10**); $-5.55/-3.40$ eV (**11**); $-5.59/-3.29$ eV (**12**). The energy levels of DBPHZ **9** are almost the same as POZ-DBPHZ ($-5.36/-3.38$ eV).²¹ The HOMO levels of these D-A-D compounds decreased in descending order of the electron-donating nature of the donors (**10** > **9** > POZ-DBPHZ > **11** > **12**). However, the LUMO levels were different. The energy level of **12** was highest and that of the other molecules decreased in the same order as the HOMO levels (**12** > **10** > **9** = POZ-DBPHZ > **11**), suggesting that HOMOs and LUMOs of DBPHZs **9–11** and POZ-DBPHZ were completely separated due to their perpendicular structures, although some HOMO/LUMO interactions would exist for DBPHZ **12**, because of the propeller structures of diphenyl amino groups.

OLED devices were fabricated using the co-evaporation technique (Figure 18). The device structure used was as follows: ITO/NPB (40 nm)/10 wt% D-A-D compound (**9–12**) in CBP (30 nm)/TPBi (50 nm)/LiF (1 nm)/Al (100 nm). The device based on **9** exhibited orange emission at 613 nm with up to 16.8% EQE, which greatly surpasses the theoretical maxima (5%) with conventional fluorescence materials, and 19.6 cd/A maximum efficiency (Figures 18a and c). The roll-off process was observed above the 7 V and the device was characterized by high luminance (>25,000 cd) (Figures 18b and d).

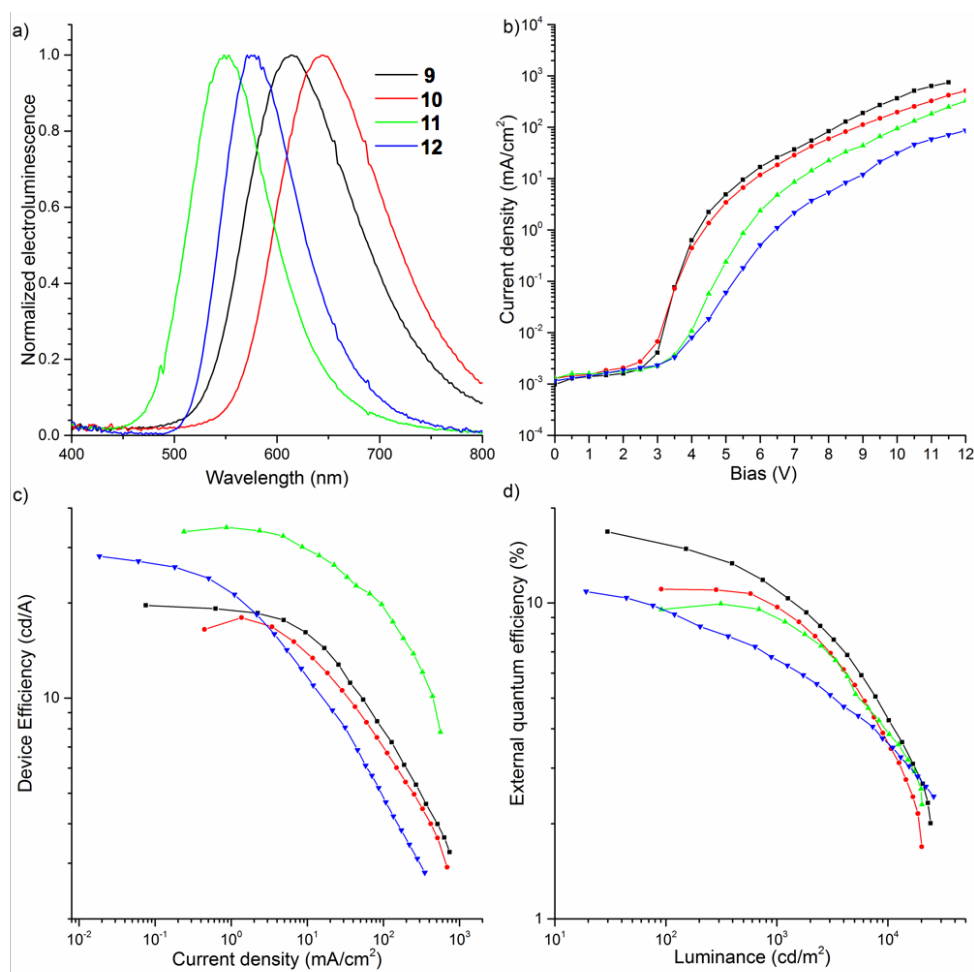


Figure 18. Characterization of OLED Devices

3-11. Conclusion

The author has succeeded in developing novel D-A-D molecules **9** and **10** that exhibit both distinct multi-color-changing MCL and efficient TADF properties by the combination of an electron deficient DBPHZ acceptor and “two-conformation-switchable” and electron-donating phenothiazine donors. The quantum chemical calculations using the DFT method indicated the existence of four possible thermodynamically interconvertible conformers of **9** derived from conformational alternation of the phenothiazine units. Compared with DBPHZ derivatives substituted with the other donor units, the necessity of the sulfur-bridge in the donor unit for drastic multi-color-changing luminochromism was demonstrated. Notably, the

single crystal X-ray analysis showed the asymmetric molecular structure of **9**_O having two conformational types of phenothiazines: one is a “quasi-equatorial” and the other a “quasi-axial”. Most importantly, the author proposes that the high-contrast luminochromic behavior would result in the switching of the LE and ICT excited states caused by conformational change of phenothiazine units. Furthermore, **9** had a very small ΔE_{ST} induced by efficient HOMO/LUMO decoupling and exhibited strong TADF. Based on **9**, TADF OLED devices were fabricated and gave orange emission with high light emitting efficiency, 16.8% EQE. The findings reported here would further guide us to a novel design principle for the construction of multi-functional materials in the future.

3-12. Experimental Section

General Remarks

All reactions were carried out under an atmosphere of nitrogen unless otherwise noted. Melting points were determined on a Stanford Research Systems MPA100 OptiMelt Automated Melting Point System. ¹H and ¹³C NMR spectra were recorded on a JEOL JMTC-400/54/SS spectrometer (¹H NMR, 400 MHz; ¹³C NMR, 100 MHz) using tetramethylsilane as an internal standard. Infrared spectra were acquired on a SHIMADZU IRAffinity-1 FT-IR Spectrometer. Mass spectra were obtained on a JEOL JMS-DX303HF mass spectrometer. High-resolution mass spectra (HRMS) were obtained on a JEOL JMS-DX303HF mass spectrometer. UV-vis spectra were recorded on a Shimadzu UV-2550 spectrophotometer. Emission spectra were recorded on a HAMAMATSU C11347-01 spectrometer with an integrating sphere. Differential scanning calorimetry (DSC) measurements were carried out on a DSC 6220 (SII) system at a scanning rate of 10 °C min⁻¹ under a N₂ atmosphere. Powder X-ray diffraction (XRD) patterns were recorded by Rigaku SmartLab X-ray diffractometer with CuK α radiation ($\lambda = 1.5418 \text{ \AA}$). Diffuse reflection spectra were collected by a JASCO V-670 UV-Vis-NIR Spectrophotometer. Cyclic voltammetry (CV) was performed with ALS-600 (BAS Inc.) system. Thermogravimetric analysis (TGA) was performed with TG/DTA-7200 (SII) system. Products were purified by chromatography on silica gel BW-300 and

Chromatorex NH (Fuji Silysia Chemical Ltd.). Analytical thin-layer chromatography (TLC) was performed on pre-coated silica gel glass plates (Merck silica gel 60 F254 and Fuji Silysia Chromatorex NH, 0.25 mm thickness). Compounds were visualized with UV lamp. Small molecules and cathode layers were thermally evaporated using Kurt J. Lesker Spectros II Deposition at 10^{-6} mbar. All organic materials and aluminum were deposited at a rate of 1 \AA s^{-1} , and the LiF layer was deposited at 0.1 \AA s^{-1} . Investigation of the characteristic of OLED devices was conducted in 10 inches integrating sphere (Labsphere) connected to a SourceMeter unit. Phosphorescence (PH), prompt fluorescence (PF), and delayed fluorescence (DF) spectra and decays were recorded using nanosecond gated luminescence and lifetime measurements (from 400 ps to 1 s) using either a high energy pulsed Nd:YAG laser emitting at 355 nm (EKSPLA) or a N_2 laser emitting at 337 nm. Emission was focused onto a spectrograph and detected on a sensitive gated iCCD camera (Stanford Computer Optics) having sub-nanosecond resolution. PF/DF time resolved measurements were performed by exponentially increasing gate and delay times.

Materials

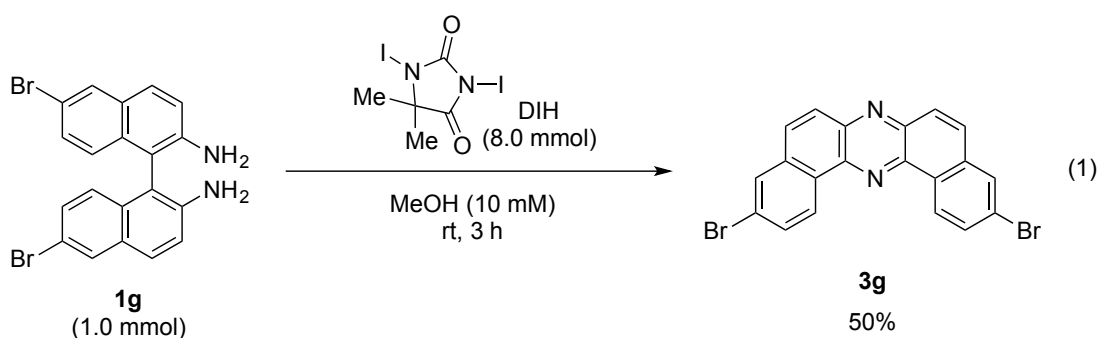
6,6'-Dibromo-1,1'-binaphthalene-2,2'-diamine (**3g**) [CAS No. 861890-12-2] was prepared from 6-Bromo-2-naphthol [CAS No. 15231-91-1] according to the procedures in literature.²⁹ 6-Bromo-2-naphthol was prepared according to the procedures in literature.³⁰ 3,7-di-*tert*-butyl-10*H*-phenothiazine [CAS No. 27075-55-4]³¹ and 9,9-dimethyl-9,10-dihydroacridine [CAS No. 6267-02-3]³² were prepared according to the procedures in literature. Tetrabutylammonium hexafluorophosphate for electrochemical measurement was purchased from TCI and used after repeated (3 times) recrystallization from EtOH. Commercial reagents were purchased from Sigma-Aldrich, TCI, or Wako Pure Chemical Industries, Ltd. and used as received. MeOH was dried over activated molecular sieves 3Å. Toluene was purchased as dehydrated grade and purified by passing through a solvent purification system (KOREA KIYON Co., Ltd.). Solvents of fluorescence spectroscopic grade were purchased from Nacalai Tesque Inc. and Kanto Chemical Co., Inc. for measurement of UV-vis and emission spectra. All organic evaporated compounds were purified by Creaphys organic sublimation system, and the following compounds were purchased from companies: CBP [4,4'-bis(*N*-carbazolyl)-1,1'-biphenyl] (Sigma Aldrich), NPB [*N,N'*-Di-1-naphthyl-*N,N'*-diphenylbenzidine] (TCI-Europe), TPBi [2,2,2'-(1,3,5-Benzinetriyl)-tris(1-phenyl-1-*H*-benzimidazole)] (LUMTEC), LiF (99.995%, Sigma Aldrich), and Aluminium wire (99.9995%,

Alfa Aesar). OLED devices were fabricated using pre-cleaned indium-tin-oxide (ITO) coated glass substrates purchased from Ossila with a sheet resistance of $20 \Omega/\text{cm}^2$ and ITO thickness of 100 nm. The formed OLED devices had a pixel size of 2 mm by 1.5 mm.

Synthetic Procedures and Spectroscopic Data of 9–12

Preparation of 3,11-Dibromodibenzo[*a,j*]phenazine

3,11-Dibromodibenzo[*a,j*]phenazine (**3g**) was prepared through a slightly modified method described in Chapter 2 as follows (Eq 1): To a two-necked round-bottomed flask (300 mL) equipped with a three-way stopcock and a magnetic stir bar, was added 6,6'-dibromo-1,1'-binaphthalene-2,2'-diamine (**1g**) (442.1 mg, 1.0 mmol) under the air. The vessel was capped with a rubber septum, evacuated, and refilled with N_2 gas for 3 times, and then MeOH (100 mL) was added through the septum. To this stirred mixture, was added 1,3-diiodo-5,5-dimethylhydantoin (DIH) (3.04 g, 8.0 mmol) under a stream of N_2 gas at room temperature. The resulting solution was stirred for 3 h before quenched with aqueous $\text{Na}_2\text{S}_2\text{O}_3$ (1.0 M, 100 mL), and the resulting mixture was extracted with CH_2Cl_2 (100 mL \times 3). The combined organic extracts were dried over Na_2SO_4 and concentrated under vacuum to give the crude product, which was purified by flash column chromatography (eluent: hexane/EtOAc 95:5–9:1) on silica gel to give product **3g** (219.0 mg, 50%). Further purification was carried out by recrystallization from CHCl_3 .



Typical procedures for the synthesis of 3,11-diaminodibenzo[*a,j*]phenazines (Scheme 1)

3,11-Diaminodibenzo[*a,j*]phenazines **9–12** were prepared through a slightly modified Pd-catalyzed amination reaction³³ of **3g** with aromatic amines as follows (*Methods A, B or B'*).

Method A: Toluene was degassed through freeze-pump-thaw cycling for 3 times before used. In a glovebox, to a two-necked reaction tube (10 mL) equipped with a three-way stopcock and

a magnetic stir bar, was added Pd[P(*t*-Bu)₃]₂ (12.8 mg, 5 mol%), and the tube was closed with a rubber septum. Outside the glovebox, dibromophenazine **3g** (219.0 mg, 0.50 mmol), 10*H*-phenothiazine (219.1 mg, 1.10 mmol), K₂CO₃ (414.5 mg, 3.0 mmol), and toluene (5 mL) were added under a stream of N₂ gas at room temperature, and the resulting mixture was stirred under reflux for 24 h. Water (5 mL) was added to the reaction mixture, and the organic layer was extracted with CH₂Cl₂ (20 mL × 3). The combined organic extracts were dried over Na₂SO₄, and the solvent was evaporated in vacuo to give the crude product, which was purified by flash column chromatography (for the detailed purification methods, see the product data).

3,11-Di(10*H*-phenothiazin-10-yl)dibenzo[*a,j*]phenazine (**9**)

Purified by flash column chromatography on NH silica gel (eluent: *n*-hexane/CH₂Cl₂ 95:5–8:2) followed by recrystallization from a two-phase solvent of *n*-hexane/CHCl₃ (3:1); Yellow solid (290.2 mg, 86%); mp 300 °C (dec.); *R*_f 0.18 (*n*-hexane/CH₂Cl₂ 8:2, NH silica); ¹H NMR (400 MHz, CDCl₃): δ 6.56 (dd, *J* = 1.6, 7.6 Hz, 4H), 6.92–7.00 (m, 8H), 7.18 (dd, *J* = 2.0, 7.2 Hz, 4H), 7.85 (dd, *J* = 2.0, 8.4 Hz, 2H), 7.97 (d, *J* = 2.0 Hz, 2H), 8.09 (d, *J* = 9.2 Hz, 2H), 8.14 (d, *J* = 9.2 Hz, 2H), 9.77 (d, *J* = 8.4 Hz, 2H); ¹³C NMR (100 MHz, CDCl₃): δ 118.3, 123.1, 123.4, 126.5, 127.0, 127.3, 127.7, 127.8, 129.7, 132.1, 135.3, 140.5, 142.8, 143.0, 143.7 (One carbon was not detected, probably due to the overlap of the signal with other aromatic peaks); IR (ATR): ν 3039, 1583, 1462, 1352, 1300, 1257, 1145, 850, 754, 740 cm⁻¹; MS (FAB): *m/z* (relative intensity, %) 675 ([M + H]⁺, 6), 674 (M⁺, 7); HRMS (FAB): *m/z* calcd for C₄₄H₂₆N₄S₂ (M⁺) 674.1599, found 674.1595.

Method B and B': Toluene was degassed through freeze-pump-thaw cycling for 3 times before used. In a glovebox, to a two-necked reaction tube (10 mL) equipped with a three-way stopcock and a magnetic stir bar, were added Pd[P(*t*-Bu)₃]₂ (12.8 mg, 5 mol%) and sodium *tert*-butoxide (115.3 mg, 1.20 mmol), and the tube was closed with a rubber septum. Outside the glovebox, dibromophenazine **3g** (219.0 mg, 0.50 mmol), amine [3,7-di-*tert*-butyl-10*H*-phenothiazine (342.6 mg), 9,9-dimethyl-9,10-dihydroacridine (230.2 mg), or diphenylamine (186.1 mg)] (1.10 mmol) and toluene (5 mL) were added under a stream of N₂ gas at room temperature, and the resulting mixture was stirred under reflux for 24 h (**Method B**) or 20 h (**Method B'**). Water (5 mL) was added to the reaction mixture, and the organic layer was extracted with CH₂Cl₂ (20 mL × 3). The combined organic extracts were dried over Na₂SO₄,

and the solvent was evaporated in vacuo to give the crude product, which was purified by flash column chromatography (for the detailed purification methods, see each product data).

3,11-Bis(3,7-di-*tert*-butyl-10*H*-phenothiazin-10-yl)dibenzo[*a,j*]phenazine (10)

Purified by flash column chromatography on NH silica gel (eluent: *n*-hexane/CH₂Cl₂ 95:5–9:1) followed by recrystallization from a two-phase solvent of *n*-hexane/CHCl₃ (20:1); Yellow solid (413.7 mg, 92%); mp 263 °C; *R*_f 0.20 (*n*-hexane/CH₂Cl₂ 8:2, NH silica); ¹H NMR (400 MHz, CDCl₃): δ 1.28 (s, 36H), 6.61 (d, *J* = 8.8 Hz, 4H), 7.02 (dd, *J* = 2.0, 8.8 Hz, 4H), 7.24 (d, *J* = 2.0 Hz, 4H), 7.80 (dd, *J* = 2.0, 8.4 Hz, 2H), 7.89 (d, *J* = 2.0 Hz, 2H), 8.04 (d, *J* = 9.2 Hz, 2H), 8.10 (d, *J* = 9.2 Hz, 2H), 9.70 (d, *J* = 8.4 Hz, 2H); ¹³C NMR (100 MHz, CDCl₃): δ 31.3, 34.2, 118.8, 123.9, 123.9, 124.5, 124.7, 126.5, 127.5, 127.7, 129.0, 132.1, 135.2, 140.6, 141.1, 142.6, 143.7, 146.8; IR (ATR): ν 2953, 1595, 1475, 1357, 1305, 1263, 1143, 856, 808, 721 cm⁻¹; MS (FAB): *m/z* (relative intensity, %) 899 ([M + H]⁺, 100), 898 (M⁺, 96); HRMS (FAB): *m/z* calcd for C₆₀H₅₈N₄S₂ (M⁺) 898.4103, found 898.4096.

3,11-Bis(9,9-dimethylacridin-10(9*H*)-yl)dibenzo[*a,j*]phenazine (11)

Purified by flash column chromatography on NH silica gel (eluent: *n*-hexane/CH₂Cl₂ 95:5–9:1) followed by recrystallization from a two-phase solvent of *n*-hexane/CHCl₃ (5:1); Yellow solid (271.0 mg, 78%); mp 315 °C (dec.); *R*_f 0.33 (*n*-hexane/CH₂Cl₂ 8:2, NH silica); ¹H NMR (400 MHz, CDCl₃): δ 1.78 (s, 12H), 6.35–6.37 (m, 4H), 6.97–6.99 (m, 8H), 7.52–7.54 (m, 4H), 7.86 (dd, *J* = 2.0, 8.4 Hz, 2H), 8.05 (d, *J* = 2.0 Hz, 2H), 8.16 (d, *J* = 9.6 Hz, 2H), 8.21 (d, *J* = 9.6 Hz, 2H), 9.92 (d, *J* = 8.4 Hz, 2H); ¹³C NMR (100 MHz, CDCl₃): δ 31.4, 36.1, 114.2, 120.9, 125.4, 126.4, 127.8, 128.3, 130.2, 130.6, 130.9, 130.9, 132.3, 135.5, 140.5, 140.9, 142.4, 143.2; IR (ATR): ν 3035, 2958, 1591, 1473, 1444, 1330, 1271, 931, 856, 796, 740 cm⁻¹; MS (EI): *m/z* (relative intensity, %) 694 (M⁺, 12), 679 ([M–Me]⁺, 100), 471 ([C₃₄H₂₁N₃]⁺, 44), 332 ([C₂₄H₁₆N₂]⁺, 81); HRMS (EI): *m/z* calcd for C₅₀H₃₈N₄ (M⁺) 694.3096, found 694.3099.

3,11-Bis(diphenylamino)dibenzo[*a,j*]phenazine (12)

Purified by flash column chromatography on NH silica gel (eluent: *n*-hexane/EtOAc 99:1–98:2) followed by recrystallization from a two-phase solvent of *n*-hexane/CHCl₃ (5:1); Orange solid (205.9 mg, 67%); mp 296 °C (dec.); *R*_f 0.25 (*n*-hexane/EtOAc 8:2, NH silica); ¹H NMR (400 MHz, CDCl₃): δ 7.13 (t, *J* = 7.2 Hz, 4H), 7.23 (d, *J* = 7.6 Hz, 8H), 7.34 (dd, *J* = 7.2, 7.6

Hz, 8H), 7.51 (d, $J = 2.4$ Hz, 2H), 7.55 (dd, $J = 2.4, 8.8$ Hz, 2H), 7.80 (d, $J = 8.8$ Hz, 2H), 7.94 (d, $J = 8.8$ Hz, 2H), 9.36 (d, $J = 8.8$ Hz, 2H); ^{13}C NMR (100 MHz, CDCl_3): δ 119.6, 123.2, 123.8, 125.2, 125.8, 126.2, 127.4, 129.5, 131.5, 134.6, 140.9, 141.7, 147.4, 149.0; IR (ATR): ν 3030, 1590, 1476, 1358, 1275, 1141, 870, 848, 790, 750 cm^{-1} ; MS (EI): m/z (relative intensity, %) 614 (M^+ , 100), 307 ($[\text{C}_{22}\text{H}_{15}\text{N}_2]^+$, 26); HRMS (EI): m/z calcd for $\text{C}_{44}\text{H}_{30}\text{N}_4$ (M^+) 614.2470, found 614.2469.

Mechanochromic Luminescence (MCL) Properties (Figures 4, 19, and Table 3)

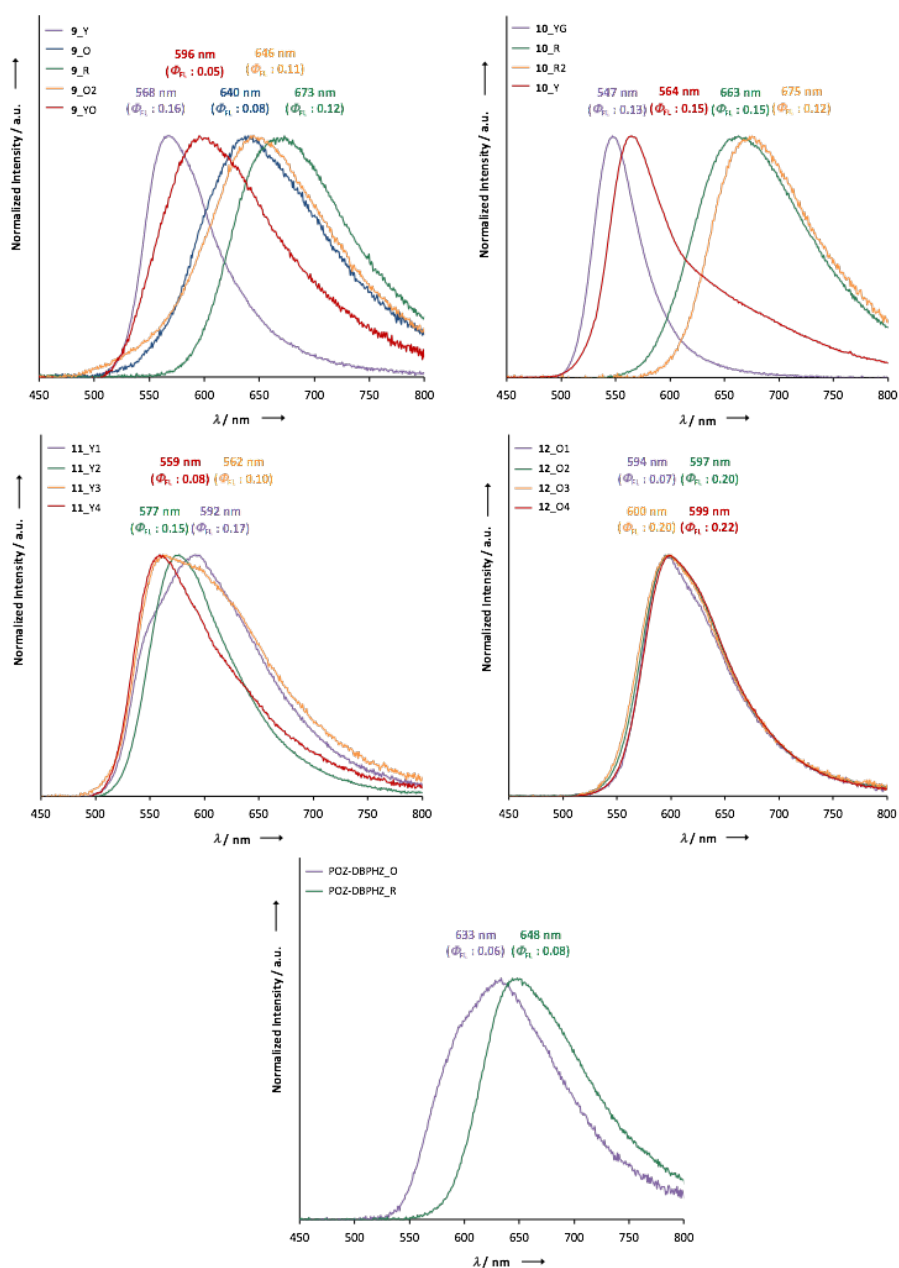


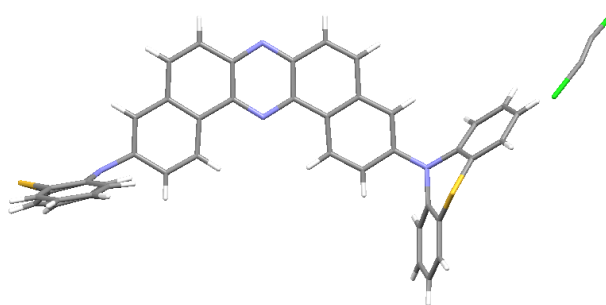
Figure 19. Emission Spectra of Solid Samples of 9–12 and POZ-DBPHZ

Table 3. Summary of MCL Properties of **9–12** and POZ-DBPHZ

Sample	λ_{ex} (nm)	λ_{em} (nm)	Φ_{FL}	Sample	λ_{ex} (nm)	λ_{em} (nm)	Φ_{FL}
9 _Y	300	568	0.16	11 _Y1	300	592	0.17
9 _O	400	640	0.08	11 _Y2	300	577	0.15
9 _R	400	673	0.12	11 _Y3	300	562	0.10
9 _O2	400	646	0.11	11 _Y4	300	559	0.08
9 _YO	400	596	0.05	12 _O1	300	594	0.07
10 _YG	300	547	0.13	12 _O2	300	597	0.20
10 _R	300	663	0.15	12 _O3	300	600	0.20
10 _R2	400	675	0.12	12 _O4	300	599	0.22
10 _Y	300	564	0.15	POZ-DBPHZ_O	400	633	0.06
				POZ-DBPHZ_R	400	648	0.08

Single Crystal X-ray Crystallographic Data (Figure 8 and Table 4)

The X-ray diffraction data of the single crystal of **9**_O were collected on a Rigaku R-Axis RAPID diffractometer with graphite monochromated CuK α radiation ($\lambda = 1.54187 \text{ \AA}$) to a $2\theta_{\text{max}}$ value of 136.5° at 123 K. The crystal structure was solved by direct methods (SIR92)³⁴ and expanded using Fourier techniques. The non-hydrogen atoms were refined anisotropically, and hydrogen atoms were refined using the riding model. The crystal data are summarized in Table 4. CCDC-1452024 contains the supplementary crystallographic data for **9**_O, which are available free of charge from the Cambridge Crystallographic Data Center (CCDC) via www.ccdc.cam.ac.uk/data_request/cif.

Table 4. Summary of Crystallographic Data of **9**_O.

Empirical Formula	C ₄₅ H ₂₆ ClN ₄ S ₂	
Formula Weight	722.30	
Crystal System	monoclinic	
Space Group	C2/c (#15)	
Unit cell dimensions	$a = 30.0933(6) \text{ \AA}$	$\alpha = 90^\circ$
	$b = 8.4390(2) \text{ \AA}$	$\beta = 95.5660(7)^\circ$
	$c = 26.6268(5) \text{ \AA}$	$\gamma = 90^\circ$
V	6730.2(3) \AA^3	
Z	8	
Density (calculated)	1.426 g/cm ³	
Absorption coefficient	24.879 cm ⁻¹	
$R_1 [I > 2\sigma(I)]$	0.1215	
wR_2 (all data)	0.4004	
Crystal size	0.300 × 0.100 × 0.100 mm	
Goodness-of-fit on F^2	1.473	
Reflections collected/unique	43374/6159 [$R(\text{int}) = 0.0648$]	

UV-vis Absorption and Emission Spectra (Figures 9, 10 and Table 2)

Solvents were purged with N₂ for 30 min before use. Steady-state UV-vis absorption and emission spectra were measured at room temperature using the solutions (1.0×10^{-5} to 1.0×10^{-3} M).

Theoretical Calculations

All the molecules were geometrically optimized by the DFT method at the B3LYP/6-31+G(d,p) level of theory using Gaussian 09 package.³⁵ The relative molecular energies of conformers **9** (Figure 3) were calculated from the sum of electronic and thermal free energies, which were obtained from frequency analysis of the optimized structures of the conformers at the B3LYP/6-31+G(d,p) level. The excitation energies of the geometrically optimized molecules were calculated with the TD-DFT method at the same level of theory. Cartesian coordinates of the initial and optimized structures of **9** are listed below (Tables 5–12).

Table 5. Cartesian Coordinates of the Initial Structure of Axial-Axial Conformer (*syn*) of **9**

atom	x	y	z
S	-1.94383	1.584678	-7.53526
S	-1.94383	1.584678	7.535259
N	-0.1227	-4.22501	0
N	0.212969	-1.42433	0
N	0.51404	0.577215	-6.18312
N	0.51404	0.577215	6.183122
C	-0.04003	-3.53497	-1.14688
C	-0.12537	-4.24203	-2.39632
C	-0.04128	-3.57549	-3.57989
C	0.136751	-2.14347	-3.63083
C	0.228934	-1.47497	-4.86787
C	0.402873	-0.09012	-4.93905
C	0.455619	0.637426	-3.72001
C	0.367217	-0.00922	-2.50195
C	0.216229	-1.40759	-2.41743
C	0.130924	-2.10807	-1.14968
C	0.130924	-2.10807	1.149681
C	0.216229	-1.40759	2.41743
C	0.367217	-0.00922	2.501955
C	0.455619	0.637426	3.720007
C	0.402873	-0.09012	4.93905
C	0.228934	-1.47497	4.86787
C	0.136751	-2.14347	3.630835
C	-0.04128	-3.57549	3.579887
C	-0.12537	-4.24203	2.396319
C	-0.04003	-3.53497	1.146883
C	0.230813	-0.10078	-7.41052
C	1.090529	-1.08326	-7.91612
C	0.778046	-1.74805	-9.10253
C	-0.37861	-1.40853	-9.81242
C	-1.21077	-0.38966	-9.34713
C	-0.90994	0.261783	-8.14519
C	-0.64448	2.616342	-6.87297
C	-0.71458	4.010944	-6.97032
C	0.319223	4.796103	-6.45833
C	1.444016	4.189658	-5.88928
C	1.525383	2.798653	-5.81371
C	0.466793	2.004107	-6.27011
C	0.466793	2.004107	6.270107
C	1.525383	2.798653	5.813715
C	1.444016	4.189658	5.889283
C	0.319223	4.796103	6.458333
C	-0.71458	4.010944	6.970321
C	-0.64448	2.616342	6.872969
C	-0.90994	0.261783	8.145194
C	-1.21077	-0.38966	9.347135
C	-0.37861	-1.40853	9.812416
C	0.778046	-1.74805	9.102527
C	1.090529	-1.08326	7.916118
C	0.230813	-0.10078	7.410521
H	-0.25825	-5.31842	-2.35198
H	-0.10761	-4.1189	-4.51891
H	0.148807	-2.06563	-5.77179
H	0.550637	1.71517	-3.73503
H	0.407039	0.564279	-1.58265
H	0.407039	0.564279	1.582646
H	0.550637	1.71517	3.735033
H	0.148807	-2.06563	5.771794
H	-0.10761	-4.1189	4.518909
H	-0.25825	-5.31842	2.351978
H	1.99214	-1.32761	-7.36342
H	1.442454	-2.52021	-9.47817
H	-0.61957	-1.91777	-10.7406
H	-2.08687	-0.09133	-9.91493
H	-1.57105	4.473344	-7.45151
H	0.257513	5.877925	-6.52721
H	2.262575	4.797772	-5.51659
H	2.399547	2.315833	-5.38845
H	2.399547	2.315833	5.388447
H	2.262575	4.797772	5.516592
H	0.257513	5.877925	6.527207
H	-1.57105	4.473344	7.451513
H	-2.08687	-0.09133	9.914932
H	-0.61957	-1.91777	10.7406
H	1.442454	-2.52021	9.478167
H	1.99214	-1.32761	7.363424

Table 6. Cartesian Coordinates of the Optimized Structure of Axial-Axial Conformer (*syn*) of **9**

atom	x	y	z
S	-1.58163	1.943157	7.538075
S	-1.58163	1.943157	-7.53808
N	4.223625	0.126701	0
N	1.42338	-0.21275	0
N	-0.57769	-0.51476	6.183422
N	-0.57769	-0.51476	-6.18342
C	3.533652	0.043191	1.146888
C	4.240666	0.129339	2.396299
C	3.57428	0.044618	3.579896
C	2.142484	-0.13528	3.630935
C	1.47416	-0.22788	4.867974
C	0.089429	-0.40318	4.939235
C	-0.63809	-0.4571	3.720222
C	0.008449	-0.36817	2.502132
C	1.406655	-0.21579	2.417517
C	2.107027	-0.12976	1.14973
C	2.107027	-0.12976	-1.14973
C	1.406655	-0.21579	-2.41752
C	0.008449	-0.36817	-2.50213
C	-0.63809	-0.4571	-3.72022
C	0.089429	-0.40318	-4.93924
C	1.47416	-0.22788	-4.86797
C	2.142484	-0.13528	-3.63094
C	3.57428	0.044618	-3.5799
C	4.240666	0.129339	-2.3963
C	3.533652	0.043191	-1.14689
C	0.101092	-0.23346	7.410837
C	1.082838	-1.09475	7.915254
C	1.74832	-0.78422	9.101797
C	1.41028	0.372068	9.812993
C	0.392322	1.205943	9.348768
C	-0.25996	0.906866	8.146848
C	-2.61518	0.645702	6.874872
C	-4.00967	0.717706	6.972522
C	-4.79635	-0.3148	6.460255
C	-4.19153	-1.44005	5.890405
C	-2.80064	-1.52316	5.814318
C	-2.0045	-0.46584	6.27095
C	-2.0045	-0.46584	-6.27095
C	-2.80064	-1.52316	-5.81432
C	-4.19153	-1.44005	-5.89041
C	-4.79635	-0.3148	-6.46026
C	-4.00967	0.717706	-6.97252
C	-2.61518	0.645702	-6.87487
C	-0.25996	0.906866	-8.14685
C	0.392322	1.205943	-9.34877
C	1.41028	0.372068	-9.81299
C	1.74832	-0.78422	-9.1018
C	1.082838	-1.09475	-7.91525
C	0.101092	-0.23346	-7.41084
H	5.316891	0.26352	2.351932
H	4.117594	0.111661	4.518924
H	2.064651	-0.14632	5.77188
H	-1.71576	-0.55279	3.735208
H	-0.56506	-0.40887	1.582869
H	-0.56506	-0.40887	-1.58287
H	-1.71576	-0.55279	-3.73521
H	2.064651	-0.14632	-5.77188
H	4.117594	0.111661	-4.51892
H	5.316891	0.26352	-2.35193
H	1.326221	-1.996	7.361522
H	2.519802	-1.44994	9.476494
H	1.920077	0.611519	10.74126
H	0.095277	2.081922	9.917428
H	-4.47076	1.574534	7.45433
H	-5.87807	-0.2517	6.529433
H	-4.80073	-2.25771	5.517514
H	-2.31926	-2.39787	5.388522
H	-2.31926	-2.39787	-5.38852
H	-4.80073	-2.25771	-5.51751
H	-5.87807	-0.2517	-6.52943
H	-4.47076	1.574534	-7.45433
H	0.095277	2.081922	-9.91743
H	1.920077	0.611519	-10.7413
H	2.519802	-1.44994	-9.47649
H	1.326221	-1.996	-7.36152

Table 7. Cartesian Coordinates of the Initial Structure of Axial-Axial Conformer (*anti*) of **9**

atom	x	y	z
S	-1.72669	7.778551	-1.34219
S	1.726692	-7.77855	-1.34219
N	0	0	4.214025
N	0	0	1.393306
N	0.662083	6.144943	-0.63405
N	-0.66208	-6.14494	-0.63405
C	0.109898	1.141667	3.518918
C	0.229265	2.385941	4.230318
C	0.347672	3.563382	3.55794
C	0.359448	3.613081	2.114904
C	0.492252	4.842499	1.439075
C	0.508747	4.91121	0.0432
C	0.35511	3.700494	-0.68412
C	0.225081	2.490091	-0.03048
C	0.23363	2.405617	1.375836
C	0.110634	1.144269	2.081972
C	-0.11063	-1.14427	2.081972
C	-0.23363	-2.40562	1.375836
C	-0.22508	-2.49009	-0.03048
C	-0.35511	-3.70049	-0.68412
C	-0.50875	-4.91121	0.0432
C	-0.49225	-4.8425	1.439075
C	-0.35945	-3.61308	2.114904
C	-0.34767	-3.56338	3.55794
C	-0.22927	-2.38594	4.230318
C	-0.1099	-1.14167	3.518918
C	0.456721	6.253753	-2.04524
C	1.355013	5.691441	-2.96048
C	1.117347	5.79218	-4.33185
C	0	6.491315	-4.80024
C	-0.86796	7.107199	-3.89762
C	-0.64349	6.985836	-2.52138
C	-0.47904	8.252838	-0.15509
C	-0.55952	9.474693	0.523234
C	0.436247	9.83069	1.433682
C	1.535046	8.988649	1.635336
C	1.627366	7.781013	0.942349
C	0.604357	7.387905	0.07098
C	-0.45672	-6.25375	-2.04524
C	-1.35501	-5.69144	-2.96048
C	-1.11735	-5.79218	-4.33185
C	0	-6.49132	-4.80024
C	0.867959	-7.1072	-3.89762
C	0.643485	-6.98584	-2.52138
C	0.47904	-8.25284	-0.15509
C	0.559524	-9.47469	0.523234
C	-0.43625	-9.83069	1.433682
C	-1.53505	-8.98865	1.635336
C	-1.62737	-7.78101	0.942349
C	-0.60436	-7.38791	0.07098
H	0.221415	2.342971	5.314911
H	0.437903	4.49822	4.105129
H	0.570309	5.743604	2.034323
H	0.324243	3.71676	-1.76554
H	0.107327	1.577425	-0.60385
H	-0.10733	-1.57743	-0.60385
H	-0.32424	-3.71676	-1.76554
H	-0.57031	-5.7436	-2.034323
H	-0.4379	-4.49822	4.105129
H	-0.22142	-2.34297	5.314911
H	2.227193	5.165142	-2.58575
H	1.810298	5.337108	-5.03289
H	-0.18211	6.579496	-5.86698
H	-1.71344	7.687405	-4.25468
H	-1.39346	10.14251	0.329597
H	0.366614	10.77511	1.964815
H	2.325525	9.277271	2.321351
H	2.481835	7.125949	1.079763
H	-2.22719	-5.16514	-2.58575
H	-1.8103	-5.33711	-5.03289
H	0.182107	-6.5795	-5.86698
H	1.713439	-7.68741	-4.25468
H	1.393456	-10.1425	0.329597
H	-0.36661	-10.7751	1.964815
H	-2.32553	-9.27727	2.321351
H	-2.48184	-7.12595	1.079763

Table 8. Cartesian Coordinates of the Optimized Structure of Axial-Axial Conformer (*anti*) of **9**

atom	x	y	z
S	-1.72669	7.778551	-1.34219
S	1.726692	-7.77855	-1.34219
N	0	0	4.214025
N	0	0	1.393306
N	0.662083	6.144943	-0.63405
N	-0.66208	-6.14494	-0.63405
C	0.109898	1.141667	3.518918
C	0.229265	2.385941	4.230318
C	0.347672	3.563382	3.55794
C	0.359448	3.613081	2.114904
C	0.492252	4.842499	1.439075
C	0.508747	4.91121	0.0432
C	0.35511	3.700494	-0.68412
C	0.225081	2.490091	-0.03048
C	0.23363	2.405617	1.375836
C	0.110634	1.144269	2.081972
C	-0.11063	-1.14427	2.081972
C	-0.23363	-2.40562	1.375836
C	-0.22508	-2.49009	-0.03048
C	-0.35511	-3.70049	-0.68412
C	-0.50875	-4.91121	0.0432
C	-0.49225	-4.8425	1.439075
C	-0.35945	-3.61308	2.114904
C	-0.34767	-3.56338	3.55794
C	-0.22927	-2.38594	4.230318
C	-0.1099	-1.14167	3.518918
C	0.456721	6.253753	-2.04524
C	1.355013	5.691441	-2.96048
C	1.117347	5.79218	-4.33185
C	0	6.491315	-4.80024
C	-0.86796	7.107199	-3.89762
C	-0.64349	6.985836	-2.52138
C	-0.47904	8.252838	-0.15509
C	-0.55952	9.474693	0.523234
C	0.436247	9.83069	1.433682
C	1.535046	8.988649	1.635336
C	1.627366	7.781013	0.942349
C	0.604357	7.387905	0.07098
C	-0.45672	-6.25375	-2.04524
C	-1.35501	-5.69144	-2.96048
C	-1.11735	-5.79218	-4.33185
C	0	-6.49132	-4.80024
C	0.867959	-7.1072	-3.89762
C	0.643485	-6.98584	-2.52138
C	0.47904	-8.25284	-0.15509
C	0.559524	-9.47469	0.523234
C	-0.43625	-9.83069	1.433682
C	-1.53505	-8.98865	1.635336
C	-1.62737	-7.78101	0.942349
C	-0.60436	-7.38791	0.07098
H	0.221415	2.342971	5.314911
H	0.437903	4.49822	4.105129
H	0.570309	5.743604	2.034323
H	0.324243	3.71676	-1.76554
H	0.107327	1.577425	-0.60385
H	-0.10733	-1.57743	-0.60385
H	-0.32424	-3.71676	-1.76554
H	-0.57031	-5.7436	2.034323
H	-0.4379	-4.49822	4.105129
H	-0.22142	-2.34297	5.314911
H	2.227193	5.165142	-2.58575
H	1.810298	5.337108	-5.03289
H	-0.18211	6.579496	-5.86698
H	-1.71344	7.687405	-4.25468
H	-1.39346	10.14251	0.329597
H	0.366614	10.77511	1.964815
H	2.325525	9.277271	2.321351
H	2.481835	7.125949	1.079763
H	-2.22719	-5.16514	-2.58575
H	-1.8103	-5.33711	-5.03289
H	0.182107	-6.5795	-5.86698
H	1.713439	-7.68741	-4.25468
H	1.393456	-10.1425	0.329597
H	-0.36661	-10.7751	1.964815
H	-2.32553	-9.27727	2.321351
H	-2.48184	-7.12595	1.079763

Table 9. Cartesian Coordinates of the Initial Structure of Equatorial-Axial Conformer of **9**

atom	x	y	z
S	-7.654	-1.77057	-1.78935
S	9.202876	-0.83293	-0.09511
N	-0.10524	4.253314	-0.26271
N	-0.02688	1.44769	0.029132
N	-6.14016	-0.70099	0.536777
N	6.202286	-0.39874	-0.0259
C	-1.22905	3.534164	-0.14659
C	-2.49734	4.211304	-0.17387
C	-3.65846	3.51485	-0.05452
C	-3.67084	2.08022	0.105815
C	-4.88615	1.384342	0.235065
C	-4.92062	-0.00456	0.395561
C	-3.68315	-0.70246	0.392407
C	-2.4857	-0.02798	0.266117
C	-2.43877	1.372596	0.129395
C	-1.19436	2.103908	0.004326
C	1.100397	2.161887	-0.089
C	2.386516	1.482995	-0.06846
C	2.486517	0.08324	0.067319
C	3.721823	-0.53982	0.082526
C	4.9043	0.22351	-0.03677
C	4.825014	1.599186	-0.17039
C	3.575048	2.255691	-0.19019
C	3.488134	3.686641	-0.33285
C	2.287732	4.325471	-0.35539
C	1.061163	3.586875	-0.23527
C	-7.39931	-0.04942	0.344283
C	-7.8598	0.932619	1.228839
C	-9.08269	1.563432	1.002079
C	-9.87375	1.189228	-0.08728
C	-9.4514	0.169549	-0.93948
C	-8.21457	-0.44681	-0.7274
C	-6.87803	-2.77135	-0.52833
C	-6.95944	-4.16649	-0.56732
C	-6.3556	-4.92515	0.434849
C	-5.7087	-4.29122	1.498827
C	-5.64915	-2.89902	1.552581
C	-6.19917	-2.13016	0.52039
C	6.684717	-0.96813	-1.23479
C	5.835116	-1.21541	-2.32504
C	6.329653	-1.76393	-3.50899
C	7.675319	-2.10602	-3.62559
C	8.529039	-1.87537	-2.54643
C	8.049531	-1.2889	-1.37424
C	8.146479	-1.04719	1.323497
C	8.712435	-1.41947	2.543724
C	7.940173	-1.44759	3.70537
C	6.588083	-1.12039	6.327022
C	6.006371	-0.78733	2.40314
C	6.773274	-0.74619	1.227645
H	-2.48435	5.29024	-0.29295
H	-4.61272	4.035449	-0.077
H	-5.80583	1.954667	0.194652
H	-3.67075	-1.78144	0.475292
H	-1.55318	-0.58186	0.263853
H	1.573571	-0.4945	0.158016
H	3.793757	-1.61863	0.185106
H	5.740039	2.177238	-0.26176
H	4.413117	4.249891	-0.42412
H	2.212719	5.403018	-0.4636
H	-7.2465	1.204078	2.082492
H	-9.42314	2.336336	1.684869
H	-10.831	1.672466	-0.25968
H	-10.0793	-0.15606	-1.76359
H	-7.49927	-4.65052	-1.37584
H	-6.41221	-6.0091	0.396942
H	-5.26279	-4.87908	2.29571
H	-5.1653	-2.39691	2.384696
H	4.782891	-0.96851	-2.25354
H	5.647098	-1.93157	-4.33746
H	8.060788	-2.5438	-4.54149
H	9.583273	-2.12917	-2.61469
H	9.770139	-1.66524	2.579794
H	8.393014	-1.71853	4.654383
H	5.968261	-1.13184	4.519254
H	4.950786	-0.54762	2.365357

Table 10. Cartesian Coordinates of the Optimized Structure of Equatorial-Axial Conformer of **9**

atom	x	y	z
S	-7.55176	-1.74085	-1.80972
S	9.197853	-0.87637	-0.09145
N	-0.12697	4.251893	-0.28345
N	-0.03682	1.451584	0.032917
N	-6.14304	-0.71499	0.607164
N	6.203205	-0.37342	-0.0282
C	-1.24834	3.531665	-0.15496
C	-2.51937	4.205242	-0.18141
C	-3.67819	3.505116	-0.04822
C	-3.68416	2.071031	0.125965
C	-4.89769	1.371488	0.269859
C	-4.9253	-0.01613	0.442303
C	-3.68609	-0.71105	0.43976
C	-2.49044	-0.03307	0.299275
C	-2.44955	1.367251	0.148575
C	-1.20718	2.102161	0.008723
C	1.087825	2.167707	-0.09702
C	2.377613	1.493678	-0.076
C	2.48464	0.094271	0.071856
C	3.723699	-0.52337	0.088345
C	4.902432	0.244254	-0.04147
C	4.816932	1.618324	-0.18755
C	3.562801	2.2702	-0.20924
C	3.469843	3.700425	-0.36514
C	2.265968	4.33543	-0.38878
C	1.042822	3.59217	-0.256
C	-7.39913	-0.06928	0.374156
C	-7.90103	0.890966	1.26033
C	-9.11552	1.524988	0.994708
C	-9.85448	1.17596	-0.14071
C	-9.39027	0.17782	-0.98926
C	-8.16158	-0.44294	-0.7444
C	-6.81745	-2.76386	-0.54262
C	-6.87923	-4.16005	-0.62081
C	-6.312	-4.93812	0.389277
C	-5.72204	-4.32483	1.499488
C	-5.68077	-2.93284	1.589402
C	-6.19385	-2.14432	0.552835
C	6.676889	-0.95972	-1.23293
C	5.825595	-1.18604	-2.32802
C	6.310213	-1.75178	-3.5095
C	7.64776	-2.13044	-3.61898
C	8.503049	-1.91737	-2.53587
C	8.034896	-1.31407	-1.36627
C	8.135272	-1.05306	1.325939
C	8.693219	-1.42479	2.551317
C	7.923366	-1.41644	3.716372
C	6.580108	-1.05094	6.336777
C	6.00477	-0.7184	2.408246
C	6.769063	-0.71832	1.228824
H	-2.51056	5.282778	-0.31055
H	-4.63355	4.023029	-0.07018
H	-5.81955	1.93811	0.232224
H	-3.66929	-1.78883	0.534124
H	-1.5564	-0.5836	0.297383
H	1.574903	-0.48665	0.171133
H	3.800178	-1.60067	0.200259
H	5.729975	2.197954	-0.28705
H	4.39141	4.26716	-0.46561
H	2.186002	5.411339	-0.50663
H	-7.32483	1.142503	2.145161
H	-9.48976	2.280133	1.679092
H	-10.8042	1.660897	-0.34484
H	-9.97975	-0.1287	-1.857
H	-7.3765	-4.62948	-1.46414
H	-6.3541	-6.02091	0.321364
H	-5.30611	-4.9286	2.300174
H	-5.23951	-2.44488	2.45277
H	4.780998	-0.90867	-2.2647
H	5.627541	-1.90187	-4.34057
H	8.025261	-2.58199	-4.53093
H	9.550127	-2.19898	-2.59883
H	9.743361	-1.69946	2.588402
H	8.370676	-1.68807	4.667245
H	5.963281	-1.0299	4.530301
H	4.957597	-0.44614	2.372039

Table 11. Cartesian Coordinates of the Initial Structure of Equatorial-Equatorial Conformer of **9**

atom	x	y	z
N	0.06101	4.307628	0
N	0.017664	1.490045	0
C	0.062068	4.327549	-2.3953
C	0.05258	3.65402	-3.57761
C	0.030659	2.212679	-3.62621
C	0.021447	1.525146	-4.86065
C	0.000237	0.141051	-4.90403
C	-0.01224	-0.59888	-3.70111
C	-0.00338	0.054197	-2.48009
C	0.01807	1.463438	-2.41688
C	0.028289	2.177248	-1.14852
C	0.050408	3.613245	-1.14732
C	0.062068	4.327549	2.395303
C	0.05258	3.65402	3.577607
C	0.030659	2.212679	3.626206
C	0.021447	1.525146	4.860647
C	0.000237	0.141051	4.904026
C	-0.01224	-0.59888	3.701114
C	-0.00338	0.054197	2.480089
C	0.01807	1.463438	2.416878
C	0.028289	2.177248	1.148522
C	0.050408	3.613245	1.147325
H	0.078799	5.411603	-2.35056
H	0.061632	4.19853	-4.51783
H	0.031143	2.083783	-5.79193
H	-0.02847	-1.68358	-3.74469
H	-0.01262	-0.50714	-1.5529
H	0.078799	5.411603	2.350558
H	0.061632	4.19853	4.517826
H	0.031143	2.083783	5.791929
H	-0.02847	-1.68358	3.744694
H	-0.01262	-0.50714	1.5529
C	1.223791	-1.01512	-6.68884
C	-1.25199	-0.97598	-6.69431
C	2.362706	-1.13165	-5.87408
C	-2.39779	-1.05627	-5.88481
C	3.566868	-1.61763	-6.38875
H	2.316222	-0.83142	-4.83494
C	2.531643	-1.9179	-8.53872
C	-3.61448	-1.5035	-6.40511
H	-2.34659	-0.75766	-4.84543
C	-2.57953	-1.83645	-8.55038
C	3.657622	-2.02343	-7.71959
H	4.431006	-1.68437	-5.73452
H	2.579286	-2.22238	-9.58014
C	-3.71203	-1.90612	-7.73644
H	-4.48332	-1.54263	-5.75488
H	-2.63211	-2.13914	-9.59209
H	4.587934	-2.41378	-8.11974
H	-4.65247	-2.26657	-8.14094
N	-0.00758	-0.51332	-6.18561
C	-1.25199	-0.97598	6.694313
C	1.223791	-1.01512	6.68884
C	-2.39779	-1.05627	5.884809
C	2.362706	-1.13165	5.874083
C	-3.61448	-1.5035	6.405111
H	-2.34659	-0.75766	4.845431
C	-2.57953	-1.83645	8.550378
C	3.566868	-1.61763	6.388745
H	2.316222	-0.83142	4.834936
C	2.531643	-1.9179	8.538719
C	-3.71203	-1.90612	7.73644
H	-4.48332	-1.54263	5.754884
H	-2.63211	-2.13914	9.592086
C	3.657622	-2.02343	7.719592
H	4.431006	-1.68437	5.734516
H	2.579286	-2.22238	9.580142
H	-4.65247	-2.26657	8.140937
H	4.587934	-2.41378	8.119741
N	-0.00758	-0.51332	6.185606
C	1.335854	-1.39386	-8.04208
C	-1.36991	-1.35088	-8.04816
S	-0.00996	-1.08682	-9.16615
C	-1.36991	-1.35088	8.048162
C	1.335854	-1.39386	8.042083
S	-0.00996	-1.08682	9.166151

Table 12. Cartesian Coordinates of the Optimized Structure of Equatorial-Equatorial Conformer of **9**

atom	x	y	z
N	-4.30808	0.002601	0
N	-1.49014	0.000735	0
C	-4.32797	0.002661	2.395281
C	-3.65443	0.002272	3.577618
C	-2.21291	0.001331	3.626233
C	-1.52531	0.000959	4.860656
C	-0.14107	0.000036	4.904038
C	0.599002	-0.00054	3.701152
C	-0.05413	-0.00017	2.48011
C	-1.46354	0.000766	2.416894
C	-2.17743	0.001196	1.148524
C	-3.61358	0.002148	1.14731
C	-4.32797	0.002661	-2.39528
C	-3.65443	0.002272	-3.57762
C	-2.21291	0.001331	-3.62623
C	-1.52531	0.000959	-4.86066
C	-0.14107	0.000036	-4.90404
C	0.599002	-0.00054	-3.70115
C	-0.05413	-0.00017	-2.48011
C	-1.46354	0.000766	-2.41689
C	-2.17743	0.001196	-1.14852
C	-3.61358	0.002148	-1.14731
H	-5.41215	0.003379	2.350557
H	-4.19899	0.002673	4.51785
H	-2.08403	0.001395	5.791947
H	1.683815	-0.00126	3.744801
H	0.507311	-0.00059	1.552941
H	-5.41215	0.003379	-2.35056
H	-4.19899	0.002673	-4.51785
H	-2.08403	0.001395	-5.79195
H	1.683815	-0.00126	-3.7448
H	0.507311	-0.00059	-1.55294
C	0.994729	-1.23866	6.691645
C	0.996418	1.237482	6.691458
C	1.092367	-2.38126	5.879536
C	1.095604	2.379835	5.879188
C	1.557896	-3.59226	6.39708
H	0.793079	-2.33216	4.840242
C	1.875235	-2.55724	8.544694
C	1.5628	3.590274	6.39655
H	0.796239	2.331	4.839906
C	1.878743	2.555129	8.544308
C	1.961838	-3.68676	7.728222
H	1.610103	-4.45894	5.744906
H	2.178775	-2.60755	9.586264
C	1.966886	3.684409	7.727673
H	1.616186	4.456792	5.744251
H	2.182358	2.605182	9.58587
H	2.336332	-4.62259	8.130644
H	2.342664	4.619784	8.129957
N	0.513385	-0.0003	6.1856
C	0.996418	1.237482	-6.69146
C	0.994729	-1.23866	-6.69165
C	1.095604	2.379835	-5.87919
C	1.092367	-2.38126	-5.87954
C	1.5628	3.590274	-6.39655
H	0.796239	2.331	-4.83991
C	1.878743	2.555129	-8.54431
C	1.557896	-3.59226	-6.39708
H	0.793079	-2.33216	-4.84024
C	1.875235	-2.55724	-8.54469
C	1.966886	3.684409	-7.72767
H	1.616186	4.456792	-5.74425
H	2.182358	2.605182	-9.58587
C	1.961838	-3.68676	-7.72822
H	1.610103	-4.45894	-5.74491
H	2.178775	-2.60755	-9.58626
H	2.342664	4.619784	-8.12996
H	2.336332	-4.62259	-8.13064
N	0.513385	-0.0003	-6.1856
C	1.371825	-1.35386	8.045097
C	1.373679	1.352371	8.044892
S	1.088027	-0.00047	9.166195
C	1.373679	1.352371	-8.04489
C	1.371825	-1.35386	-8.0451
S	1.088027	-0.00047	-9.1662

Table 13. Selected Excitation Energies and Oscillator Strength (f) of the Conformers of **9**^a

	Axial-Axial (<i>syn</i>)	Axial-Axial (<i>anti</i>)	Equatorial-Axial	Equatorial-Equatorial
λ [nm] (f)	439.04 (0.5653)	439.84 (0.5688)	538.22 (0.0001)	596.35 (0)
transition mode	H→L (95%)	H→L (95%)	H→L (99%)	H→L (99%)
λ [nm] (f)	354.80 (0.1493)	355.13 (0.1599)	449.23 (0.3059)	389.79 (0.3807)
transition mode	H-2→L (48%)	H-2→L (46%)	H-1→L (97%)	H-4→L (90%)
λ [nm] (f)	339.81 (0.6522)	340.28 (0.6491)	348.29 (0.5908)	377.05 (0.0214)
transition mode	H-1→L+1 (37%)	H-1→L+1 (36%)	H-1→L+1 (66%)	H-5→L (94%)
λ [nm] (f)	338.43 (0.1207)	338.79 (0.1211)	305.77 (0.1559)	317.19 (0.0216)
transition mode	H-3→L (50%)	H-3→L (50%)	H-1→L+5 (22%)	H-6→L (50%)
λ [nm] (f)				315.23 (0.0255)
transition mode				H-11→L (57%)

^a The coefficient percentages of orbitals involved in the transitions are shown in parentheses.

Time-Resolved Photoluminescence Analysis (Figures 20, 21 and 22)

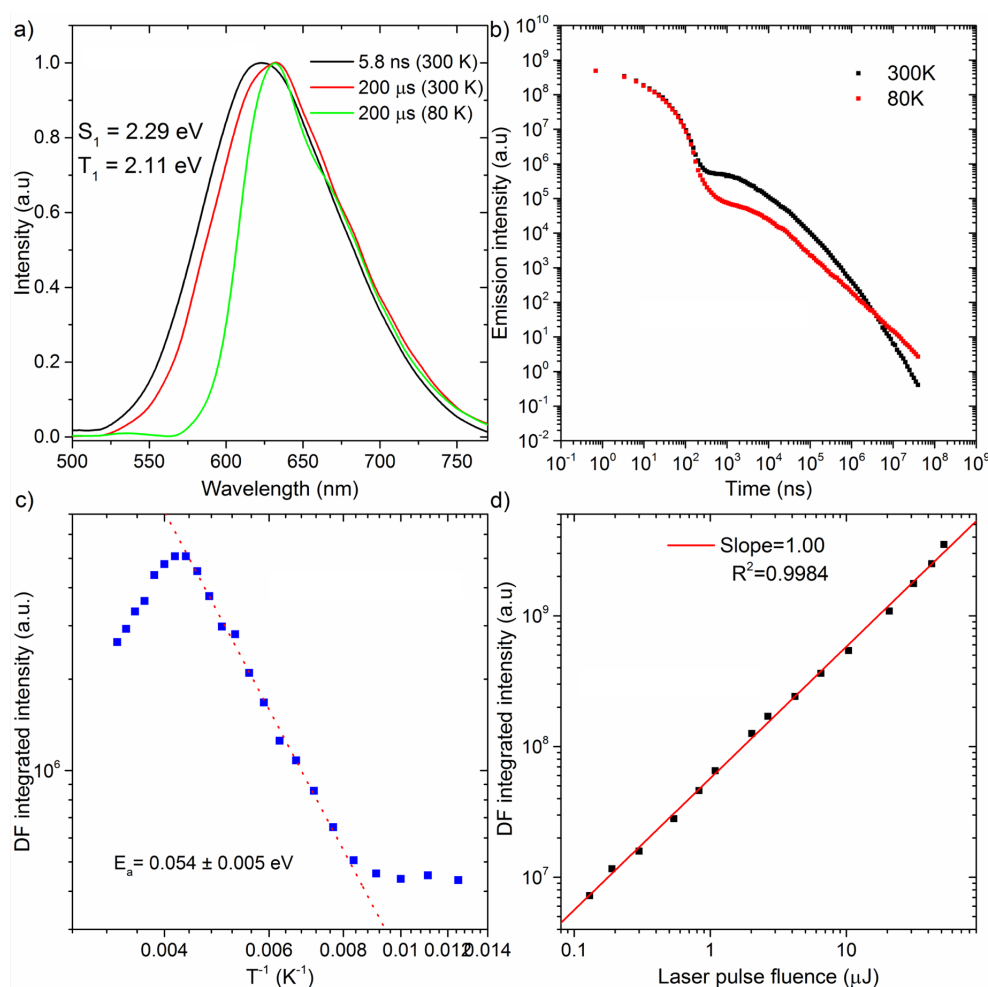


Figure 20. a) PF, DF and PH Spectra of 10 wt% **10**:CBP Blended Film. b) Transient Decays of 10 wt% **10**:CBP Blended Film at 300K and 80K. c) Temperature Dependence of Delayed Fluorescence of 10 wt% **10**:CBP Blended Film. d) Power Dependence of Delayed Fluorescence of 10 wt% **10**:CBP Blended Film at 300K.

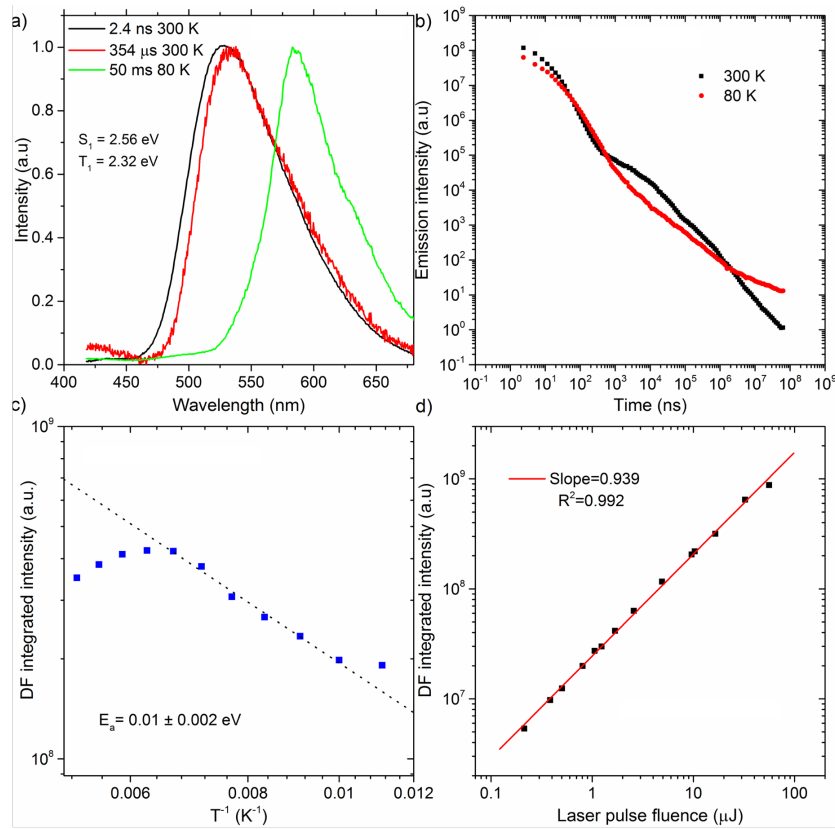


Figure 21. a) PF, DF and PH Spectra of 10 wt% 11:CBP Blended Film. b) Transient Decays of 10 wt% 11:CBP Blended Film at 300K and 80K. c) Temperature Dependence of Delayed Fluorescence of 10 wt% 11:CBP Blended Film. d) Power Dependence of Delayed Fluorescence of 10 wt% 11:CBP Blended Film.

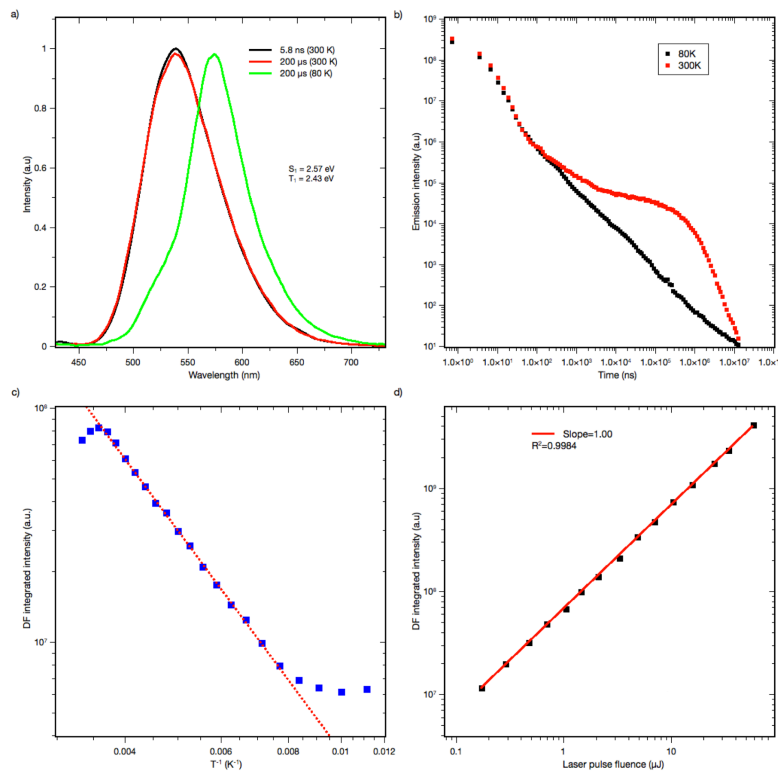


Figure 22. a) PF, DF and PH Spectra of 10 wt% 12:CBP Blended Film. b) Transient Decays of 10 wt% 12:CBP Blended Film at 300K and 80K. c) Temperature Dependence of Delayed Fluorescence of 10 wt% 12:CBP Blended Film. d) Power Dependence of Delayed Fluorescence of 10 wt% 12:CBP Blended Film.

Thermogravimetric Analysis (TGA) (Figure 23)

The TGA profiles of solid samples 9–12 were recorded under the N₂ gas flow (200 mL/min), starting from 40 °C to 800 °C at the ramp rate of 10 °C/min.

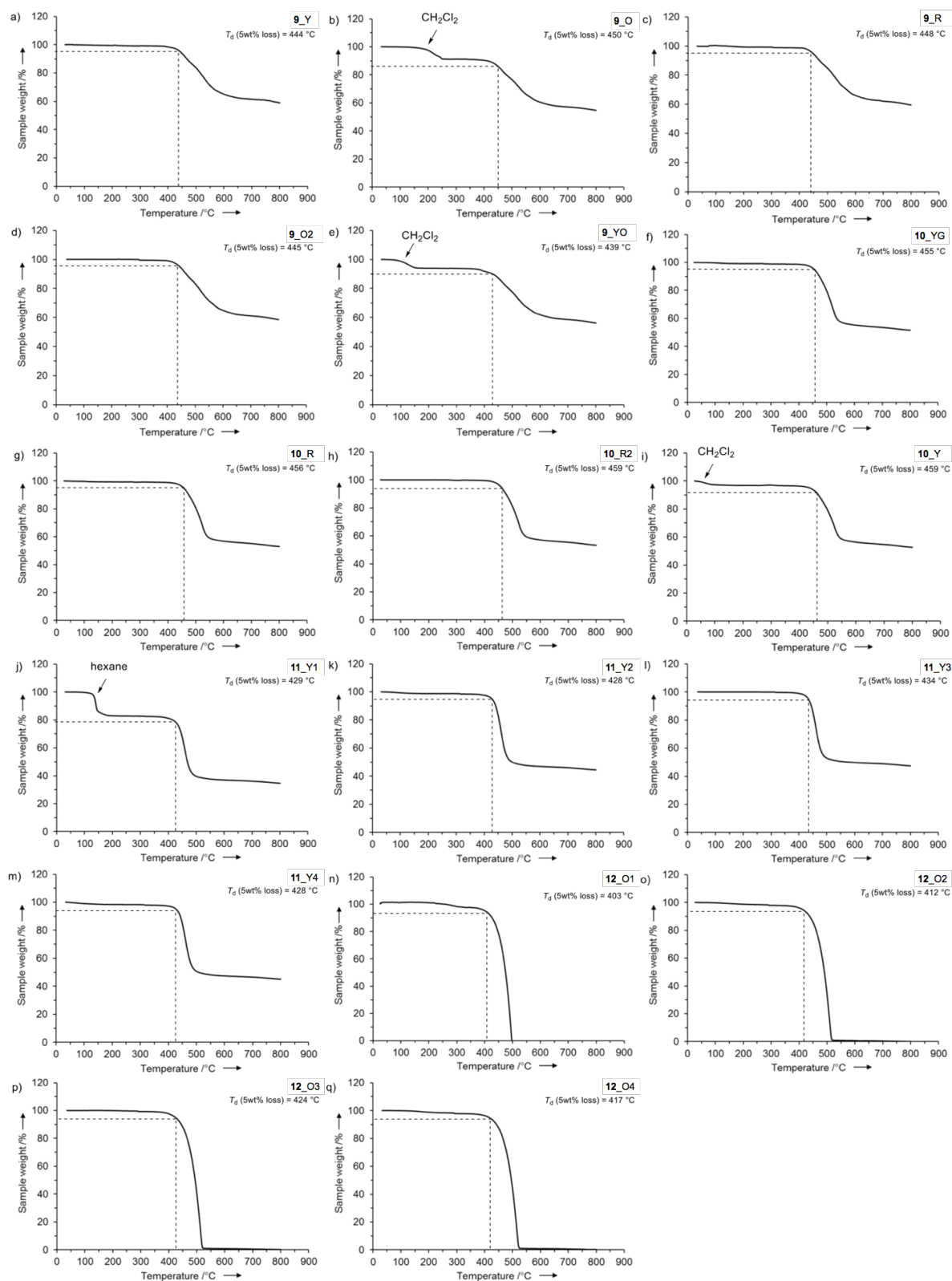


Figure 23. TGA Profiles of 9–12

Cyclic Voltammograms (Figure 24)

CV experiments were conducted at room temperature using degassed CH_2Cl_2 solutions of **9–12** (concentration: 1.0×10^{-3} M) containing 0.1 M $n\text{-Bu}_4\text{PF}_6$ as a supporting electrolyte in a cell equipped with a Pt as the working electrode (scanning rate: 100 mV/s). A Pt and Ag wires were applied as the counter and the reference electrode, respectively. The HOMO/LUMO energy levels were calculated by the following equation using the onset potentials corrected against the Fc/Fc^+ (Fc = ferrocene) couple: $E_{\text{HOMO}} = -(5.1 + {}^{\text{ox}}E_{\text{onset}})$ [eV]; $E_{\text{LUMO}} = -(5.1 + {}^{\text{red}}E_{\text{onset}} \text{ vs. } \text{Fc}/\text{Fc}^+)$ [eV].^{36–39}

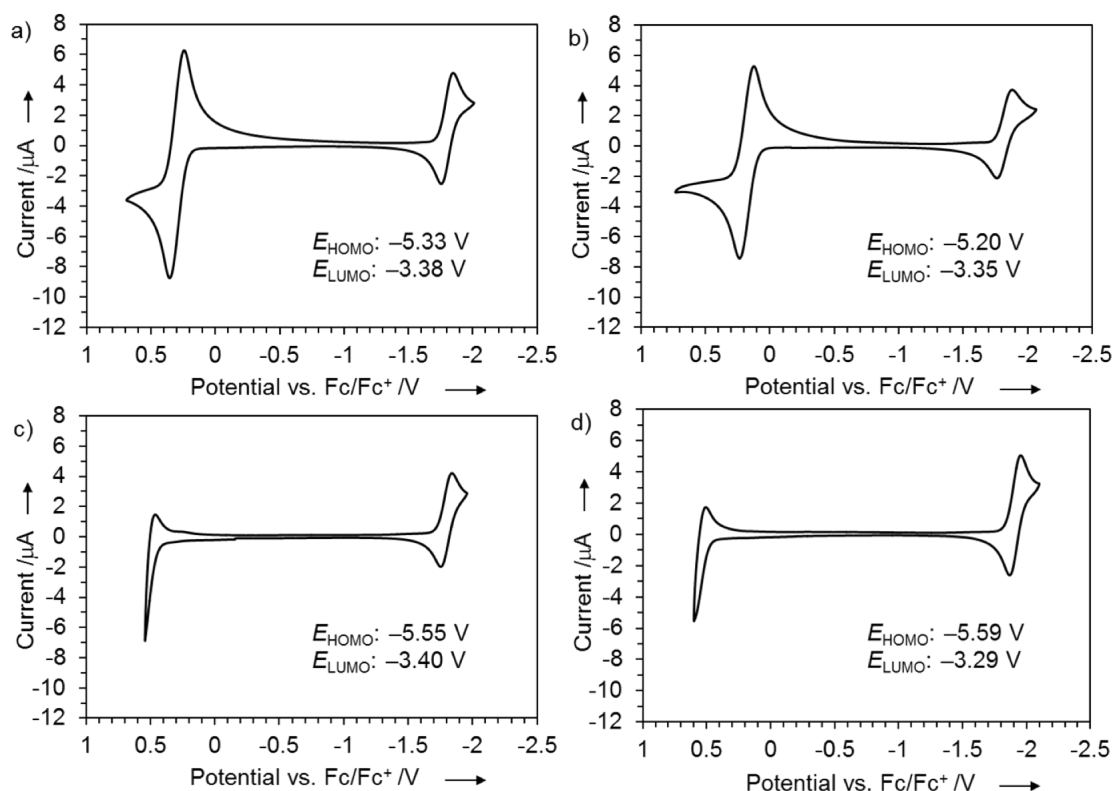


Figure 24. Cyclic Voltammograms of a) **9**, b) **10**, c) **11**, and d) **12**

3-13. References and Notes

1. Sagara, Y.; Yamane, S.; Mitani, M.; Weder C.; Kato, T. *Adv. Mater.* **2016**, *28*, 1073–1095.
2. (a) Sagara, Y.; Kato, T.; *Nat. Chem.* **2009**, *1*, 605–610. (b) Pucci, A.; Bizzarri R.; Giacomo, R. *Soft Matter* **2011**, *7*, 3689–3700. (c) Chi, Z.; Zhang, X.; Xu, B.; Zhou, X.; Ma, C.; Zhang, Y.; Liu, S.; Xu, J. *Chem. Soc. Rev.* **2012**, *41*, 3878–3896. (d) Zhang, X.; Chi, Z.; Zhang, Y.; Liu, S.; Xu, J. *J. Mater. Chem. C* **2013**, *1*, 3376–3390.

3. (a) Sagara, Y.; Mutai, T.; Yoshikawa, I.; Araki, K. *J. Am. Chem. Soc.* **2007**, *129*, 1520–1521. (b) Kunzleman, J.; Kinami, M.; Crenshaw, B. R.; Protasiewicz, J. D.; Weder, C. *Adv. Mater.* **2008**, *20*, 119–122. (c) Ooyama, Y.; Kagawa, Y.; Fukuoka, H.; Ito, G.; Harima, Y. *Eur. J. Org. Chem.* **2009**, 5321–5326. (d) Zhang, G.; Lu, J.; Sabat, M.; Fraser, C. L. *J. Am. Chem. Soc.* **2010**, *132*, 2160–2162.
4. (a) Mizukami, S.; Houjou, H.; Sugaya, K.; Koyama, E.; Tokuhisa, H.; Sasaki, T.; Kanamoto, M. *Chem. Mater.* **2005**, *17*, 50–56. (b) Ito, H.; Saito, T.; Oshima, N.; Kitamura, N.; Ishizaka, S.; Hinatsu, Y.; Wakeshima, M.; Kato, M.; Tsuge, K.; Sawamura, M. *J. Am. Chem. Soc.* **2008**, *130*, 10044–10045.
5. (a) Sagara, Y.; Kato, T. *Angew. Chem., Int. Ed.* **2008**, *47*, 5175–5178. (b) Kozhevnikov, V. N.; Donnio, B.; Bruce, D. W. *Angew. Chem., Int. Ed.* **2008**, *47*, 6286–6289. (c) Sagara, Y.; Yamane, S.; Mutai, T.; Araki, K.; Kato, T. *Adv. Funct. Mater.* **2009**, *19*, 1869–1875.
6. Ma, Z.; Wang, Z.; Teng, M.; Xu, Z.; Jia, X. *ChemPhysChem* **2015**, *16*, 1811–1828.
7. (a) Sagara, Y.; Kato, T. *Angew. Chem., Int. Ed.* **2011**, *50*, 9128–9132. (b) Luo, X.; Zhao, W.; Shi, J.; Li, C.; Liu, Z.; Bo, Z.; Dong, Y. Q.; Tang, B. Z. *J. Phys. Chem. C* **2012**, *116*, 21967–21972. (c) Dong, Y.; Xu, B.; Zhang, J.; Tan, X.; Wang, L.; Chen, J.; Lv, H.; Wen, S.; Li, B.; Ye, L.; Zou, B.; Tian, W. *Angew. Chem., Int. Ed.* **2012**, *51*, 10782–10785. (d) Choi, S. J.; Kuwabara, J.; Nishimura, Y.; Arai, T.; Kanbara, T. *Chem. Lett.* **2012**, *41*, 65–67. (e) Nagura, K.; Saito, S.; Yusa, H.; Yamawaki, H.; Fujihisa, H.; Sato, H.; Shimoikeda, Y.; Yamaguchi, S. *J. Am. Chem. Soc.* **2013**, *135*, 10322–10325. (f) Ma, Z.; Teng, M.; Wang, Z.; Yang, S.; Jia, X. *Angew. Chem., Int. Ed.* **2013**, *52*, 12268–12272. (g) Yagai, S.; Okamura, S.; Nakano, Y.; Yamauchi, M.; Kishikawa, K.; Karatsu, T.; Kitamura, A.; Ueno, A.; Kuzuhara, D.; Yamada, H.; Seki, T.; Ito, H. *Nat. Commun.* **2014**, *5*, 4013. (h) Seki, T.; Ozaki, T.; Okura, T.; Asakura, K.; Sakon, A.; Uekusa, H.; Ito, H. *Chem. Sci.* **2015**, *6*, 2187–2195. (i) Zhang, Y.; Wang, K.; Zhuang, G.; Xie, Z.; Zhang, C.; Cao, F.; Pan, G.; Chen, H.; Zou, B.; Ma, Y. *Chem. Eur. J.* **2015**, *21*, 2474–2479.
8. (a) Kim, H.-J.; Whang, D. R.; Gierschner, J.; Lee, C. H.; Park, Y. *Angew. Chem., Int. Ed.* **2015**, *54*, 4330–4333. (b) Matsunaga, Y.; Yang, J.-S. *Angew. Chem., Int. Ed.*

- 2015**, *54*, 7985–7989. (c) Park, S. K.; Cho, I.; Gierschner, J.; Kim, J. H.; Kim, J. H.; Kwon, J. E.; Kwon, O. K.; Whang, D. R.; Park, J.-H.; An, B.-K.; Park, S. Y. *Angew. Chem., Int. Ed.* **2016**, *55*, 203–207.
9. Parker, C. A.; Hatchard, C. G. *Trans. Faraday Soc.* **1961**, *57*, 1894–1904.
10. Tao, Y.; Yuan, K.; Chen, T.; Xu, P.; Li, H.; Chen, R.; Zheng, C.; Zhang, L.; Huang, W. *Adv. Mater.* **2014**, *26*, 7931–7958.
11. Uoyama, H.; Goushi, K.; Shizu, K.; Nomura, H.; Adachi, C. *Nature* **2012**, *492*, 234–238.
12. Nakanotani, H.; Higuchi, T.; Furukawa, T.; Masui, K.; Morimoto, K.; Numata, M.; Tanaka, H.; Sagara, Y.; Yasuda, T.; Adachi, C. *Nat. Commun.* **2014**, *5*, 4016.
13. Ishimatsu, R.; Matsunami, S.; Kasahara, T.; Mizuno, J.; Edura, T.; Adachi, C.; Nakano, K.; Imato, T. *Angew. Chem., Int. Ed.* **2014**, *53*, 6993–6996.
14. Xiong, X.; Song, F.; Wang, J.; Zhang, Y.; Xue, Y.; Sun, L.; Jiang, N.; Gao, P.; Tian, L.; Peng, X. *J. Am. Chem. Soc.* **2014**, *136*, 9590–9597.
15. (a) Dias, F. B.; Bourdakos, K. N.; Jankus, V.; Moss, K. C.; Kamtekar, K. T.; Bhalla, V.; Santos, J.; Bryce, M. R.; Monkman, A. P. *Adv. Mater.* **2013**, *25*, 3707–3714. (b) Jankus, V.; Data, P.; Graves, D.; McGuinness, C.; Santos, J.; Bryce, M. R.; Dias, F. B.; Monkman, A. P. *Adv. Funct. Mater.* **2014**, *24*, 6178–6186. (c) Santos, P. L.; Ward, J. S.; Data, P.; Batsanov, A. S.; Bryce, M. R.; Dias, F. B.; Monkman, A. P. *J. Mater. Chem. C* **2016**, *4*, 3815–3824.
16. Gibson, J.; Monkman, A. P.; Penfold, T. J. *ChemPhysChem* **2016**, *17*, 2956–2961.
17. (a) Endo, A.; Sato, K.; Yoshimura, K.; Kai, T.; Kawada, A.; Miyazaki, H.; Adachi, C. *Appl. Phys. Lett.* **2011**, *98*, 083302. (b) Méhes, G.; Nomura, H.; Zhang, Q.; Nakagawa, T.; Adachi, C. *Angew. Chem., Int. Ed.* **2012**, *51*, 11311–11315. (c) Zhang, Q.; Li, J.; Shizu, K.; Huang, S.; Hirata, S.; Miyazaki, H.; Adachi, C. *J. Am. Chem. Soc.* **2012**, *134*, 14706–14709. (d) Li, J.; Nakagawa, T.; MacDonald, J.; Zhang, Q.; Nomura, H.; Miyazaki, H.; Adachi, C. *Adv. Mater.* **2013**, *25*, 3319–3323. (e) Lee, J.; Shizu, K.; Tanaka, H.; Nomura, H.; Yasuda, T.; Adachi, C. *J. Mater. Chem. C* **2013**,

- I*, 4599–4604. (f) Lee, S. Y.; Yasuda, T.; Yang, Y. S.; Zhang, Q.; Adachi, C. *Angew. Chem., Int. Ed.* **2014**, *53*, 6402–6406. (g) Takahashi, T.; Shizu, K.; Yasuda, T.; Togashi, K.; Adachi, C. *Sci. Technol. Adv. Mater.* **2014**, *15*, 034202. (h) Lee, S. Y.; Yasuda, T.; Park, I. S.; Adachi, C. *Dalton Trans.* **2015**, *44*, 8356–8359. (i) Kaji, H.; Suzuki, H.; Fukushima, T.; Shizu, K.; Suzuki, K.; Kubo, S.; Komino, T.; Oiwa, H.; Suzuki, F.; Wakamiya, A.; Murata, Y.; Adachi, C. *Nat. Commun.* **2015**, *6*, 8476. (j) Suzuki, K.; Kubo, S.; Shizu, K.; Fukushima, T.; Wakamiya, A.; Murata, Y.; Adachi, C.; Kaji, H. *Angew. Chem., Int. Ed.* **2015**, *54*, 15231–15235.
18. (a) Cho, Y. J.; Jeon, S. K.; Chin, B. D.; Yu, E.; Lee, J. Y. *Angew. Chem., Int. Ed.* **2015**, *54*, 5201–5204. (b) Albrecht, K.; Matsuoka, K.; Fujita, K.; Yamamoto, K. *Angew. Chem., Int. Ed.* **2015**, *54*, 5677–5682. (c) Kawasumi, K.; Wu, T.; Zhu, T.; Chae, H. S.; Voorhis, T. V.; Baldo, M. A.; Swager, T. M. *J. Am. Chem. Soc.* **2015**, *137*, 11908–11911.
19. Ward, J. S.; Nobuyasu, R. S.; Batsanov, A. S.; Data, P.; Monkman, A. P.; Dias, F. B.; Bryce, M. R. *Chem. Commun.* **2016**, *52*, 2612–2615.
20. Selective synthesis of dibenzo[*a,j*]phenazines was described in Chapter 2.
21. Data, P.; Pander, P.; Okazaki, M.; Takeda, Y.; Minakata, S.; Monkman, A. P. *Angew. Chem., Int. Ed.* **2016**, *55*, 5739–5744.
22. (a) Xie, Z.; Chen, C.; Xu, S.; Li, J.; Zhang, Y.; Liu, S.; Xu, J.; Chi, Z. *Angew. Chem., Int. Ed.* **2015**, *54*, 7181–7184. (b) Rajamalli, P.; Senthilkumar, N.; Gandeepan, P.; Ren-Wu, C.-Z.; Lin, H.-W.; Cheng, C.-H. *J. Mater. Chem. C* **2016**, *4*, 900–904. (c) Xu, B.; Mu, Y.; Mao, Z.; Xie, Z.; Wu, H.; Zhang, Y.; Jin, C.; Chi, Z.; Liu, S.; Xu, J.; Wu, Y.-C.; Lu, P.-Y.; Lien, A.; Bryce, M. R. *Chem. Sci.* **2016**, *7*, 2201–2206.
23. (a) Daub, J.; Engl, R.; Kurzawa, J.; Miller, S. E.; Schneider, S.; Stockmann, A.; Wasielewski, M. R. *J. Phys. Chem. A* **2001**, *105*, 5655–5665. (b) Stockmann, A.; Kurzawa, J.; Fritz, N.; Acar, N.; Schneider, S.; Daub, J.; Engl, R.; Clark, T. *J. Phys. Chem. A* **2002**, *106*, 7958–7970. (c) Acar, N.; Kurzawa, J.; Fritz, N.; Stockmann, A.; Roman, C.; Schneider, S.; Clark, T. *J. Phys. Chem. A* **2003**, *107*, 9530–9541.

24. Tanaka, H.; Shizu, K.; Nakanotani, H.; Adachi, C. *J. Phys. Chem. C* **2014**, *118*, 15985–15994.
25. Shimizu, M.; Kaki, R.; Takeda, Y.; Hiyama, T.; Nagai, N.; Yamagishi, H.; Furutani, H. *Angew. Chem., Int. Ed.* **2012**, *51*, 4095–4000.
26. (a) Zhu, X.; Liu, R.; Li, Y.; Huang, H.; Wang, Q.; Wang, D.; Zhu, X.; Liu, S.; Zhu, H. *Chem. Commun.* **2014**, *50*, 12951–12954. (b) Qin, Z.; Wang, Y.; Lu, X.; Chen, Y.; Peng, J.; Zhou, G. *Chem. Asian J.* **2016**, *11*, 285–293.
27. For a summary of the crystal data of **9**_O, see the Experimental Section. CCDC 1452024 contains the supplementary crystallographic data for this thesis. These data are available free of charge from the Cambridge Crystallographic Data Center via www.ccdc.cam.ac.uk/data_request/cif.
28. The concentration effect of **9** could not be measured, because of its poor solubility in cyclohexane.
29. Yan, P.; Millard, A. C.; Wei, M.; Loew, L. M. *J. Am. Chem. Soc.* **2006**, *128*, 11030–11031.
30. Vilches-Herrera, M.; Miranda-Sepúlveda, J.; Rebolledo-Fuentes, M.; Fierro, A.; Lühr, S.; Iturriaga-Vasquez, P.; Cassels, B. K.; Reyes-Parada, M.; *Bioorg. Med. Chem.* **2009**, *17*, 2452–2460.
31. Kormos, A.; Móczár, I.; Sveiczter, A.; Baranyai, P.; Párkányi, L.; Tóth, K.; Huszthy, P. *Tetrahedron* **2012**, *68*, 7063–7069.
32. Andrew, T. L.; Swager, T. M. *J. Org. Chem.* **2011**, *76*, 2976–2993.
33. Ono, K.; Joho, M.; Saito, K.; Tomura, M.; Matsushita, Y.; Naka, S.; Okada, H.; Onnagawa, H. *Eur. J. Inorg. Chem.* **2006**, 3676–3683.
34. Altomare, A.; Cascarano, G.; Giacovazzo, C.; Guagliardi, A.; Burla, M.; Polidori, G.; Camalli, M. *J. Appl. Cryst.* **1994**, *27*, 435–436.
35. Gaussian 09, Revision A.02, Frisch, M. J.; Trucks, G. W.; Schlegel, H. B.; Scuseria, G. E.; Robb, M. A.; Cheeseman, J. R.; Scalmani, G.; Barone, V.; Mennucci, B.; Petersson, G.

- A.; Nakatsuji, H.; Caricato, M.; Li, X.; Hratchian, H. P.; Izmaylov, A. F.; Bloino, J.; Zheng, G.; Sonnenberg, J. L.; Hada, M.; Ehara, M.; Toyota, K.; Fukuda, R.; Hasegawa, J.; Ishida, M.; Nakajima, T.; Honda, Y.; Kitao, O.; Nakai, H.; Vreven, T.; Montgomery Jr., J. A.; Peralta, J. E.; Ogliaro, F.; Bearpark, M.; Heyd, J. J.; Brothers, E.; Kudin, K. N.; Staroverov, V. N.; Kobayashi, R.; Normand, J.; Raghavachari, K.; Rendell, A.; Burant, J. C.; Iyengar, S. S.; Tomasi, J.; Cossi, M.; Rega, N.; Millam, J. M.; Klene, M.; Knox, J. E.; Cross, J. B.; Bakken, V.; Adamo, C.; Jaramillo, J.; Gomperts, R.; Stratmann, R. E.; Yazyev, O.; Austin, A. J.; Cammi, R.; Pomelli, C.; Ochterski, J. W.; Martin, R. L.; Morokuma, K.; Zakrzewski, V. G.; Voth, G. A.; Salvador, P.; Dannenberg, J. J.; Dapprich, S.; Daniels, A. D.; Farkas, O.; Foresman, J. B.; Ortiz, J. V.; Cioslowski, J.; Fox, D. J. Gaussian, Inc., Wallingford CT, 2009.
36. Rybakiewicz, R.; Gawrys, P.; Tsikritzis, D.; Emmanouil, K.; Kennou, S.; Zagorska, M.; Pron, A. *Electrochim. Acta* **2013**, *96*, 13–17.
37. Trasatti, S. *Pure Appl. Chem.* **1986**, *58*, 955–966.
38. Data, P.; Motyka, R.; Lapkowski, M.; Suwinski, J.; Monkman, A. P. *J. Phys. Chem. C* **2015**, *119*, 20188–20200.
39. Bredas, J.-L. *Mater. Horiz.* **2014**, *1*, 17–19.

Conclusion

The present thesis deals with the synthesis of aza-PACs through three novel oxidative transformations of BINAMs and the applications of the resulting aza-PACs to functional emissive molecules. The results obtained through the studies are summarized as follows:

Chapter 1 describes the development of a facile synthetic method for 7,8-diaza[5]helicenes, which comprises of an oxidative ring-closing process of BINAMs with a chlorine-containing oxidant (*t*-BuOCl) in the presence of a base (2,6-lutidine). This method is applied to functionalized BINAMs to provide various diazahelicenes in a single-step. Furthermore, high electron-accepting abilities of the diazahelicenes are revealed from cyclic voltammetry experiments.

Chapter 2 describes two novel oxidative skeletal rearrangements of BINAMs with an iodine-containing oxidant (1,3-diiodo-5,5-dimethylhydantoin: DIH) to produce two aza-PACs, that are dibenzo[*a,j*]phenazines and spiro[benzo[*e*]indole-1,1'-inden]-2-amines, and their

applications to the creation of functional emissive molecules. One rearrangement involves the cleavage of a C–C single bond of the binaphthalene unit and the nitrogen migration to provide dibenzo[*a,j*]phenazines, and the other involves the ring-contractive and -closing skeletal rearrangement to give spiro[benzo[*e*]indole-1,1'-inden]-2-amines. Dibromo-substituted dibenzo[*a,j*]phenazine serves as a building block for the construction of π -extended emissive molecules. Especially, the dibenzo[*a,j*]phenazine-cored D–A–D molecules (D = amino groups) exhibit red-shifted and strong emission from the intramolecular charge-transfer (ICT) excited states. The resulting spiro[benzo[*e*]indole-1,1'-inden]-2-amine is transformed into the aggregation-induced emission enhancement (AIEE) -active BF₂ complex by taking advantage of the amidino functionality.

Chapter 3 describes the development of novel D-A-D π -conjugated multi-functional molecules comprising of dibenzo[*a,j*]phenazine as an acceptor and phenothiazines as donors. Most importantly, the D-A-D compounds exhibit not only distinct tricolor-changeable MCL properties but also efficient TADF. Quantum chemical calculations, X-ray diffraction analysis, and systematic studies on photophysical properties indicate that the “two-conformation-switchable” phenothiazine units play a highly important role in achieving multi-color-changing MCL. Time-resolved photophysical measurements reveal that developed D-A-D compound also exhibit efficient orange-TADF. Furthermore, OLED devices fabricated with the new TADF emitters achieve high EQEs up to 16.8%, which significantly exceeds theoretical maximum (~5%) with conventional fluorescent emitters.

The developments in Chapter 1 and 2 provide three novel oxidative transformations of BINAMs to produce three different aza-PACs, that are 7,8-diaza[5]helicenes, dibenzo[*a,j*]phenazines, and spiro[benzo[*e*]indole-1,1'-inden]-2-amines, depending on the reaction conditions such as (the equivalents of) a halogen-containing oxidant and reaction

temperature. These results indicate that BINAMs can serve as a platform for the synthesis of novel aza-PACs. Furthermore, making the use of developed aza-PAC scaffolds, functional emissive molecules are designed and created. The study on the physicochemical properties of the resulting aza-PACs contributes to the development of phenothiazine-dibenzo[*a,j*]phenazine-phenothiazine triads exhibiting tricolor-changing MCL and TADF properties in Chapter 3.

The findings obtained through this study as mentioned above would provide novel synthetic strategies for aza-PACs and design principles for the construction of functional emissive molecules that consist of aza-PAC scaffolds.

List of Publications

The content of this thesis has been published in the following papers.

- 1) Oxidative skeletal rearrangement of 1,1'-binaphthalene-2,2'-diamines (BINAMs) *via* C–C bond cleavage and nitrogen migration: a versatile synthesis of U-shaped azaacenes
Youhei Takeda, Masato Okazaki, and Satoshi Minakata
Chem. Commun. **2014**, 50, 10291–10294.
- 2) A facile synthesis of functionalized 7,8-diaza[5]helicenes through an oxidative ring-closure of 1,1'-binaphthalene-2,2'-diamines (BINAMs)
Youhei Takeda, Masato Okazaki, Yoshiaki Maruoka, and Satoshi Minakata
Beilstein J. Org. Chem. **2015**, 11, 9–15.
- 3) Ring-contractive and -closing skeletal rearrangement of 1,1'-binaphthalene-2,2'-diamines (BINAMs) induced by an iodine-containing oxidant: synthesis of spiro[benzo[*e*]indole-1,1'-inden]-2-amines and application to an AIEE-active BF₂ complex
Masato Okazaki, Kosuke Takahashi, Youhei Takeda, and Satoshi Minakata
Heterocycles, prepress. (DOI: 10.3987/COM-15-S(T)33)
- 4) Thermally activated delayed fluorescent phenothiazine-dibenzo[*a,j*]phenazine-phenothiazine triads exhibiting tricolor-changing mechanochromic luminescence
Masato Okazaki, Youhei Takeda, Przemyslaw Data, Piotr Pander, Heather Higginbotham, Andrew P. Monkman, and Satoshi Minakata
Chem. Sci., accepted. (DOI: 10.1039/C6SC04863C)

List of Supplementary Publication

- 1) Dibenzo[*a,j*]phenazine-cored donor–acceptor–donor compounds as green-to-red/NIR thermally activated delayed fluorescence organic light emitters
Przemyslaw Data, Piotr Pander, Masato Okazaki, Youhei Takeda, Satoshi Minakata, and Andrew P. Monkman
Angew. Chem., Int. Ed. **2016**, 55, 5739–5744.

Copyright

The author has obtained the permissions to reuse contents. The author wishes to express his thanks to Copyright Clearance Center, Creative Commons, Royal Society of Chemistry, Beilstein-Institut, and the Japan Institute of Heterocyclic Chemistry.

Credits

Reprinted with permission from Takeda, Y.; Okazaki, M.; Minakata, S. *Chem. Commun.* **2014**, *50*, 10291–10294. Copyright Royal Society of Chemistry.

Reprinted with permission from Takeda, Y.; Okazaki, M.; Maruoka, Y.; Minakata, S. *Beilstein J. Org. Chem.* **2015**, *11*, 9–15. Copyright Beilstein-Institut.

Reprinted with permission from Okazaki, M.; Takahashi, K.; Takeda, Y.; Minakata, S. *Heterocycles*, prepress. (DOI: 10.3987/COM-15-S(T)33). Copyright the Japan Institute of Heterocyclic Chemistry.

Reprinted with permission from Okazaki, M.; Takeda, Y.; Data, P.; Pander, P.; Higginbotham, H.; Monkman, A. P.; Minakata, S. *Chem. Sci.* (DOI: 10.1039/C6SC04863C). Copyright Royal Society of Chemistry.

Acknowledgement

The author would like to express his greatest gratitude to Professor Dr. Satoshi Minakata, Department of Applied Chemistry, Graduate School of Engineering, Osaka University for his continuous guidance, many invaluable suggestions, and encouragement with warm enthusiasm throughout this work. The author wishes to express his deeply thanks to Professor Dr. Takashi Hayashi and Professor Dr. Hidehiro Sakurai for their reviewing this dissertation with helpful comments and suggestions.

The author also wishes to make a grateful acknowledgement to Associate Professor Dr. Youhei Takeda for his helpful teaching, valuable suggestions, and constant encouragement during the course of this study. He also thanks Assistant Professor Dr. Kensuke Kiyokawa for his helpful suggestions, discussions, and kind encouragement.

The author is deeply grateful to Dr. Nobuko Kanehisa and Associate Professor Dr. Toshiyuki Moriuchi for their assistance in single-crystal X-ray diffraction experiments. The author is indebted to Assistant Professor Dr. Takashi Tsujimoto for his assistance in DSC measurements and to Associate Professor Dr. Yumi Yakiyama for her assistance in diffuse

reflection spectra measurements. The author thanks Assistant Professor Dr. Taro Uematsu for his assistance in emission spectra measurements. The author would also like to express his gratitude to Dr. Przemyslaw Data, Mr. Piotr Pander, Dr. Heather Higginbotham and Professor Dr. Andrew P. Monkman for their valuable discussion and excellent collaboration about fabrication of OLED devices and measurements of their performances.

The author deeply thanks Ms. Yoshimi Shinomiya, Dr. Eiko Mochizuki, and Ms. Junko Ohmagari for their kind help and heart-warming encouragement.

Thanks are also due to the Instrumental Analysis Center, Graduate School of Engineering, Osaka University, for the measurement of spectral and analysis data.

The author is deeply indebted to Dr. Sota Okumura, Dr. Toshiki Nagamachi, Mr. Yoshiaki Maruoka and Mr. Kosuke Takahashi for their valuable discussion and active collaboration. Thanks are also due to all students of Minakata Laboratory for their hearty encouragement, constant support and kind friendship.

Finally, the author is deeply grateful to his family, Eiichi Okazaki, Momoyo Okazaki and Hayato Okazaki for their full understanding and perpetual support. It also gives the author pleasure to thank his grandparents, Haruo Okazaki, Kayoko Okazaki, Jin-itsu Kubo and Teruko Kubo for their warm encouragement.

Masato Okazaki